Instability in a quantum system can be probed by Out-of-Time-Ordered Correlators. We discover that they have a transition phenomenon governed by local instabilities differentiating integrable dynamics from generic chaos. It is a promising route to reliably detect quantum chaos. In the case that chaos is properly identified, its characteristic exponential sensitivity and mixing property give a novel protocol for controlling many-body quantum chaos. Utilizing chaos as a resource achieves exponentially fast targeting of macroscopically occupied single-particle states and offers a coherent procedure for state preparation in experimental platforms. Additionally, we explore the manifestation of chaos in ground states for many-body systems relevant to quantum computation. We leverage the recent progress in neural networks driven by artificial intelligence, in order to extend the numerical boundaries of many-body simulations reaching system sizes with a hundred sites.

Universität Regensburg
UNIVERSITÄTSBIBLIOTHEK

ISBN 978-3-88246-539-6
9 783882 465396

Signatures of Instability in Bosonic Many-Body Systems

Mathias Steinhuber

Mathias Steinhuber

Signatures of Instability in Bosonic Many-Body Systems

Eine Publikation der
Universitätsbibliothek Regensburg

Signatures of Instability in Bosonic Many-Body Systems

Dissertation zur Erlangung des Doktergrades der
Naturwissenschaften (Dr. rer. nat.) der Fakultät für Physik
der Universität Regensburg

vorgelegt von

Mathias Steinhuber

aus Sammarei

im Jahr 2025

Erstgutachter (Betreuer): Prof. Dr. Klaus Richter

Zweitgutachterin: Prof. Dr. Annabelle Bohrdt

Tag der Prüfung: 28. Oktober 2025

Bibliografische Information der Deutschen Nationalbibliothek

Die Deutsche Nationalbibliothek verzeichnet diese Publikation in der Deutschen Nationalbibliografie. Detaillierte bibliografische Daten sind im Internet unter http://dnb.dnb.de abrufbar.

ISBN (Print): 978-3-88246-539-6

ISBN (PDF): 978-3-88246-540-2

DOI: 10.5283/epub.78114

Link zur Online-Version: https://epub.uni-regensburg.de/78114

Satz und Layout: Mathias Steinhuber

Umschlaggestaltung: Peter Brünsteiner

Titelbild: Mathias Steinhuber

Herstellung: Universitätsbibliothek Regensburg

Erscheinungsort: Regensburg, 2026

Druck und Bindung: Digital Print Group o. Schimek GmbH, Nürnberg

Abstract

The central research objects are bosonic many-body systems and their instabilities. One powerful approach to probing these instabilities in quantum systems is through *Out-of-Time-Ordered Correlators* (OTOCs), and they are the focus of the first chapter. We investigate a transition phenomenon governed primarily by local instabilities, which differentiates integrable dynamics from generic chaotic behavior. This transition provides a promising route to reliably detect quantum chaos in many-body systems, motivating us to study the onset of chaos as a system evolves from integrable to mixed and fully chaotic regimes. Under the assumption that chaos is properly identified, we exploit its characteristic exponential sensitivity and mixing properties in the second part of our work. Here, we propose a novel protocol for *Controlling Many-Body Quantum Chaos*, utilizing chaos as a resource to achieve exponentially fast targeting of macroscopically occupied single-particle states, connected via chaotic heteroclinic trajectories. This theoretical framework offers a coherent targeting procedure for state preparation in experimental platforms. Finally, in the third part, we explore the manifestation of quantum chaos in low-energy states of many-body systems relevant for quantum computation, as system size increases. Recent advances in *Neural Quantum States* (NQS), leveraging machine learning progress driven by the surge of artificial intelligence, have significantly extended the numerical boundaries of many-body simulations, such that we now reach system sizes with a hundred sites. These developments open new opportunities for understanding chaos in large-scale quantum systems.

Dedicated to my dad, Sepp

List of published publications:

- F. Meier, M. Steinhuber, J. D. Urbina, D. Waltner, and T. Guhr, "Signatures of the interplay between chaos and local criticality on the dynamics of scrambling in many-body systems", Phys. Rev. E **107**, 054202 (2023), covered in Sec. 5.
- M. Steinhuber, P. Schlagheck, J. D. Urbina, and K. Richter, "Dynamical transition from localized to uniform scrambling in locally hyperbolic systems", Phys. Rev. E **108**, 024216 (2023), covered in Sec. 4.
- L. Beringer, M. Steinhuber, J. Diego Urbina, K. Richter, and S. Tomsovic, "Controlling many-body quantum chaos: Bose-Hubbard systems", New Journal of Physics **26**, 073002 (2024), covered in Chap. II.

List of publications in preparation:

- M. Steinhuber, J. Rigo, J. D. Urbina, K. Richter and M. Schmitt, "Emerging chaotic signatures at large system sizes", covered in Chap. III.
- T. Michel, M. Steinhuber, J. D. Urbina and P. Schlagheck, "Probing the transition towards chaotic scrambling", covered partially in Sec. 6.
- L. Beringer, M. Steinhuber, J. D. Urbina, K. Richter and S. Tomsovic, "The role of quantum chaos in controllability", not covered in the thesis.

Contents

Introduction

1. Motivation and Summary

One of the underlying and unfinished debates in the quantum chaos community is the very definition of quantum chaos in a many-body system. With respect to their classical limit, many-body quantum systems namely fall into one of two broad classes depending on the dimension of the local Hilbert space[1]. On the one extreme of large local Hilbert space, we have a precise classical limit. Together with a precise notion of when and how - via semiclassical methods [4–6] - the classical description actually faithfully reproduces the quantum dynamics [7]. Large spin and bosonic systems with many particles are examples for many-body systems with large local Hilbert spaces. On the other extreme, we have systems with small local Hilbert space like spin-1/2 chains or fermionic particles in a lattice. In the latter case, a classical limit can be defined, but the system lacks a notion of classical regime, i.e., the classical description is not guaranteed to faithfully reproduce the quantum dynamics and the semiclassical approximation breaks down.

Quantum chaos is explicitly associated to classical chaos in (many-body) systems with classical limit [5]. As characterized in Fig. 1.1, we are in the unfortunate situation of many-body systems not possessing a faithful classical description[2]. There is no direct link to the well-defined classical chaos [9, 10]. From this missing link, the community generalizes the definition of quantum chaos and classifies many-body systems to be quantum chaotic if its hallmarks are present. Examples of such quantum-chaos signatures are the validity of random matrix theory, following level spacing statistics [5, 11], exponential and saturating Out-of-Time-Ordered Correlators (OTOCs) [12], scars [13] etc.

We agree on the concept to adapt the definition of quantum chaos towards the presence of these certain effects. Nevertheless, as it is illustrated in Fig. 1.1, the community redirects the way of reasoning, which must be carefully considered and needs further refinement. There are exceptions, where false positives are identified, in particular for the Out-of-Time-Ordered Correlator [14–17]. This measure leads us to the first topic of our thesis and how to refine it to correctly detect integrable from chaotic quantum systems.

[1] We specify under the term *local Hilbert space* the allowed many-body configurations at a single (lattice) site. See Tab. 1.1 for an overview for different many-body system types.

[2] There are single-particle systems with no classical limit, e.g. quantum graphs [8], further single-particle systems without classical limit are a single electron or a single spin particle.

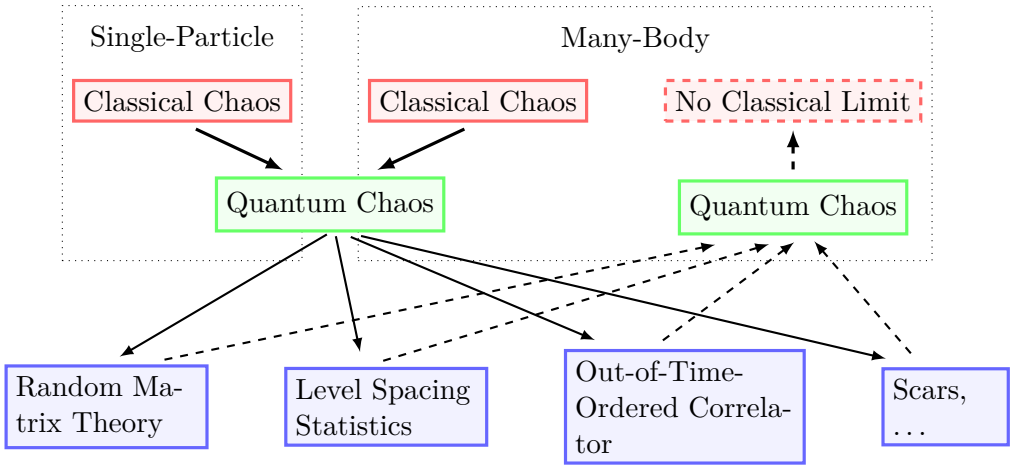

Figure 1.1: Quantum chaos in single-particle and many-body systems. Quantum chaos is directly connected to classical chaos in the single-particle[2] and many-body systems if a classical limit is adequate. We directly observe the signatures (blue) due to (classical) chaos. Many-body systems without classical limit are identified as quantum chaotic via the presents of these signatures [5]. The reversed reasoning (illustrated with dashed and opposite arrows) must be carefully verified due to false positives.

Out-of-Time-Ordered Correlators

The study of quantum many-body systems unveils profound phenomena that challenge our understanding of information, dynamics, and thermalization beyond our single-particle intuition [18–23]. Among these, the scrambling of quantum information - the delocalization of initially localized correlations across a system's degrees of freedom - has emerged as a central theme in modern many-body quantum physics. Scrambling is not only fundamental for understanding equilibration and thermalization in isolated systems, but also plays a pivotal role in topics such as the black hole information paradox [18, 24] and the quantum-classical correspondence [25].

A key diagnostic tool for probing information scrambling is the Out-of-Time-Ordered Correlator (OTOC), first introduced in the context of superconductivity [25] and later recognized for its deep connection to quantum chaos [7, 26]. OTOCs capture the sensitivity of operators under the Heisenberg time evolution, thereby quantifying how local information becomes distributed across the degrees of freedom. Their relevance spans a broad range of physical settings, including models of black holes [18, 27–30], strongly interacting many-body systems like the famous Sachdev-Ye-Kitaev (SYK) model [31, 32], and even systems that lack a classical counterpart [33]. The conceptual appeal of OTOCs lies in their ability to bridge semiclassical intuition with quantum dynamics, making them indispensable for both theoretical studies of chaos and thermalization. It even drives efforts for experimental proposals [34] and realizations [35–38].

Traditionally, quantum chaos has been explored in few-body systems [5], where semiclassical techniques allow for the identification of classical counterparts and Lyapunov exponents. In this context, the exponential growth of the

OTOC $C(t) \sim \exp(2\lambda_q t)$ at early times has been interpreted as the quantum analog of classical sensitivity to initial conditions, leading to the introduction of the quantum Lyapunov exponent λ_q and matching the classical Lyapunov exponent λ_L in fully chaotic models [39]. In semiclassical systems, this quantity can often be related to classical instability measures through canonical quantization. It links the squared commutator structure, e.g. $|[\hat{q}(t), \hat{p}]|^2$, of OTOCs to squared Poisson brackets $\{q(q_0, p_0, t), p_0\}^2$ in the classical limit [12, 25] and provides a direct link to the classical Lyapunov exponent via the classical monodromy matrix $\{q(q_0, p_0, t), p_0\}^2 = (\partial q(q_0, p_0, t)/\partial q_0)^2 \sim \exp(2\lambda_L t)$.

However, this interpretation is far from straightforward and strict. Recent studies have revealed that exponential OTOC growth does not uniquely signal classical chaos. Even integrable systems, those devoid of chaotic trajectories and have regular motion meaning $\lambda_L = 0$, can exhibit exponential growth in OTOCs if their classical phase space contains local instabilities, such as hyperbolic fixed points [14–16, 40]. This raises critical questions about the meaning of OTOC growth rates and their suitability as chaos diagnostics, since they would classify such integrable systems with a hyperbolic fixed point false positively as quantum chaotic systems. Intriguingly, numerical and analytical investigations have reported conflicting results: Ref. [15] finds that $2\lambda_q = \lambda_s$ coincides with the classical local stability exponent λ_s of the hyperbolic fixed point, while Ref. [14] suggests a doubling,$2\lambda_q = 2\lambda_s$. Understanding this discrepancy is essential for properly interpreting OTOCs as probes of quantum chaos and scrambling. Based on our publication [2], this thesis addresses the gap by uncovering a universal crossover between the two reported regimes. We demonstrate that in systems with a low-dimensional classical analog and a semiclassical limit, the early-time growth of OTOCs exhibits a transition from $2\lambda_s$ to λ_s within the pre-Ehrenfest time regime. This transition originates from a dynamical evolution of the initial quantum state in phase space and becomes sharply defined in the classical limit $\hbar_{\text{eff}} \to 0$. By engineering the wave-packet's shape around the hyperbolic fixed point, let us tune the transition to the two limits $2\lambda_q = 2\lambda_s$ and $2\lambda_q = \lambda_s$ resolving the conflicting results [14, 15]. Our results establish this crossover as a hallmark of integrable systems with local instabilities and propose its use as a diagnostic tool for distinguishing between integrable and chaotic dynamics.

We continue and focus our analysis on systems with a low-dimensional classical limit and mixed phase space, where both local and global indicators of instability, such as positive stability exponents λ_s and Lyapunov exponents λ_L, coexist. We propose in Ref. [1] that in such mixed systems, the exponential growth rate of OTOCs in the early-time regime reflects a nontrivial interplay between these local and global dynamical features. Specifically, we hypothesize that the growth exponent λ_q of the OTOC encodes contributions from both types of instabilities, and that the temporal profile of OTOCs can thus reveal underlying phase-space structures.

In addition to static models, we explore periodically driven (kicked) systems as a means to study the transition from integrable to mixed and chaotic phase spaces. Kicked systems provide a controllable way to tune the strength of chaos,

offering a unique testbed for analyzing how the OTOC growth behavior evolves as the system moves from regular to chaotic dynamics. This allows us to connect the $2\lambda_s$ to λ_s crossover mechanism in purely integrable settings to the onset of chaos in mixed systems.

Finally, we emphasize the importance of proper regularization when evaluating thermal OTOCs, particularly in the early-time regime where deviations from the bound on chaos [18] can arise in finite-size systems [31]. Our numerical results highlight that such regularization is essential for extracting meaningful exponents and ensuring consistency with the theoretical bound. Despite the importance of the regularization at finite $\hbar_{\text{eff}}$, our results indicate that the regularization has diminishing effect at the exponential growth in both semiclassical and thermodynamical limits, i.e., the regularization agrees with the unregularized thermal OTOC.

Our investigation into OTOCs is primarily restricted to times shorter than the Ehrenfest time τ_E, beyond which the direct quantum-classical correspondence breaks down [41, 42]. Prior to τ_E, the temporal behavior of OTOCs typically follows a three-stage evolution: a polynomial pre-exponential regime (up to an ergodic or dissipation time τ_s), an exponential growth regime ($\tau_s < t < \tau_E$) and eventual oscillations in integrable regions or saturation governed by the finite dimensionality of the quantum Hilbert space depending on the initial state [18, 43–45]. While the terminology varies - some works [18, 44] refer to τ_E as the scrambling time t_* - we adopt the semiclassical perspective and refer to it as the Ehrenfest time, emphasizing its role in the breakdown of classical predictability. The first chapter systematically analyzes OTOC growth in the pre-Ehrenfest regime, where we aim to provide a unified framework for understanding how local instabilities influence early-time quantum dynamics. In particular, we show how the $2\lambda_s$ to λ_s crossover emerges naturally and offers insight into its connection with the underlying phase-space dynamics in the Bose-Hubbard model. Our findings promise a robust diagnostic tool for exploring the nature of quantum (reversible) scrambling in integrable versus chaotic systems.

One other clear signature marking the end of the classical-quantum correspondence - a wave packet diverging from the classical description - brings us to the next topic of the thesis: guiding wave packets on fast heteroclinic trajectories beyond the Ehrenfest time which requires controlling chaos by intervening its breakdown due to interplay of classical spreading and quantum interference.

Controlling (Many-Body) Chaos

The first chapter examines the signatures of chaos. In particular, the exponential instability inherent in chaotic dynamics typically drives a system toward relaxation, equilibration, or thermalization due to the strongly mixing nature of the chaotic motion [9, 10]. This same property, however, makes controlling chaotic systems fundamentally challenging. Yet, under certain conditions, chaos can be harnessed as a resource for control. Classic examples include Ulam's

conjecture of gravity assist [46] and nicely applied by the diversion of the International Sun-Earth Explorer satellite to a Giacobini-Zinner comet flyby [47, 48]. More comprehensively, these are ideas belonging to the theory of *classical targeting* [49–53], which falls under the more general moniker *controlling chaos* [54].

For fully chaotic systems, this control capability originates from the existence of heteroclinic trajectories - special solutions first identified by Poincaré [55] and Lyapunov [56]. In essence, there exists a set of initial conditions whose trajectories diverge from a reference trajectory at the maximal exponential rate. Conversely, there is a corresponding set of trajectories that approach the desired final conditions at the maximal exponential rate. Trajectories belonging to both sets constitute the heteroclinic connections. These rare paths make it possible to achieve a drastic reduction in transition time between two phase-space regions with an extremely small, but precisely chosen, adjustment of the initial conditions.

For quantum systems, this closeness is naturally limited by the minimal phase-space volume occupied by a quantum state, roughly h^L, where h is Planck's constant [57] and L is the system size (degrees of freedom). Among the infinitely many heteroclinic connections, one achieves the shortest possible transition time, denoted $t_{\min}$, given this constraint. The immediate neighborhood of trajectories approximating this optimal heteroclinic path has a volume on the order of $h^L \exp\big(-h_{\mathrm{KS}} t_{\min}\big)$, where h_{KS} is the Kolmogorov - Sinai entropy [58, 59], equal to the sum of positive Lyapunov exponents. For an extensive system, where the mean Lyapunov exponent remains constant and h_{KS} scales linearly with L, this neighborhood shrinks exponentially with system size. Consequently, much of the effort in classical chaos control focuses on identifying these exceedingly rare heteroclinic trajectories that enable optimal steering of the system. General numerical strategies for identifying these rare solutions have been developed, such as the approach described in Ref. [60], and are essential for our implementing efficient targeting protocols.

Recently, the concept of classical targeting has been extended into the quantum domain and applied to a paradigmatic chaotic system - the kicked rotor [61, 62] - as introduced in [63, 64]. For quantum systems possessing a well-defined classical analog, heteroclinic structures can similarly be exploited to guide the system toward a predetermined, potentially exotic, target state in a significantly accelerated manner, all within unitary evolution, thereby maintaining full coherence. The critical new ingredient absent in the classical setting arises from the uncertainty principle [65]. A quantum state cannot be localized to an exact phase-space point; instead, its closest classical counterpart is a minimum-uncertainty wave packet or coherent state, depending on context. Through Wigner transform analysis [57], these states correspond most closely to a Liouvillian distribution of initial conditions rather than a single trajectory. Therefore, a quantum analog of classical targeting must control the Liouvillian flow surrounding the heteroclinic pathway (see Fig. 1.2). Otherwise, the Liovillian distribution quickly disperses with generic time evolution in the quantum setup

after the Ehrenfest timescale [41, 42].

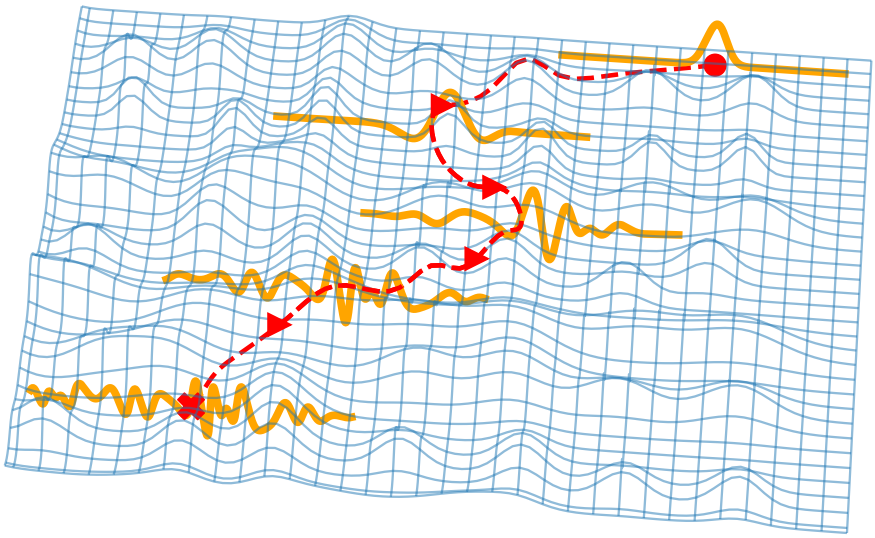

Figure 1.2: Schematic illustration of an initially localized quantum state guided along a classical transport trajectory. A localized quantum state, here represented as an orange cut through its Wigner function, centered around an initial phase-space point (upper right red dot) should be guided to a specific target state (lower left cross) by following a solution of the classical limit (red dashed line with arrows). In a generic system exhibiting quantum chaos, the localized state would equilibrate in a logarithmically short time period visualized by the diffusion of the orange wave packet. Thus, the spreading must be counteracted in a control protocol. The blue grid schematically represents a Hamiltonian energy landscape generating unstable dynamics. Reprinted from Ref. [3].

This additional requirement has motivated the development of two strategies for optimal coherent quantum targeting. The first approach employs local stability analysis to periodically counteract wave-packet spreading [63]. The second approach leverages quantum simulation techniques [66], whereby a different, engineered Hamiltonian reproduces the heteroclinic evolution in a stable manner [64]. In this work, we apply the latter technique to a prominent, experimentally realizable many-body system, namely the Bose-Hubbard model [67, 68].

Quantum control, as a broader field, has a long-standing history, originally driven by the ambition to steer chemical reactions [69–74], and more recently extended to many-body systems [75–77]. The comprehensive survey [78] and the review of optimal control theory [79] provide a broad overview. However, these efforts generally do not address the unique challenges posed by quantum chaos, where exponential instability can be transformed from an obstacle into a resource. Although a few works touch upon related ideas [80–86], none of them develop general strategies for optimal coherent targeting in quantum chaotic

many-body systems.

The potential benefits of quantum targeting in isolated many-body chaotic systems are significant. Chaotic dynamics guarantees ergodicity and, eventually, all accessible states are explored regardless of the starting point. This implies that, in principle, any classically allowed target state can be reached. However, in a phase space of exponentially growing volume, as in many-body systems, the time required for such an ergodic exploration becomes astronomically large. By contrast, heteroclinic trajectories provide rare but exceptionally fast routes connecting specific initial and target states, offering a dramatic acceleration toward the desired configuration.

Bosonic ultracold atomic systems present an ideal platform for implementing coherent quantum targeting. They combine exquisite experimental control over tunable parameters with the capability to realize quantum simulations [87–96]. Furthermore, these systems admit a clear classical analog in the large-particle-number mean-field limit, governed by the Gross-Pitaevskii equation or, on a lattice, by discrete non-linear Schrödinger equation [97] for the Bose-Hubbard model [68, 98]. This enables a phase-space formulation, identification of strongly chaotic regimes [99, 100], and analysis of heteroclinic dynamics. Additional advantages include continuous $U(1)$ and discrete dynamical symmetries, which can be exploited in control protocols for mapping between different lattice dimensions and broadening the range of applicable initial conditions. Finally, experimental techniques allow for tuning on-site interactions and chemical potentials with high precision [101–103] - a critical requirement for implementing our proposed control scheme. Within a chaotic phase-space volume, any initial and target state - represented by a phase-space cell each via coherent states [104] and respecting the system's conserved quantities[3] - can, in principle, be connected by a trajectory. Indeed, ergodicity guarantees that almost all trajectories will eventually establish such a connection. However, the associated timescale is prohibitively large. The reason is that the phase-space volume grows exponentially with the number of degrees of freedom L (the number of lattice sites in the Bose-Hubbard model), and an unguided exploration would therefore require an astronomically long time. To overcome this, one must seek these exceptional heteroclinic trajectories that connect the initial and final points in minimal time.

The dilemma of large system-sizes brings us to the third topic: pushing the numerical boundaries via machine learning methods, where exactly we use neural networks for quantum states allowing us to go beyond system sizes in the first two parts.

[3]For the Bose-Hubbard mean-field limit, these conserved quantities are the energy and the total particle number.

Large Systems Sizes: Chaotic Signatures via Neural Quantum States

The third part of this thesis addresses a fundamental limitation present in all numerical quantum simulations discussed so far: they are constrained to small system sizes and a small number of degrees of freedom. The challenge of simulating many-body quantum systems arises because the dimension of the Hilbert space grows exponentially with system size L summarized in Tab. 1.1.

Many-body system type	$\dim \mathcal{H}_{\text{loc}}$	$\dim \mathcal{H}$
Spins with spin quantum number s	$2s+1$	$(2s+1)^L$
Spin-1/2 fermions	4	4^L
Bosons with local Hilbert space dimension $\dim \mathcal{H}_{\text{loc}}$	$\dim \mathcal{H}_{\text{loc}}$	$(\dim \mathcal{H}_{\text{loc}})^L$
Bosons with fixed total particle number N	$N+1$	$\binom{N+L-1}{L-1}$

Table 1.1: Scaling of the Hilbert space dimension for different particle types (only a selection, not a complete list). All show an exponential scaling in the system size L with the base being the local Hilbert space dimension. An exception are systems with conservation laws like bosons with fixed total particle number, however the binomial coefficient is still exponential in L.

It is irrelevant which specific particle type one considers - the scaling remains exponential. This limitation is not a minor inconvenience if our goal is to study signatures of quantum chaos in systems relevant for experiments [105] or even modern quantum computers [106, 107]. These devices involve hundreds of sites, leading to astronomically and intractably large Hilbert space dimensions. Consequently, simulations using standard exact diagonalization methods, as employed in the previous sections for quantities such as the *Out-of-Time-Ordered Correlator* or the *Controlling Quantum Chaos* application, are infeasible.

Recent developments in (quantum) physics due to machine learning offer a promising path beyond exact methods. The integration of machine learning is occurring broadly: learning from experimental data [108, 109], characterizing measurements, or reinforcement learning [110], entangling qubits, or extrapolating classical dynamics [111], predicting turning points, and many more applications [112]. In particular, neural networks have been proposed as a new ansatz to represent quantum states [113]. Owing to their success in modeling complex structured data, neural networks are now explored for representing

quantum states [108, 113–121]. These representations have been aptly named *Neural Quantum States* (NQS).

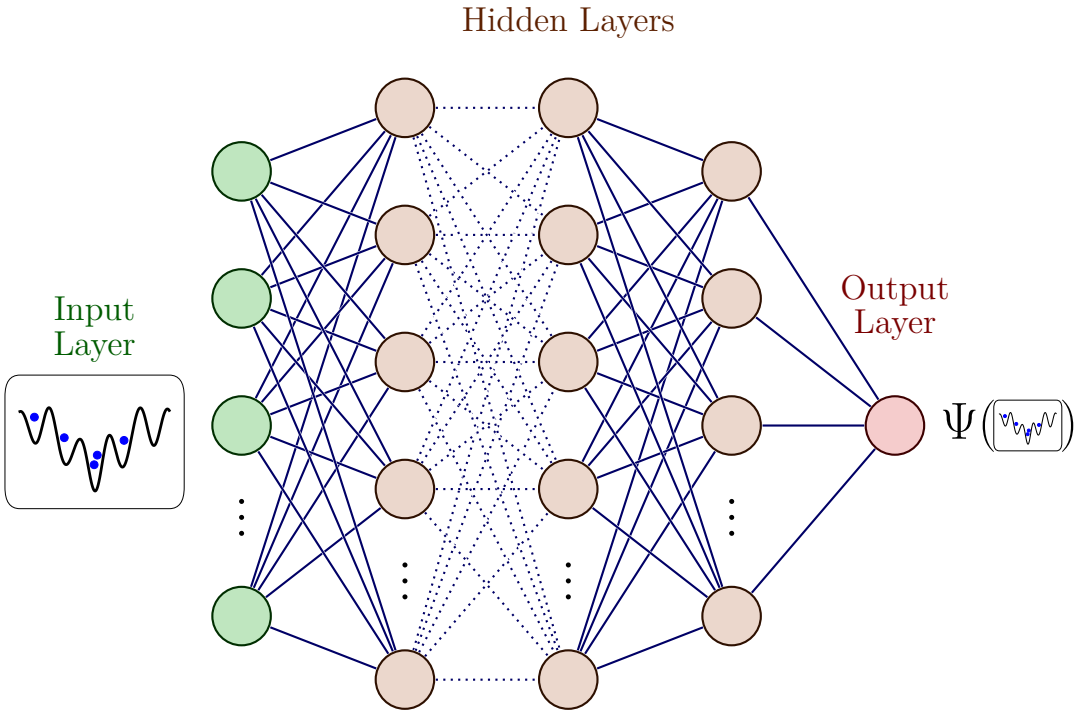

Figure 1.3: Schematic representation of a neural quantum state (NQS) using a feed-forward network. A configuration is inserted into the input layer (green), is processed through hidden layers (orange), and the output layer returns the complex amplitude. Non-linear activations and layer depth encode the wave-function through trainable parameters (weights and biases). Later on in the thesis, we use more sophisticated neural network architectures.

The neural network ansatz alleviates the storage problem inherent to exact diagonalization by evaluating amplitudes on demand instead of storing all basis configurations. Efficient parallel evaluation combined with the universal approximation theorem [122] is its main advantage and is typically done by feeding each configuration into an input layer, processed through hidden layers in order to obtain the wave-function amplitude at the output layer which we illustrate in Fig. 1.3 for a feed-forward network. Due to the flexibility of the input topologies and architectures, various applications are possible which are arguments for using NQS. Alternatively, tensor networks [123–125] provide an excellent ansatz for low entanglement states, especially in one-dimensional systems. But with aiming beyond one-dimensional systems, we focus on the NQS approach because, among others [119], Ref. [126] demonstrates that NQS is a good description in two-dimensional lattices.

Provided that the target quantity can be expressed as a loss function or as a propagation estimable via Monte Carlo methods. This NQS approach enables us

to study system sizes beyond the reach of exact diagonalization. Fundamental for the success is that optimizing and propagating the NQS ansatz leverage efficient Monte Carlo estimations and gradient computation in the neural network variational parameters.

Reaching larger system sizes is crucial for probing chaotic behavior expected to emerge in many-body systems as size increases [127]. This is particularly relevant in coupled transmon arrays with detuning, which is a leading quantum computing platform [106, 107, 128–131]. Refs. [127, 132] report chaotic signatures that could challenge the stability of transmon arrays as quantum computing hardware, as envisioned in [106]. However, their quantum calculations hinting towards delocalization of computational states are limited to small system sizes. In an effective transmon model, where excitations map to strongly attractive bosons described by a Bose-Hubbard Hamiltonian with disorder, we aim to confirm the absence of many-body localization [21, 133] in the Bose-Hubbard ground state. For such bosonic models, the NQS ansatz has demonstrated their ability to describe the quantum system in various contexts [134–138].

By employing language models as an NQS ansatz, we show that the ground state delocalizes with increasing system size illustrated in Fig. 1.4, where the particle localization vanishes. We do not observe any phase transition towards a localized ground state. However, due to numerical challenges, we have not yet reached the typical coupling values [127]. Our results show that smaller coupling of the transmons lead to more localized ground states, although they still delocalize as the system size increases. Our interpretation is that while low coupling reduces delocalization, it does not fully suppress it. Since particles in the effective Bose-Hubbard model represent excitations that, in low numbers, resemble computational states, we predict that its delocalization behavior over system size also manifests in transmon systems [106, 107, 128–131]. Consequently, scaling up quantum computers beyond their current sizes could be more challenging, as stronger delocalization effects - destabilizing the computational states - would need to be mitigated. An alternative transmon-based approach to quantum computing exists [139–142], in which the individual transmons are effectively decoupled during idle periods. Google's Sycamore processor [139] is an example of this second class, to which our results do not apply. For our model, the transmon must be coupled statically (during idle periods) by a finite residual amount like in the setups [106, 107, 129–131].

In order to proceed beyond ground states, we outline an adiabatic transport approach [143, 144] for NQS, granting access to excited states corresponding to computational states in transmon chips across system parameters. This approach is an alternative to an extended ground-state minimization algorithm [145] calculating the lowest l excited states. We favor the adiabatic method due to its flexibility to follow any eigenstate in the spectrum compared to the limitation to the lowest eigenstates next to the ground state. In addition, the adiabatic transport scales linearly, $O(l)$, with the number of eigenstates, in contrast to the quadratic scaling, $O(l^2)$, of the adapted minimization [145]. Moreover, since our system of interest has no symmetries, a symmetry-based approach for excited

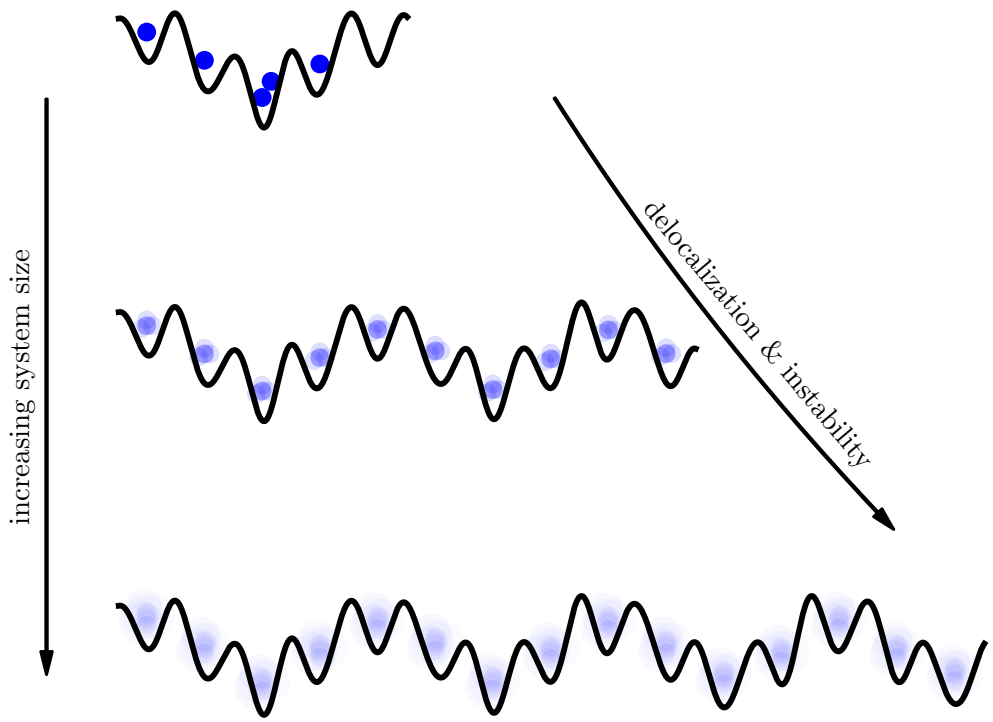

Figure 1.4: Illustration of chaos emerging in low-energy states as system size increases. With fixed quantum scale $\hbar$, adding degrees of freedom causes initially regular states to delocalize and develop classical instabilities. For visualization purposes, delocalization is shown as particle position smearing.

states [146] is infeasible. At present, we demonstrate a proof-of-concept adiabatic transport calculation for small system sizes. Consistent with [127, 132], the excited states exhibit avoided crossings, a hallmark of quantum chaos, hinting towards avoided crossings to be present in devices proposed in coupled transmon arrays with detuning.

2. Outline of the Thesis

The topics in the thesis are structured in three main chapters which reflect the projects and phases of the overall PhD-project.

Chapter I: Probing Quantum Chaos with Out-of-Time-Ordered Correlators

This chapter comprises six sections. We begin in Sec. 3 with the fundamental concepts necessary to understand OTOCs. In Sec. 4, we provide a heuristic explanation for the emergence of different exponential regimes for hyperbolic fixed points and the associated crossover from $2\lambda_s$ to λ_s for the quantum Lyapunov exponent. We conduct an extensive study of the Bose-Hubbard dimer, presenting results from [2]. Building on this, Sec. 5 explores mixed and chaotic Bose-Hubbard lattices through OTOCs, addressing aspects of the conjectured link between mixed stability and quantum Lyapunov exponents, as we discuss in [1]. Due to numerical limitations in larger systems, we return in Sec. 6 to the kicked dimer to investigate the transition to chaos. Before summarizing in Sec. 8, we also discuss preliminary results on thermal OTOCs in Sec. 7.

Chapter II: Controlling Many-Body Quantum Chaos

Based on [3], we shift focus from probing chaos to harnessing it as a resource for state preparation. After introducing necessary background in Sec. 9, including heteroclinic dynamics and notational conventions, we review the Bose-Hubbard model in Sec. 10 which focuses on coherent and Fock states, truncated Wigner approximation and a reference periodic trajectory given by the density wave. Next, the strategy in Sec. 11 is introduced to control and guide a wave packet along a trajectory. Sec. 12 demonstrates coherent quantum targeting in one-dimensional lattices, followed by an analysis of protocol robustness in Sec. 13. The chapter concludes in Sec. 14 with a summary of our approach to controlling many-body quantum chaos.

Chapter III: Towards Larger System Sizes: Neural Quantum States

This chapter addresses large-system simulations using Neural Quantum States (NQS). After introducing neural network approaches and Monte Carlo methods in Sec. 15, we detail autoregressive methods in Sec. 16, namely the architectures, Gumbel sampling and quantum-number-preserving sampling. Algorithms are reformulated as Monte Carlo estimations and optimization problems (trainings) to enable gradient-based techniques in Sec. 17. Before presenting results, we briefly show how low-lying excitations of the transmon model map to a strongly repulsive Bose-Hubbard Hamiltonian in Sec. 18. In Sec. 19, we demonstrate ground-state delocalization with increasing system size and in Sec. 20 we provide a proof-of-concept calculation for adiabatic transport of low-lying excited states in

smaller systems. Sec. 21 closes the chapter with a summary, highlighting challenges and future directions.

We give a final conclusion in Chap. IV providing an inclusive short overlook over the key results in the three topics and future fascinating perspectives. An appendix gives further details to aspects of classical physics in App. A, to the Wigner-Moyal expansion in App. B, to localized quantum states in App. C, to regularization in the harmonic oscillator in App. D, and to the time evolution in control systems in App. E. The last part of the appendix, App. F, contains the visualizations of all ground-state training runs. Afterwards and before the bibliography, the most important section comes: the acknowledgments granting my personal tribute to the people who contributed to this work.

I. Probing Quantum Chaos with Out-of-Time-Ordered Correlators

To find a reliable way of classifying a many-body system as chaotic or integrable is a topic of ongoing research in the quantum chaos community [7]. One of the proposed quantities is the *Out-of-Time-Ordered Correlator* (OTOC). Its exponential increase is primarily associated with chaos, but recently there are several reported false positives [14–16] showing that its exponential increase is not due to chaos but just due to local instabilities in integrable models. One of our goals in this first chapter is to study the false-positive cases in more details. Thereby, we look into hyperbolic integrable systems to find less obtrusive differences to mixed and chaotic systems. Afterwards we go on to mixed and chaotic systems and in the last part we present findings for the thermal OTOC.

3. Preliminaries for the Out-of-Time-Ordered Correlator

We begin by setting a common ground by fixing basic definitions, known concepts and approximations, before we go on with specific results of the thesis. Nevertheless, we still assume that the reader has an advanced understanding of classical mechanics (integrable and chaotic dynamics, etc.) and quantum physics (Heisenberg time evolution, operator algebra, Wigner-Moyal representation, etc.). Some of the necessary details about classical physics we repeat in App. A, but let us begin with the definition of the OTOC.

3.1. Out-of-Time-Ordered Correlator

Given two operators $\hat{A}$ and $\hat{B}$, we define the so-called *Out-of-Time-Ordered Correlator* (OTOC) by the correlator

$$C(t) = C(t) = \mathrm{tr}\left\{\hat{\rho}\big[\hat{A}(t),\hat{B}\big]^\dagger\big[\hat{A}(t),\hat{B}\big]\right\}, \tag{3.1}$$

where $\hat{\rho}$ is a density operator specifying the state. Whenever we calculate the OTOC for some state, this means we set its density operator accordingly into Eq. (3.1)[1]. The operator $\hat{A}(t)$ is time-evolved in the Heisenberg picture, i.e., $\hat{A}(t)$

[1]This definition includes pure and mixed states, later on in Eq. (7.2) we see a distributed regularized version, where the density matrix is split between the operators.

is given by applying the time-evolution operator $\hat{U}(t)$ via $\hat{A}(t) = \hat{U}^\dagger(t)\hat{A}\hat{U}(t)$. In contrast, the second operator $\hat{B}$ is not time-evolved and static.

At a first sight, Eq. (3.1) is an ordinary expectation value, but when the squared commutator of the OTOC in Eq. (3.1) is expanded in individual contributions

$$\begin{aligned} C(t) = &\operatorname{tr}\{\hat{\rho}\hat{B}^\dagger\hat{A}^\dagger(t)\hat{A}(t)\hat{B}\} + \operatorname{tr}\{\hat{\rho}\hat{A}^\dagger(t)\hat{B}^\dagger\hat{B}\hat{A}(t)\} \\ &- 2\,\mathrm{Re}\Big\{\operatorname{tr}\{\hat{\rho}\hat{A}^\dagger(t)\hat{B}^\dagger\hat{A}(t)\hat{B}\}\Big\}, \end{aligned} \tag{3.2}$$

one obtains besides contributions admitting a standard time-ordering extra irreducibly unordered correlations [18, 25]. Their anomalous dynamical behavior is the central object of study in this chapter. To be specific, in Eq. (3.2), the first line contains time-ordered products of operators and the second line has mixed and unordered combinations of the time-evolved operator $\hat{A}(t)$ and the non-time-evolved operator $\hat{B}$. Hence, the name *Out-of-Time-Ordered Correlator* is given to the object in Eq. (3.1).

If the operators $\hat{A}$ and $\hat{B}$ are unitary, the OTOC simplifies further and reduces to the out-of-time ordered part only. Since each time-ordered part is equal to the identity respectively due to $\hat{A}^\dagger(t)\hat{A}(t) = \mathbb{1}$ and $\hat{B}^\dagger\hat{B} = \mathbb{1}$, the OTOC of unitary operators

$$C^{\text{unitary}}(t) = 2 - \mathrm{Re}\Big\{\operatorname{tr}\{\hat{\rho}\hat{A}^\dagger(t)\hat{B}^\dagger\hat{A}(t)\hat{B}\}\Big\} = 2 - F(t)$$

is given by the quantity $F(t)$ which is also commonly called out-of-time ordered correlator (OTOC) [18, 25], although we denote the term OTOC only for the squared commutator in Eq. (3.1).

3.2. Wigner-Weyl Representation of the OTOC

In chaotic systems, the prominent property of the OTOC is exponential growing at early times before the so-called Ehrenfest time [7, 41]. In such a case, its exponent is quantified by the so-called *quantum Lyapunov exponent* in order to separate it from the Lyapunov exponent of a classical system. But in chaotic quantum systems with a classical limit, the quantum Lyapunov exponent is related to the (classical) Lyapunov exponent of classical chaotic motion. Their connection is either based on the Wigner-Weyl formalism or on a semiclassical derivation with encounters [147–150].

We only discuss the former derivation from the leading order in the semiclassical parameter $\hbar_{\text{eff}}$ of the Wigner-Weyl expansion, namely the Truncated-Wigner Approximation (TWA) of the OTOC and we encourage looking at App. B for details of the expansion. By keeping only the leading-order term in $\hbar_{\text{eff}}$, we get

$$\begin{aligned} C(t) \;&= \hbar_{\text{eff}}^2 \iint_{\text{PS}} \mathrm{d}^L q\, \mathrm{d}^L p\; W_\rho(\vec{q},\vec{p}) \Big|\Big\{A_{\text{W}}(\vec{q},\vec{p},t), B_{\text{W}}(\vec{q},\vec{p})\Big\}\Big|^2 \\ &\quad + O(\hbar_{\text{eff}}^3). \end{aligned} \tag{3.3}$$

In short, we replace commutators by the Poisson brackets and the leading order is $\hbar_{\text{eff}}^2$ for the OTOC, since replacing each commutator leads to one factor of $\hbar_{\text{eff}}$. The integral $\iint_{\text{PS}}$ is a double integral with respect to the classical position $\vec{q}$ and momentum $\vec{p}$ over the whole phase space (PS). The quantities A_{W} and B_{W} are the Weyl symbols of the operators which are defined by

$$O_{\text{W}}(\vec{q},\vec{p}) = \frac{1}{\sqrt{2\pi\hbar_{\text{eff}}}^L} \int_{-\infty}^{\infty} \mathrm{d}^L y \, \langle \vec{q} - \vec{y}/2| \, \hat{O} \, |\vec{q} + \vec{y}/2\rangle \exp\{i\vec{p}\cdot\vec{y}/\hbar_{\text{eff}}\} \tag{3.4}$$

and the Wigner function $W_\rho(\vec{q}_0,\vec{p}_0)$ which is the Weyl symbol of the density operator of the initial state ρ

$$W_\rho(\vec{q},\vec{p}) = \rho_{\text{W}}(\vec{q},\vec{p}) = \frac{1}{\sqrt{2\pi\hbar_{\text{eff}}}^L} \int_{-\infty}^{\infty} \mathrm{d}^L y \, \langle \vec{q} - \vec{y}/2| \, \hat{\rho} \, |\vec{q} + \vec{y}/2\rangle \exp\{i\vec{p}\cdot\vec{y}/\hbar_{\text{eff}}\}, \tag{3.5}$$

whereby our convention is to denote it with $W(\vec{q},\vec{p})$ instead of $\rho_{\text{W}}(\vec{q},\vec{p})$. The Wigner function is classified as a quasi-probability distribution. Quantum Mechanics can be formulated exactly via this phase-space picture, where the Wigner function acts as a normalized probability distribution, but its densities can be negative. How much negativity a quantum states exhibits in its Wigner function is a signature of its non-classicality, its quantumness [104]. The general form for the Weyl symbol of an operator can be complicated, but for example the position $(\hat{q}_j)_{\text{W}}(\vec{q},\vec{p}) = q_j$ and momentum operator $(\hat{p}_j)_{\text{W}}(\vec{q},\vec{p}) = p_j$ have their classical counterpart as their Weyl symbols.

By staying consistently in the leading order expansion of $\hbar_{\text{eff}}^2$, the Heisenberg time dynamics of the quantum operator A_{W} is mapped to time dynamics of the classical observable $A_{\text{W}}(\vec{q}_0,\vec{p}_0,t) = A(\vec{q}_0,\vec{p}_0,t) = A(\vec{q}(\vec{q}_0,\vec{p}_0,t),\vec{p}(\vec{q}_0,\vec{p}_0,t))$, which arises from the classical propagation of the initial condition $(\vec{q}_0,\vec{p}_0)$. We refer to App. B which gives further details to the connections via the expansion of the quantum time evolution in $\hbar_{\text{eff}}$.

We define the *quantum Lyapunov exponent* λ_{q} by one half of the exponent to which the OTOC grows at early times. Assuming a classical chaotic system (definition in App. A) and choosing $\hat{A} = \hat{q}_j$, $\hat{B} = \hat{q}_l$ (without loss of generality), we see via

$$C(t) \propto \hbar_{\text{eff}}^2 e^{2\lambda_{\text{L}} t} = \hbar_{\text{eff}}^2 e^{2\lambda_{\text{q}} t} \tag{3.6}$$

that the quantum Lyapunov exponent is the classical Lyapunov exponent. This follows from the Possion bracket

$$\{q_j(\vec{q}_0,\vec{p}_0,t), q_{l0}\} = \frac{\partial q_j(\vec{q}_0,\vec{p}_0,t)}{\partial p_{l0}} \propto e^{\lambda_{\text{L}} t}$$

which gives an element of the monodromy matrix (see Sec. A.1.2). The monodromy matrix $(\partial\vec{x}(\vec{x}_0,t)/\partial\vec{x}_0)_{jl}$ encodes the stability of the classical motion at an initial point $\vec{x}_0 = (\vec{q}_0,\vec{p}_0)$ in phase space. Except for special cases (see again

App. A.1.2), it grows in leading order with the Lyapunov exponent λ_{L} (> 0 in the chaotic region). In several chaotic systems, this quantum Lyapunov exponent has been reported [39, 151] and the OTOC measures the classical instability of a chaotic system via its early-time exponential growth.

We specify two timescales defining the early-time region of the OTOC: the *ergodic time* $\tau_{\mathrm{s}} = 1/\lambda_{\mathrm{L}}$ is the start time, where the exponential growth becomes dominant, $\lambda_{\mathrm{L}} t > 1$, compared to the sub-exponential initial behavior. The validity of Eq. (3.6) - the exponential growth region - brings us to the second important timescale, namely the Ehrenfest time [41, 42]

$$\tau_{\mathrm{E}} = \frac{1}{\lambda_{\mathrm{L}}} \ln \frac{1}{\hbar_{\mathrm{eff}}}. \tag{3.7}$$

At this timescale, the leading order in the TWA Eq. (3.6) reaches the magnitude $O(1)$. Consequently, higher orders of the expansion are necessary which lead to a saturation of the OTOC in the chaotic case [12]. Still, the TWA gives us the region $[\tau_{\mathrm{s}}, \tau_{\mathrm{E}}]$ of exponential growth between the ergodic time τ_{s} and Ehrenfest time τ_{E}. Therefore, the length of the exponential region depends on the Lyapunov exponent and the effective Planck constant $\hbar_{\mathrm{eff}}$. The latter has different expressions in different contexts. It is given by the usual Planck constant divided by a typical action, $\hbar/S_{\mathrm{typ}}$. in the single-particle case [5, 152, 153], and the inverse of the total spin quantum number $1/S$ for spin systems [16, 31, 154–156]. In one case of interest here, interacting bosonic systems, $\hbar_{\mathrm{eff}} = 1/N$ is given by the inverse of the total particle number N after convenient rescaling of the interaction strength [6, 7, 157].

At this point, we understand the generic chaotic approximation in Eq. (3.6), our aim in the next sections is to withdraw from the fully chaotic setup and instead study the integrable case in depth, because there is another local source which gives us exponential growth for the OTOC which requires no chaos at all.

4. OTOC in Integrable Systems with Local Hyperbolicity

With the Truncated-Wigner Approximation in the previous section, we establish a basic understanding how the OTOC behaves for short times. Namely, it follows the average of the classical time evolution of the squared Poisson bracket of the classical quantities over the Wigner function, the quasi probability of the quantum state defined on the phase space. Hence in a chaotic system, the OTOC grows exponentially with twice the Lyapunov exponent. The long-time (post-Ehrenfest) saturation of generic OTOCs has been subject of several studies, both in the chaotic [147, 151] and integrable [14, 158] regimes where interference effects beyond a pure quasi-classical (Truncated Wigner) approach appear [159]. However, our focus is the short time-frame, and this quasi-classical approach based on the Wigner-Moyal expansion, which is a regular expansion

around $\hbar_{\text{eff}} \to 0$ [104, 160, 161], is perfectly appropriate. We investigate integrable systems in the following, which is part of the publication [2] and our goal is to refine the pre-Ehrenfest theory for reversible scrambling around hyperbolic fixed points embedded in regular motion. In particular, we attempt to relate the localization properties of the initial state to the observed quantum Lyapunov exponent in [14, 15].

4.1. Heuristic Derivation of an Early-Time Transition

Without loss of generality, we keep the same operators $\hat{A} = \hat{q}_j$ and $\hat{B} = \hat{q}_l$ from Sec. 3.2, as they are exemplary for hermitian operators, whose classical counterparts are generalized coordinates. The Wigner-Moyal expansion of the OTOC in Eq. (3.3) gives us the squared Possion bracket of classical coordinate functions in leading order. Similar to the chaotic case before, this Poisson bracket simplifies for this specific choice to

$$\{q_j(\vec{q}_0, \vec{p}_0, t), q_l(\vec{q}_0, \vec{p}_0)\} = \frac{\partial q_j(\vec{q}_0, \vec{p}_0, t)}{\partial p_{l0}},$$

i.e., it is an element of the monodromy matrix $\partial\vec{x}(\vec{x}_0, t)/\partial\vec{x}(0)$ with $\vec{x} = (\vec{q}, \vec{p})$, see also App. A.1.2. In contrast to chaotic systems, an integrable system shows a zero monodromy matrix almost everywhere, except it is equal to the positive (in-)stability exponent for an unstable fixed point (FP). If the initial state is well-localized around such a FP, the classical limit of the OTOC in Eq. (3.3) is given by the maximal local stability exponent $\lambda_{\text{s}}(\vec{q}_0, \vec{p}_0)$ of the stability matrix instead of the Lyapunov exponent[2]

$$C(t) \ \sim \hbar_{\text{eff}}^2 \langle W_\rho(\vec{q}_0, \vec{p}_0) \exp\left\{2\lambda_{\text{s}}(\vec{q}_0, \vec{p}_0)t\right\}\rangle_{\text{PS}}, \tag{4.1}$$

such that the quantum Lyapunov exponent is $\lambda_{\text{q}} = \lambda_{\text{s}}(\vec{q}_0, \vec{p}_0)$, the averaged local stability exponent over the phase-space integral denoted by $\langle . \rangle_{\text{PS}}$. At this point, it is convenient to introduce two local time-scales in analogy to the chaotic case[3]:

- After the local ergodic time $\tau_{\text{s}} = 1/\lambda(\vec{q}_0, \vec{p}_0)$, the exponential growth of the OTOC begins to be visible. Before τ_{s}, we have sub-exponential and polynomial behavior linked to system-specific mechanisms.

- The Wigner-Weyl approximation breaks down when the leading order of the integrand in Eq. (3.3) becomes large compared to $\hbar_{\text{eff}}^2$. Then next order effects, beginning with $\hbar_{\text{eff}}^4$, are relevant and lead to interference effects via encounters [5]. This breakdown timescale defines the local Ehrenfest time $\tau_{\text{E}} = \lambda_{\text{s}}^{-1}(\vec{q}_0, \vec{p}_0) \ln(1/\hbar_{\text{eff}})$ and in our bosonic many-body case $\tau_{\text{E}} = \lambda_{\text{s}}^{-1}(\vec{q}_0, \vec{p}_0) \ln N$.

[2] The Lyapunov exponent is zero in any integrable system, see App. A.1.1.

[3] We do not distinguish between integrable (local) and chaotic case in the notation. It is clear in which case we are by the system we study.

We exploit the experimentally tunable localization features of quantum mechanical states [162] as a tool to probe the local unstable dynamics around a hyperbolic fixed point (FP) and consider a coherent-like state $\hat{\rho}$ centered around it. In the linearized region around the FP, the dynamics can be precisely described, and we replace $\lambda(\vec{q}_0, \vec{p}_0)$ by the maximal stability exponent λ_s of the FP. In general, however, the linearized region is bounded and we express this by the fact that the relation $\{A(\vec{q}_0, \vec{p}_0, t), B(\vec{q}_0, \vec{p}_0)\} = e^{\lambda_\mathrm{s} t}$ is valid only if the unstable manifold coordinate/projection $u(\vec{q}_0,\, \vec{p}_0)$ is smaller than a threshold $c > 0$. The exponential growth $u(\vec{q}_0, \vec{p}_0, t) = u(\vec{q}_0, \vec{p}_0) e^{\lambda_\mathrm{s} t}$ is only valid in the linearized region, where the condition $u(\vec{q}(t), \vec{p}(t), t) < c$ is still fulfilled. Beyond the threshold, we need to replace the time dynamics of the unstable manifold by a sub-exponential function. We refer to this mechanism as a kind of *leaking* from the linearized region, which the authors in Ref. [15] introduced for the infinite temperature state.

The key observation is the following: although the sub-exponential function describes the classical evolution outside and it is therefore negligibly small compared to the exponential growth in the linearized region, its contribution is weighted by a portion of phase space that grows exponentially. These considerations allow us to heuristically account for the leaking mechanism by modifying the Eq. (4.1) as

$$C(t) \;\sim \hbar_\mathrm{eff}^2 e^{2\lambda_\mathrm{s} t} \langle W_\rho(\vec{q}_0, \vec{p}_0) \Theta(c - e^{\lambda_\mathrm{s} t} u(\vec{q}_0, \vec{p}_0)) \rangle_\mathrm{LR}, \tag{4.2}$$

where we restrict the phase-space integration to the dominant linearized region (LR) around the FP.

For definiteness, let us consider now a Gaussian wave packet with an initial linear width Δu along the unstable manifold $u(\vec{q}, \vec{p})$. In this situation, the wave packet reaches the boundary of the linear region by a finite time $\tau_\mathrm{L} = \lambda_\mathrm{s}^{-1} \ln\big(c/\Delta u\big)$, which we correspondingly call the leaking time. After τ_L, we must take the leaking of the wave packet into account and the phase-space volume causing the exponential growth shrinks exponentially with $e^{-\lambda_\mathrm{s} t}$, i.e.,

$$\langle W_\rho(\vec{q}_0, \vec{p}_0) \Theta(c - e^{\lambda_\mathrm{s} t} u(\vec{q}_0, \vec{p}_0)) \rangle_\mathrm{LR} \;\sim \begin{cases} \text{const.} & , t < \tau_\mathrm{L} \\ e^{-\lambda_\mathrm{s} t} & , t > \tau_\mathrm{L} \end{cases} .$$

Hence, the exponential growth of the OTOC in Eq. (4.2) switches from $e^{2\lambda_\mathrm{s} t}$ to $e^{\lambda_\mathrm{s} t}$ after the leaking time τ_L. This finally leads to a short-time behavior of the OTOC around an unstable fixed point summarized by

$$C(t) \;\sim \begin{cases} \text{poly.} & , t < \tau_\mathrm{s} \\ e^{2\lambda_\mathrm{s} t} & , \tau_\mathrm{s} < t < \tau_\mathrm{L} \\ e^{\lambda_\mathrm{s} t} & , \tau_\mathrm{L} < t < \tau_\mathrm{E} \\ \text{osc.} & , \tau_\mathrm{E} < t \end{cases}, \tag{4.3}$$

that is schematically displayed in Fig. 4.1 showing two exponential regions. It is important to note that there is a hierarchy of timescales: the leaking time is

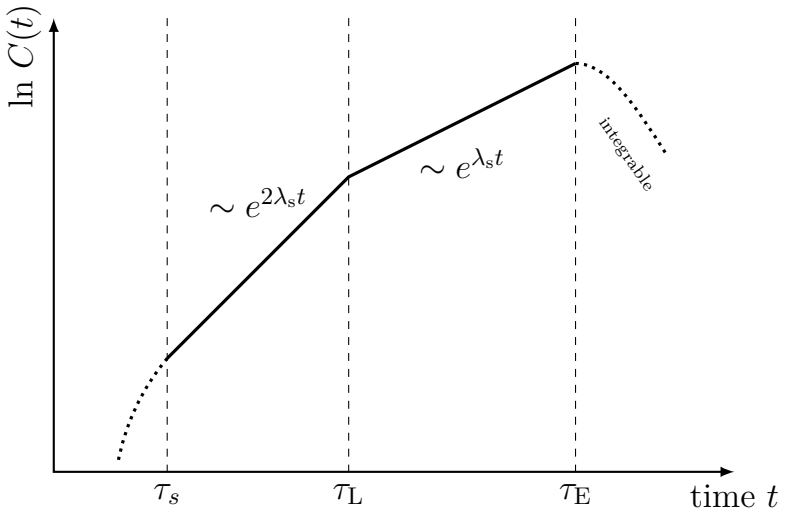

Figure 4.1: Expected behavior of an OTOC centered at a FP if $\tau_\mathrm{s} < \tau_\mathrm{L} < \tau_\mathrm{E}$. The OTOC grows polynomially for times shorter τ_s, exponential with $2\lambda_\mathrm{s}$ for times shorter τ_L, exponential with λ_s for times shorter τ_E, but greater than τ_L. Post-Ehrenfest timescales display oscillatory behavior if the system is integrable [158] and saturation if the system is chaotic [12, 148]. Adapted from Ref. [2].

only relevant if $\tau_\mathrm{L} < \tau_\mathrm{E}$, otherwise the Wigner-Weyl approximation (in leading order), see Eq. (3.3), is already invalid.

Assuming the linear width Δu scales with some power $\hbar_\mathrm{eff}^\alpha$ for typical states, we obtain an asymptotic expression for the leaking time by $\tau_\mathrm{L} \sim \frac{\alpha}{\lambda_\mathrm{s}} \ln N + O(\ln c)$. Therefore for $\hbar_\mathrm{eff} \to 0$, the Ehrenfest time and the leaking time are directly proportional $\tau_\mathrm{L} \sim \alpha \tau_\mathrm{E}$ given by the power-law exponent α of the linear width $\Delta u \sim \hbar_\mathrm{eff}^\alpha$. Let us explore the localization of the initial states via the exponent α. We identify three cases for the leaking time, i.e., $\tau_\mathrm{L} < \tau_\mathrm{s}$, $\tau_\mathrm{s} < \tau_\mathrm{L} < \tau_\mathrm{E}$ and $\tau_\mathrm{E} \leq \tau_\mathrm{L}$ (which is equivalent to $\alpha \approx 0, < 1, \approx 1$):

i) **Delocalized/uniform states:** $\tau_\mathrm{L} < \tau_\mathrm{s}$**,** $\alpha \approx 0$
Under the assumption that there is only one unstable FP of the classical dynamics, the OTOC is still governed by Eq. (4.3) and the $e^{2\lambda_\mathrm{s} t}$-regime vanishes such that only $e^{2\lambda_\mathrm{s} t}$ is present [15]. Typical examples here are high temperature states ($T \to \infty$). If there are several unstable fixed points, we expect the largest one, $\max_{j \in \mathrm{FPs}} \lambda_\mathrm{s}^j$, to be visible.

ii) **Localized states:** $\tau_\mathrm{s} < \tau_\mathrm{L} < \tau_\mathrm{E}$**,** $0 < \alpha < 1$
In this case we have the $2\lambda_\mathrm{s} - \lambda_\mathrm{s}$ transition and asymptotically (for $N \to \infty$) we expect a sharp kink to appear at τ_L. The prime example are the coherent states centered at a FP. They usually have a linear size of $\hbar_\mathrm{eff}^{1/2}$ in all phase-space directions.

iii) **Well-localized states:** $\tau_\mathrm{L} \approx \tau_\mathrm{E}$**,** $\alpha \approx 1$
The second $e^{\lambda_\mathrm{s} t}$-region is vanishing, only the one $e^{2\lambda_\mathrm{s} t}$-region is visible [14]. Fock states are candidates for the third class. Their linear width is $\hbar_\mathrm{eff}$ in

the classical occupation numbers, such that $\alpha \approx 1$ if the unstable manifold is aligned in the parallel direction.

The case $\alpha > 1$ is unphysical and can be excluded. The uncertainty principle requires the product of the width of the Wigner function to be $\geq \hbar_{\text{eff}}/2$ for each pair of conjugated variables in phase space. Hence, if $\alpha > 1$, the state must increase its width in one direction if $\hbar_{\text{eff}} \to 0$. Consequently, this direction becomes delocalized if we approach the classical limit contradicting the fact that the state is associated by a well-defined point in phase space.

At this point, we can explain the dynamical behavior of OTOCs reported in Refs. [14] and [15]. In the first publication [14], the authors investigate a number-projected coherent state which is simultaneously a Fock state[4]. Its unstable manifold is parallel to the occupation direction [163], therefore it falls into the case iii) and they see only the $2\lambda_{\text{s}}$-exponential window. Correspondingly, the authors of the second paper [15] use the infinite temperature state, hence their state directly falls into the first case and the only exponential window is given by $e^{\lambda_{\text{s}} t}$.

In the next subsection, we numerically explore the validity Eq. (4.3) for a Bose-Hubbard dimer with the aim to carefully investigate the new case ii), where the hierarchy of timescales $\tau_{\text{s}} < \tau_{\text{L}} < \tau_{\text{E}}$ implies, from our analysis, the presence of a $2\lambda_{\text{s}} - \lambda_{\text{s}}$ transition.

4.2. Bose-Hubbard Dimer

The Bose-Hubbard dimer describes bosonic degrees of freedom occupying two discrete levels or sites. Prime physical setups are individual Josephson junctions [164] or cold atoms within a small two-sited optical lattice [165–170]. In all these cases, one ends up with an effective description in terms of the Hamiltonian

$$\hat{H} = -2J\big(\hat{a}_2^\dagger \hat{a}_1 + \hat{a}_1^\dagger \hat{a}_2\big) + \frac{U}{2}\big(\hat{a}_1^{\dagger 2}\hat{a}_1^2 + \hat{a}_2^{\dagger 2}\hat{a}_2^2\big), \tag{4.4}$$

where the parameter J is the hopping and U is the (local) interaction strength between particles given in units of energy. This Hamiltonian model with two bosonic operators is equivalent to the *Lipkin-Meshkov-Glick* (LMG) model [171] with a single large spin operator [15, 16] using the Jordan-Schwinger map. Concerning conventions, our Bose-Hubbard dimer Hamiltonian differs from the usual dimer Hamiltonian, the hopping coefficient $2J$ (instead of J) is motivated to be consistent with a ring topology for higher number of wells. Consequently, the two-site ring has a doubly counted hopping term. We introduce a new dimensionless parameter Θ such that we have $J = \epsilon_0 \cos\Theta$ and $U = \epsilon_0 \frac{2}{N} \sin\Theta$, with $\epsilon_0 = \sqrt{J^2 + \big(UN/2\big)^2}$ representing a global energy scale. We set $\epsilon_0 = 1$ for a convenient unit system, yielding also the time unit $\hbar/\epsilon_0 = 1$. The parameter

[4]The state is a Fock state which has only occupations on a single site $|0, N, 0\rangle$.

space is thus compactified to $\Theta \in [-\pi/2, \pi/2]$, where $\Theta = -\pi/2$ is pure attractive interaction between the bosons with no hopping, $\Theta = 0$ is pure hopping with no interaction and $\Theta = \pi/2$ is pure repulsive interaction. Furthermore, the interval $(+\pi/2, 3\pi/2]$, switched sign for the hopping term, can be mapped to the interval $[-\pi/2, \pi/2]$ via a global sign.

4.2.1. Classical Mean-Field Limit

We follow the textbook approach [172] to derive the classical limit for bosons and replace the operators by complex numbers (mean fields)

$$\hat{a}_j, \hat{a}_j^\dagger \longmapsto \psi_j, \psi_j^*$$

within the normal-ordered quantum Hamiltonian in Eq. (4.4) to obtain a classical mean-field system

$$H(\vec{\psi}, \vec{\psi}^*) = -2J \,\mathrm{Re}\{\psi_1 \psi_2^*\} + \frac{U}{2}\Big(|\psi_1|^4 + |\psi_2|^4\Big).$$

The discrete nonlinear Schrödinger equation $i\dot{\psi}_j = \frac{\partial H}{\partial \psi_j^*}$ yields Hamilton's equations of motion that define the classical dynamics. Instead of introducing the quadrature operators $\psi_j = (q_j + ip_j)/\sqrt{2}$, we take advantage of the conserved total particle number N and we define a new set of conjugated classical variables

$$\begin{aligned} N &= n_1 + n_2\,, \qquad \phi = \tfrac{1}{2}(\varphi_1 + \varphi_2)\,, \\ n &= \tfrac{1}{2}(n_1 - n_2)\,, \quad \varphi = \varphi_1 - \varphi_2 - \pi\,, \end{aligned}$$

where the two mean-fields $\psi_j = \sqrt{n_j} e^{i\varphi_j}$ are written in terms of phase φ_j and occupations n_j. We shift the relative phase φ by π to obtain the so-called *off-phase fixed point* in the origin of the phase space ahead. Hence, the Hamiltonian takes the form

$$H(N, \phi, n, \varphi) = 2\cos\Theta\sqrt{N^2 - 4n^2}\cos\varphi + \sin\Theta\left(\frac{2n^2}{N} + \frac{N}{2}\right). \tag{4.5}$$

We can reduce the dynamics to an one-dimensional system with a single conjugated pair (z, φ) given by the population imbalance $z = 2n/N$ and relative phase difference $\varphi = \varphi_1 - \varphi_2 - \pi$ [173]. With these coordinates, the equations of motion are two coupled real-valued ODEs

$$\begin{aligned} \dot{z} &= -4\cos\Theta\sqrt{1 - z^2}\sin\varphi \\ \dot{\varphi} &= 4\cos\Theta\frac{z\cos\varphi}{\sqrt{1 - z^2}} - 2\sin\Theta\, z, \end{aligned} \tag{4.6}$$

which is a one-degree-of-freedom system. Conveniently, the mean-field system derived from Eq. (4.6) is integrable and can thus be exactly solved up to quadrature, as we have not utilized the energy conservation yet [174].

4.2.2. Fixed Points of the Classical Motion

A straightforward calculation shows that there are two fixed points (FPs) located at $(z = 0,\ \varphi = \pi)$ and $(z = 0,\ \varphi = 0)$, which are independent of the system parameter Θ. We call these two FPs the *in-phase* and *off-phase* FP, since both have homogeneous occupations and a zero or π phase difference between site one and two. For better visualization of the phase-space structure around the off-phase FP in Fig. 4.2, we set the zero point for the relative phase $\varphi = \varphi_1 - \varphi_2 - \pi$ to the unstable off-phase FP.

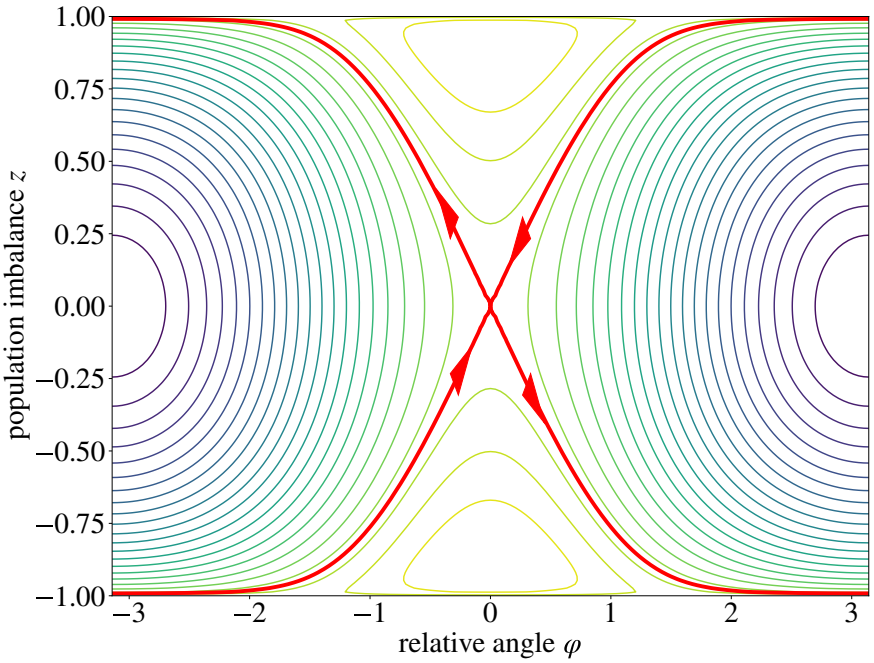

Figure 4.2: Reduced phase-space structure (z, φ) for $\Theta_* \approx 1.35$: contour lines of the Hamiltonian correspond to the classical trajectories. There are three elliptic fixed points and one hyperbolic fixed point whose associated separatrix is highlighted in red. Arrows on the separatrix indicate the stable (approaching) and unstable (escaping) manifolds. Reprinted from Ref. [2].

Two bifurcations appear: at $\Theta = -\arctan 2\,(\approx -1.107)$ for the in-phase FP and at $\Theta = \arctan 2$ for off-phase FP. We restrict our discussion to the off-phase FP, since there is a symmetry between these two FPs under a change of sign of the parameter Θ, i.e., they switch their properties by $\Theta \to -\Theta$. The stability diagram of the off-phase FP, displayed in Fig. 4.3, shows the bifurcation at $\Theta = \arctan 2$, where the stability exponent becomes positive. Its maximum $\lambda_s = 0.97$ is reached at $\Theta_* \approx 1.35$.

To complete the picture of local instability in an integrable system, Fig. 4.2 shows the reduced phase-space structure of the system, generated by the equations of motion in Eq. (4.6) at the maximal unstable parameter Θ_*.

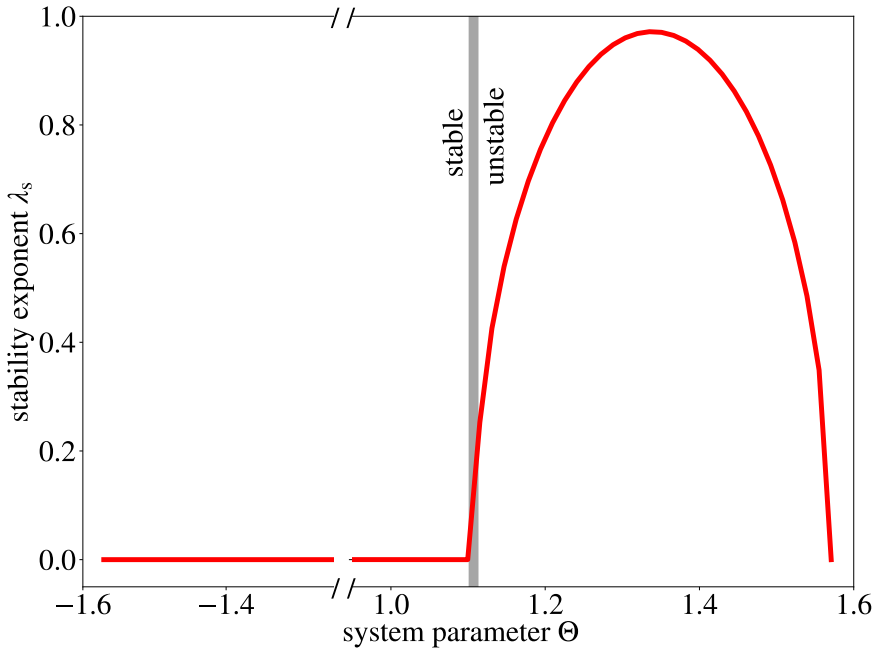

Figure 4.3: Stability exponent of the off-phase FP over the whole system parameter space Θ. A change from stable to unstable behavior occurs at the bifurcation point $\Theta = \arctan 2$. The in-phase FP has the same behavior if we switch Θ to $-\Theta$. Reprinted from Ref. [2].

To clarify any potential confusion about the flat two-dimensional illustration of the phase space, the topology of the phase space is actually a sphere S^2 and not a cylinder. There are periodic boundaries in relative phase φ, but additionally for $z = \pm 1$ a relative phase φ is undefined (zero occupations on one of the sites). Therefore, the relative phase φ must be compactified at $z = \pm 1$ and we have a sphere[5]. Note in particular the (red) separatrix defined by the unstable and stable manifold originating from the off-phase FP. The merging of stable and unstable manifolds indicates that the linearized regime is bounded, namely, any classical trajectory on the unstable manifolds converges to the stable manifold leading (in infinite time) back to the hyperbolic FP. The exact size of the linearized regime, modeled by the constant c in the previous Sec. 4, plays a negligible role for $\hbar_{\text{eff}} \to 0$, since it is additive and $\hbar_{\text{eff}}$-independent constant in the leaking time $\tau_{\text{L}} = \lambda_{\text{s}}^{-1} \ln(c/\Delta u) \sim \lambda_{\text{s}}^{-1} \ln(1/\hbar_{\text{eff}})/2 + \lambda_{\text{s}}^{-1} \ln c$ in Eq. (4.2) with $\Delta u \sim \hbar_{\text{eff}}^{1/2}$ (for a coherent state). Therefore we leave c unspecified in the subsequent discussion.

Furthermore, as shown in Fig. 4.2 for Θ_*, the *off-phase* FP is the only unstable FP in the classical mean-field limit. This is also true for the whole range $\Theta \in (\arctan 2, \pi/2)$, where the *off-phase* FP is unstable. This FP is the only source of instability in the system, any exponential growth visible in the OTOC is traced

[5]Despite being topologically a sphere, the phase space is similar to the pendulum system, except the momentum of the angle is unbounded for the pendulum. For the dimer, the population imbalance z is limited by ± 1. Nevertheless, the reference model of a hyperbolic fixed point is the unstable upright position in the pendulum.

back to it. Armed with this very specific phase-space structure, we conduct an in-depth analytical study of the OTOC $C(t)$ for the dimer.

4.2.3. Microscopic Approach: Separatrix Dynamics

Our analysis from the previous part is not restricted to position or momentum, any operator associated to canonical coordinates can be used in the OTOC. It is convenient therefore to choose the operators $\hat{A} = \hat{B} = \hat{n}_1$ to be the number operator $\hat{n}_1 = \hat{a}_1^\dagger \hat{a}_1$ at the first site[6] for the dimer. Therefore, we get

$$C(t) = \langle |||[\hat{n}_1(t), \hat{n}_1]|||^2 \rangle = \langle |||[\hat{n}(t), \hat{n}]|||^2 \rangle, \tag{4.7}$$

where we exploit the particle conservation to rewrite the OTOC with the imbalance operator $\hat{n} = \frac{1}{2}(\hat{n}_1 - \hat{n}_2)$. Based from this OTOC, we are interested in evaluating the classical expression (the TWA in Eq. (3.3)) which is given by

$$O(t) = \iint \mathrm{d}n_0 \, \mathrm{d}\varphi_0 \, W(n_0, \varphi_0) \left(\frac{\partial n(n_0, \varphi_0, t)}{\partial \varphi_0} \right)^2, \tag{4.8}$$

with the Wigner function $W(n, \varphi)$ associated with the initial state. The latter is, for the sake of simplicity, modeled as a coherent quantum state $\exp\left(\sqrt{N_0}(\hat{a}_-^\dagger - \hat{a}_-)\right)|0\rangle$ with $\hat{a}_- = \hat{a}_1 - \hat{a}_2$. Keeping in mind that for large N_0, this coherent state features very similar properties as a number-projected coherent state with total particle number N_0 as far as the site population exchange dynamics is concerned. We refer to App. C.1 (coherent states) and App. C.2 (number-projected coherent states) for more details. The Wigner function associated with this initial state is given by

$$W(N, \phi, n, \varphi) \simeq \frac{1}{\pi^2} \exp\left(-\frac{(N - N_0)^2}{2N_0} - 2N_0\phi^2 - \frac{2n^2}{N_0} - \frac{N_0\varphi^2}{2} \right) \tag{4.9}$$

in the framework of a quadratic expansion valid for $N_0 \gg 1$. Since the Wigner function W describes a tight localization of N about N_0, we set $N_0 = N$ henceforth and model the initial quantum state concerning the inter-site population exchange dynamics by the Wigner function

$$W(n, \varphi) = \frac{1}{\pi} \exp\left(-\frac{2n^2}{\omega N} - \frac{N\omega\varphi^2}{2} \right), \tag{4.10}$$

where the squeezing parameter ω allows for some flexibility in the definition of the initial quantum state.

Let us begin with the dynamical part of Eq. (4.8) and discuss the linearized dynamics in the vicinity of the off-phase FP $(n, \varphi) = (z, \varphi) = (0, 0)$. Expanding Eq. (4.6), we obtain the linearized equations of motion

$$\begin{aligned} \dot{z} &= -4 \cos\Theta \, \varphi \\ \dot{\varphi} &= -2(\sin\Theta - 2\cos\Theta) z \,, \end{aligned} \tag{4.11}$$

[6] Choosing the number operator at the second site $\hat{n}_2$ for $\hat{A}$ or $\hat{B}$ does not change the OTOC for the dimer, since we can express $\hat{n}_2 = N - \hat{n}_1$, and both, the total particle number N and the sign, drop out in the squared commutator.

which is readily solved as

$$\begin{aligned} z_t &= z_0 \cosh \lambda_\mathrm{s} t - \frac{4 \cos\Theta \varphi_0}{\lambda_\mathrm{s}} \sinh \lambda_\mathrm{s} t \,, \\ \varphi_t &= \varphi_0 \cosh \lambda_\mathrm{s} t - \frac{\lambda_\mathrm{s} z_0}{4 \cos\Theta} \sinh \lambda_\mathrm{s} t \end{aligned} \tag{4.12}$$

in terms of the stability exponent

$$\lambda_\mathrm{s} = 4 \cos\Theta \sqrt{\frac{\gamma}{2} - 1} \,, \tag{4.13}$$

where we defined the nonlinearity parameter $\gamma = \tan\Theta = UN/JL$. The latter becomes purely imaginary for $\gamma < 2$, which implies that $(n, \varphi) = (0, 0)$ turns into a stable fixed point if the nonlinearity parameter γ is decreased below two, as it is plotted in Fig. 4.3.

Considering $\gamma > 2$ henceforth, and assuming that the point (z_0, φ_0) is located very closely to the origin of the phase space, we can, as in the previous section, identify a timescale $\tau_\mathrm{s} \gg \lambda_\mathrm{s}^{-1}$. Before $t < \tau_\mathrm{s}$, we still have $|z_t| \ll 1$ and $|\varphi_t| \ll 1$, such that the above linearization Eq. (4.11) of the classical equations of motion remains valid until $t = \tau_\mathrm{s}$. Since at the same time we have $\lambda_\mathrm{s}\tau_\mathrm{s} \gg 1$ by assumption, the solution in Eq. (4.12) of the linearized Eq. (4.11) for $t = \tau_\mathrm{s}$ simplifies to

$$z_{\tau_\mathrm{s}} = \left(\frac{z_0}{2} - \frac{2 \cos\Theta \varphi_0}{\lambda_\mathrm{s}} \right) e^{\lambda_\mathrm{s}\tau_\mathrm{s}} \tag{4.14}$$

$$\varphi_{\tau_\mathrm{s}} = \left(\frac{\varphi_0}{2} - \frac{\lambda_\mathrm{s} z_0}{8 \cos\Theta} \right) e^{\lambda_\mathrm{s}\tau_\mathrm{s}}. \tag{4.15}$$

From the time τ_s on, we can safely assume that the trajectory under consideration very closely follows the separatrix structure emanating from the unstable off-phase fixed point $(z, \varphi) = (0, 0)$. This separatrix structure is obtained through the identification of the energy

$$H(n, \varphi) = 2 \cos\Theta N + \sin\Theta \frac{N}{2} = H(n = 0, \varphi = 0) \tag{4.16}$$

of the classical Hamiltonian Eq. (4.5), from which follows the identity

$$\cos\varphi = \frac{1 - \frac{\gamma}{4} z^2}{\sqrt{1 - z^2}} \,.$$

Inserting this expression into Eq. (4.6) yields the differential equation

$$\dot{z} = z \sqrt{\lambda_\mathrm{s}^2 - \sin^2\Theta z^2}$$

describing the motion along the upper or lower separatrix branch. This equation is straightforwardly integrated yielding

$$\begin{aligned} t - \tau_\mathrm{s} &= \int_{z_{\tau_\mathrm{s}}}^{z_t} \frac{\mathrm{d}z}{z \sqrt{\lambda_\mathrm{s}^2 - \sin^2\Theta z^2}} \\ &= -\frac{1}{\lambda_\mathrm{s}} \left[\operatorname{arcosh}\left(\frac{\lambda_\mathrm{s}}{\sin\Theta |z_t|} \right) - \operatorname{arcosh}\left(\frac{\lambda_\mathrm{s}}{\sin\Theta |z_{\tau_\mathrm{s}}|} \right) \right] , \end{aligned}$$

from which we obtain

$$z_t = \frac{\mathrm{sgn}(z_{\tau_\mathrm{s}})\lambda_\mathrm{s}/\sin\Theta}{\cosh\left[\mathrm{arcosh}\left(\frac{\lambda_\mathrm{s}}{\sin\Theta|z_{\tau_\mathrm{s}}|}\right) - \lambda_\mathrm{s}(t-\tau_\mathrm{s})\right]}\,. \tag{4.17}$$

Using $|z_{\tau_\mathrm{s}}| \ll 1$ and hence also $\sin\Theta|z_{\tau_\mathrm{s}}|/\lambda_\mathrm{s} \ll 1$ for finite values of $\sin\Theta$ and λ_s, we define

$$\begin{aligned} x_t &= \mathrm{sgn}(z_{\tau_\mathrm{s}})\exp\left[-\mathrm{arcosh}\left(\frac{\lambda_\mathrm{s}}{\gamma|z_{\tau_\mathrm{s}}|}\right) + \lambda_\mathrm{s}(t-\tau_\mathrm{s})\right] \\ &\simeq \frac{\sin\Theta}{2\lambda_\mathrm{s}}\left(\frac{z_0}{2} - 2\cos\Theta\frac{\varphi_0}{\lambda_\mathrm{s}}\right)e^{\lambda_\mathrm{s}t} \\ &\simeq \frac{\sin\Theta}{\lambda_\mathrm{s}}\left(\frac{n_0}{N} - 2\cos\Theta\frac{\varphi_0}{\lambda_\mathrm{s}}\right)\sinh(\lambda_\mathrm{s}t)\,, \end{aligned} \tag{4.18}$$

where we make use of the asymptotic expression

$$\mathrm{arcosh}(u) = \ln\left(u + \sqrt{u^2-1}\right) \simeq \ln(2u) + O(u^{-2}) \tag{4.19}$$

for large u, in combination with Eq. (4.14). With $(\cosh u)^{-1} = 2e^u/(1+e^{2u})$ we can thus rewrite Eq. (4.17) in terms of the expression Eq. (4.18) as

$$z_\tau = \frac{2\lambda_\mathrm{s}}{\sin\Theta}\frac{x_t}{1+x_t^2}\,, \tag{4.20}$$

which yields

$$n_t = \frac{N\lambda_\mathrm{s}}{\sin\Theta}\frac{x_t}{1+x_t^2} = n(n_0,\varphi_0,t)\,. \tag{4.21}$$

Replacing $e^{\lambda_\mathrm{s}t}$ with $2\sinh(\lambda_\mathrm{s}t)$ in Eq. (4.18) is clearly valid for large $\lambda_\mathrm{s}t \gg 1$ and has the additional advantage that the short-time regime in the time evolution of n_t is thereby correctly captured as well within Eq. (4.21). With Eq. (4.21), we write down the needed derivative

$$\begin{aligned} \frac{\partial n_t}{\partial\varphi_0} &= \frac{N\lambda_\mathrm{s}}{\sin\Theta}\frac{1-x_t^2}{(1+x_t^2)^2}\frac{\partial x_t}{\partial\varphi_0} \\ &\simeq \frac{-2\cos\Theta}{\lambda_\mathrm{s}}\sinh(\lambda_\mathrm{s}t)\frac{1-x_t^2}{(1+x_t^2)^2}. \end{aligned}$$

The classical limit of the quantum OTOC, Eq. (4.8), is then evaluated by substituting n_0 by x_t via Eq. (4.18) and integrating out the Gaussian integral in φ_0, yielding

$$\begin{aligned} O(t) \;&= \frac{2\cos^2\Theta N^2}{\sqrt{\pi}a\lambda_\mathrm{s}^2}\sinh(\lambda_\mathrm{s}t) \\ &\quad\times \int_{-\infty}^{\infty}\mathrm{d}x\,\frac{(1-x^2)^2}{(1+x^2)^4}\exp\left[-\left(\frac{x}{2a\sinh(\lambda_\mathrm{s}t)}\right)^2\right], \end{aligned} \tag{4.22}$$

where the dimensionless scale a is defined as

$$a = \frac{\sin\Theta/\lambda_\mathrm{s}}{\sqrt{8\omega N}}\sqrt{\omega^2 + \frac{16\cos^2\Theta}{\lambda_\mathrm{s}^2}}\,. \tag{4.23}$$

The short-time behavior of the OTOC, for $t \ll \tau_\mathrm{L} = -\lambda_\mathrm{s}^{-1}\ln a$, is approximated as

$$O(t) \simeq 4\cos^2\Theta\frac{N^2}{\lambda_\mathrm{s}^2}\sinh^2(\lambda_\mathrm{s}t), \tag{4.24}$$

while for $t \gg \tau_\mathrm{L}$ we obtain

$$O(t) \simeq \cos^2\Theta\frac{\sqrt{\pi}N^2}{4a\lambda_\mathrm{s}^2}e^{\lambda_\mathrm{s}t}. \tag{4.25}$$

These two limits correspond to the $2\lambda_\mathrm{s} - \lambda_\mathrm{s}$ transition that we heuristically derived in Sec. 4.1, as expressed in Eq. (4.3), and now we obtained the same result by a careful study of the TWA around the off-phase FP specifically for the Bose-Hubbard dimer. Note that the leaking time τ_L defined above (between Eq. (4.24) and Eq. (4.23)) agrees with the case ii) in Sec. 4.1. The dimensionless constant $\ln a$ encodes the linear width of the wave packet (via the squeezing parameter ω) along the unstable direction.

With this detailed classical calculation at hand, we analyze the OTOC centered around this local hyperbolic off-phase FP, considering the parameter Θ_* at which the value of the stability exponent is maximal, i.e., the stability exponent is $\lambda_\mathrm{s} = 0.97$.

4.2.4. Numerical Results for the Out-of-Time-Ordered Correlator

We proceed now with the numerical study and calculate the OTOC via Eq. (4.7) by means of numerically exact simulations for the operators $\hat{A} = \hat{B} = \hat{n}_1$. We consider the state

$$|\vec{\xi}\rangle = \frac{1}{\mathcal{N}}\left(\xi_1\hat{a}_1^\dagger + \xi_2\hat{a}_2^\dagger\right)^N|0\rangle\,, \tag{4.26}$$

which is a number-projected coherent state centered around the mean-field off-phase FP $\vec{\xi} = (\xi_1, \xi_2) = (\sqrt{N/2}, -\sqrt{N/2})$ with the normalization constant $\mathcal{N} = \sqrt{N^N N!}$.

For large total particle number N, the projected coherent state inherits properties from the coherent state, in particular the linear width of $\hbar_\mathrm{eff}^{1/2}$ in each phase-space direction [175], including the unstable direction of the off-phase FP in Fig. 4.2. Furthermore, it sets the squeezing parameter $\omega = 1$ in the classical analysis in Eq. (4.23). Following the discussion in Sec. 4.1, case ii), the leaking time τ_L is therefore half the Ehrenfest time τ_E. We display our numerical OTOCs for increasing particle number $N = 10^3,\ 10^4,\ 5\cdot10^4$ in Fig. 4.4, where we observe the predicted $2\lambda_\mathrm{s} - \lambda_\mathrm{s}$ transition, precisely following the heuristic arguments of Sec. 4.1 and the more refined classical analysis of Sec. 4.2.3. In particular, the analytical result Eq. (4.22) for the classical OTOC follows very

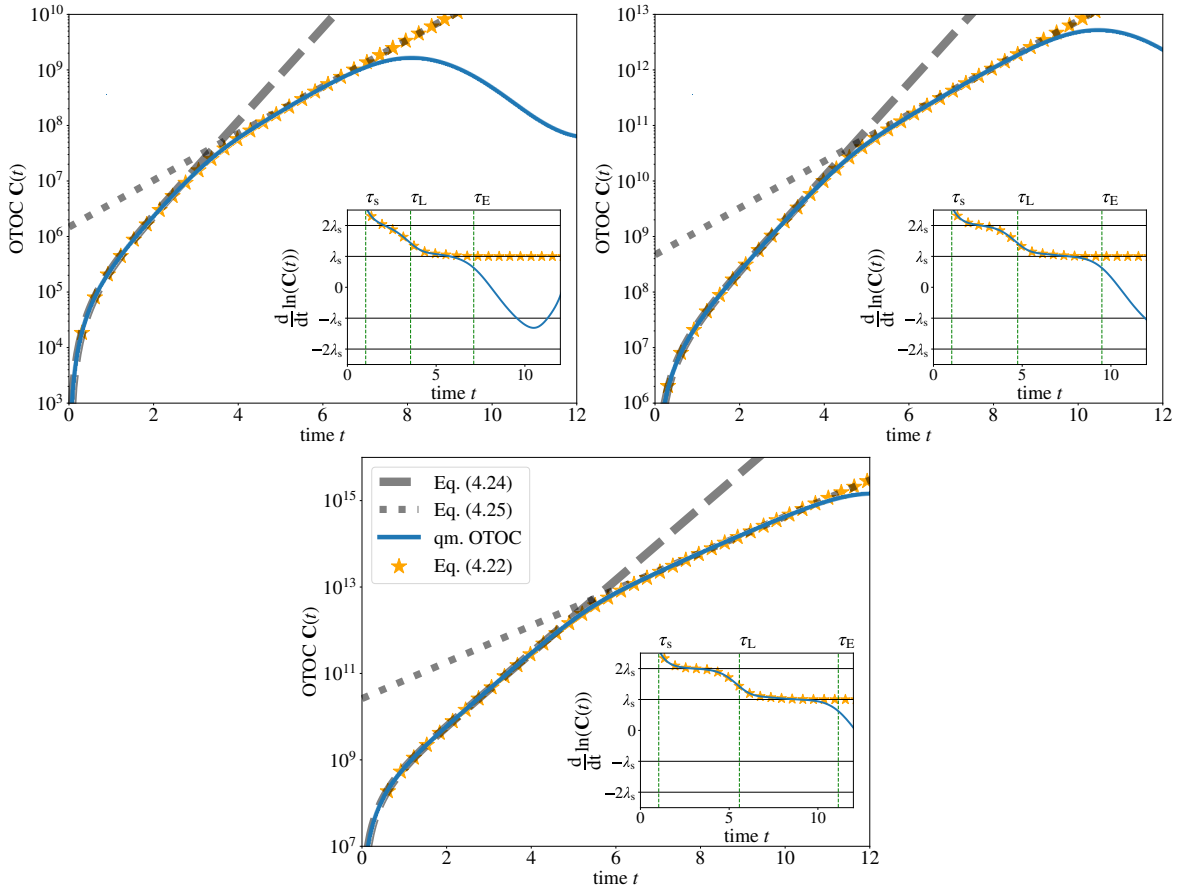

Figure 4.4: Top to bottom: OTOC $C(t)$ for $N = 10^3$, 10^4, $5 \cdot 10^4$ and $\Theta\mathrm{t} = 1.35$; developing the kink from the $2\lambda_s - \lambda_s$ transition at $\tau_L = \tau_E/2$; the classical expression Eq. (4.22) (orange stars) perfectly fits the OTOC during the pre-Ehrenfest time. Its approximations via Eqs. (4.24) and (4.25) tightly fit the OTOC in each region showing $\exp(2\lambda_s t)$ and $\exp(\lambda_s t)$ exponential growth rates. Adapted from Ref. [2].

well the quantum OTOC $C(t)$, i.e., it captures both regimes and the transition. The kink at the transition becomes sharper for $N \to \infty$. This is also seen in the insets showing the time derivative of $\ln C(t)$ and it confirms that with increasing N there are more and more pronounced $2\lambda_s$ and λ_s regions of exponential growth.

In order to illustrate the leaking from the linearized region around the FP, we visualize the time evolution of a wave packet at four time points in Fig. 4.5 via its Husimi distribution that emanates from the projected coherent state Eq. (4.26) with $N = 10^3$. Over time, the wave packet spreads along the separatrix and evolves to the upper right and lower left corners of the phase space. We see that at the time $\tau_L = \tau_E/2$ the wave packet folds back from the unstable to the stable manifold. This back-folding corresponds to the dynamical crossover of leaking from the linearized regime and the end of the exponential growth.

Calculations for different values of the system parameter Θ yield qualitatively similar behavior in the range where the off-phase FP is unstable, again with excellent agreement between the quantum OTOC Eq. (4.7) and its classical approximation Eq. (4.22). To demonstrate this we compute the relative logarithmic

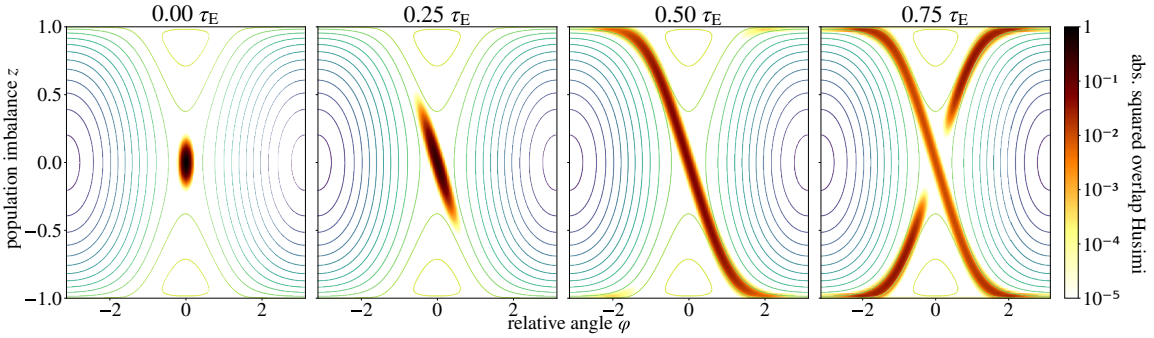

Figure 4.5: Time evolution of the Husimi-distribution for the state $|\vec{\xi}\rangle$ centered at the hyperbolic off-phase FP with $N = 10^3$ particles and system parameter $\Theta_* = 1.35$. The logarithmic scale visualizes clearly the sharp localization at the offset FP. We observe scrambling along the unstable manifold on the separatrix until $t \approx \tau_L$. The thin lines indicate the classical energy contours to visualize the spreading along the unstable manifold of the off-phase FP. Reprinted from Ref. [2].

deviation between Eq. (4.22) and Eq. (4.7), defined by

$$\eta(t) = \left| \frac{\ln O(t) - \ln C(t)}{\ln O(t)} \right| \tag{4.27}$$

for the number-projected state $|\vec{\xi}\rangle$. Fig. 4.6 displays, for various choices of the total particle numbers N, the time evolution of η up to the Ehrenfest time for the most unstable system parameter $\Theta = 1.35$ (right panel) as well as its maximal value

$$\eta_{\max} = \max_{t \leq 0.8\tau_E} \eta(t) \tag{4.28}$$

in the interval $0 \leq t \leq 0.8\tau_E$ as a function of the system parameter Θ (left panel). We restrict the domain for the maximal error to $0.8\tau_E$, since already at the Ehrenfest time τ_E the OTOC begins to oscillate because of the integrable dynamics. At the edges of the instability region (i.e., for $\Theta \to \arctan(2)$ or $\pi/2$), the maximal deviation significantly increases. There we have $\lambda_s \to 0$ and thus cannot, for finite $\hbar_{\text{eff}}$, justify the assumption that the time evolution of all phase-space points covered by the initial Wigner function very closely follows the separatrix arc. Nevertheless, the deviations clearly tend to zero in the semiclassical limit $\hbar_{\text{eff}} \to 0$, independently of the values of the system parameter $\Theta \in (\arctan(2), \pi/2)$ inside the unstable region and the time $t \in [0, \tau_E]$ before the Ehrenfest time. This confirms that the $2\lambda_s - \lambda_s$ transition is independent of the specific value of Θ, i.e., it is a robust signal of a dynamical crossover.

4.2.5. Squeezing – Engineering the Leaking Time τ_L

An important feature of the leaking mechanism is that the linear extent of the initial state along the unstable manifolds is the key ingredient for the exact position of the $2\lambda_s - \lambda_s$ transition. In order to confirm this dependence, we

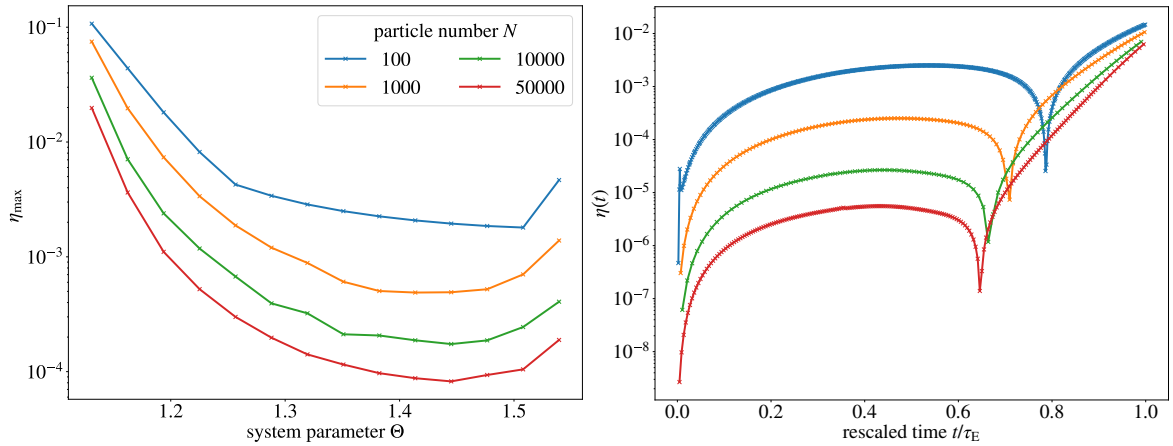

Figure 4.6: Left panel: maximal relative logarithmic deviation Eq. (4.28) plotted as a function of the system parameter Θ in the instability region. Right panel: relative logarithmic deviation Eq. (4.27) plotted as a function of time for the most unstable system parameter $\Theta_* = 1.35$. The calculations were done for the total particle numbers (from top to bottom) $N = 100$, 1000, 10000, and 50000. Reprinted from Ref. [2].

squeeze the coherent state on the off-phase FP and subsequently calculate the OTOC.

As a matter of fact, squeezed states in optical lattices can be achieved experimentally to an exquisite degree [162]. A squeezing protocol that is convenient for our purpose can be effectively (and unitarily) realized by reversing the time evolution, which in the experimental practice would amount to forward time propagation with reversed signs of the hopping parameter and the interaction parameter (to be done by Floquet engineering [169, 176] combined with Feshbach tuning). This means, we replace the initial state $|\xi\rangle$ (being a projected coherent state centered on the FP, see Eq. (4.26)) by

$$|\xi(t_0)\rangle = \hat{U}(t_0)\,|\xi\rangle$$

exemplary with $t_0 = -3\tau_E/4$, where $\hat{U}(t_0)$ is the time-evolution operator. Then we calculate the OTOC, Eq. (4.7), for the initial state $\hat{\rho}(t_0) = |\xi(t_0)\rangle\,\langle\xi(t_0)|$. The corresponding scrambling dynamics is then shown in the left panel of Fig. 4.7 for $N = 10^3$, while the right panel depicts the initial Husimi distribution of the squeezed state. This backward-time evaluated coherent state has a reduced linear extent along the unstable manifold. If we choose $t_0 = -3\tau_E/4$ (τ_E is the previous Ehrenfest time for the non-squeezed coherent state), we effectively transform $\Delta u \sim \hbar_{\text{eff}}^{1/2}$ into $\Delta u \sim \hbar_{\text{eff}}$. Thus, the new leaking time τ_L^* is now right at the Ehrenfest time, and no $2\lambda_s - \lambda_s$ transition is expected to exist, as we fully confirm by the numerical simulations shown in the left panel of Fig. 4.7.

Having established clean results for the integrable case that shows a novel transition, we now turn to the mixed setup, which is substantially more challenging to analyze OTOCs.

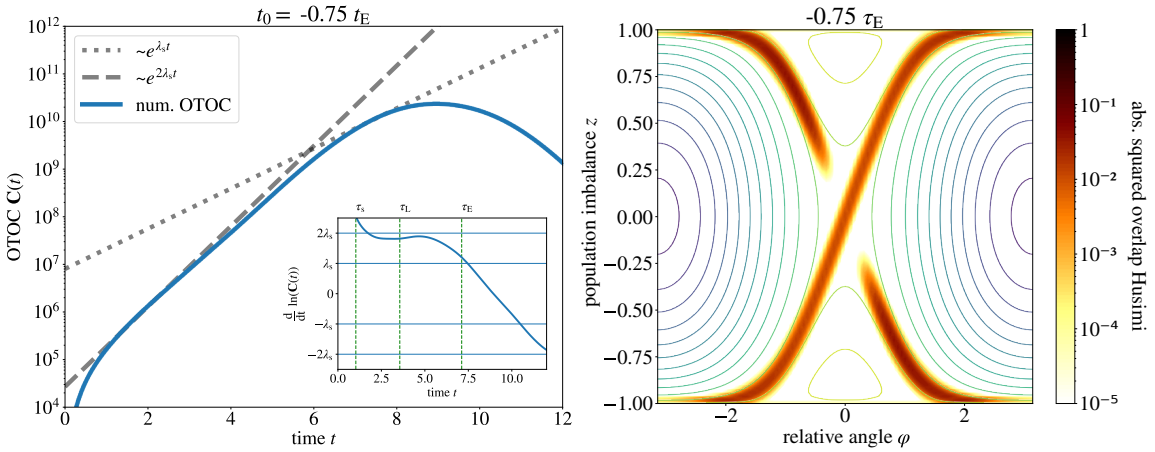

Figure 4.7: Left panel: OTOC for a squeezed coherent state for the system parameter $\Theta = 1.35$ and particle number $N = 10^3$. The crossover to λ_s vanishes. Right panel: Husimi distribution of the squeezed coherent state. The state is distributed along the stable manifold of the off-phase FP and features tight localization, with a width $\sim \hbar_{\text{eff}}$, along the unstable manifold. Reprinted from Ref. [2].

5. Conjecture: Short Time OTOC in Mixed Systems

In order to focus on separatrix effects like the leaking mechanism, requiring a very well controlled classical phase space, we restricted our numerical findings and the corresponding analytical theory to integrable systems, for which the theory in Sec. 4 assumes a bounded linearized regime around the fixed point. An ansatz generalizing these concepts to the realm of chaotic systems is that the role of the stability exponent λ_s from the fixed point is translated to the Lyapunov exponent λ_L from the chaotic sea, thus providing a bridge to exponential growth laws of OTOCs that were found for quantum maps with the exponents $2\lambda_L$ [39, 151] and only one λ_L [177], respectively.

A first numerical exploration of this matter, focusing on the behavior of OTOCs in chaotic separatrix layers, was carried out in [1], which we discuss below in more details. The main focus is a conjecture which we pose in [1]: the quantum Lyapunov exponent λ_q can be written as

$$\begin{aligned} &\lambda_q = \frac{1}{2t} \ln C(t) \;\approx\; f_q(\lambda_L(\vec{x}+\vec{\epsilon}), \lambda_s(\vec{x})), \\ &t \in [\tau_s, \tau_E], \quad f_q \in \mathcal{C}^0(\mathbb{R}_0^+, \mathbb{R}_0^+) \end{aligned} \tag{5.1}$$

for general operators $\hat{A}$ and $\hat{B}$ in the OTOC defined in Eq. (3.1) if we center the initial state on a fixed point $\vec{x}$ in a mixed phase space. Further on, the timescales, τ_s ergodic time, τ_E Ehrenfest time, are defined previously. The quantity f_q is an element of the positive-valued continuous functions on the space in which (λ_L, λ_s) is situated[7]. The hypothesis states that the quantum Lyapunov exponent is

[7]The Lyapunov exponent should be calculated not directly on the fixed point $\vec{x}$, but on

a linear combination of the stability exponent λ_s and the Lyapunov exponent λ_L of the surrounding chaotic layer. It represents an open question which exponent is crucial here, the short-time local stability exponent of the FP or the long-time Lyapunov exponent of the chaotic sea. Of course, the localization of the Wigner function around the FP must be considered here: on the one side, the more localized, the more the properties of the FP are dominant. On the other side, the less localized it is around the FP, the more the chaotic region with its Lyapunov exponent is dominant, but at the same time the Ehrenfest time τ_E scales via $\hbar_\mathrm{eff}$ which also scales the localization of the state around the FP. Hence, this is a complicated question which exponent we observe for the mixed phase space in the OTOC, our hypothesis states that the observed exponent is a linear combination of both.

In our joint publication [1], we investigated two models in light of this conjecture. We do not study the first system in [1], namely two interacting large spins investigated by Felix Meier. This system has the clear advantage of having a few enough degrees of freedom so that a very detailed study of the edge of chaos can be carried out, with the corresponding detailed analysis of the OTOC and the hypothesis. The expected universality of this conjecture that arises from generic mechanisms responsible for the emergence of chaotic layers around hyperbolic fixed points must be checked in other Hamiltonian systems displaying an edge of chaos. Therefore, we focus on our own contribution and come back to a system of N spinless bosons localized in L wells in a ring topology ($L+1 \equiv 1$), which we describe by a Bose-Hubbard Hamiltonian

$$\hat{H} = -J \sum_{j=1}^{L} \left(\hat{a}_{j+1}^\dagger \hat{a}_j + \hat{a}_j^\dagger \hat{a}_{j+1} \right) + \frac{U}{2} \sum_{j=1}^{L} \hat{a}_j^\dagger \hat{a}_j^\dagger \hat{a}_j \hat{a}_j. \tag{5.2}$$

Like in the previous Sec. 4 for the dimer, we use the same conventions, i.e., we express the hopping $J = \cos\Theta$ together with the interaction $U = \frac{L}{N} \sin\Theta$ via the convenient system parameter Θ and the Planck constant is unchanged given by the inverse particle number $\hbar_\mathrm{eff} = 1/N$.

But for three or more sites ($L \geq 3$), the number of conserved quantities (particle number N and the energy E) is less than the site number (degrees of freedom in the mean-field limit) to have integrable dynamics. We calculate the OTOC for number-projected coherent states defined by

$$|\vec{\phi}\rangle = \frac{1}{\sqrt{N!}} \left(\vec{\phi} \cdot \hat{\vec{a}}^\dagger \right)^N |0\rangle, \tag{5.3}$$

where $\vec{\phi}$ is a complex vector $\phi_j = (q_j + i p_j)/\sqrt{2}$ which is associated to a point of the classical mean-field phase space with fixed norm $||\vec{\phi}||_2 = 1$. Note that we use a different convention for the number-projected coherent state normalization in Eq. (4.26), i.e., the normalization is changed due to the fixed norm to one. Both

$\vec{x} + \vec{\epsilon}$ with a small deviation $\vec{\epsilon}$. Otherwise, we obtain the stability exponent and not the Lyapunov exponent of the chaotic region, see App. A.1.2.

definitions are equivalent and give the same definition of the number-projected coherent state.

By the same procedure as in the dimer, the classical mean-field system (approaching $\hbar_{\text{eff}} \to 0$) is given by replacing the operators to complex numbers in the normal ordered Hamiltonian,

$$H(\vec{q},\vec{p}) = -\cos(\Theta)\sum_{j=1}^{L}(q_j q_{j+1} + p_j p_{j+1}) + \frac{\sin(\Theta)L}{8}\sum_{j=1}^{L}(q_j^2+p_j^2)^2. \tag{5.4}$$

In contrast to the large spin system described in our publication [1], the domain in phase space is given just by $\mathcal{P} = \mathbb{R}^{2L}$, which is restricted to a $2L-1$ dimensional sphere S^{2L-1} (as the particle number is a conserved quantity, i.e., the mean-field norm $||\vec{\phi}||_2 = 1$ is a constant of motion). Having more than three sites makes it impossible to define a reduced classical system like in the dimer in Sec. 4.2.1. Hence we use the quadrature representation $\vec{x} = (\vec{q},\vec{p})$. But there is a trivial $U(1)$ symmetry left in the quadrature representation, which must be considered when searching for fixed points. We compensate the global phase by adding a frequency $\frac{\mu}{2}\sum_{j=1}^{L}(q_j^2+p_j^2)$ to the Hamiltonian H, i.e., we search for fixed points of the flow equations as zeros of the Hamiltonian vector field

$$\frac{\mathrm{d}}{\mathrm{d}t}\vec{x} = \frac{\mathrm{d}}{\mathrm{d}t}\begin{pmatrix}\vec{q}\\ \vec{p}\end{pmatrix} = \begin{bmatrix} \Big\{-\cos(\Theta)(p_{j+1}+p_{j-1})+ \\ \quad +\frac{\sin(\Theta)L}{2}(q_j^2+p_j^2)p_j + \mu p_j\Big\}_{j=1,\dots,L} \\ \Big\{\cos(\Theta)(q_{j+1}+q_{j-1})+ \\ \quad -\frac{\sin(\Theta)L}{2}(q_j^2+p_j^2)q_j - \mu q_j\Big\}_{j=1,\dots,L}\end{bmatrix} \stackrel{!}{=} 0 \tag{5.5}$$

for a phase-space point $\vec{x} = (\vec{q},\vec{p})$ and a frequency μ. Thus we extend the notion[8] for fixed point for classical mean-field solution having a trivial time-evolution [97]. We focus on the homogeneous fixed point $\vec{x}^{\mathrm{H}}$ given by

$$\begin{aligned} q_j^{\mathrm{H}} &= \sqrt{\frac{2}{L}},\ p_j^{\mathrm{H}} = 0,\ \phi_j^{\mathrm{H}} = \frac{1}{\sqrt{L}} \\ \mu^{\mathrm{H}} &= \sin(\Theta) - 2\cos(\Theta), \end{aligned}$$

because it is uniquely defined for every site number L. A straightforward stability analysis shows that the fixed point $\vec{x}^{\mathrm{H}}$ is unstable inside the parameter region defined by $-\frac{\pi}{2} < \Theta < \arctan\big(-1+\cos\big(\frac{2\pi}{L}\big)\big)$ [174], where the interaction is attractive. We want to study the hypothesis Eq. (5.1) for the Bose-Hubbard rings $L=3,\ N=100$ and $L=4,\ N=40$. Inter alia, the homogeneous fixed point is unstable in the parameter region $\Theta \in [-1.4,-1.1]$ for both systems, as well as embedded inside a chaotic layer of the phase space ($\lambda_{\mathrm{L}} > 0$, see red data points in Fig. 5.1). Unfortunately, the Poincaré surface of section analysis does not yield a convenient visualization in the high-dimensional phase space,

[8] This is the generalization for any sites L. In the previous Sec. 4.2, we only considered two sites and in the reduced representation (population imbalance z and the relative phase φ) the $U(1)$ symmetry is already included.

since $2L-1$ dimensions require several cuts to reduce the dimensionality to a two-dimensional plot.

The setup of an unstable FP inside a chaotic sea is given, we investigate the quantum Lyapunov exponent and, in order to be specific, we calculate the following OTOC for the three and four site Bose-Hubbard system:

$$C(t) = \mathrm{tr}\left\{|\vec{\phi}^{\mathrm{H}}\rangle\langle\vec{\phi}^{\mathrm{H}}|[\hat{n}_1(t),\hat{n}_1]^\dagger|[\hat{n}_1(t),\hat{n}_1]\right\} = \langle\vec{\phi}^{\mathrm{H}}|\Big|[\hat{n}_1(t),\hat{n}_1]\Big|^2|\vec{\phi}^{\mathrm{H}}\rangle.$$

It is the same OTOC as in Sec. 4.2.4 and we investigate again the squared commutator of the occupations at the first site of the ring $\hat{n}_1 = \hat{a}_1^\dagger\hat{a}_1$ at times t and 0. We choose again the first site like in Sec. 4 for the dimer, but in contrast, the choice of sites matters and we restrict our study to only $\hat{n}_1$.

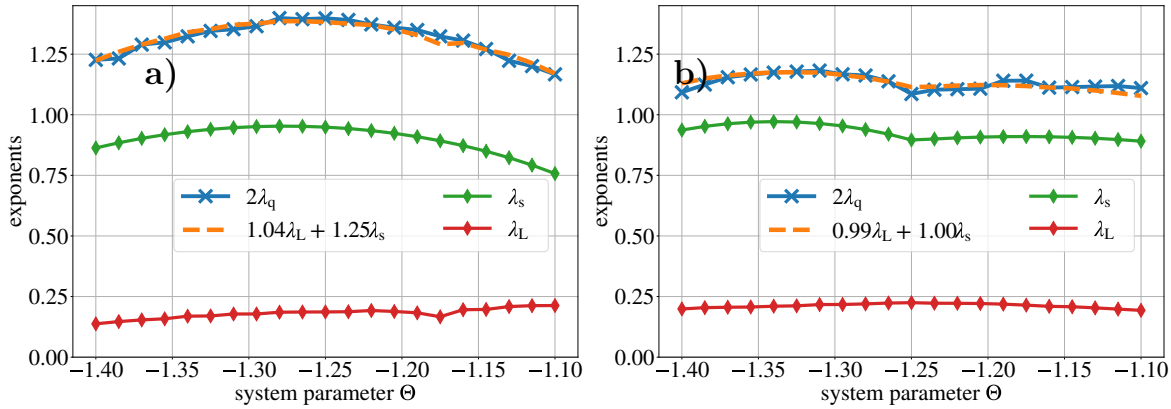

Figure 5.1: Examination of hypothesis Eq. (5.1) for OTOC calculated at the fixed point $\vec{x}^{\mathrm{H}}$: left panel **a)** 3-site ring; right panel **b)** 4-site ring. We compare the fitted quantum Lyapunov exponent λ_{q} (blue) with a linear combination (orange) of the stability exponent λ_{s} (green) and Lyapunov exponent λ_{L} (blue). In both rings, we obtain an excellent agreement between the fitted quantum Lyapunov exponent (blue) and the linear combination (orange) for the hypothesis Eq. (5.1). Adapted from Ref. [1].

We extract from Fig. 5.1 that the magnitude of the local instability λ_{s} is three to four times larger than the Lyapunov exponent[9] λ_{L} for the in-phase FP. In order to obtain the quantum Lyapunov exponent, we find an optimal exponential fit within the time-window $[\tau_{\mathrm{s}}, \tau_{\mathrm{E}}]$ using

$$g_{\mathrm{q}}(t) = a + b\exp(ct) \tag{5.6}$$

where the fitting variable $c \approx 2\lambda_{\mathrm{q}}$ gives the quantum Lyapunov exponent. The bounds of the fit window are defined by the local instability of the homogeneous fixed point, i.e., $\tau_{\mathrm{s}} = 1/\lambda_{\mathrm{s}}$ and $\tau_{\mathrm{E}} = \ln(N)/\lambda_{\mathrm{s}}$. We use the local instability λ_{s}

[9] For the Lyapunov exponent, we verify that the value λ_{L} is not depending on its point of calculation inside the chaotic sea, see App. A.1.2.

instead of the Lyapunov exponent λ_L because of their difference in magnitude. The numerical OTOC between system parameter $\Theta \in [-1.4, -1.1]$ are displayed in Fig. 5.2. We recognize clearly that the exponential region is given by the stability exponent λ_s instead of λ_L, since the fit-window $[\tau_s, \tau_E]$ would be at least by a factor of three bigger not matching the early time growth. We identify a

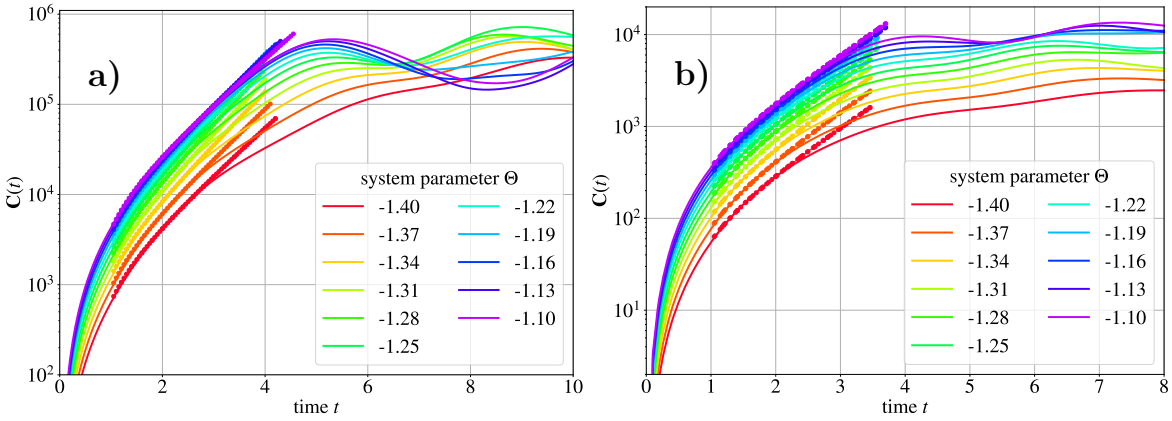

Figure 5.2: Numerical exact OTOC for the three-site ring (left panel a) with $N = 100$ particles and four site ring (right panel) with $N = 40$ particles, the early-time exponential region is mostly between $[1/\lambda_s, \ln(N)/\lambda_s]$ due to the difference of magnitude between λ_s and λ_L. Fits in this time window are displayed in the same color but with dotted lines.

small exponential regime compared to the data from the dimer (in Sec. 4.2.4 with a much higher total particle number) and extract the exponents via the fitting procedure in Fig. 5.1. Our key observation in Fig. 5.1 is that the quantum Lyapunov exponent $2\lambda_q$ is roughly the sum of the local instability and the Lyapunov exponent. The exact values of the coefficients indicate, however, that they depend on the localization of the initial wave packet and therefore on $\hbar_{\text{eff}}$ (width of the Wigner function scales with $\sqrt{\hbar_{\text{eff}}}$ [104]). For $L = 3$, the contribution of the stability exponent λ_s is greater than for $L = 4$, as the corresponding quantum scale $\hbar_{\text{eff}}$ is with $1/100$ smaller than $1/40$ respectively.

We check how the combination for the quantum Lyapunov λ_q on the Lyapunov exponent λ_L and on the instability exponent λ_s changes, when we move away from the fixed point. To this end, we fix the classical energy of the homogeneous fixed point, the q_1-coordinate in the range $[0, q_1^H]$ and numerically find the other coordinates, such that the particle number and energy are conserved. The numerical result of the coordinate search is shown for exemplary parameters $L = 4$, $N = 40$ and $\Theta = -1.1$ in panel a) of Fig. 5.3, where we target distances (measured from $\vec{x}^H$) between 0 and 0.04. The distance scale is fixed through the constraint $||\vec{\phi}|| = 1$ of the particle conservation[10]. In the

[10]The maximal distance $||\vec{\phi} - \vec{\psi}||$ between two phase-space points $\vec{\phi}$ and $\vec{\psi}$ is therefore two.

second panel b) of Fig. 5.3, we observe a constant Lyapunov exponent, when we increase the distance to the in-phase FP. Since a Lyapunov exponent is invariant inside a chaotic region, this verifies that we stay inside the chaotic sea emerging from the in-phase FP.

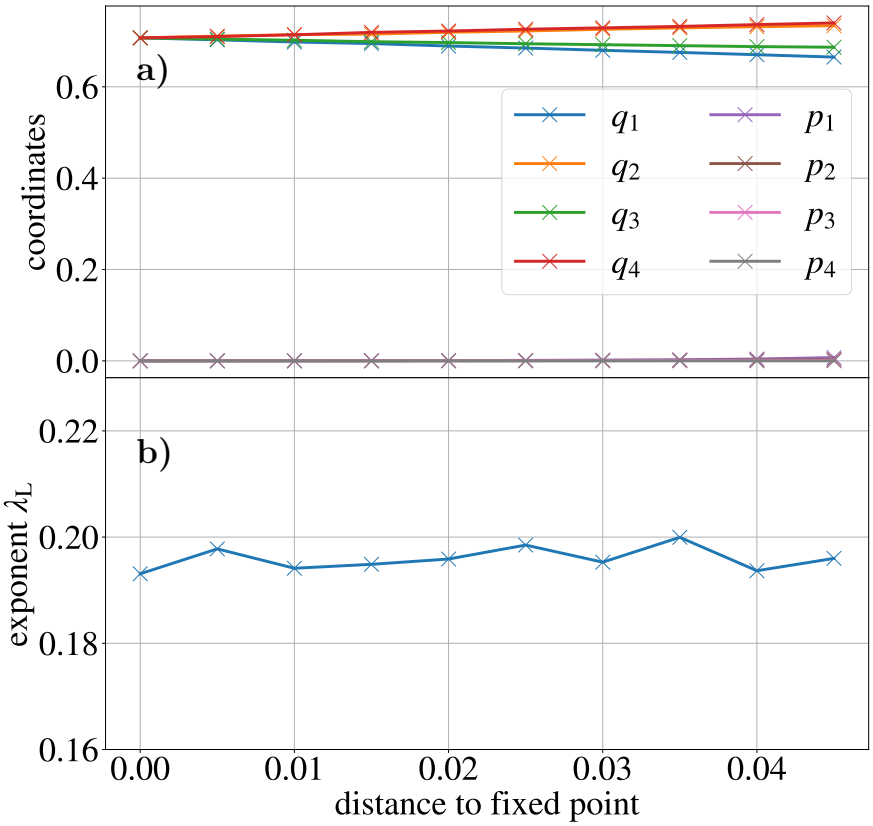

Figure 5.3: Moving away from the homogeneous fixed point for $L = 4$, $N = 40$ and $\Theta = -1.1$; top panel **a)**: we fix the energy and decrease the q_1 coordinate from $\sqrt{2/L}$; the coordinates p_1, p_2, p_3, p_4 lay on top of each other; bottom panel **b)**: the Lyapunov exponent remains constant indicating we remain inside the chaotic region around the homogeneous fixed point $\vec{x}^{\mathrm{H}}$. Reprinted from Ref. [1].

We repeat this procedure for each Θ-value and each ring ($L = 3, 4$). With these sets of phase-space points, we calculate the OTOCs, carry out the fitting procedure and plot the exponents in Fig. 5.5, where the distance to the FP is encoded in the color gradient. The plots of the OTOCs are displayed in Fig. 5.4 with the same color code.

The exponential growth rate has the tendency to decrease with increasing distance to the fixed point, but for several system parameters Θ we observe a stagnant quantum exponent. This two-sided behavior (a decreasing or stagnant exponent) is directly visible in the OTOC plots in the upper row of Fig. 5.4 for $L = 3$ in the left a) versus right b) panel. We interpret the different behavior of exponential growth as a complex dependence on the phase-space structure.

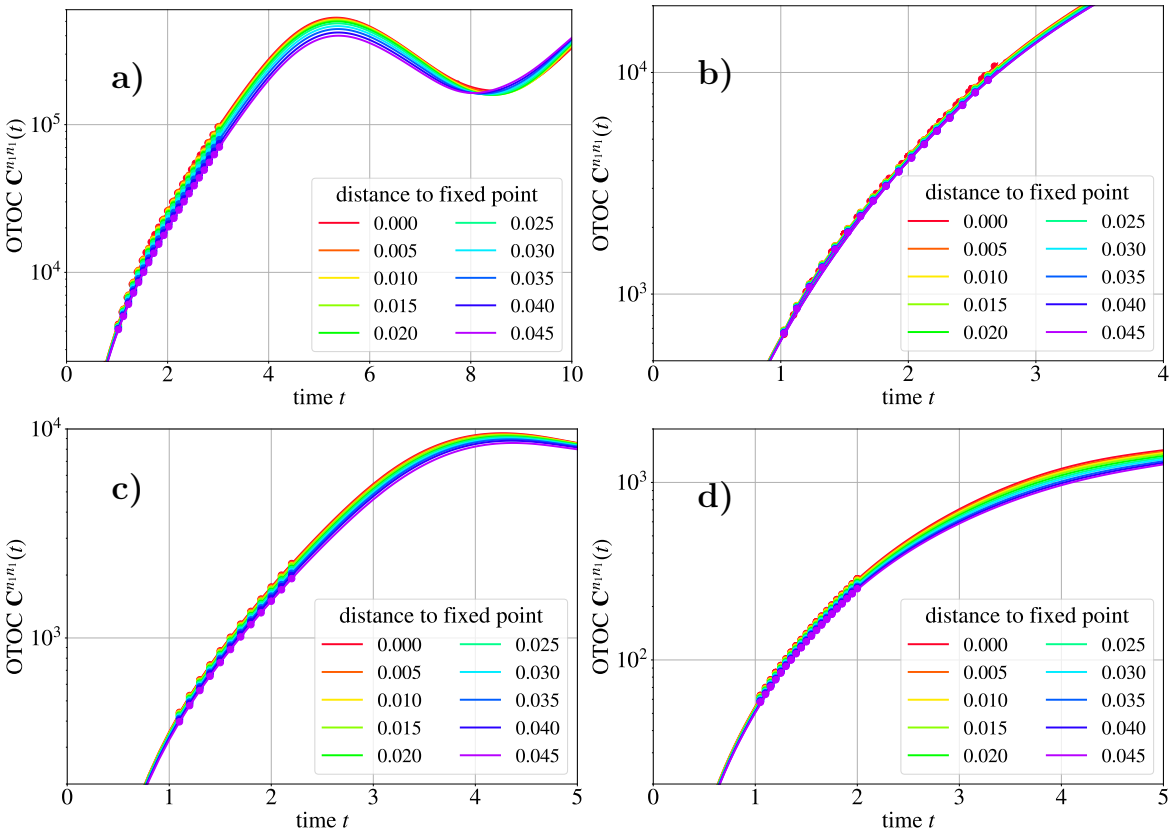

Figure 5.4: OTOC plots for $L = 3$, $N = 100$ with $\Theta = -1.1$ (panel **a**), for $\Theta = -1.4$ (panel **b**) and for $L = 4$, $N = 40$ with $\Theta = -1.1$ (panel **c**), for $\Theta = -1.4$ (panel **d**); color encodes the distance to the fixed point $\vec{x}^{\mathrm{H}}$, dotted points mark the fitted exponential function $g_{\mathrm{q}}(t)$ Eq. (5.6). OTOCs tend to decrease with the distance to the fixed point or to be highly stagnant, e.g. panel **b**. Reprinted from Ref. [1].

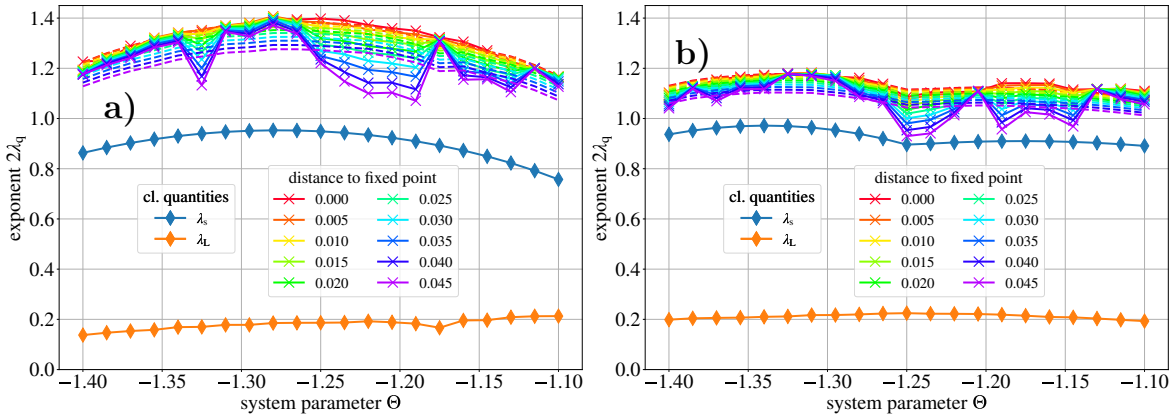

Figure 5.5: Quantum Lyapunov exponent for states on the energy shell of the fixed point; left panel **a)**: $L = 3$, $N = 100$; right panel **b)**: $L = 4$, $N = 40$; color code represents the distance to the FP $\vec{x}^{\mathrm{H}}$; dashed lines represent the fit via the hypothesis Eq. (5.1). Reprinted from Ref. [1].

For the stagnant exponents, our explanation is that the actual point is not only close to the FP but additionally lying on the un- or stable manifold emerging from the FP. Lying on this manifold and being close enough leads the OTOC

to be dominated by the FP $\vec{x}^{\mathrm{H}}$ and results in stagnant exponents we observe in Fig. 5.5.

In contrast, if the phase-space point is not directly related to the FP via an un- or stable manifold, there is no dynamical connection to the FP. It only remains the overlap of the wave packet with the fixed point causing the exponential growth rate with the local stability exponent λ_{s}. Hence, we observe a decrease of the exponent because of the hierarchy $\lambda_{\mathrm{L}} < \lambda_{\mathrm{s}}$, when we increase the distance to the fixed point and therefore diminish the overlap.

Our argument is supported by the results for the spin system [1], as there we choose the phase-space points from the Poincaré surface of section in such a way that we are clearly not on the un- or stable manifold. Hence, we do not have any stagnant behavior when we move the coherent state away from the FP in the two large spin system.

Contrary to the clean situation displayed in Fig. 5.1, the two different behaviors, shown in Fig. 5.5 when moving away from the fixed point $\vec{x}^{\mathrm{H}}$, are not captured completely by our hypothesis Eq. (5.1). Nevertheless, we still can find Θ-independent variables a and b such that $a\lambda_{\mathrm{L}} + b\lambda_{\mathrm{s}}$ fits the quantum Lyapunov exponent $2\lambda_{\mathrm{q}}$ (dashed lines in Fig. 5.5 display the fit via the coefficients a and b), but the validity of the fitting decreases due to the less chaotic nature of the system. Further, we observe a general decrease of both coefficients of a and b displayed in Fig. 5.6 versus the distance to the fixed point.

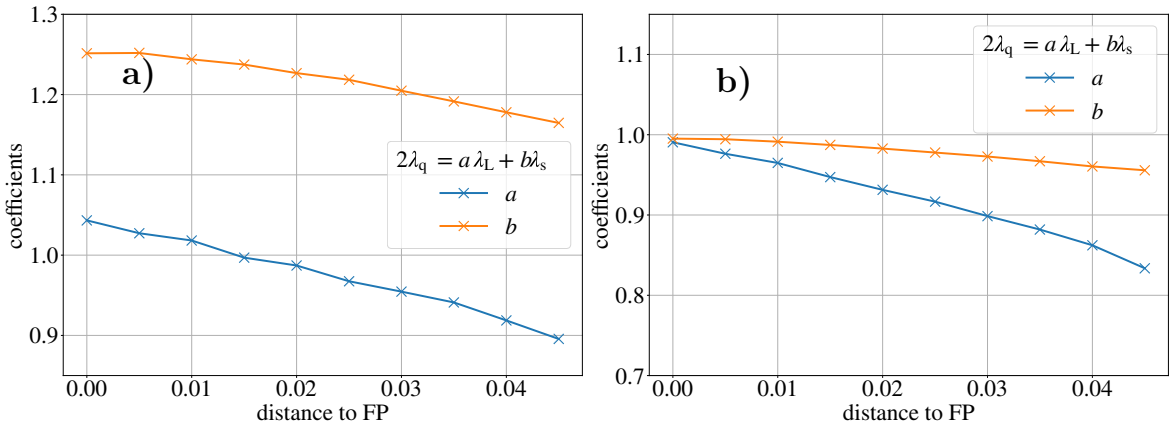

Figure 5.6: Fitted coefficients a and b from hypothesis Eq. (5.1); left plot **a)**: $L = 3$, $N = 100$; right plot **b)**: $L = 4$, $N = 40$. Remarkable and noticeable is that the sum of the coefficients are close to two. Reprinted from Ref. [1].

Like for the spin systems in [1], we find an interesting condition, that the sum $a + b$ of the fit coefficients is close to the value two. We trace the decreasing sum $a + b$ back to the issue with stagnating exponents for several system parameters, since we are stuck on an unstable manifold.

We believe that our results for Bose-Hubbard system, however, do not imply that hypothesis Eq. (5.1) is falsified. On the contrary, our conclusion is that

we need to ensure not to remain on fixed point's manifolds. Otherwise, we are still directly connected to the fixed point via the classical time evolution. A hint comes from the previous Sec. 4.2.5 in the integrable hyperbolic system, where squeezing a state around the stable manifold leaves the OTOC keeping the exponential growth by the instability exponent. This needs a more detailed exploration of the phase space along the energy sub-manifold of the homogeneous in-phase fixed point. Due to numerical limitations preventing smaller $\hbar_{\text{eff}}$, we choose to take a different approach which we discuss next.

6. Transition from Integrable to Chaotic Kicked Bose-Hubbard Systems

Our observations, λ_{s} vs. λ_{L} in Sec. 5 plus the integrable $2\lambda_{\text{s}} - \lambda_{\text{s}}$ transition in Sec. 4, motivate us to further investigate the transition from integrability to mixed and chaotic systems via OTOCs in order to see if we can find a common explanation for the signatures we have. We are limited by computational cost in the analysis of the early pre-Ehrenfest time regime which scales logarithmically with the particle number N. Together with the problematic scaling of Hilbert-space size in the Bose-Hubbard system ($\dim \mathcal{H} \propto N^{L-1}$), our results from exact diagonalization for $L > 2$ only reach low number of particles[11] and thereby small Ehrenfest times τ_{E}. The exponential region $[\tau_{\text{s}}, \tau_{\text{E}}]$ is too short for reliable fits and therefore many numerical simulations are inconclusive with respect to further statements in the previous section. A major concern is that due to large $\hbar_{\text{eff}} = 1/N$ that there could be several transitions between different exponential regions in the OTOC and they overlap. For example looking closely at Fig. 5.2, there could be a transition between two exponents forming for smaller $\hbar_{\text{eff}}$ which is still overlapping in the presented $\hbar_{\text{eff}}$ value. This overlap could provide an alternative explanation for the validity of the hypothesis Eq. (5.1). By still using exact diagonalization, an idea for pushing the results to lower values of $\hbar_{\text{eff}}$ is to adjust the Bose-Hubbard dimer ($L = 2$) to be chaotic. Several options can be chosen; any (non-trivial) time-dependent terms in the Hamiltonian make the dynamics chaotic where at least we need to break the energy conservation. A simple option to make the dimer non-integrable is transforming the hopping (or the interaction) to be kicked which leads to this section: the *kicked Bose-Hubbard systems*. We together with Thomas Michel and Prof. Peter Schlagheck are actively investigating this approach and we present here our own current results.

[11] For practical calculations, we reach for $N = 100$ particles for $L = 3$ and $N = 40$ particle for $L = 4$ in [1]. Slightly larger particle numbers are possible, but for a broad exploration we choose to compromise towards the presented particle numbers. Additionally, slightly larger particle numbers have limited effect due to the logarithmic scaling of the Ehrenfest time.

6.1. General Kicked Bose-Hubbard Systems

We define the kicked Bose-Hubbard Hamiltonian by adjusting the hopping term via discontinuous kicks of strength $J\tau$ and period[12] τ, which results to

$$\hat{H} = -J\tau \sum_{j=1}^{L} \left(\hat{a}_j^\dagger \hat{a}_{j+1} + \hat{a}_{j+1}^\dagger \hat{a}_j \right) \sum_{n=-\infty}^{\infty} \delta(t - n\tau) + \frac{U}{2} \sum_{j=1}^{L} \hat{a}_j^\dagger \hat{a}_j^\dagger \hat{a}_j \hat{a}_j. \tag{6.1}$$

By choosing the linear scaling of kicking strength $J\tau$ with the kicking period τ, we obtain the continuous Bose-Hubbard model in the limit $\tau \to 0$, because introducing kicks is equivalent to the Trotterization of the time-dynamics of the continuous Bose-Hubbard model.

As it is a time-periodic Hamiltonian, the time evolution can be discretely expressed via the Floquet operator over one period τ

$$\hat{U}(\tau) = \exp\Big\{ -i\tau J \sum_{j=1}^{L} \left(\hat{a}_j^\dagger \hat{a}_{j+1} + \hat{a}_{j+1}^\dagger \hat{a}_j \right) \Big\} \exp\Big\{ i\tau \frac{U}{2} \sum_{j=1}^{L} \hat{a}_j^\dagger \hat{a}_j^\dagger \hat{a}_j \hat{a}_j \Big\}, \tag{6.2}$$

which we can interpret by two separate "free" subsequent propagations[13]. Next, we show that the difficulty of the calculation is reduced to the basis change between site Fock-number basis and the momentum Fock-number basis for the ring.

We need the basis from site-Fock basis (interaction part is diagonal) in terms of the (quasi-) momentum-Fock basis (hopping part is diagonal). For the single-particle kicked rotor, its Floquet operator (similar to Eq. (6.2)) is efficiently computed numerically via the Fast-Fourier-Transform [178]. Unfortunately, this many-body version of changing from position to momentum is not applicable for Fast-Fourier-Transform. Instead we have to start with transforming the many-body operators. In order to diagonalize the hopping term, the momentum many-body operators $\hat{b}_j$ are given by

$$\begin{aligned} \hat{b}_k &= \frac{1}{\sqrt{L}} \sum_{j=1}^{L} e^{\frac{2\pi i}{L} jk} \hat{a}_j \qquad & \hat{b}_k^\dagger &= \frac{1}{\sqrt{L}} \sum_{j=1}^{L} e^{-\frac{2\pi i}{L} jk} \hat{a}_j^\dagger \\ \hat{a}_j &= \frac{1}{\sqrt{L}} \sum_{k=1}^{L} e^{-\frac{2\pi i}{L} jk} \hat{b}_k \qquad & \hat{a}_j^\dagger &= \frac{1}{\sqrt{L}} \sum_{k=1}^{L} e^{\frac{2\pi i}{L} jk} \hat{b}_k^\dagger. \end{aligned} \tag{6.3}$$

We call $\{\hat{b}_k, \hat{b}_k^\dagger\}$ the (many-body) momentum basis and there the hopping term is diagonal

$$-J \sum_{j=1}^{L} \left(\hat{a}_j^\dagger \hat{a}_{j+1} + \hat{a}_{j+1}^\dagger \hat{a}_j \right) = -2J \sum_{k=1}^{L} \cos\left(\frac{2\pi}{L} k \right) \hat{b}_k^\dagger \hat{b}_k,$$

[12] The units of the kicking period τ is one over energy (or time), and together with the δ-distribution in time which has a unit of energy, this is well-defined according to units.

[13] "Free" means that the two separated exp functions represent the propagation of τ with only hopping or interaction respectively.

where we insert Eq. (6.3) and use $\sum_{j=1}^{L} \exp\{-\frac{2\pi i}{L} j(k-k')\} = L\delta_{k,k'}$. Both parts of the Floquet operator are diagonal in the respective basis, thereby we need to express a site-Fock state in momentum-Fock states

$$\begin{aligned}
|\vec{n}\rangle &= \frac{1}{\sqrt{n_1! \dots n_L!}} \prod_{j=1}^{L} (\hat{a}_j^\dagger)^{n_j} |0\rangle \\
&= \frac{1}{\sqrt{n_1! \dots n_L!}} \frac{1}{L^{N/2}} \prod_{j=1}^{L} \Big\{ \sum_{k=1}^{L} e^{\frac{2\pi i}{L} kj} \hat{b}_k^\dagger \Big\}^{n_j} |0\rangle \\
&= \frac{1}{\sqrt{n_1! \dots n_L!}} \frac{1}{L^{N/2}} \prod_{j=1}^{L} \Big\{ \sum_{\substack{m_1^j, \dots, m_L^j = 0 \\ m_1^j + \dots + m_L^j = n_j}}^{n_j} \binom{n_j}{m_1^j, \dots, m_L^j} \prod_{k=1}^{L} (e^{\frac{2\pi i}{L} kj}\ \hat{b}_j^\dagger)^{m_k^j} \Big\} |0\rangle \,.
\end{aligned}$$

The presented form is expressing the basis change for the general L-site Bose-Hubbard system. It is the famous and difficult *Bose sampling* problem [179]. Luckily, our interest is only the dimer system, so let us set $L = 2$, such that we can simplify the expression above to

$$|n_1, n_2\rangle = \frac{1}{\sqrt{2^N n_1!(N-n_1)!}} \sum_{m=0}^{n_1} \sum_{o=0}^{n_2} \binom{n_1}{m} \binom{n_2}{o} (-\hat{b}_1^\dagger)^m (\hat{b}_2^\dagger)^{n_1-m} (\hat{b}_1^\dagger)^o (\hat{b}_2^\dagger)^{n_2-o} |0\rangle \,,$$

where we rename m_1^1 and m_1^2 to m and o. The multinomial coefficients are just binomial coefficients and we use the particle conservation $n_1 + n_2 = N$ to obtain

$$= \frac{1}{\sqrt{2^N n_1!(N-n_1)!}} \sum_{m=0}^{n_1} \sum_{o=0}^{N-n_1} \binom{n_1}{m} \binom{N-n_1}{o} (-1)^m (\hat{b}_1^\dagger)^{m+o} (\hat{b}_2^\dagger)^{N-m-o} |0\rangle$$

and we rewrite the sums over (m, o) to $(m, \nu = m + o)$

$$= \frac{1}{\sqrt{2^N n_1!(N-n_1)!}} \sum_{m=0}^{n_1} \sum_{\nu=m}^{N-n_1+m} \binom{n_1}{m} \binom{N-n_1}{\nu-m} (-1)^m (\hat{b}_1^\dagger)^\nu (\hat{b}_2^\dagger)^{N-\nu} |0\rangle \,.$$

Afterward we carefully switch the order of the sums $(m, \nu) \to (\nu, m)$

$$|n_1, n_2\rangle = \frac{1}{\sqrt{2^N n_1!(N-n_1)!}} \sum_{\nu=0}^{N} \sum_{\substack{m = \\ \max(0, N-n_1-\nu)}}^{\min(\nu, n_1)} \binom{n_1}{m} \binom{N-n_1}{\nu-m} (-1)^m (\hat{b}_1^\dagger)^\nu (\hat{b}_2^\dagger)^{N-\nu} |0\rangle$$

and we identify momentum Fock-number states

$$|n_1, n_2\rangle = \sum_{\nu=0}^{N} c_\nu^{n_1,N} |\nu, N-\nu\rangle_{\text{moment}}$$

with its coefficients

$$c_\nu^{n_1,N} = \frac{\sqrt{\nu!(N-\nu)!}}{\sqrt{n_1!(N-n_1)!}} \frac{1}{2^{N/2}} \sum_{m=\max(0,N-n_1-\nu)}^{\min(\nu,n_1)} \binom{n_1}{m} \binom{N-n_1}{\nu-m} (-1)^m. \tag{6.4}$$

In the end, the basis-change matrix from site to momentum is given by these coefficients

$$\hat{B} = \left(c_\nu^{n_1}\right)_{\nu,n_1} \tag{6.5}$$

and must be calculated only once and stored. We denote it by $\hat{B}$ as an operator, since it can be viewed as a basis-change operator. The numerical effort of this is $O(N^3)$, since we need $O(N^2)$ entries[14] and for each entry the sum in Eq. (6.4) with $O(N)$ terms must be contracted, but thankfully they are independent of each other, such that parallel calculation is feasible and gives a substantial speed up.

With the operator notation, the (stepwise) time evolution is a series of matrix multiplications

$$\hat{U}(\tau) = \hat{B}^\dagger \hat{J}_\mathrm{m} \hat{B} \hat{I}_\mathrm{s}, \tag{6.6}$$

where $\hat{J}_\mathrm{m}$ is the hopping in the momentum Fock-number basis

$$\hat{J}_\mathrm{m} = \left(\exp(-2iJ\tau(2\nu - N))\delta_{\nu,\nu'}\right)_{\nu,\nu'}$$

and where $\hat{I}_\mathrm{s}$ is the interaction in the site Fock-number basis,

$$\hat{I}_\mathrm{s} = \left(\exp\left(\frac{iU\tau}{2} n_1(n_1-1) + (N-n_1)(N-n_1-1)\right)\delta_{n_1,n_1'}\right)_{n_1,n_1'}.$$

Both $\hat{J}_\mathrm{m}, \hat{I}_\mathrm{s}$ are diagonal and can be efficiently applied after the basis change to a quantum state, such that the numerical effort of a single time step via the Floquet time-evolution scales with $O(N^2)$, because the Hilbert space dimension is $N+1$ in the dimer.

With the time evolution prepared, we can evaluate the OTOC for any pure quantum state. Specifically, we again investigate the unstable off-phase FP for the number-projected coherent states in the kicked setup. Before we do that, we verify that the off-phase FP is indeed a fixed point, which requires us to introduce the classical mean-field limit of the kicked dimer.

6.2. Kicked Mean-Field Dimer

We introduce shortly the general L-site mean-field Hamiltonian and come to the dimer afterwards. The classical limit of the kicked Bose-Hubbard system is analogously defined, we replace the operators by complex mean fields, $\hat{a}_i \to \phi_j = 1/\sqrt{2}\left(q_i + ip_i\right)$, in the classical limit $\hbar_\mathrm{eff} \to 0$ which gives us following classical Hamiltonian function

$$\begin{aligned} H(\vec{q},\vec{p}) = & -2J\tau \sum_{j=1}^{L} \left(q_j q_{j+1} + p_j p_{j+1}\right) \sum_{n=-\infty}^{\infty} \delta(t - n\tau) \\ & + \frac{U}{8} \sum_{j=1}^{L} (q_j^2 + p_j^2)(q_j^2 + p_j^2 - 2), \end{aligned} \tag{6.7}$$

[14]The Hilbert dimension is $N+1$ for the dimer if we have particle conservation.

Like in the continuous setup, the time dynamics are given by the Hamilton's equations, but one has to be careful about the discreteness of the kicks. In the complex mean-field notation $\{\phi_j, \phi_j^*\}$, the time evolution is done by the two separate but successive time evolutions

$$\begin{aligned} \vec{\phi}^{n+1} &= e^{iJ\tau\mathbf{T}}\vec{\phi}^{n+1/2} \\ \phi_j^{n+1/2} &= e^{-iU\tau|\phi_j^n|^2}\phi_j^n, \end{aligned} \tag{6.8}$$

where we introduced half-steps to stress the total time evolution of a period τ is again a two-step calculation in general. The matrix $\mathbf{T}_{ij} = (\delta_{i,j+1}+\delta_{i,j-1})$ is given by the next-neighbor hopping with periodic boundaries. For a general L-sited ring, we can not proceed in a meaningful way, but we can simplify the Eq. (6.8) for the dimer due to the total particle conservation.

With the details given in App. A.2, we utilize the relative phase φ and the population imbalance z like in Sec. 4.2.1 again. In these conjugated pair of variables, the classical map Eq. (A.5) takes the form

$$\begin{aligned} z_{n+1} &= z_n\cos(4J\tau) + \sqrt{1-z_n^2}\sin(\varphi_n - U\tau z_n)\sin(4J\tau) \\ \varphi_{n+1} &= \arctan2\Big(\cos(\varphi_n - U\tau z_n), \\ &\qquad \frac{-z_n}{\sqrt{1-z_n^2}}\sin(4J\tau) + \sin(\varphi_n - U\tau z_n)\cos(4J\tau)\Big), \end{aligned} \tag{6.9}$$

which is a convoluted expression, but remains analytical, hence this version is very convenient compared to the complex mean-field version in App. A.2. With the analytical Eq. (6.9), we can proceed analogously to the continuous dimer only that we have a discrete time. To continue with the classical analysis of the fixed points, we plot the reduced phase space via the same conjugated pair (φ, z) of relative phase and population imbalance in Fig. 6.1. We choose the same system parameter $\Theta = 1.35$ like in Sec. 4.2.1 with different kicking periods $\tau \in \{0.05, 0.5, 1.0, 1.5, 2.0, 2.5\}$ and recover the continuous dimer at low kicking periods, as we are approximating the continuous dimer via Trotterization. When the kicking period τ is enlarged, we see a transition from the integrable continuous dimer ($\tau \to 0$) via KAM resonances (at $\tau \approx 1$) to mixed and chaotic motion [9, 10, 180].

These phase-space plots in Fig. 6.1 give a fascinating picture seeing the integrable tori breaking up into periodic orbits (PO) such that stable and unstable manifolds are developing, deforming and breaking into a cascade until pure chaos emerges. But even for high kicking periods, there are some small regions of integrability left just as for certain values of the kicking period. See App. A.2 for the specific condition to have integrable resonance windows in τ. Unsurprisingly, the first chaotic region forms around the hyperbolic FP, which is precisely the off-phase FP in Sec. 4.2. The phase space gets more and more mixed and the chaotic region increases its size until it almost covers the whole phase space of the dimer. This means tuning the kicking period allows us to study the transition

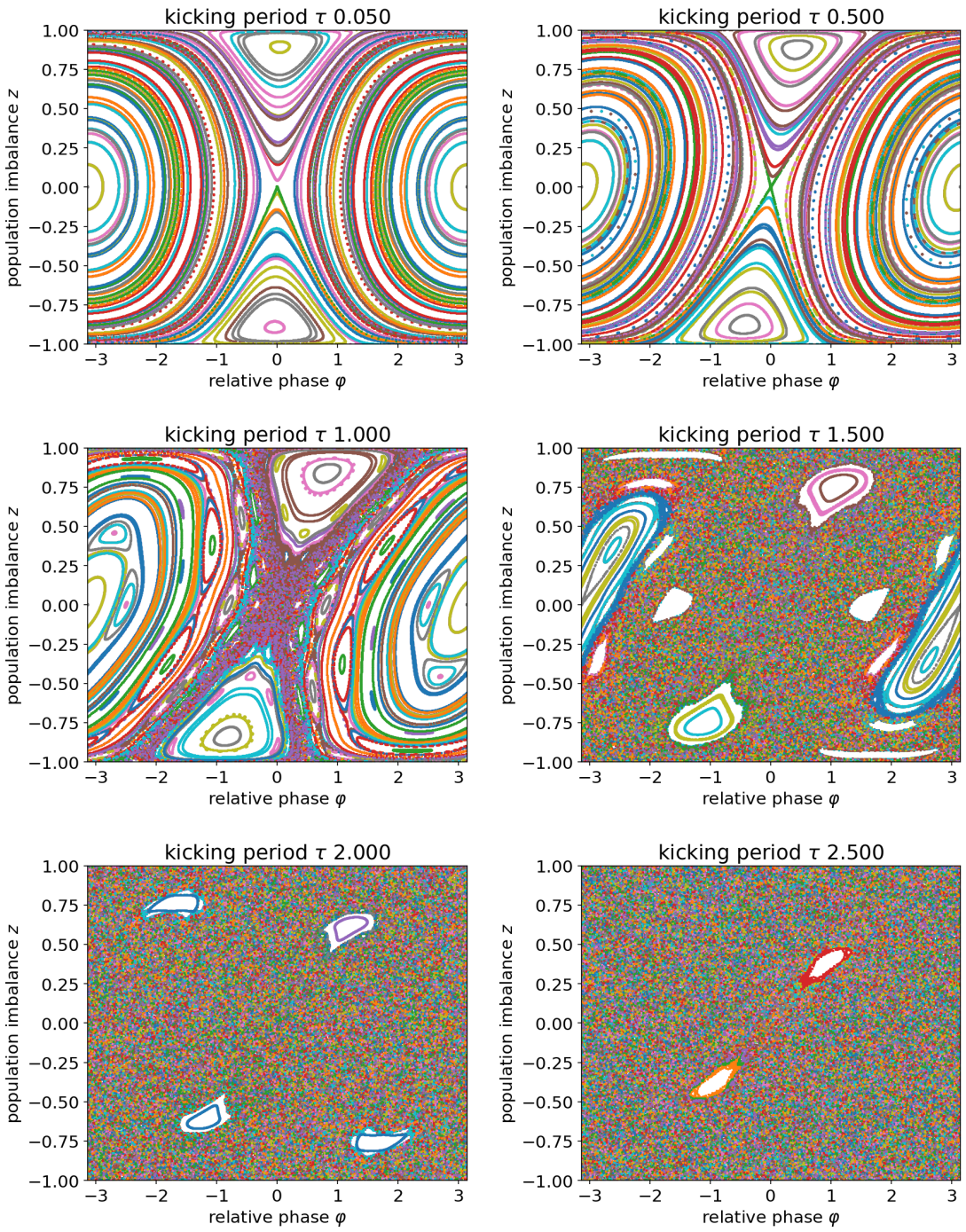

Figure 6.1: Phase-space plots with fixed $U = 1.952$, $J = 0.218$ ($\Theta = 1.35$) display the transition from integrability to chaos via increasing kicking periods $\tau \in \{0.05, 0.5, 1.0, 1.5, 2.0, 2.5\}$. At low kicking periods ($\tau = 0.05, 0.5$), we see the continuous limit beginning to tilt and then a transition from fully integrable to mixed and chaotic dynamics (almost fully chaotic at $\tau > 1.5$). Breaking tori (KAM resonances) are visible at $\tau = 1$ and a small region of emerging chaos. The region of chaos extends until only small integrable islands survive at $\tau = 2.0$ and 2.5.

from a integrable to mixed to (almost) fully chaotic system in the many-body context. Exactly what we need in order to study the open question of λ_s vs. λ_L

in the previous Sec. 5.

In all plotted phase-spaces and from the map in Eq. (6.9), we confirm that the previous in- and off-phase FP are also fixed points in the kicked dimer. Before we go to the off-phase FP in depth, we observe that the in-phase FP changes from stable to unstable (visible from $\tau = 1$ to $\tau = 1.5$) and emerges into a chaotic sea afterward ($\tau = 2$). One can marvel here the text-book like behavior, when integrable motion is perturbed by introducing discontinuous time evolution, and this results into KAM-resonances which destroys integrable tori in the phase space producing chaos.

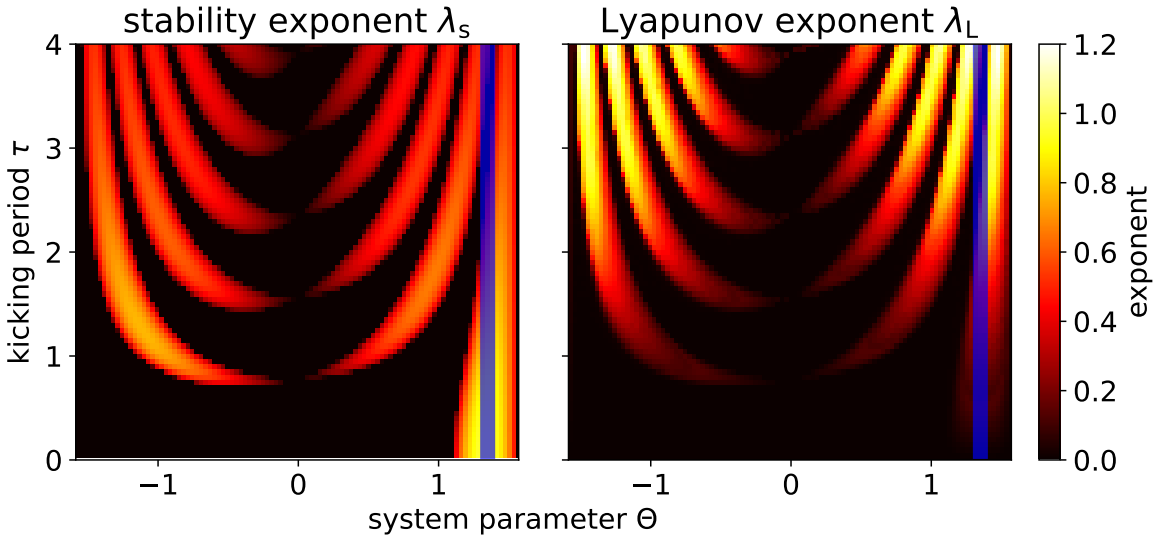

Figure 6.2: Heat maps for the exponents of the off-phase fixed point over system parameter Θ and kicking period τ, left panel shows the stability and the right panel the Lyapunov exponent. The blue shaded line is at $\Theta = 1.35$ which maximize the instability exponent λ_s at the continuous limit. The blue cut is displayed in Fig. 1.16 showing the dependence along the kicking period. There are bands of instability visible which are separated by integrable islands, see App. A.2.

Returning to the off-phase FP, we have a FP at our hand which is integrable unstable at the continuous limit and gets chaotically unstable by tuning the kicking period. It allows us to study the transition to chaos from local hyperbolical dynamics, so we analyze its stability and Lyapunov exponent in the upper panel of Fig. 6.2 over the system parameter Θ and kicking period τ. If the off-phase FP is stable (stability exponent $\lambda_s = 0$), also the Lyapunov exponent λ_L is zero, since a stable FP has at least a regular island in its vicinity. There are bands of instability in Fig. 6.2, they are separated due to integrable resonances (see App. A.2). The length of these integrable bands decrease when we go to higher and higher interaction values (both repulsive and attractive limits $\Theta \to \pm\pi/2$)[15].

[15]This is just a coincident of smaller and smaller hopping strength $J = \cos(\Theta)$, if we would keep J constant, the length of the bands are of roughly constant width.

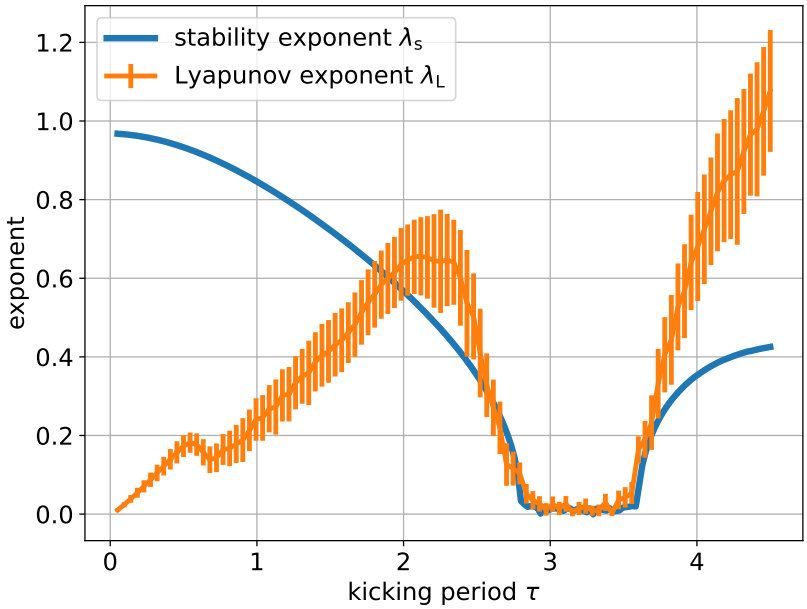

Figure 6.3: Exponents for the off-phase fixed point extracted from the blue shaded line in Fig 6.2 at the system parameter $\Theta_* = 1.35$. The Lyapunov exponent is increasing with the kicking period τ until an integrable resonance is reached. After the integrable window at $\tau > 3.6$, the Lyapunov exponent is larger than the instability exponent.

Unsurprisingly, we find that at the same maximal instability parameter Θ_* like in the continuous dimer the stability exponent and the Lyapunov exponent are the largest along the kicking period τ shown in Fig. 6.3. Hence, we choose this system parameter $\Theta_* \approx 1.35$ again in order to calculate the OTOC for various kicking periods which means we tune the system via τ from integrable to chaotic. A key observation is that for low enough kicking periods we are always in a region where $\lambda_L < \lambda_s$, hence the primary source of instability is always the FP itself here. The other case $\lambda_s < \lambda_L$ would be very much of interest, as we still need to investigate this case. Unfortunately, in our setup it is only possible for too large kicking periods, such that we do not have any time resolution at early times (pre-Ehrenfest $t < \tau_E$) for analyzing the quantum Lyapunov exponent λ_q reliably there.

6.3. OTOC at the Off-Phase Fixed Point

First, we verify our implementation of quantum calculations for the kicked dimer in the left panel of Fig. 6.4, i.e., we evaluate Eq. (4.7) for the off-phase FP for $N = 10^4$ particles. Thereby, the state is chosen to be a particle number-projected coherent state, which is centered onto the FP. Starting with a small kicking period $\tau = 0.05$, we compare the OTOC in the kicked dimer with the one in the continuous dimer[16] in the left panel of Fig. 6.4 and both versions overlap completely. It confirms that our implementation of the quantum time

[16] We choose to plot the continuous model only up to $t = 20$. At late times, one can see some deviations due to the discretization error of the Trotterization.

propagation is correct, since the kicked model with $\tau = 0.05$ is a valid Trotterized approximation of the continuous dimer.

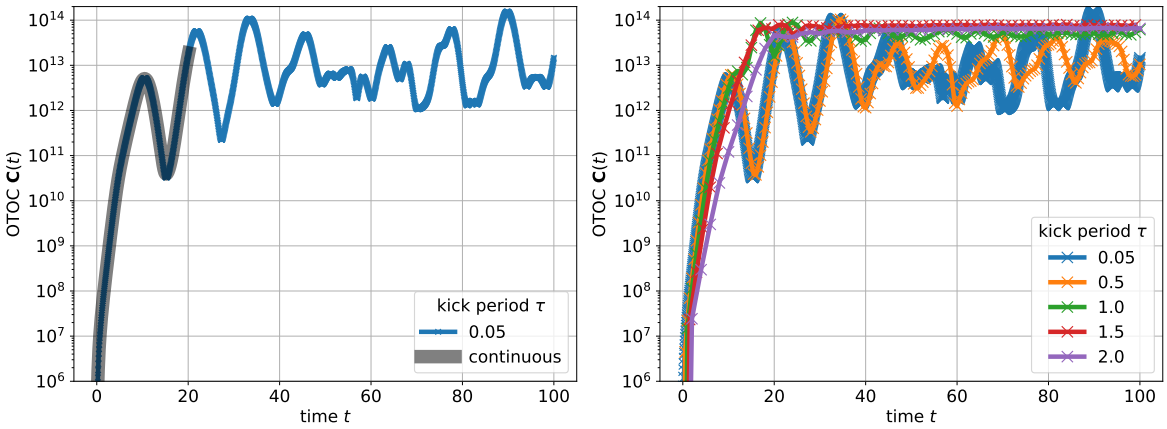

Figure 6.4: The off-phase fixed point omits exponential OTOCs in the kicked dimer with $N = 10^4$ and $\Theta_* = 1.35$. For small kicking strength ($\tau = 0.05$), we regain the continuous results (left panel). By increasing the kicking strength, longtime oscillations vanish and OTOC saturates (right panel) after the Ehrenfest time.

By increasing the kicking period above $\tau > 1$, we see a clear signature of the presence of chaos around the off-phase FP via the transition from oscillations to saturation for long times. The long time behavior is known and expected [151] and it fits the picture in the phase-space plots from Fig. 6.1 and the positive Lyapunov exponent in Fig. 6.3 at these kicking periods.

In the panels of Fig. 6.5, we compare the fits of the stability exponents $2\lambda_\mathrm{s} - \lambda_\mathrm{s}$ (left panels) and the Lyapunov exponents $2\lambda_\mathrm{L} - \lambda_\mathrm{L}$ (right panels) to the early-time exponential growth rate of the OTOC centered at the off-phase FP with $N = 10^4$ particles. For low kicking periods τ, when integrable mean-field dynamics are still present, we see an excellent agreement with the $2\lambda_\mathrm{s} - \lambda_\mathrm{s}$ transition like in Sec. 4. As long as there are long-time oscillations from the integrable dynamics (small τ), a small underlying exponential growth via once the Lyapunov exponent is visible. When we look at the two bottom panels of Fig. 6.5, the kicking period is sufficiently large and we see that the Lyapunov exponent and stability exponent are nearly the same size. This circumstance makes it infeasible to identify which exponent fits better. There is the possibility of the existence of time regions for each exponent. Even that increasing the particle number N is helpful to extend the exponential regime, but we are already at the limit of numerically feasible computation times and resources which scale with $O(N^3)$, whereas the Ehrenfest time scales only logarithmically with N. Hence, for example, doubling the particle number has limited benefit, as it only extends the Ehrenfest time by $\sim 1/\lambda_\mathrm{s} \ln 2$ and at the same time the computational cost increases by a factor of eight, such that this is out of

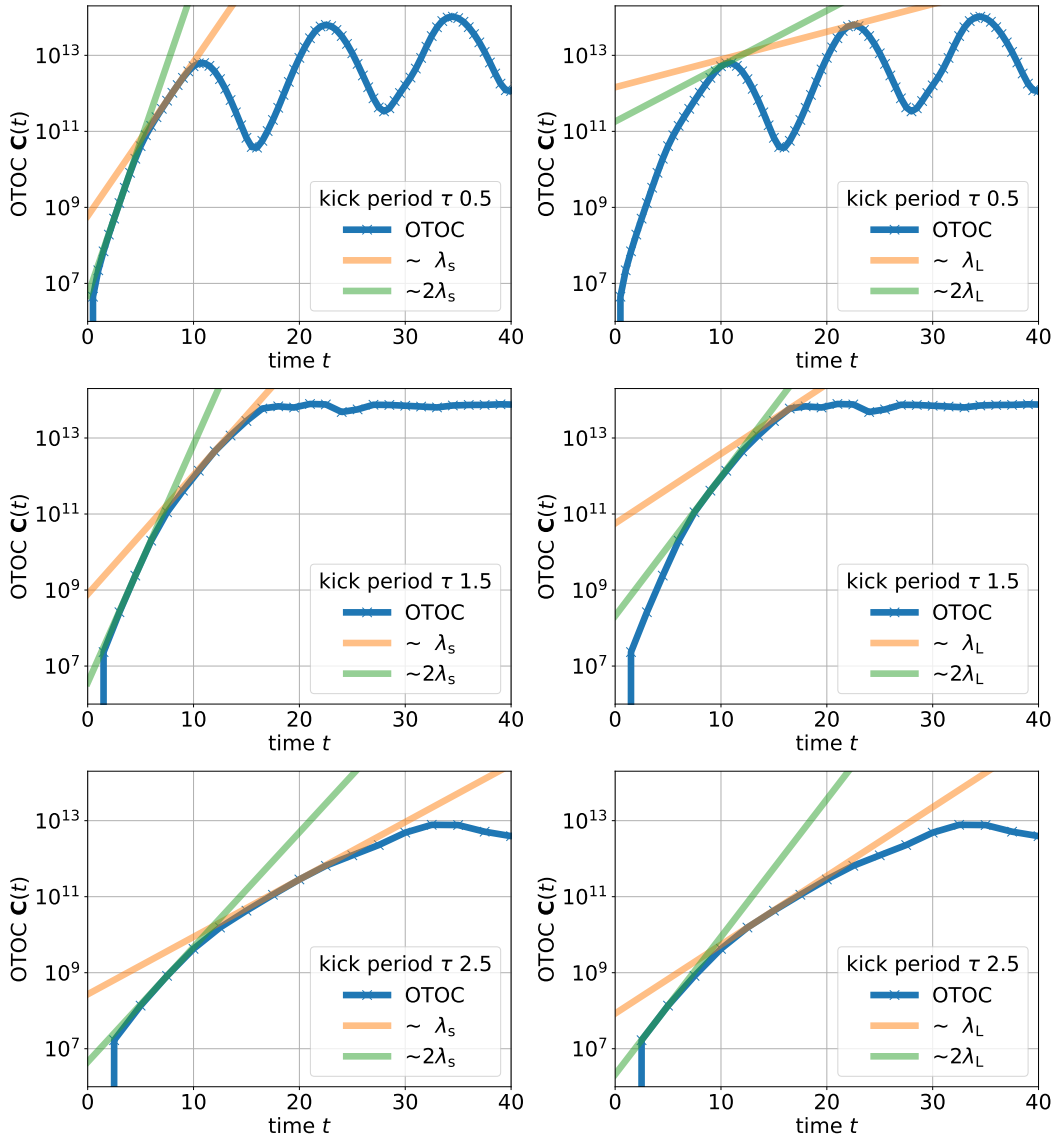

Figure 6.5: Fitting the stability and Lyapunov exponent to the early time exponential region (pre-Ehrenfest time) of the OTOC centered at the off-phase fixed point in the kicked dimer with $N = 10^4$ and $\Theta_* = 1.35$: for small kicking strength ($\tau = 0.5$, upper panels) we regain the continuous results, namely the $2\lambda_s - \lambda_s$ transition. By increasing the kicking strength, longtime oscillations vanishes and the OTOC saturates.

reach for us. Increasing the kicking strength further brings us into an integrable resonance (see Fig 6.3), such that we need to increase the kicking strength at least above $\tau \approx 3.6$, but thereby we only have three periods before we reached the Ehrenfest time and we can not extract any meaningful quantum Lyapunov exponent with three time data points.

To summarize, the analysis shows that the $2\lambda_s - \lambda_s$ transition is robust under breaking the integrability. It does not disappear, but due to our inconclusive results we need further investigations to clarify whether there are several transitions and if the regimes of λ_s and λ_L mix and give rise to the hypothesis in Eq. (5.1).

6.4. Periodic Orbits – Outlook

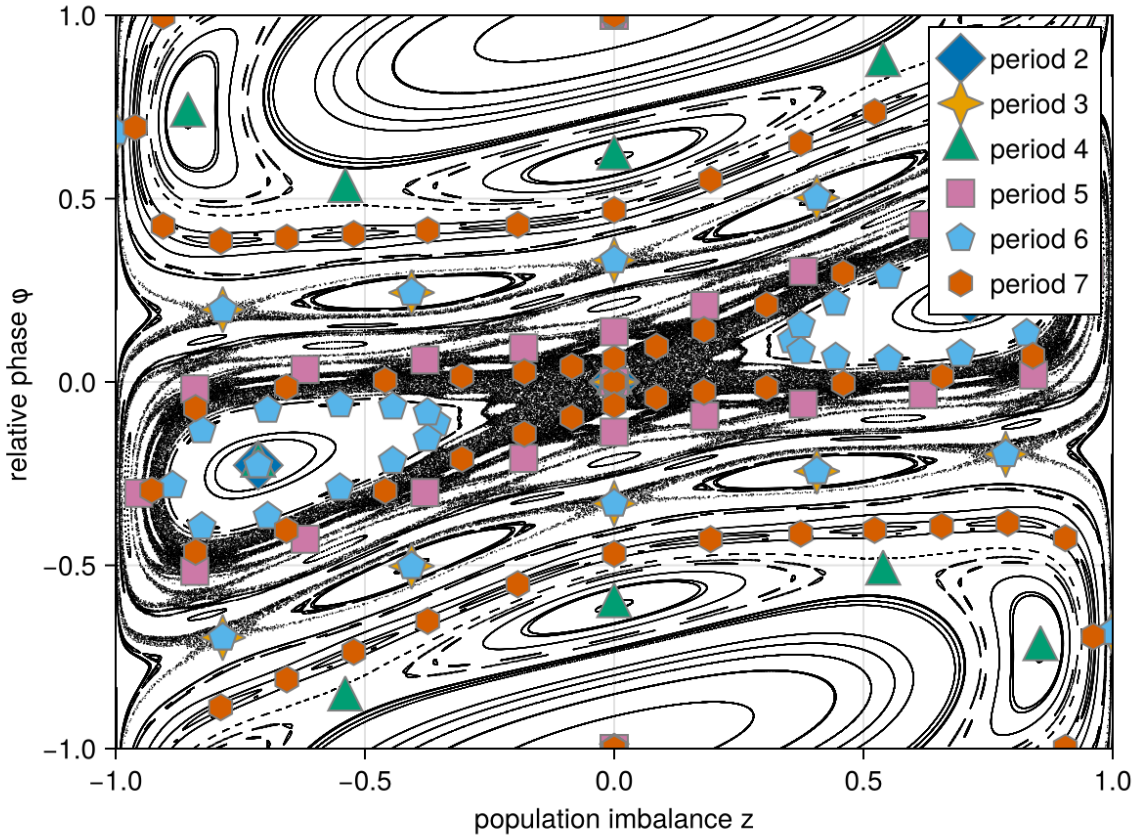

Figure 6.6: A selection of periodic orbits are marked in the near-integrable phase space of the kicked dimer for the system parameters $J = 1$, $U = 4$ and $\tau = 0.5$. We see several broken up tori into heteroclinic tangles with emerging periodic orbits. Around the off-phase FP, a chaotic region already appears.

We outline an idea, as until now we focus only on fixed points which are periodic orbits with just a period of one. What if we look at periodic orbits with larger periods? One can find many, namely a dense set inside any chaotic region just with a large periodicity. For an example, we mark a selection of periodic orbits in Fig 6.6 for $U = 4$ and $J = 1$ (system parameter $\Theta = \arctan(4) \approx 1.33$). We can view them as fixed points in an iterated phase space if we apply the map in Eq. (6.9) accordingly to their period.

For this thesis, we leave their investigation for future studies and also acknowledge that centering a state on a periodic orbit probably evolves creating a superpositions over all phase-space points belonging to the periodic orbit. Anyhow, we put a collection together in the Tab. 6.1 with their stability properties. We want to pose a question we find worth investigating for in the future: does the Heller criterion (for the existence of *scars* [181]) play a role for the $2\lambda_s - \lambda_s$

periodic orbit $[z, \frac{\pi}{2}\varphi]$	period T	stability exponent λ_s	Lyapunov exponent λ_L	Heller criterion $\lambda_\mathrm{L} T < 2\pi$
$[0.714057, 0.227291]$	2	0.173481	-0.000184164	True
$[0.785286, -0.197134]$	3	0.499913	0.0598964	True
$[0, -0.331807]$	3	0.627403	0.0729992	True
$[0.406446, -0.243627]$	3	0.447021	-2.79269e-5	True
$[-0.406446, -0.502379]$	3	0.526016	-0.00012772	True
$[0.539416, -0.521662]$	4	0.436446	0.0440727	True
$[0., -0.610524]$	4	0.34215	-8.87072e-5	True
$[0.841144, 0.0190654]$	5	0.484488	0.0458314	True
$[0.841144, 0.516423]$	5	0.430259	0.133332	True
$[-0.18149, -0.20834]$	5	0.368255	0.000178609	True
$[0.18149, -0.0928]$	5	0.328767	4.86956e-5	True
$[0.695158, 0.0761859]$	6	0.335638	0.0106481	True
$[0.444248, 0.215469]$	6	0.227643	0.0138379	True
$[0., -0.331807]$	6	0.492223	0.0632018	True
$[0.785286, -0.197134]$	6	0.424444	0.0525561	True
$[0.827302, 0.132141]$	6	0.337957	0.000323441	True
$[0.714057, 0.227291]$	6	0.0985127	1.54696e-5	True
$[0.550293, 0.0614302]$	6	0.308772	-0.000351986	True
$[-0.406446, -0.502379]$	6	0.266606	-0.00011253	True
$[0.406446, -0.243627]$	6	0.22693	-3.28998e-5	True
$[0.839815, 0.46315]$	7	0.462665	0.155467	True
$[-0.839815, -0.46315]$	7	0.462665	0.0929886	True
$[0.656715, -0.393052]$	7	0.278145	0.0158009	True
$[0.374103, -0.413601]$	7	0.332165	0.0146834	True
$[0.927718, 0.295302]$	7	0.645063	0.000672102	True
$[0.084848, -0.0423394]$	7	0.115697	-0.00012383	True
$[-0.193252, -0.551742]$	7	0.391396	8.59015e-5	True
$[0.193252, -0.428714]$	7	0.358653	-0.00010505	True

Table 6.1: We show a limited selection of periodic orbits in the kicked dimer for the system parameters $J = 1$, $U = 4$ and $\tau = 0.5$. The map is nearly integrable, but it shows already a small chaotic region around the off-phase FP in Fig. 6.6. Most of the Lyapunov exponents are small, as their associated periodic orbits are embedded in an integrable region.

transition or seeing the Lyapunov exponent λ_L in the early-time exponential growth of the OTOC? At our point of writing, we could only find periodic orbits which fulfill the Heller criterion, not a single one which does not. The likely reason is that the periodic orbits we find are mostly embedded into an integrable region, where we have a near-zero Lyapunov exponent. Finding and isolating periodic orbits inside a chaotic sea is more difficult and a future challenge. This brings us to the end of our investigation into integrable and chaotic motion via the OTOC. Before we conclude the OTOC entirely, we report on the findings for the thermal OTOC in the final section of the chapter.

7. Ongoing Study of Regularized and Unregularized Thermal OTOCs

One original goal of this thesis is to find quantum systems which saturate the *bound on chaos* [18]. The purpose of this chapter is presenting the results for the thermal OTOC, which are inconclusive and incomplete and require a more detailed and carefully in-depth study. Especially, we want to focus on one specific detail: one needs to address the regularization when we investigate the bound on chaos for a finite Planck constant $\hbar_{\text{eff}}$.

7.1. Regularization for the OTOC

Assuming a general expectation value, we understand regularization as the procedure to replace the operators by ($\hat{\rho}$ thermal state) smeared operators

$$\hat{O} \longmapsto \hat{\tilde{O}} = \hat{\rho}^{\alpha} \hat{O} \hat{\rho}^{\alpha}, \tag{7.1}$$

where we choose the exponent $\alpha = (2\,\#\text{operators})^{-1}$ to be the inverse of twice the number of operators appearing in the expectation value. The regularization originates from quantum field theories [18] and is introduced for convergence purposes. In this way, a full density operator is distributed to all the operators and we drop the explicit density operator out from the trace. In the case of the OTOC, we have $\alpha = 1/8$ and consequently the regularized OTOC is

$$\begin{aligned} C^{\text{reg}}(t) &= \operatorname{tr}\left\{ \left[\hat{\tilde{A}}(t), \hat{\tilde{B}}\right]^{\dagger} \left[\hat{\tilde{A}}(t), \hat{\tilde{B}}\right] \right\} \\ &= \operatorname{tr}\left\{ \left[\hat{\rho}^{1/8} \hat{A}(t) \hat{\rho}^{1/8}, \hat{\rho}^{1/8} \hat{B} \hat{\rho}^{1/8}\right]^{\dagger} \left[\hat{\rho}^{1/8} \hat{A}(t) \hat{\rho}^{1/8}, \hat{\rho}^{1/8} \hat{B} \hat{\rho}^{1/8}\right] \right\}, \end{aligned} \tag{7.2}$$

where the last line is only true for canonical thermal ensemble $\hat{\rho} = e^{-\beta \hat{H}}/Z$, since it commutes with the time-evolution operator $\hat{U}(t)$. Remember that there is no explicit density operator in the trace of the smeared operators in the first line of Eq. (7.2) anymore, it is fully absorbed into the smeared operators.

Let us discuss the thermal limits: an obvious consequence for $\beta \to \infty$ (temperature approaches zero $T \to 0$) is that any smeared operator $\hat{\tilde{O}}$ goes to the ground-state-projected operator

$$\hat{\tilde{O}} \overset{\beta \to \infty}{\longrightarrow} \langle E_0 | \hat{O} | E_0 \rangle \, | E_0 \rangle \langle E_0 | \,. \tag{7.3}$$

Trivially, the regularized OTOC vanishes for $\beta \to \infty$, because all ground-state projections in the commutator $[\hat{\tilde{A}}, \hat{\tilde{B}}] \overset{\beta \to \infty}{\longrightarrow} 0$ go to zero for all operators $\hat{A}$ and $\hat{B}$. This shows that the regularized OTOC fulfills the bound on chaos [18]

$$\lambda_{\text{q}} < \frac{2\pi}{\beta} = 2\pi T \tag{7.4}$$

in the limit of the ground state (zero temperature). In the other limit for infinite temperature $\beta = 0$, the un- and regularized versions agree. Assuming a finite Hilbert space, the canonical density operator becomes proportional to the identity, i.e., $\hat{\rho} \propto \mathbb{1}$ which commutes with every operator, such that the distribution of $\hat{\rho}^{\alpha}$ in Eq. (7.2) is irrelevant. In a system with infinite Hilbert space dimension, there can be small differences, e.g. a factor of two which we observe in Fig. 7.1 for the harmonic oscillator later on. Unfortunately for finite temperature, we have no explicit expression available, but we can explore through a numerical exploration the regularization effect. We study the difference between unregularized OTOC Eq. (3.1) and regularized OTOC Eq. (7.2) in the following systems: the harmonic oscillator, double-well potential and the trimer (a three-sited Bose-Hubbard model).

7.2. Standard Harmonic Oscillator

We start with the vanilla harmonic oscillator to understand the difference in the regularized and unregularized OTOC in a system where it shows oscillatory behavior. We use the standard harmonic oscillator Hamiltonian with an oscillation-frequency ω

$$\hat{H} = \frac{1}{2m}\hat{p}^2 + \frac{m\omega^2}{2}\hat{x}^2 = \hbar\omega\Big(\hat{a}^{\dagger}\hat{a} + \frac{1}{2}\Big), \tag{7.5}$$

where we introduce the standard ladder operators $\hat{a}$ and $\hat{a}^{\dagger}$. Unsurprisingly, we have oscillations in the unregularized OTOC

$$\langle\Big|\big[\hat{x}(t), \hat{x}\big]\Big|^2\rangle_{\beta} = \Big(\frac{\hbar}{m\omega}\Big)^2 \sin^2(\omega t) = \frac{1}{2}\Big(\frac{\hbar}{m\omega}\Big)^2 (1 - \cos(2\omega t)) \tag{7.6}$$

and only oscillations with twice the frequency ω, as it is an one-degree of freedom integrable system. If we compare to the temperature-dependent regularized OTOC

$$\langle\Big|\big[\hat{\tilde{x}}(t), \hat{\tilde{x}}\big]\Big|^2\rangle_{\beta} = \Big(\frac{\hbar}{m\omega}\Big)^2 \frac{\sin^2(\omega t)}{\cosh\left(\frac{\beta\omega\hbar}{2}\right) + 1}, \tag{7.7}$$

an important observation is that the amplitude of the oscillations are temperature-independent and the regularization alone causes a temperature dependence. The derivation of the regularized expression is lengthy and the details are shown in App. D. The amplitudes from regularization Eq. (7.7) and unregularized Eq. (7.6) are illustrated in Fig. 7.1. From this first simple example, we show that the regularization causes a temperature dependence despite being oscillatory here. We show in the next parts that this behavior persists for systems with exponential OTOCs.

7.3. Double-Well Potential

The easiest way to have an exponential OTOC with a temperature dependence is to quench the previous harmonic oscillator to an inverted harmonic oscillator,

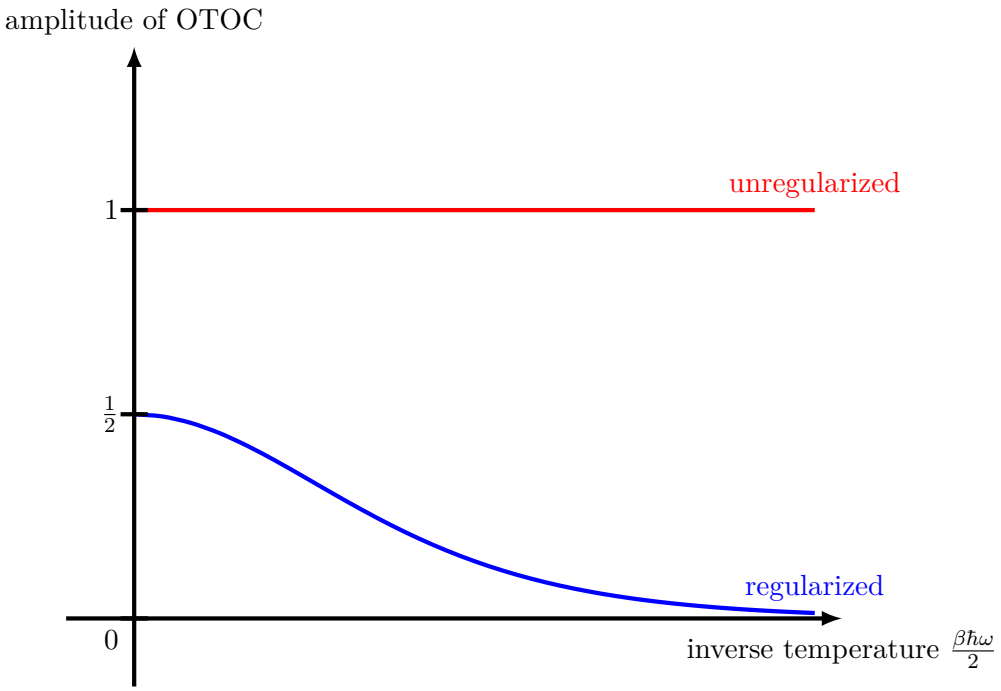

Figure 7.1: Oscillation amplitudes of the regularized vs. unregularized OTOC in the harmonic oscillator: the unregularized version has no temperature dependence, whereas the regularized version has an exponential decay of the amplitude with the inverse temperature. Interestingly, the infinite temperature limit ($\beta = 0$) shows a factor two difference which we trace back to the infinite Hilbert space dimension of the harmonic oscillator.

but a thermal state in an inverted harmonic oscillator is ill-defined. A Hamiltonian must be bounded from below to have a well-defined thermal state. To cure this we add a quartic confinement to the inverted harmonic oscillator, such that we end up to the next closest system which is a double-well potential

$$\hat{H} = \frac{1}{2m}\hat{p}^2 + \mu\hat{x}^4 - \lambda\hat{x}^2. \tag{7.8}$$

Around the origin we locally have the behavior of an inverted harmonic oscillator. For our numerical analysis, we fix $\mu = 1/4$ and $\lambda = 2$ and set the mass $m = 1$ and the Planck constant $\hbar = 1$. At the phase-space origin ($x = 0, p = 0$), we have one unstable fixed point with its local stability exponent $\lambda_s = \lambda = 2$. The eigenspectrum can be calculated numerically, using a shooting algorithm to find solutions for the boundary-value problem. We display the lower ten energy wave-functions of the system in Fig. 7.2. There is nearly a degeneracy at the ground state which we find to be important for an exponential growing OTOC at low temperature later on.

In order to calculate the OTOC, we calculate eigenfunctions up to $E = 300$ (natural units), which gives 87 eigenenergies. We truncate higher energies in further calculations and calculate the position operator as a matrix $\langle E_i|\hat{x}|E_j\rangle$ in this new finite Hilbert space. Thus, the calculations of the regularized and unregularized OTOC are straightforward.

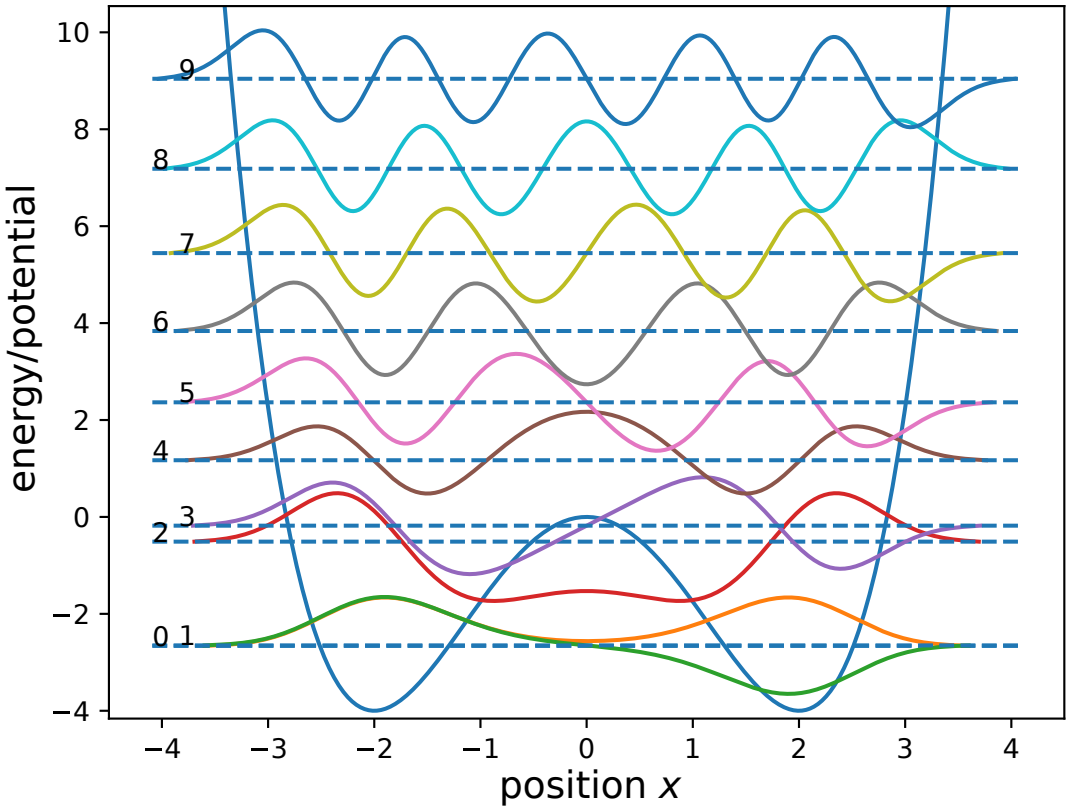

Figure 7.2: First ten eigenfunctions of the double-well potential shifted by their eigenenergies and numbered by their energy order. There are small energy splittings between the ground and first excited state, and between the second and third excited state due to the even-odd similarity.

Due to the truncation of the energy spectrum to $E < 300$, we can not approximate perfectly up to infinite temperature (or $\beta \to 0$), but assuming an equidistant energy spectrum above $E > 300$, the error should be bounded by $\sim e^{-30}$ for the density operator $\hat{\rho}$ at max $\beta = 0.1$. By increasing the energy cutoff to $E < 1000$, we verify that the shapes of the curves do not change significantly for the displayed temperatures. One clear observation in Fig. 7.3 is that at high temperatures the effect of regularization is minimal, as expected for $T \to \infty$, whereas for low temperature the behavior is fundamentally different. Persistent exponential growth is present in the unregularized OTOC at $T \to 0$ and the regularized OTOC transits from exponential to oscillatory behavior. Figure 7.4 verifies this by displaying a stagnant and vanishing exponent for $T \to 0$ respectively. The smeared operators, defined in Eq. (7.3), are stronger and stronger projecting to the low energy states, such that there are only some frequencies left between these contributing energy states. And these small number energy frequencies naturally lead to oscillations in the regularized OTOC. It is important to stress that we have the truncation/projection at every step/operator when calculating the correlator, which leads to the strong confinement around the low

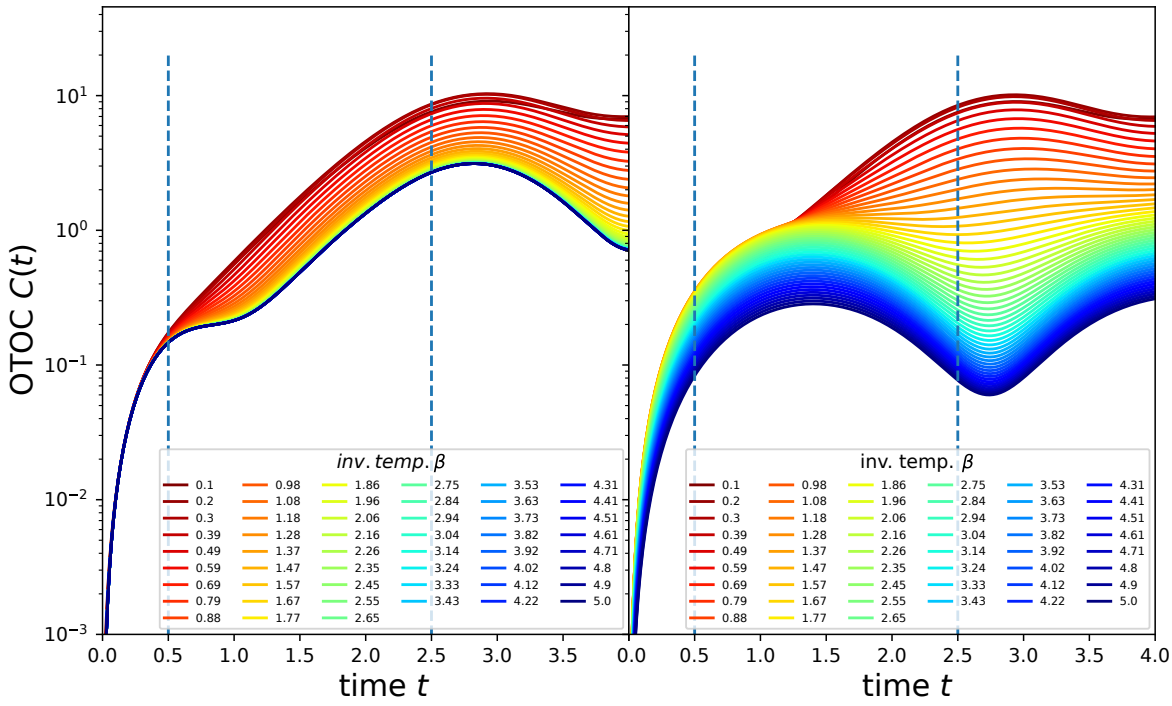

Figure 7.3: Temperature dependence of the unregularized OTOC (left panel) and regularized OTOC (right panel), the unregularized OTOC shows exponential growths even for $T \to 0$ ($\beta \to \infty$), in contrast to oscillations for the regularized OTOC. Blue dashed vertical lines show the fit window for the quantum Lyapunov exponent in Fig. 7.4.

energy states for low temperature. The unregularized OTOC is only affected once by $\hat{\rho}$ itself and an instability near the ground state is not damped. Further at low temperatures, the quality of the exponential fit decreases drastically in the time window of the fit depicted by the vertical blue dashed lines in Fig. 7.3. We quantify this in Fig. 7.5, where we display the averaged error between the fit and the OTOC inside the region of fitting.

These calculations are done by finite Planck constant, namely $\hbar = 1$, we come back to the double-well potential in Sec. 7.5, where we show how important finite $\hbar$ is when we approach the classical limit.

7.4. Thermal OTOC in the Trimer

The final system we investigate the thermal OTOC for is the Bose-Hubbard system we started the chapter with. For minimal $\hbar_{\text{eff}}$, we focus here on the three site version with $N = 100$ particles and find the same results to the single-particle double-well potential in Fig. 7.6. We tune the system parameter $\Theta = -0.942$ in the Bose-Hubbard 3-site system, such that the classical mean-field limit undergoes a bifurcation near the classical ground state (the homogeneous in-phase fixed point) [174]. Due to the bifurcation, we have instability near the ground state. This is exactly the case modeled by the double-well potential in the pre-

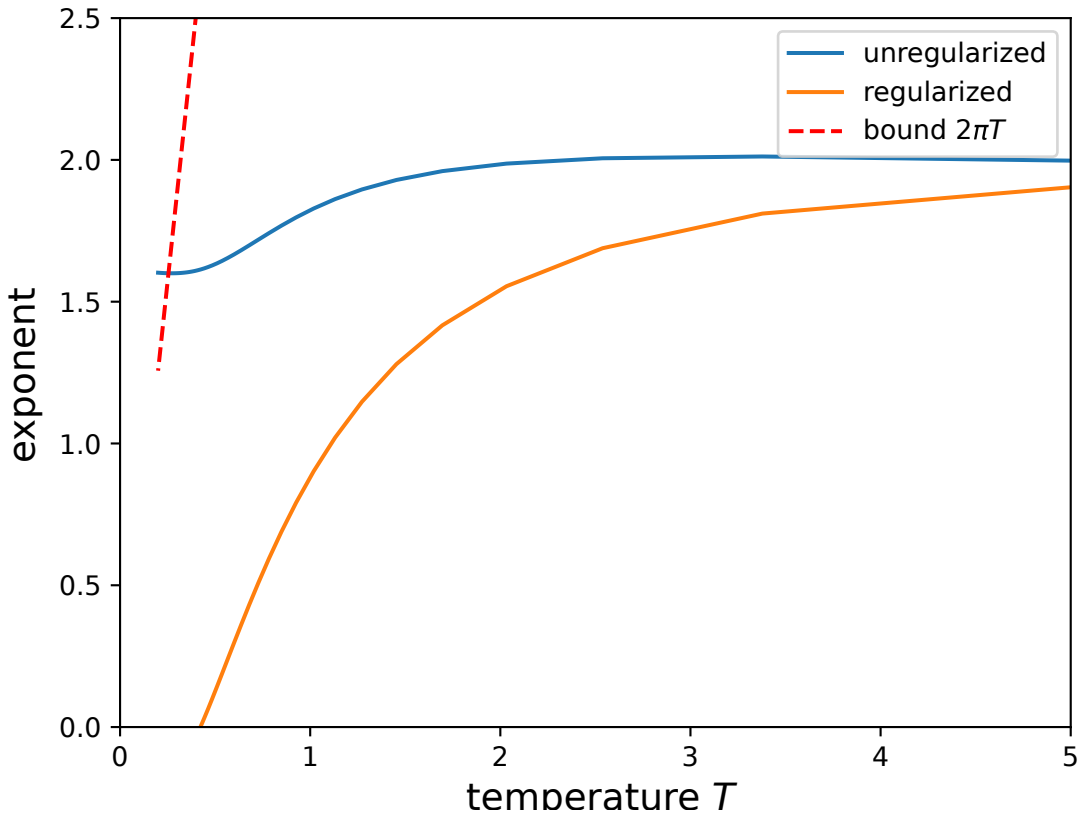

Figure 7.4: The quantum Lyapunov exponent λ_q is extracted from an exponential fit for the double-well potential depending on the inverse temperature β between the dashed blue lines in Fig. 7.3. The unregularized OTOC has a stagnant positive exponent even for $T \to 0$, in contrast to the vanishing quantum Lyapunov exponent for the regularized OTOC. For low temperatures, the regularized OTOC shows linear behavior and stays well below the bound on chaos reaching a vanishing exponent before zero temperature.

vious section. Figure 7.6 compares the unregularized and regularized OTOC in each panel for a single temperature. Both versions of the OTOC agree at infinite temperature, since the trimer has a finite Hilbert space[17] and the density operator is directly proportional to the identity. Lowering the temperature affects the unregularized OTOC minimally, since the ground state overlaps with the instability region and remains a source of exponential growth in the OTOC due to finite $\hbar_{\text{eff}}$. On the contrary, the regularized version develops smaller and smaller sub-exponential growth for small times when we lower the temperature and henceforth goes to zero which is the same behavior as in the single-particle double-well potential.

To summarize, we see again the same stagnant exponential behavior of the unregularized OTOC and the transition to oscillations and sub-exponential behavior for the regularized OTOC. It is a sign of universal behavior that the unregularized OTOC has exponential growth for finite $\hbar_{\text{eff}}$ if we have instability near the ground state, as it is the case, when the classical ground state under-

[17] Remember that the factor 2 difference in the harmonic oscillator case comes from infinite Hilbert space dimension.

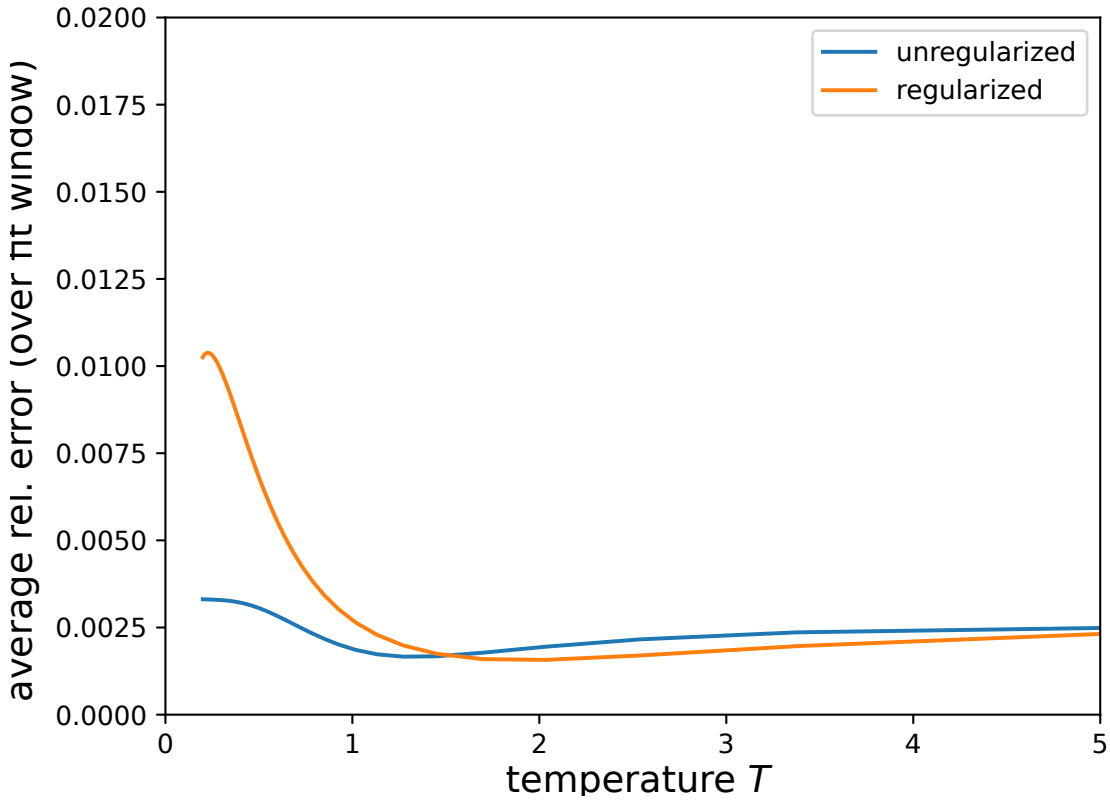

Figure 7.5: The validity of the fit is quantified by the averaged error of the exponential fit inside the vertical blue dashed lines of Fig. 7.3 in the double-well potential. For the regularized OTOC, the quality decreases significantly for low temperatures indicating the change to oscillatory behavior.

goes a transition via a bifurcation [174]. The dependence on $\hbar_{\text{eff}}$ is subject of discussion in the next subsection.

7.5. Heuristic Argument for an $\hbar$-Dependence in the Thermal OTOC

As already mentioned, our observation is that the OTOC can have exponential growth at early times in the unregularized version even at zero temperatures. This contradicts the bound on chaos [18], but it is not a violation, as the bound on chaos should be understood in the thermodynamic limit or semiclassical limit if one uses the unregularized OTOC. We speculate that either of the limits prohibit to have the situation we find in the trimer or the double-well potential that we have a ground state overlapping with a chaotic region. As in the classical limit, where the effective Planck constant $\hbar_{\text{eff}}$ goes to zero, the ground state is well localized in a global minimum which means no overlap with instable or even chaotic classical regions in the classical phase-space representation (Wigner function of the ground state) and no exponential classical OTOC at zero temperature.

We test the classical limit via a TWA simulation in the double-well potential

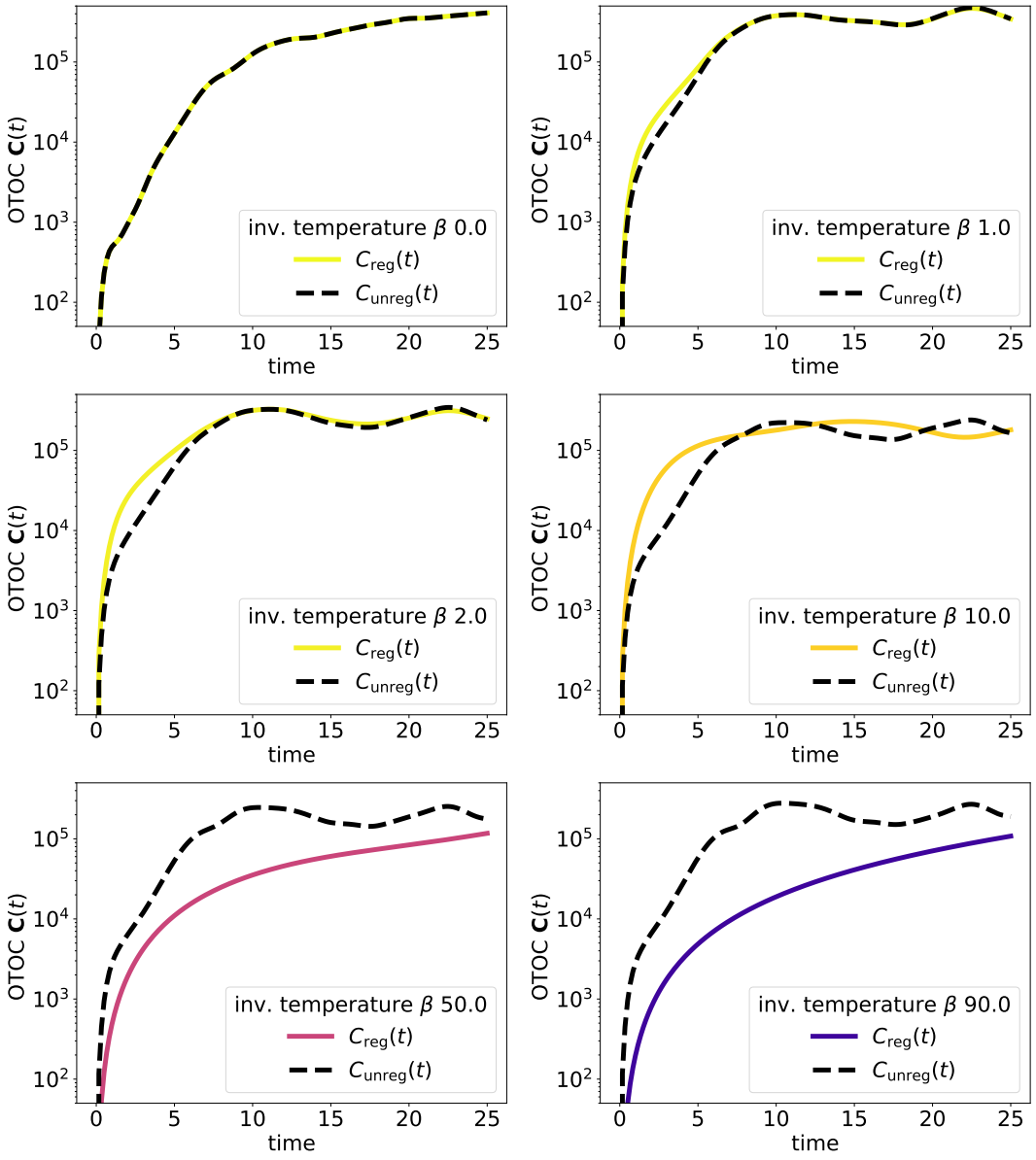

Figure 7.6: Temperature snapshots of the unregularized (black dashed) and regularized (colorful, solid) OTOC for $\beta \in \{0, 1, 2, 4, 5, 10, 50, 90\}$ in the trimer at the system parameter $\Theta = -0.942$ and with $N = 100$ particles. The unregularized OTOC stays exponential, the unregularized OTOC switches to sub-exponential growth and goes with lower temperature more towards zero.

with a classical thermal state $\rho(q,p) = e^{-\beta H(q,p)}/Z(\beta)$. The double-well potential parameters we choose are $\mu = 0.25$ and $\lambda = 0.5$, so the stability exponent is $\lambda_s = \lambda = 0.5$. There is no notion of regularization in the TWA, since the classical quantities commute and their order is irrelevant. We calculate the usual TWA OTOC in Eq. (3.3) with the thermal Wigner function which we call the thermal classical OTOC. In Fig. 7.7, the classical thermal OTOC shows a clear temperature behavior which is the same as the regularized OTOC with finite $\hbar_{\text{eff}}$ quantum calculation. There is a transition from the high temperature exponential growth to oscillatory behavior reflecting the classical ground state being

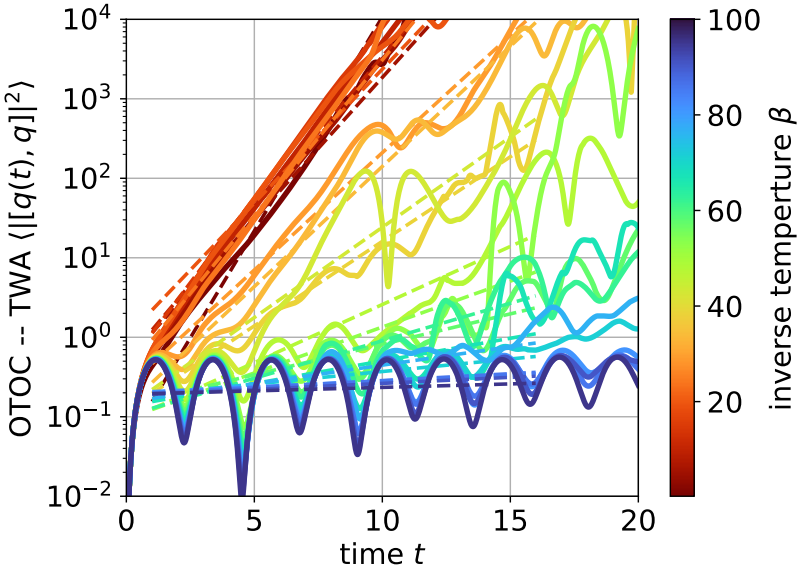

Figure 7.7: The classical thermal OTOC visualized for several inverse temperatures for the double-well potential. The exponential behavior vanishes in the classical limit, when the temperature is decreased. Dashed colored lines show exponential fit curve which are used to extract the exponent which is depicted in Fig. 7.8 to quantify its temperature dependence.

the global minimum of the potential. In contrast to the regularized quantum OTOC, the classical TWA OTOC does not go to zero and just stays oscillatory if we approach zero temperature.

When we extract the early-time exponent via a fit of an exponential increase in Fig. 7.8, we quantify the observation with a vanishing fitted exponent. At high temperatures, we see an exponential exponent saturating at $2\lambda_q = 1$, which is twice the stability exponent, and at lower temperature we see a linear and quartic dependence. The origin of these power laws remains unexplained and represents an open avenue for future research. In particular, it is of interest to investigate whether these laws are related to the bound on chaos [18].

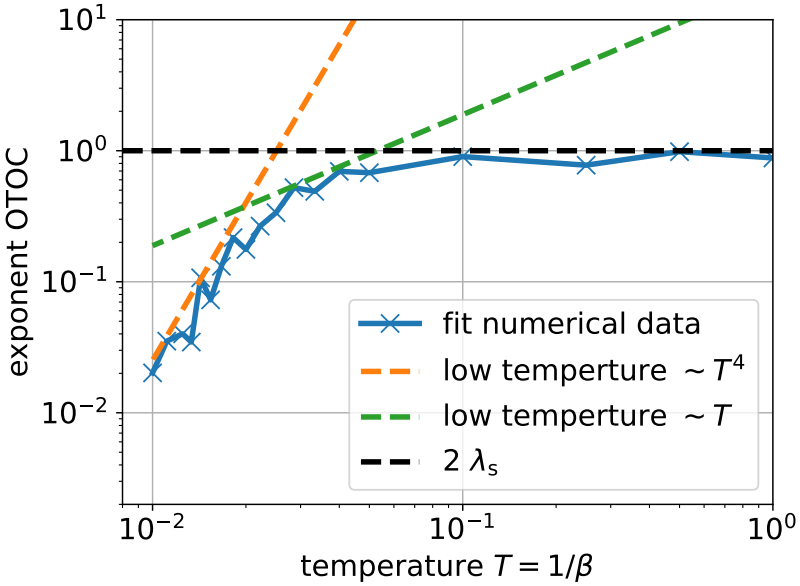

Figure 7.8: Extracted quantum Lyapunov exponents from the classical thermal OTOC are depicted over the temperature in the double-well potential. The early-time exponent shows a temperature dependence, i.e., it approaches zero with low temperatures and stays at the stability exponent of the hyperbolic FP at $(q = 0, p = 0)$. The fit quantifies that in the classical limit of Eq. (4.8) a temperature dependence is present which is compatible with the bound on chaos.

8. Summary – Out-of-Time-Ordered Correlators

Out-of-Time-Ordered Correlators are a valuable tool to quantify if a quantum system exhibits instabilities by early-time (pre-Ehrenfest) exponential growth. Its rate of exponential growth, the quantum Lyapunov exponent, is then related to the local stability or the Lyapunov exponent or even a mixture of them as shown by our findings in the systems discussed in Secs. 4, 5 together with Sec. 6. Finally, Sec. 7 focuses on the subtle, but important difference a regularization makes if thermal OTOCs are calculated in finite system sizes. Figure 8.1 illustrates all topics investigated and highlights that our findings in the mixed systems and for the thermal OTOC need future studies, but direct proceedings are limited partially by numerical limitations.

Looking closer, the purely integrable case shows a remarkable transition of the quantum Lyapunov exponent from twice to once the stability exponent due to the initial state being localized around the source of instability, a hyperbolic fixed point. Depending on the shape of the initial state around the FP, the transition can be moved in the early-time window bounded by the Ehrenfest time from above. In the edge cases, the quantum Lyapunov exponent can be tuned to be only once the stability exponent for the infinite temperature state or purely twice the stability exponent for a state localized along the stable manifold of the FP. The property of the quantum state is essential in determining which quantum Lyapunov exponent one observers, and it bridges a gab between two contradicting reported quantum Lyapunov exponents in [14, 15] for integrable

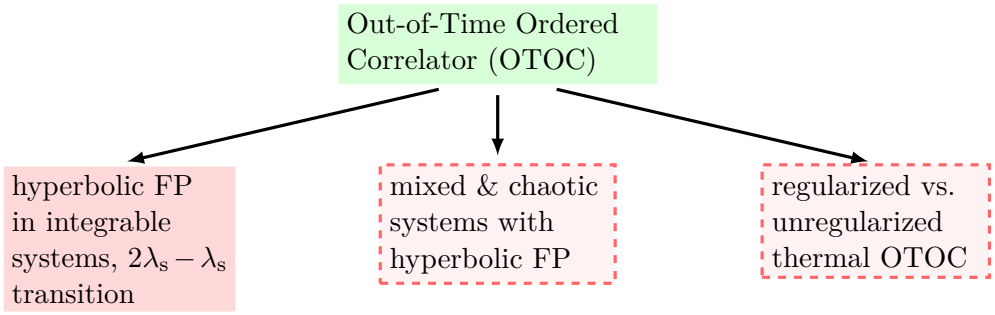

Figure 8.1: The overview illustrates the different topics in Chap. I. The quantity OTOC is investigated in different setups: first integrable systems with a local hyperbolic FP showing a transition in the early time exponent; second mixed systems showing combined Lyapunov and stability exponents; third thermal OTOC with and without regularization showing a temperature-dependence or a stagnant quantum Lyapunov exponent. The last two setups (dashed boxes) need future study to have a final and reliable statement.

systems with a hyperbolic fixed point.

Motivated by the integrable transition, we search the early-time regime for specific behavior setting the integrable and mixed or chaotic OTOC apart. We find both for larger system sizes and finite as well as relatively large[18] effective Planck constants that the pre-Ehrenfest OTOC in the Bose-Hubbard model is fitted well by a linear combination of stability and Lyapunov exponent which accounts for the conjecture we give at the beginning of Sec. 5. This conjecture points towards the possibility that the quantum Lyapunov exponent can differentiate between hyperbolic FP and intrinsic chaos curing a flaw of false-positive signatures for quantum chaos mentioned in the introduction.

With all the indications from the previous sections and in order to study the crossing from integrable to mixed and chaotic systems, we went back to the Bose-Hubbard dimer and turned it into a time-dependent periodically kicked system. Through scaling the strength with the period of the kicks, we have then a system at hand which is the continuous integrable dimer in the limit of zero kicking period and gets chaotic for large enough periods. Our kicked dimer enables us to look at OTOC in the near-integrable and chaotic system configurations depending how large the kicking period is chosen. Sitting again on a hyperbolic FP, we confirm a robust transition in the early-time quantum Lyapunov exponent if we gradually move to a mixed system. Our numerical simulations are conclusive if the stability exponent is clearly larger than the Lyapunov exponent of the emerging chaotic sea. With respect to the other case at larger periods, it is unclear whether the Lyapunov or stability exponent is the cause. Unfortunately, the dependencies of the stability and Lyapunov exponent are too indistinguishable to have a reliable interpretation in this region of interest. Even larger kicking periods have a intriguing regime of the Lyapunov exponent being larger than the stability exponent. Regrettable again,

[18] Large means compared to the integrable numerical simulations, where we observe the transition.

large kicking periods shrink the number of time-points inside the pre-Ehrenfest time, such that no exponent can be extracted. Enlarging the early-time region via the semiclassical parameter, the particle number, is not possible due to computational limitations. One of our ideas to proceed further in the future is to move away from fixed points and investigate periodic orbits with higher period (fixed points are periodic orbits of period one) in order to find new signatures like further transitions during the pre-Ehrenfest time window.

Going from localized states around hyperbolic fixed point to thermal states, we looked at single-particle and the many-body systems and demonstrate that parameters can be tuned such that we observe an exponential growth for the unregularized OTOC even at zero temperature which technically violates the bound on chaos [18]. Our interpretation to this point of writing is that a finite Planck constant $\hbar$ ($\hbar_{\text{eff}}$ for many-body) makes the regularization necessary to fulfill the bound on chaos. It fits into the phase-space picture, where the ground state overlaps with instabilities of the classical dynamics because of quantum width given by the Planck constant. We support our interpretation by a TWA-calculation of the thermal OTOC in the single-particle double well. It is the classical limit ($\hbar \to 0$) in the system and the thermal OTOC shows a decreasing quantum Lyapunov exponent going to zero temperature, i.e., the OTOC goes from exponential to oscillatory behavior. A special feature of (many-body) quantum systems with finite $\hbar_{\text{eff}}$ is that the ground state can overlap with a chaotic region in the Bose-Hubbard trimer. Due to the contributions from chaos, the exponential growth persists again even at the ground state (zero temperature) for the unregularized OTOC. In the Figs. 7.3 and 7.6 throughout the last section, the numerical data shows that the regularized OTOC cures the apparent violation of the bound. Unfortunately, we only can prove this in the limit of zero temperature in Sec. 7 via the smeared operators. Nevertheless in the semiclassical limit, the quantum Lyapunov exponent should be smooth over the temperature, especially there must be some dependence on temperature when the regularized quantum Lyapunov exponent goes from infinite (equal the biggest instability and agreeing with the unregularized version) to zero temperature. When we approach the classical limit $\hbar_{\text{eff}} = 1/N \to 0$ in the trimer, the overlap to regions of instability has to decreases for low energy states, specifically the ground state localizes inside the global minimum of the mean-field energy landscape. Therefore, the exponential growth must decrease for both OTOCs in the regularized and unregularized version, until we converge to the TWA of the thermal OTOC. The TWA, the classical limit, has no regularization, since the classical quantities commute. Concisely, the bound on chaos is fulfilled for the systems we investigate in this thesis, when we approach the classical limit. We suspect the bound to be saturated only for fully chaotic systems [18] and that the systems need to have some scaling behavior with the temperature which brings us to the next point.

Let us compare our many-body Bose-Hubbard system to systems reporting saturation [26, 28], the so-called fast scramblers. The issue is the very definition of temperature in our systems itself. Temperature is defined in a thermodynamic

limit, which is not reached in our limited finite size systems. This leads us to the following question in our many-body setup: how do we approach the thermodynamic limit in our Bose-Hubbard system? Do we increase the number of sites L with a fixed number of particles N or a constant filling factor $\nu = N/L$? Or do we just increase the particle number N and keep the number of sites L constant? In our opinion, we support the idea that the thermodynamic limit is well-defined when increasing the system size keeping the filling factor constant. This enlargement leaves the classical extended mean-field limit[19] invariant which resembles a bit the scaling laws of thermodynamics.

Clearly, there is need for exploring more systems, we suspect more hidden nuggets like the $2\lambda_\mathrm{s} - \lambda_\mathrm{s}$ in the early-time window. We are confident that they are waiting to be discovered. There is the need to study more fixed points and periodic orbits in mixed and chaotic phase space with OTOCs and, if possible, with smaller quantum scale $\hbar$ to enlarge the exponential time-window, in the hope of finding a clear reliable chaos signature.

Connecting to the next chapter, we do not only want to find, but we now want to utilize chaos in many-body systems. The instabilities we can detect with OTOCs help us find extremely fast trajectories between two points in the mean-field phase space. But on the other hand as in the OTOC due to chaos, a wave packet diverges from the classical prediction after the Ehrenfest time. This departure hinders us to directly move a quantum state along any classical trajectory. Therefore, our goal is to prevent these deviations and guide wave packets coherently along these fast trajectories beyond the Ehrenfest time, i.e., we want to control quantum chaos.

[19] Periodically extended solutions are reducible to the symmetry frame for their classical dynamics [174].

II. Controlling Many-Body Quantum Chaos

Before we dive into the physics of controlling chaos, we point out that the majority of this chapter is adapted from our publication [3] which is a collaboration with substantial contribution by Lukas Beringer. In the following, we focus on the core application in one-dimensional Bose-Hubbard systems. For the interested reader, we refer to our publication for more applications and its supplementary material which includes several instructive animations. We especially recommend the animations, as they provide a better illustration of the time evolution for quantum states along mean-field trajectories.

We started the thesis by discussing how chaos or instabilities can be detected in quantum systems via the OTOC in Chap. I. Next to exponential sensitivity, chaos leads to equilibration effects, like long term saturation in the OTOC (see Fig. 6.4). However in the ongoing second quantum revolution [182, 183], the precise control in out-of-equilibrium situations is necessary. Imagining a quantum device levering coherent superpositions of certain quantum states [184], then this equilibrating behavior emerging from chaos is unwanted. Especially if we look into the direction of quantum computing, specific states or their superpositions are needed for computations. The challenge of large systems is that they are usually at least partially chaotic, so one needs to account for and combat chaotic features, e.g. equilibration or the exponential sensitivity. Contrary to our case instead, we intend to use chaos to our advantage. More precisely, we harvest the instability and ergodicity (mixing flow) as resources to find fast control mechanisms which allow for the preparation of macroscopical occupied single-particle states. We outline an approach to use chaos as an ally to overcome exponential scaling in system sizes of many-body systems. Specifically, our goal is to describe coherent quantum targeting and its application to Bose-Hubbard models. We are extending the classical version of controlling chaos, e.g. finding trajectories for satellites in space [46–51], to the many-body quantum systems inspired by and based on the single-particle version [63, 64].

In order to understand the advantages chaos can offer, it is helpful to introduce the basics concerning heteroclinic orbits emerging from chaotic dynamics. Later we revisit Bose-Hubbard systems, their mean-field limits and symmetries, (number-projected) coherent states, truncated Wigner approximations. Finally, we introduce the protocol for the optimal coherent quantum targeting itself. Some topics are reintroduced from the first chapter since we use different conventions in our publication [3] compared to our OTOC-themed publications [1, 2]. These subtleties are important for the correct comprehension and interpre-

tation of the results. With this said, let us begin by path finding via *heteroclinic motion* in chaotic systems. It is our first topic and it brings us a prime advantage for timescales in our proposed control scheme.

9. Path Finding: Heteroclinic Motion and Timescales

Before we discuss the details of the path finding, we highlight the central advantage of our approach, namely short time-scales. Therefore, we assume an optimized trajectory is identified. Of great interest is how short the timescale $t_{\min}$ can be[1] connecting the start and target points. We give a rough estimate for an extensive system: the available phase-space volume per degree of freedom has a geometric mean, $\mathcal{V}_1$, so that the number of quantum coarse-grained cells for the full system is $N_L = (\mathcal{V}_1/h)^L$. There is a timescale for moving from a phase-space cell to an adjacent cell, t_0, which is also the time for the quantum dynamics to move to the "closest" orthogonal state. The timescale for an ordinary meandering chaotic trajectory to connect two random cells is proportional to $N_L t_0$. Because N_L scales exponentially with the degrees of freedom L, $N_L t_0$ is an extraordinarily long time for connecting randomly two cells. This is completely different from the optimal heteroclinic trajectory. The path is found somewhere inside a cell stretching as $\exp(h_{\rm KS} t)$ which scales with the Kolmogorow-Sinai entropy $h_{\rm KS}$ [59, 185]. This grows to the order of N_L on a very short timescale given approximately by the relation

$$t_{\min} \propto \frac{1}{h_{\rm KS}} \ln N_L = \frac{1}{\lambda} \ln \frac{\mathcal{V}_1}{h}, \tag{9.1}$$

where $\lambda = h_{\rm KS}/L$ is the average positive Lyapunov exponent. This is another example of a so-called log-time typically found in chaotic systems. The quintessential example is the Ehrenfest time at which quantum and classical dynamics must diverge, which is a log-time [7, 42, 186, 187] for a chaotic system, also where the OTOC diverges from the classical TWA description in Sec. 4.

This rather simplistic logic gives a vastly shorter timescale than $N_L t_0$. It is logarithmic in Planck's constant, and, rather surprisingly, it is independent of the number of degrees of freedom. Perhaps a more realistic calculation would lead to some weak system size dependence. After all, only generic dynamical systems are uniformly hyperbolic, most chaotic systems are non-uniform, i.e., different cells are more or less difficult to approach. But clearly, even a more realistic estimate would still lead to the conclusion that the optimal heteroclinic motion gives something close to an *exponential* timescale speed-up compared with $N_L t_0$ and very weak dependence on Planck's constant. This turns out to

[1] Quantum computing devices in laps have limited coherence times before the model Hamiltonian loses its validity. Therefore, one is interested to have control protocols that are as short as possible. Especially, one wants a preferable scaling the system size in order to reach feasible number of qubits and longer run times.

be the remarkable way in which chaos becomes a targeting resource. The cost of this speed up is the difficulty of identifying the requisite *exponentially rare* trajectory.

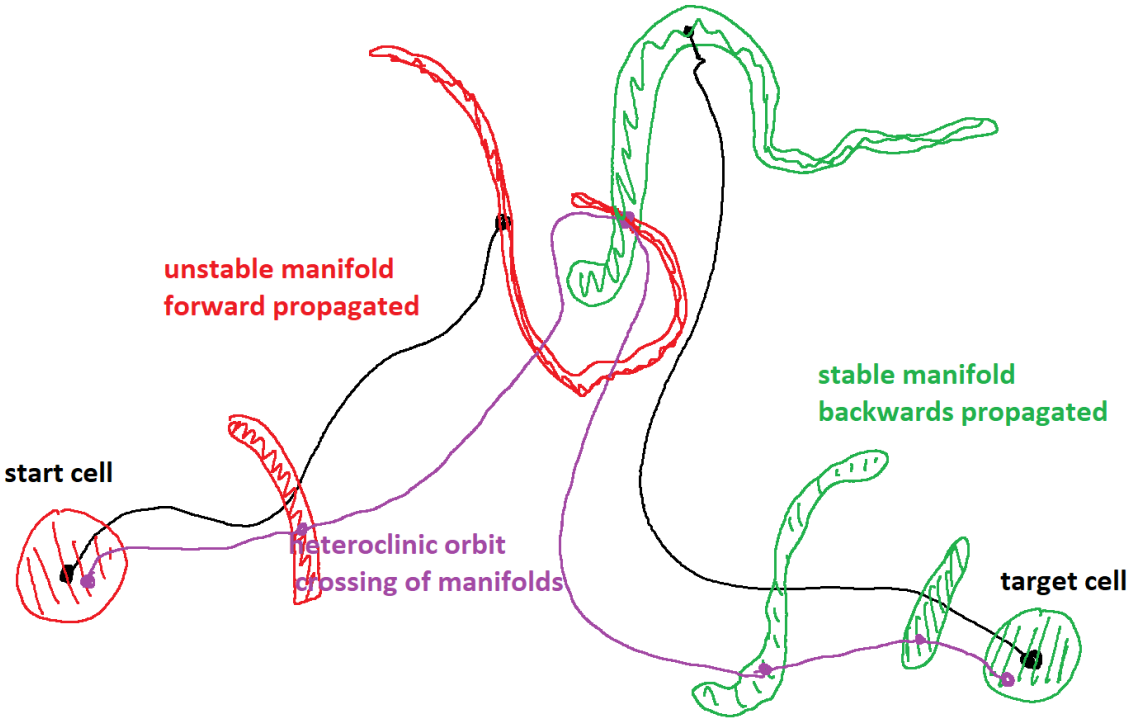

Figure 9.1: Schematic illustration of heteroclinic orbit connecting two phase-space cells (circles at the start and target). Unstable manifold of the start point is propagated forward (exp. diverging away from the central trajectory of the start point), while at the same time the stable manifold of the target point is propagated backwards (exp. converging to the central trajectory of the final point). Whenever a crossing is found, a heteroclinic orbit (purple trajectory) is identified which exponentially diverges from the start point (trajectory) and exponentially approaches to the final point (trajectory).

Our method is based on finding these rare heteroclinic paths and guiding wave packets coherently along them. We see them as an optimal class of paths; they have the advantage of exponential escaping from and approaching towards reference trajectories; see Fig. 9.1 for a schematic sketch. Due to two different reference trajectories - an initial and a final (black solid curves in Fig. 9.1), these paths are called *heteroclinic*[2]. The exponential behavior gives rise to the time advantage mentioned that gives a lower bound $t_{\min}$ (defined in Eq. (9.1)) for the propagation between phase-space cells.

[2]If the initial and final references are the same, then we would have a homoclinic trajectory, which is not the case for the targeting purpose, but of interest if we want o stabilize quantum states on periodic orbits [3].

Numerically, they are found by propagating a region around the initial (start) and target point forward and backwards in time respectively. These two volumes develop into the so called unstable (red) and stable (green) manifolds in Fig. 9.1. When a crossing is detected (purple dot), a heteroclinic trajectory is identified, since it belongs to both manifolds connecting start and target cell. One further neat property is that the minimal time $t_{\min}$ is primarily system-size independent, i.e., the lower bound finding heteroclinic trajectories does not scale linearly, when we increase the system size.

Even thought the minimal time $t_{\min}$ is system-size independent, the search space for the heteroclinic trajectories scales linearly with the system size and their appearance is exponentially rare [188]. The art of finding good heteroclinic trajectories has met its match in Lukas Beringer who manages to find them for low-dimensional Bose-Hubbard systems by a sophisticated Monte Carlo search in a reduced search space. Conveniently though, chaotic systems usually allow for substantial reduction of the search space, as explicitly demonstrated for the case of heteroclinic trajectories and complex saddles in a Bose-Hubbard system in [188]: for any phase-space point located inside a chaotic region, the local dynamics can be decomposed into pairs of stable and unstable manifolds, resulting from the pairing rule of the Lyapunov exponents mentioned in App. A.1.2. By disregarding all stable directions and those corresponding to constants of the motion (energy and particle number), any search in a Bose-Hubbard system can be reduced to an $(L-2)$-dimensional search-problem, where L denotes the degrees of freedom and is the number of sites of the Bose-Hubbard model ahead. By focusing only on the most unstable directions an even further reduction is sometimes possible. Nevertheless, a systematic search in higher-dimensional systems is typically futile. Luckily, a further significant reduction of the search-space dimension is possible in cases where symmetries are present in the initial and final states. And indeed, our publication [3] focuses on Bose-Hubbard systems possessing discrete symmetries, periodic boundary conditions, and symmetric initial conditions leading to a reduced-dimensional symmetry plane of the mean-field dynamics [174]. The reduced-dimensional dynamics can be mapped onto larger systems with each dimension in the lattice (one, two, or three) being any integer multiple of the reduced value, including infinity. As a result, the search space remains the same reduced-dimensional value independent of the size or dimension of the lattice. Here in this thesis, we only use it for the density wave in Sec. 10.4.

For applications we discuss, the symmetry-reduced value of the lattice dimension is $L = 4$. This allows an optimized search which can be performed in a 2-dimensional space no matter what the entire lattice size is. Thus, it turns out that a simple Monte Carlo search in the reduced phase space around the initial state's centroid is sufficient to determine the suitable heteroclinic pathway, i.e., our control trajectory.

Note that the control scheme can be applied to tasks in which a certain time for reaching the target state is given, as long as it is greater than the minimal time $t_{\min}$ in Eq. (9.1) discussed in the introduction. For such larger times, there

always exists a corresponding heteroclinic trajectory that can be used as optimal transport path [188]. We now assume that the technical problem of identifying suitable control trajectories is solved for the specific application in Sec. 12 and continue with a recap of Bose-Hubbard systems.

10. Bose-Hubbard Systems – Recap

In analogy to the OTOCs in Chap. I, we choose the Bose-Hubbard model to investigate coherent quantum control via guiding trajectories. It turns out that the Bose-Hubbard model is an ideal bosonic many-body system for three main reasons. On the one hand, this model is experimentally relevant for transmons [189], time-crystals [190] and ultracold atoms in an optical lattice [68], so the theoretical results could be of relevance for future experiments. On the other hand, a classical limit is defined by a mean-field limit of large occupation numbers. On an imaginary third hand, the specific form of the interaction greatly facilitates the control implementation as discussed in Sec. 11 ahead.

A convenient property is that a quadrature phase-space representation leads to a Hamiltonian formalism with canonically conjugate real variables $\vec{x} = (\vec{q}, \vec{p})$ which we already introduced in Chap. I. Furthermore, the control protocol works on a many-body version of minimum uncertainty states in the form of coherent states, and crucially all the results apply equally well to their total number-projected coherent states[3]. Finally, for the control system, the truncated Wigner approximation becomes a critical analysis tool as its dynamics become essentially exact.

10.1. Hamiltonian and Classical (Mean-Field) Limit

We recap the Bose-Hubbard Hamiltonian from Chap. I, describing a gas of N ultracold bosonic atoms. They are subject to a sufficiently strong periodic optical trapping potential generating a one-, two-, or three-dimensional lattice and well described by the Bose-Hubbard model [68]. Here the Bose-Hubbard Hamiltonian is only given for a periodic one-dimensional lattice of L sites ($L + 1 \equiv 1$)

$$\hat{H} = -J \sum_{j=1}^{L} \left(\hat{a}_j^\dagger \hat{a}_{j+1} + \hat{a}_{j+1}^\dagger \hat{a}_j \right) + \frac{U}{2} \sum_{j=1}^{L} \hat{n}_j \left(\hat{n}_j - 1 \right) + \sum_{j=1}^{L} \mu_j \hat{n}_j \,, \tag{10.1}$$

since we only discuss one-dimensional applications later on. In contrast to the Bose-Hubbard systems in Eq. (5.2) of Chap. I, the chemical potentials μ_j are added[4], such that the individual sites are offset by μ_j. As before, it remains unchanged that the Hamiltonian energetically accounts for the possible hopping of bosons to neighboring sites, governed by the kinetic hopping parameter J, as

[3] The number-projected coherent states are used in the calculations of the OTOCs presented in the previous Secs. 4, 5 and 6 of the first chapter.

[4] Later on, we see that they are necessary to design the control protocol and also to adjust energy shells of target and initial phase-space cell.

well as on-site interactions between the bosons given by an interaction strength U, which is related to the s-wave scattering length of the two-body collisions between atoms. A simplified rendition of such an one-dimensional ring is displayed in Fig. 10.1. There, the different terms in the Hamiltonian are color coded, e.g., the hight difference displays the chemical potentials.

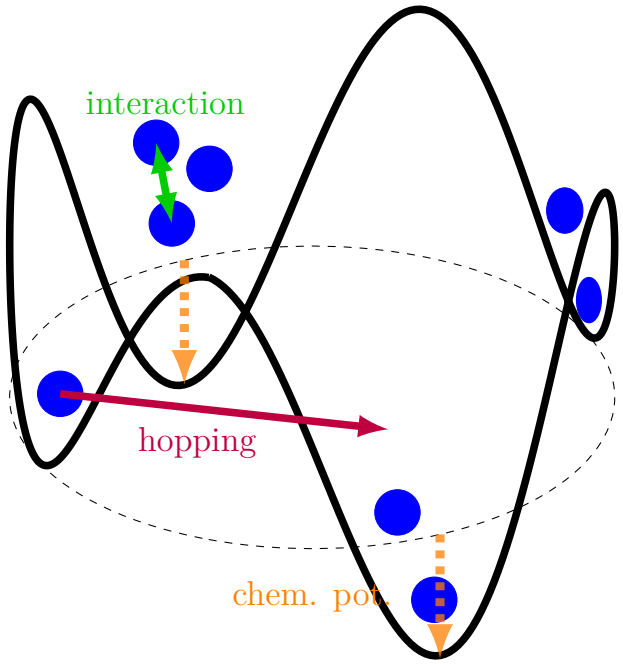

Figure 10.1: Schematic representation of an one-dimensional Bose-Hubbard ring. Cold atoms are trapped in an one-dimensional periodic lattice, here consisting of four sites. The model includes nearest-neighbor hopping, on-site interactions between atoms, as well as energetic offsets for each site given by individual chemical potentials. Reprinted from Ref. [3].

With the Bose-Hubbard Hamiltonian in Eq. (10.1), there are two unchanged preserved quantities, energy $\hat{H}$ and total particle number $\hat{N} = \sum_{j=1}^{L} \hat{n}_j$ ($[\hat{H}, \hat{N}] = 0$). With two degrees of freedom, the dimer ($L = 2$) is always integrable (see Sec. 4) for all parameters. Furthermore the limiting parameter cases of $U = 0$ or $J = 0$ are integrable, where the absence of any interactions leads to a superfluid ground state and the absence of hopping gives a Mott insulator phase. For $L > 2$ and in the parameter range $J \sim UN$, the quantum system is known to exhibit quantum chaos [99, 100], which is the dynamical regime of our interest.

From the quantum Hamiltonian, a mean-field limit, which depends on the effective Planck constant, can be defined equal to the inverse filling factor, $\hbar_{\text{eff}} = L/N$. We use here a slightly different definition for the effective Planck constant compared to Chap. I, where the effective Planck constant is inverse proportional to the particle number $1/N$. As $\hbar_{\text{eff}} \to 0$, quantum fluctuations turn to be negligible, and the mean-field approximation becomes exact. A unique classical

Hamiltonian dynamics arise for the mean field, if the ratio

$$\gamma = \frac{1}{\hbar_{\text{eff}}} \frac{U}{J}, \tag{10.2}$$

is fixed. Otherwise, the hopping term becomes negligible, since the interaction strength grows with $\propto N^2$ and the hopping term only grows linearly $\propto N$. It is possible to introduce Hermitian operators in terms of $\hat{a}_j$ and $\hat{a}_j^\dagger$ known as quadratures that obey position-momentum-like commutation relations via

$$\hat{a}_j = \frac{(\hat{q}_j + i\hat{p}_j)}{\sqrt{2\hbar_{\text{eff}}}}, \quad \hat{a}_j^\dagger = \frac{(\hat{q}_j - i\hat{p}_j)}{\sqrt{2\hbar_{\text{eff}}}}, \quad [\hat{q}_j, \hat{p}_j] = i\hbar_{\text{eff}}, \tag{10.3}$$

which expresses the Bose-Hubbard Hamiltonian from Eq. (10.1) as

$$\hat{H} = -\frac{J}{\hbar_{\text{eff}}} \sum_{j=1}^{L} (\hat{q}_j \hat{q}_{j+1} + \hat{p}_j \hat{p}_{j+1}) + \frac{U}{2\hbar_{\text{eff}}^2} \sum_{j=1}^{L} \left(\frac{\hat{q}_j^2 + \hat{p}_j^2}{2} \right)^2 + \sum_{j=1}^{L} \frac{\mu_j - U}{\hbar_{\text{eff}}} \left(\frac{\hat{q}_j^2 + \hat{p}_j^2}{2} \right). \tag{10.4}$$

Here, an irrelevant constant energy offset has been dropped (which is also effectively an $O(\hbar_{\text{eff}}^2)$ correction to the spectrum and in any case beyond semiclassical argumentation used ahead). The prefactor $U/(2\hbar_{\text{eff}}^2)$ in the second term, the quartic interaction contribution, shows the need of rescaling U with $\hbar_{\text{eff}}$ via γ in Eq. (10.2). Together with multiplying both sides of Eq. (10.4) by $\hbar_{\text{eff}}/J$ results in a modified Hamiltonian

$$\hat{H}' = -\sum_{j=1}^{L} (\hat{q}_j \hat{q}_{j+1} + \hat{p}_j \hat{p}_{j+1}) + \frac{\gamma}{2} \sum_{j=1}^{L} \left(\frac{\hat{q}_j^2 + \hat{p}_j^2}{2} \right)^2 + \sum_{j=1}^{L} \mu_j' \left(\frac{\hat{q}_j^2 + \hat{p}_j^2}{2} \right), \tag{10.5}$$

where we introduce $\mu_j' = (\mu_j - U)/J$. This Hamiltonian is in a sufficiently symmetric operator form for a full time-dependent WKB approximation [191], i.e., good to $O(\hbar_{\text{eff}}^2)$, just through the association of $\hat{q} \to q$ and $\hat{p} \to p$. The classical analog Hamiltonian (mean-field limit) is given by

$$\mathcal{H}(\vec{q}, \vec{p}) = -\sum_{j=1}^{L} (q_j q_{j+1} + p_{j+1} p_j) + \frac{\gamma}{2} \sum_{j=1}^{L} \left(\frac{q_j^2 + p_j^2}{2} \right)^2 + \sum_{j=1}^{L} \mu_j' \left(\frac{q_j^2 + p_j^2}{2} \right) \tag{10.6}$$

and its degree of chaos is determined by the value of the rescaled interaction parameter γ. Typically, the strongest chaos is approximately in the range $1 < \gamma < 3$; see [99, 188]. The dynamics of the quadratures is thus governed by Hamilton's equation of motion

$$\dot{\vec{x}} = \Sigma \vec{\nabla}_{\vec{x}} \mathcal{H} \quad \text{with } \vec{x} = (\vec{q}, \vec{p}) \text{ and } \Sigma = \begin{pmatrix} 0 & \mathbb{1} \\ -\mathbb{1} & 0 \end{pmatrix}, \tag{10.7}$$

in a $2L$-dimensional phase space. Like the quantum Hamiltonian, the classical dynamics conserve energy and total number of particles along each trajectory,

i.e., each mean-field solution has a well-defined fixed total particle number and energy. For any targeting application using the Bose-Hubbard model, this implies that the space of possible targeting states is restricted to those associated to phase-space points sharing the same energy and particle number surface as the corresponding initial state. Choosing the initial chemical potentials μ_j' of the individual sites however allows for quite a bit of freedom in putting initial and target states on the same energy surface, so the constraint posed by energy conservation can be largely evaded.

10.2. Coherent States

Similar to the single-particle application in [63, 64], the protocol for the many-body case needs initially localized states in the quadrature phase space. Coherent states are a natural choice, because they are minimum uncertainty states and they are the most classical possible. Defined as eigenstates of all annihilation operators

$$\hat{a}_j|\vec{\phi}\rangle_{\text{coh}} = \phi_j|\vec{\phi}\rangle_{\text{coh}}\,, \tag{10.8}$$

they can be written explicitly as

$$|\vec{\phi}\rangle_{\text{coh}} = \exp\left\{-\frac{\|\vec{\phi}\|^2}{2} + \vec{\phi}\cdot\hat{\vec{a}}^\dagger\right\}|0\rangle\,. \tag{10.9}$$

Their phase-space representation is given by the Wigner function and is a $2L$-dimensional Gaussian wave packet

$$W\left(\vec{q},\vec{p}\right) = \left(\pi\hbar_{\text{eff}}\right)^{-L}\exp\left\{-\frac{\left(\vec{q}-\vec{q}_\alpha\right)^2}{\hbar_{\text{eff}}} - \frac{\left(\vec{p}-\vec{p}_\alpha\right)^2}{\hbar_{\text{eff}}}\right\}, \tag{10.10}$$

centered around the mean-field point $\vec{\phi}_\alpha = (\vec{q}_\alpha + i\vec{p}_\alpha)/\sqrt{2\hbar_{\text{eff}}}$. Its derivation and further details can be found in App. C.1. As Eq. (10.10) represents a non-squeezed coherent state [188], it has a variance per degree of freedom given by $\sigma^2 = \hbar_{\text{eff}}/2$. For a single degree of freedom, the 2σ-contour encloses a phase-space volume of $2\pi\hbar_{\text{eff}}$. All together, the minimal volume per quantum state is $(2\pi\hbar_{\text{eff}})^L$ [57], since coherent states are minimizing the uncertainty condition. This minimal phase-space volume of a state motivates also to search in such a region around the start and target point for a heteroclinic orbit in Sec. 9.

Note that there are different normalization conventions throughout the thesis: here, we use $||\vec{x}||^2 = ||\vec{q}||^2 + ||\vec{p}||^2 = 2L$ or $||\vec{\phi}||^2 = N$ for the complex mean fields compared to Chap. I, where we use $||\vec{x}||^2 = 2N$ with $||\vec{\phi}||^2 = N$ in Sec. 4 and also $||\vec{x}||^2 = 2$ with $||\vec{\phi}||^2 = 1$ in Sec. 5. A personal choice of including $\hbar_{\text{eff}}$ into the definition of $(\vec{q},\vec{p})$ and changing the effective Planck constant from $1/N$ to $\hbar_{\text{eff}} = L/N$ leads to this adaption.

As a many-body system with particle conservation, the Bose-Hubbard system possesses a dynamical $U(1)$-symmetry, which in mean-field quadratures equates

to an $SO(2)$ symmetry. Each trajectory maps perfectly[5] onto another by simultaneously rotating each pair (q_j, p_j) through any given angle $0 \leq \theta < 2\pi$. This symmetry allows a generalization of the control protocol in a straightforward manner. The same scheme as for a coherent state also works for a number-projected coherent state

$$|\vec{\phi}\rangle_{\text{proj}}^{N} = \frac{1}{\sqrt{\|\vec{\phi}\|^{2N} N!}} \left(\vec{\phi} \cdot \hat{\vec{a}}^{\dagger}\right)^{N} |0\rangle \,, \tag{10.11}$$

which has a fixed number of particles N. Interestingly, $|\vec{\phi}\rangle_{\text{proj}}^{N}$ is a Fock state, if we choose a basis with $\vec{\phi}$ as one basis vector [192]. This additional class of states is of great physical significance just by virtue of fixing the particle number. It also contains interesting cases such as $\phi_j^{\alpha} = \exp\left(2\pi i \alpha j / L\right)$ with $\alpha = 0$ corresponding to the non-interacting ground state of the superfluid phase and $\alpha = 1$ being the first excited state of the momentum operator. Another class of states that can be represented as number-projected coherent states are all Fock states concentrated on a single site k, e.g., $\phi_j = \sqrt{L}\delta_{j,k}$. Further details about number-projected states, like the connection to coherent states or their Wigner function, can be found in App. C.2.

Due to their simpler representation via the Wigner function (Gaussian), the discussion follows only coherent states. However we want to stress that all results are equally applicable to the number-projected counterparts due to the $U(1)$-symmetry in Bose-Hubbard systems. They are more relevant in experimental setups, where during the runtime of the experiment the total particle number is fixed.

10.3. TWA for the Time Evolution of States

The Wigner function can be used to describe the state of a system and it is the backbone of the phase-space formulation of quantum mechanics [57, 193, 194]. In quadratures or any canonical coordinates, the propagation of any state, specified by its Wigner function $W(\vec{q}, \vec{p})$, is given by the Moyal bracket $\{\mathcal{H}, .\}_{\text{MB}}$ [193] with the classical Hamilton function $\mathcal{H}$

$$\begin{aligned} \frac{\mathrm{d}}{\mathrm{d}t} W\left(\vec{q}, \vec{p}, t\right) &= \left\{\mathcal{H}\left(\vec{q}, \vec{p}\right), W\left(\vec{q}, \vec{p}, t\right)\right\}_{\text{MB}} \\ &= \frac{2}{\hbar_{\text{eff}}} \mathcal{H}\left(\vec{q}, \vec{p}\right) \sin\left[\frac{\hbar_{\text{eff}} \overleftrightarrow{\Lambda}}{2}\right] W\left(\vec{q}, \vec{p}, t\right), \end{aligned} \tag{10.12}$$

with $\overleftrightarrow{\Lambda} = \frac{\overleftarrow{\partial}}{\partial \vec{q}} \frac{\overrightarrow{\partial}}{\partial \vec{p}} - \frac{\overleftarrow{\partial}}{\partial \vec{p}} \frac{\overrightarrow{\partial}}{\partial \vec{q}}$ denoting the symplectic operator, which acts like the Poisson bracket, but includes higher orders. Dropping third and higher order terms in $\hbar_{\text{eff}}$ yields the truncated Wigner approximation (TWA) [195, 196] in

[5] To be precise: when $\{(q_j(t), p_j(t))\}_{j=1,\ldots,L}$ is a mean-field solution, then the rotated set $\{(\cos(\theta) q_j(t) + \sin(\theta) p_j(t), -\sin(\theta) q_j(t) + \cos(\theta) p_j(t))\}_{j=1,\ldots,L}$ is also a solution of the mean-field dynamics in Eq. (10.7) for all angles $\theta \in [0, 2\pi]$.

which quantum zero-point fluctuations are encoded in the Wigner transforms, but otherwise quantum interference between mean-field paths is dropped. The distribution of initial conditions, the Wigner function, evolves under a classical Liouville equation

$$\frac{\mathrm{d}}{\mathrm{d}t}W\left(\vec{q},\vec{p},t\right)=\left\{\mathcal{H}\left(\vec{q},\vec{p}\right),W\left(\vec{q},\vec{p},t\right)\right\}, \tag{10.13}$$

where $\{.,.\}$ denotes the classical Poisson bracket. The Gaussian form for coherent states of Eq. (10.10) is straightforward to implement within the TWA. First, the Wigner function is positive and can be interpreted as a probability distribution. Second, sampling via a Gaussian distribution is a standard procedure and well-implemented. Both properties enable us to use Monte Carlo sampling and render the TWA an excellent analysis tool for this work.

An important consequence of Eq. (10.12) is that for any quadratic Hamiltonian all higher order terms vanish. In the original and non-quadratic Bose-Hubbard Hamiltonian, TWA is an approximation due to the quartic interaction. However, we will switch the interaction off in the control protocol introduced ahead. Hence for the quadratic control Hamiltonian, the TWA time dynamic is exact and we use TWA in order to calculate and visualize the evolution of the state in both systems - controlled and uncontrolled - despite being an approximation in the uncontrolled Bose-Hubbard Hamiltonian.

10.4. Density Wave

In order to give us a reference point to compare propagation times of chaotic trajectories, it is useful to define a timescale depending on a typical periodic mean-field trajectory. What we call a density wave is the highly symmetrical and homogeneous mean-field state given by occupied and unoccupied sites $\vec{\phi}_{\mathrm{DW}}=\sqrt{2/\hbar_{\mathrm{eff}}}\,(1,0,1,0,\ldots)$ which gives us this reference time. Quantum mechanically the density wave corresponds to coherent states centered on its mean fields $\vec{\phi}_{\mathrm{DW}}$.

Under the assumption that the chemical potentials share this odd-even symmetry, the mean-field solutions, using initial conditions based on their centroid values, can be mapped to and from the dimer [174], which is an integrable system. They are special solutions to Hamilton's equations given by initially populating every second site equally, while leaving the rest unoccupied. The resulting trajectories exhibit periodic population inversion for $\gamma<4$ with a period $\tau_{\mathrm{DW}}(\gamma)$, see Fig. 10.2a. For larger interactions $\gamma>4$, the system is in a self-trapping regime where the solution is still periodic, but only a partial population inversion is achieved. If $\vec{\phi}_{\mathrm{DW}}$ lies on the symmetry plane separatrix of the dimer at $\gamma=4$ [174], the period diverges as shown in Fig. 10.2. Due to these special properties, it serves as a convenient initial state for the applications discussed throughout this chapter. Although theoretically, any other state with a centroid located in a chaotic phase-space region could be used. The high symmetry of the density wave makes τ_{DW} a natural choice for a dynamical

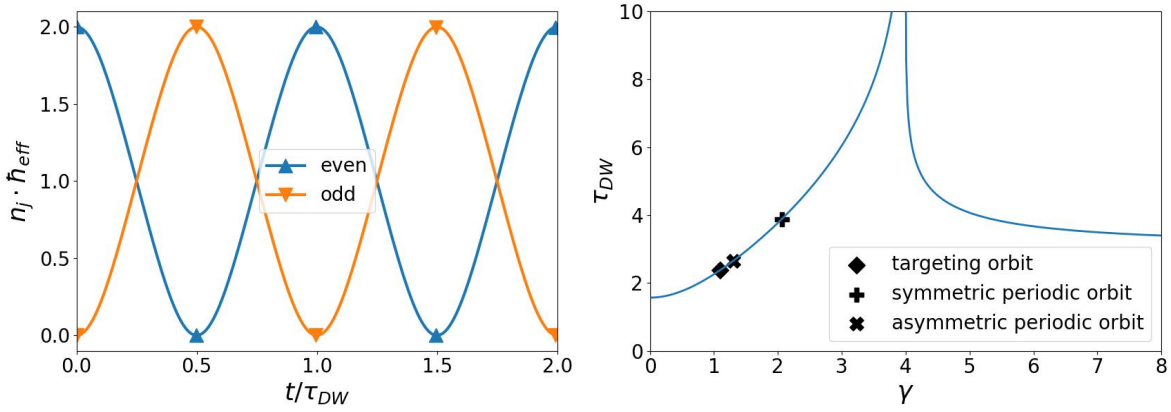

(a) **(b)**

Figure 10.2: Dynamical properties of a density wave. The mean-field dynamic of a density wave, initially centered on $\vec{\phi}_{\mathrm{DW}} = \sqrt{2/\hbar_{\mathrm{eff}}}\,(1,0,1,0,\ldots)$, exhibits partial or full periodic population inversion with a period τ_{DW} as illustrated in **(a)**. How the period depends on dynamical parameter γ, Eq. (10.2), of the system is shown in **(b)**. Except for $\gamma = 4$ where the period diverges since $\vec{\phi}_{\mathrm{DW}}$ lies on a separatrix of the mean-field dimer, τ_{DW} provides a well-defined timescale of the system. The time scales are marked for all the specific trajectories used throughout the work, whereas the periodic orbits are only discussed in [3]. Reprinted from Ref. [3].

timescale, as long as the systems considered are sufficiently removed from the singularity at $\gamma = 4$, as is done ahead. The corresponding timescale τ_{DW} of this work's specific case is depicted with a diamond marker in Fig. 10.2b. The plus and cross markers show reference time scales used in further applications in [3] which are not discussed here.

11. Control Hamiltonian

Finally, given that a (presumably heteroclinic) control trajectory $(\vec{q}(t), \vec{p}(t))_c$ connecting the mean-field centers of the initial and target state at time $t \gtrsim t_{\mathrm{min}}$ is identified, the goal is to guide a localized state along this solution without spreading.

Unfortunately, the Bose-Hubbard Hamiltonian in Eq. (10.5) needs adjustments, as coherent states spread over time, and we need to combat the origin of decoherence. Because of the quartic polynomial in quadratures present in the interaction term of Eq. (10.5), the initially localized state spreads exponentially in time, as the dynamics are strongly chaotic in the dynamical regimes of interest. This spreading is so rapid that without some control mechanism, a quantum targeting is impossible beyond an exceedingly short logarithmic timescale in $\hbar_{\mathrm{eff}}$ (proportional to the Ehrenfest time τ_{E} from Chap. I). Figure 11.1 demonstrates the fast equilibration for the example of a coherent state initially centered on a

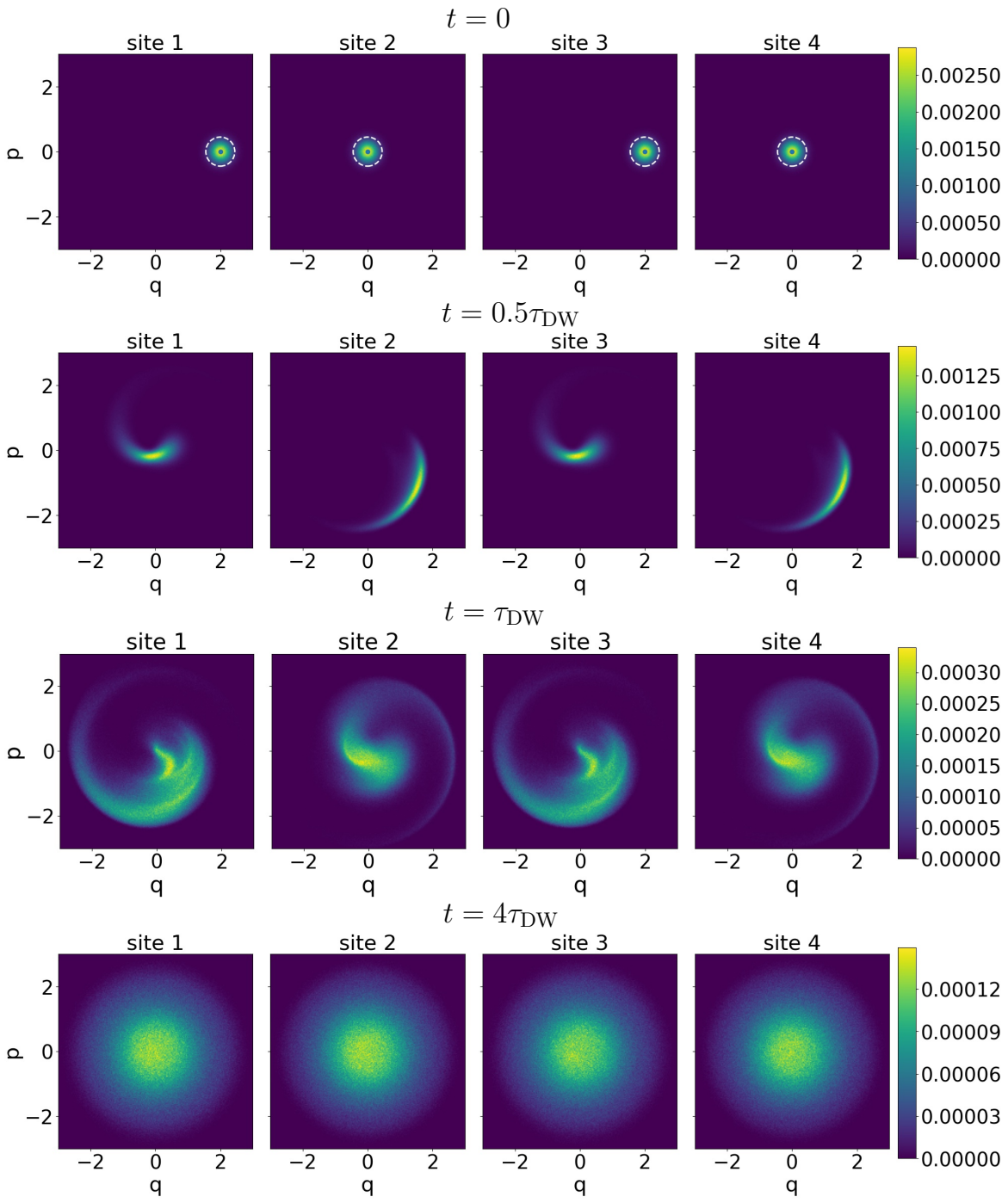

Figure 11.1: Spreading of a localized coherent state in a Bose-Hubbard system. A minimum uncertainty coherent state is propagated in the Bose-Hubbard system ($\gamma \simeq 1.965$) using the TWA. Here for illustration purposes, we set $\hbar_{\mathrm{eff}} = 1/10$, the coherent state is initially centered on the density wave $\vec{\phi}_\alpha = \vec{\phi}_{\mathrm{DW}} = \sqrt{2/\hbar_{\mathrm{eff}}}\,(1,0,1,0)$ (its phase-space point is indicated as dot in the upper panel). With the scaled dynamics, the mean-field corresponds to the phase-space point $\vec{q}_\alpha = (2,0,2,0)$ and $\vec{p}_\alpha = (0,0,0,0)$, independent of $\hbar_{\mathrm{eff}}$. The state, whose volume is for $t = 0$ well contained in the 2σ-contour (white dashed circle), quickly spreads, already being far from its initial Gaussian shape after one period τ_{DW} of the density wave. At time $t = 4\tau_{\mathrm{DW}}$ the state shows full equilibration in the (q,p)-projections of the Wigner function. Reprinted from Ref. [3].

density wave[6]. This equilibrated state resembles thermalization, which it is not, since the time-evolved state remains pure due to the unitary time evolution. Nevertheless, the Wigner function is well distributed in the accessible phase space, as well as the coefficients are typically spread all over the basis[7].

One possibility is to proceed as in [63] and apply an additional unitary transformation to the system sufficiently often, such that it counteracts the spreading. However, this method generally introduces terms in the time evolution that are not particle number conserving and thus challenging to simulate numerically and uninteresting with respect to experimental realization. Our approach here is based on the much simpler strategy developed for the kicked rotor in [64]. It introduces a new time-dependent simulation control Hamiltonian $\hat{H}_c$ that is uniquely designed for some particular targeting problem with fixed initial and final quadrature conditions. Of course, the downside is that we need to implement a time-dependent numerical simulation which is challenging for the full quantum simulation. But as mentioned we can instead use TWA to simulate the time evolution under the control Hamiltonian such that it becomes exact for sufficiently large sample sizes.

Let us start with the derivation by considering classical Hamilton's equations for each mean-field quadrature component using Eq. (10.6)

$$\begin{aligned}
\dot{q}_j &= \left.\frac{\partial \mathcal{H}\left(\vec{q},\vec{p}\right)}{\partial p_j}\right|_{\vec{q}(t),\vec{p}(t)} \\
&= \left[\mu_j' + \gamma\left(\frac{q_j^2+p_j^2}{2}\right)\right] p_j - p_{j+1} - p_{j-1}, \\
\dot{p}_j &= -\left.\frac{\partial \mathcal{H}\left(\vec{q},\vec{p}\right)}{\partial q_j}\right|_{\vec{q}(t),\vec{p}(t)} \\
&= -\left[\mu_j' + \gamma\left(\frac{q_j^2+p_j^2}{2}\right)\right] q_j + q_{j+1} + q_{j-1}.
\end{aligned} \tag{11.1}$$

Our goal is to find a quadratic Hamiltonian (possibly time dependent) that does not change the control trajectory. The idea is to evaluate the large square parentheses at the control trajectory $\left(\vec{q}(t),\vec{p}(t)\right)_c$, such that they are replaced by time-dependent values that are no longer functions of $(\vec{q},\vec{p})$ but of $\left(\vec{q}(t),\vec{p}(t)\right)_c$. With exactly this replacement, it is straightforward to see that a non-interacting control Hamiltonian can be created of the form

$$\mathcal{H}_c\left(\vec{q},\vec{p},t\right) = -\sum_{j=1}^{L}\left(q_j q_{j+1} + p_{j+1}p_j\right) + \sum_{j=1}^{L}\mu_j(t)\left(\frac{q_j^2+p_j^2}{2}\right), \tag{11.2}$$

which is in essence a collection of harmonic oscillators with chemical potentials that are time-dependent functions of the control trajectory's site occupancies

$$\mu_j(t) = \mu_j' + \gamma\left(\frac{q_j^2(t)+p_j^2(t)}{2}\right) = \mu_j' + \gamma n_j(t). \tag{11.3}$$

[6]The full time evolution is provided in Animation 1 in the supplementary material of Ref. [3].
[7]This is basis dependent. In the energy eigenbasis, the coefficients are static up to a phase.

In a nutshell, the control Hamiltonian makes use of the chemical potentials $\mu_j(t)$ as purely time-dependent functions evaluated along the chosen (heteroclinic) control trajectory $(\vec{q}(t), \vec{p}(t))_c$. It effectively replaces the originally cubic terms in quadrature mean-field differential equations with time-dependent linear terms. In this way, the control trajectory $(\vec{q}(t), \vec{p}(t))_c$ is a solution[8] of the mean-field Hamilton's equations for both Hamiltonians $\mathcal{H}(\vec{q}, \vec{p})$ and $\mathcal{H}_c(\vec{q}, \vec{p}, t)$.

Furthermore, due to the $\mathcal{H}_c(\vec{q}, \vec{p}, t)$ having a quadratic form[9], higher orders in the Wigner-Moyal expansion (Eq. (10.12)) vanish. This leads to the TWA being exact for its quantized version

$$\hat{H}_{\mathrm{c}}(t) = -\sum_{j=1}^{L} \left(\hat{a}_j^\dagger \hat{a}_{j+1} + \hat{a}_{j+1}^\dagger \hat{a}_j - \mu_j(t) \hat{a}_j^\dagger \hat{a}_j \right) \tag{11.4}$$

and there is no longer any spreading in the neighborhood of $(\vec{q}(t), \vec{p}(t))_c$, or for that matter, anywhere else. We give an explicit proof using operator algebra for coherent states in App. E, i.e., we show that a coherent state follows $(\vec{q}(t), \vec{p}(t))_c$ while staying an unchanged Gaussian wave packet (its minimal width remains the same). Although due to chaos, the guiding trajectory $(\vec{q}(t), \vec{p}(t))_c$ is an exponentially unstable solution of $\mathcal{H}(\vec{q}, \vec{p})$, it is a stable solution of $\mathcal{H}_c(\vec{q}, \vec{p}, t)$.

Up to this point, there is a broad freedom in the choice of a particular chaotic Hamiltonian that may serve as a black box to produce a desired control solution. The apparently natural choice of a Bose-Hubbard type of system however points to a deeper connection between the dispersionless dynamics generated by Eq. (11.4) and the precise form of the interaction (quartic) term in Eq. (10.6). In addition, this choice is quite favorable from the point of view of a practical implementation. Among the infinity of nonlinear systems that one might consider for producing a control trajectory, a key selection criteria is the desire to have a minimal alteration of a realistic experimental setup. The Bose-Hubbard Hamiltonian, describing a broad range of self-interacting bosonic systems, satisfies this condition. Thanks to the technical possibilities to tune the interaction [101–103] and chemical potential parameters, implementing Eq (11.4) should be possible. Of course in our theoretical discussion, one could add additional terms to the original mean-field Hamiltonian Eq. (10.6), like general non-local interaction terms, to find more suitable transport trajectories. This would lead generally to time-dependent hopping terms which we find to be unnecessary and with a cold-atom experimental setup in mind more unfeasible [68, 87]. Given the simple form of Eq. (11.4), the actual realization of the protocol requires switching off the interactions [101–103] and controlling the chemical potentials of each individual site in a time-dependent fashion. For sake of completion, we mention that there is a connection via the path-integral formalism, which is available in [3].

[8] It is a straightforward calculation to verify, one derives the equation of motion with the Hamiltonian function $\mathcal{H}_c$ in Eq. (11.2), plugs the guide trajectory $(\vec{q}(t), \vec{p}(t))_c$ in and observes that they give the same equations as for the original Hamiltonian function $\mathcal{H}$ in Eq. (10.6).

[9] The time-dependence $\mu_j(t)$ in Eq. (11.3) is not an issue here, since it is only a time-dependent coefficient, not a time-dependent operator by itself.

It shows how the control Hamiltonian is a solution when using the Feynman propagator with auxiliary fields to display the time evolution.

We conclude here the theory part and move on to numerical results, which we split into two parts: first we demonstrate the protocol exemplary for the one-dimensional lattice in Sec. 12. Second we show aspects of the protocol robustness to imperfections in Sec. 13, to complement the discussion of this section, where we assume exact implementation and a perfect transport path.

12. Coherent Quantum Targeting in One-Dimensional Lattices

We focus on a representative example application of the protocol, namely targeting a state on an one-dimensional periodic lattice. Preparing states with well-defined phase relations between the condensates on different sites is covered here, while the creation of non-trivial periodic evolution or higher dimensional applications are not discussed in this section, but can be found in our publication [3]. We want to highlight that the path finding and the TWA calculations, together with the visualization of the results are fabulously done by Lukas Beringer.

As it turns out, even though the idea of placing quantum states on classical trajectories is semiclassical in nature, the control system is quadratic and therefore harmonic[10]. Thus the time evolution of a (projected) coherent state behaves purely classical which means that the coherent state follows the central mean-field trajectory. Among other things, the control protocol applies independently of the particle numbers, which is our semiclassical parameter, such that the method works not only in the dilute quantum regime but also in the limit of a single particle.

In principle, any state of the form of Eqs. (10.9) or (10.11) can be prepared by targeting the corresponding mean-fields. Important is that the starting point and the target point share the same energy (and particle number surfaces) which can be done by adjusting the chemical potentials. As mentioned in Sec. 10.2, the states we cover with this protocol are usually called single-particle states, since they are many-body states occupying a mean-field state. Therefore, they can be transformed via a linear base change to a coherent state or N-particle Fock state at a single site in the new basis. This includes states where the condensates on each site carry well-defined, non-trivial phase relations [103]. As a proof of principle, we choose our target to be such a many-body occupied single-particle state, where the bosons occupy the first excited momentum eigenstate[11] on a four-site ring. The mean-field vector corresponds to $\vec{\phi}_\beta = \vec{\phi}_{\mathrm{M},k=1} =$

[10] We can change to a time-dependent operator basis $\{\hat{\tilde{a}}_{t,j}\}$, where the Hamiltonian is diagonal and has the form of a multidimensional harmonic oscillator $\hat{\tilde{H}} = \sum_{j=1}^{L} \epsilon_j(t) \hat{\tilde{a}}_{t,j}^\dagger \hat{\tilde{a}}_{t,j}$.

[11] Momentum eigenstate means a basis state in which the hopping part is diagonal, see Eq. (6.3) for the definition of the momentum basis, where $k = 1$ corresponds to the first excited momentum eigenstate. The corresponding mean-field state is given by the coefficients of the site operators in Eq. (6.3).

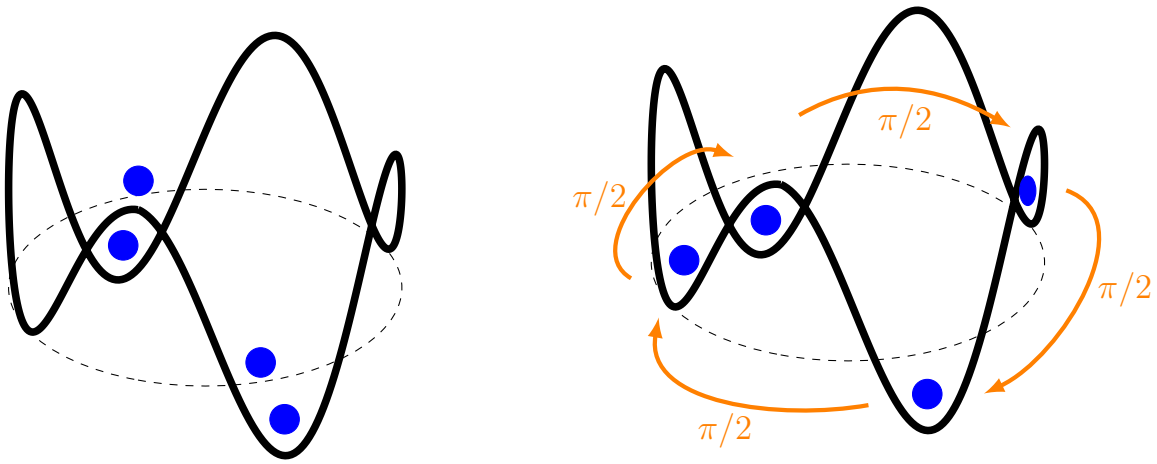

Figure 12.1: Schematic of initial and target quantum state. Raising the unoccupied sites energetically by choosing $\vec{\mu}' = (0, \gamma, 0, \gamma)$ puts the density wave $\vec{\phi}_\alpha = \vec{\phi}_{\mathrm{DW}}$ as the initial state, left panel, and the excited momentum eigenstate $\vec{\phi}_\beta = \vec{\phi}_{\mathrm{M},k=1}$ as the target state, right panel, on the same classical energy surface. This enables us to find a control trajectory, connecting both mean-fields in quadrature phase space. The corresponding initial coherent quantum state can be guided along the control trajectory into the target quantum state by driving the control system with the associated time-dependent occupation numbers. Adapted from Ref. [3].

$1/\sqrt{\hbar_{\mathrm{eff}}}(1, i, -1, -i)$ with a non-trivial $\pi/2$-phases between neighboring sites, see Fig. 12.1b for a visualization with four particles ($\hbar_{\mathrm{eff}} = 1$) inside the lattice ring. With the target state specified, we take a coherent state centered on a density wave $\vec{\phi}_\alpha = \vec{\phi}_{\mathrm{DW}} = \sqrt{2}/\sqrt{\hbar_{\mathrm{eff}}}(1, 0, 1, 0)$ as an initial phase-space point (displayed in Fig. 12.1a) for the protocol which is also our reference point for timescale τ_{DW} (propagation via the uncontrolled Bose-Hubbard Hamilton, see Sec. 10.4).

There is an energy discrepancy, i.e., these two mean-field phase-space points have different energies for $\vec{\mu}' = 0$. But by choosing the static chemical potential offset accordingly via $\vec{\mu}' = (0, \gamma, 0, \gamma)$, both mean-fields share the same classical energy surface for every value of the system parameter γ. Being on the same energy shell allows us to connect them with an exemplary transport trajectory. The left column of Fig. 12.2 shows a heteroclinic trajectory with a control time of less than five oscillations of the density wave τ_{DW} (Fig. 10.2b), which is quite short. If greater precision is required, then ergodicity and the nature of unstable and stable manifolds guarantees the existence of trajectories closer to the initial and target mean-fields at the expense of a longer control time. Again this trade-off can be exploited if the concrete application is either flexible in the fidelity or the accessible operating time (coherence time of an experiment).

The initial state $|\vec{\phi}_\alpha\rangle_{\mathrm{coh}}$ then evolves under the control Hamiltonian, Eq. (11.4), by driving the system with the time-dependent chemical potentials. The time-dependent part of the chemical potentials $\mu(t)$ is determined by the respective

site occupations shown in the right panel of Fig. 12.2, i.e., time-dependent chemical potentials follow from Eq. (11.3) and the definition of the static contribution μ'_j is given in the text immediately after Eq. (10.5). A TWA simulation is used to calculate the propagation of the state. Note that the TWA calculation exactly matches the quantum calculation due to the quadratic nature of the control Hamiltonian and they cannot be distinguished in this case.

Figure 12.3 shows the initial and final state of the protocol in the upper and lower panels[12]. In contrast to the spreading observed in Fig. 11.1 via the original Bose-Hubbard Hamiltonian, the coherent state keeps its minimum uncertainty form throughout the entire propagation, successfully arriving close the target mean-field. For completeness, a full quantum simulation of the time evolution is performed and it gives the same results. Figure 12.2 shows that the quantum expectation values (black dotted line) of the occupations follow the classical mean-field solution (blue solid line) perfectly in the control system, whereas they almost immediately deviate and equilibrate when evolving in the original interacting Bose-Hubbard system (gray dotted line)[13]; see the equilibration in Fig. 11.1 for the Wigner function of the density wave in an uncontrolled time evolution.

We demonstrate that the procedure works if executed precisely. But until now, the small shifts between initial $\vec{x}_\alpha = (\vec{q}_\alpha, \vec{p}_\alpha)$ and target $\vec{x}_\beta = (\vec{q}_\beta, \vec{p}_\beta)$ quadrature centers to the initial and final points of the control trajectory $\vec{x}_c(t) = (\vec{q}(t), \vec{p}(t))_c$ are not taken into account. So far we start at the control trajectory $\vec{x}_c(0)$ which is in proximity to the start point $\vec{x}_\alpha$. Therefore, a fidelity punishment is introduced by centering a coherent state at $\vec{x}_\alpha$ instead of $\vec{x}_c(0)$. Secondly, we assume the interactions to be exactly zero, but due to imperfections residual interactions can be present and disturb the procedure. Both effects introduce an $\hbar_{\text{eff}}$ dependence to the fidelity of the protocol and are addressed in following Sec. 13 about the robustness of the protocol. Furthermore, we investigate the influence of white noise on the control fields $\mu_j(t)$ and answer how big white noise can be before the protocol becomes unfeasible depending on the wanted accuracy.

[12] We refer to [3], where the full time evolution is visualized in Animation 2 of the supplementary material.

[13] The saturation values (gray dotted lines in Fig. 12.2) differ from the filling factor ($N/L = 1$) and depend on even and odd sites due to the imbalance in the chemical potentials.

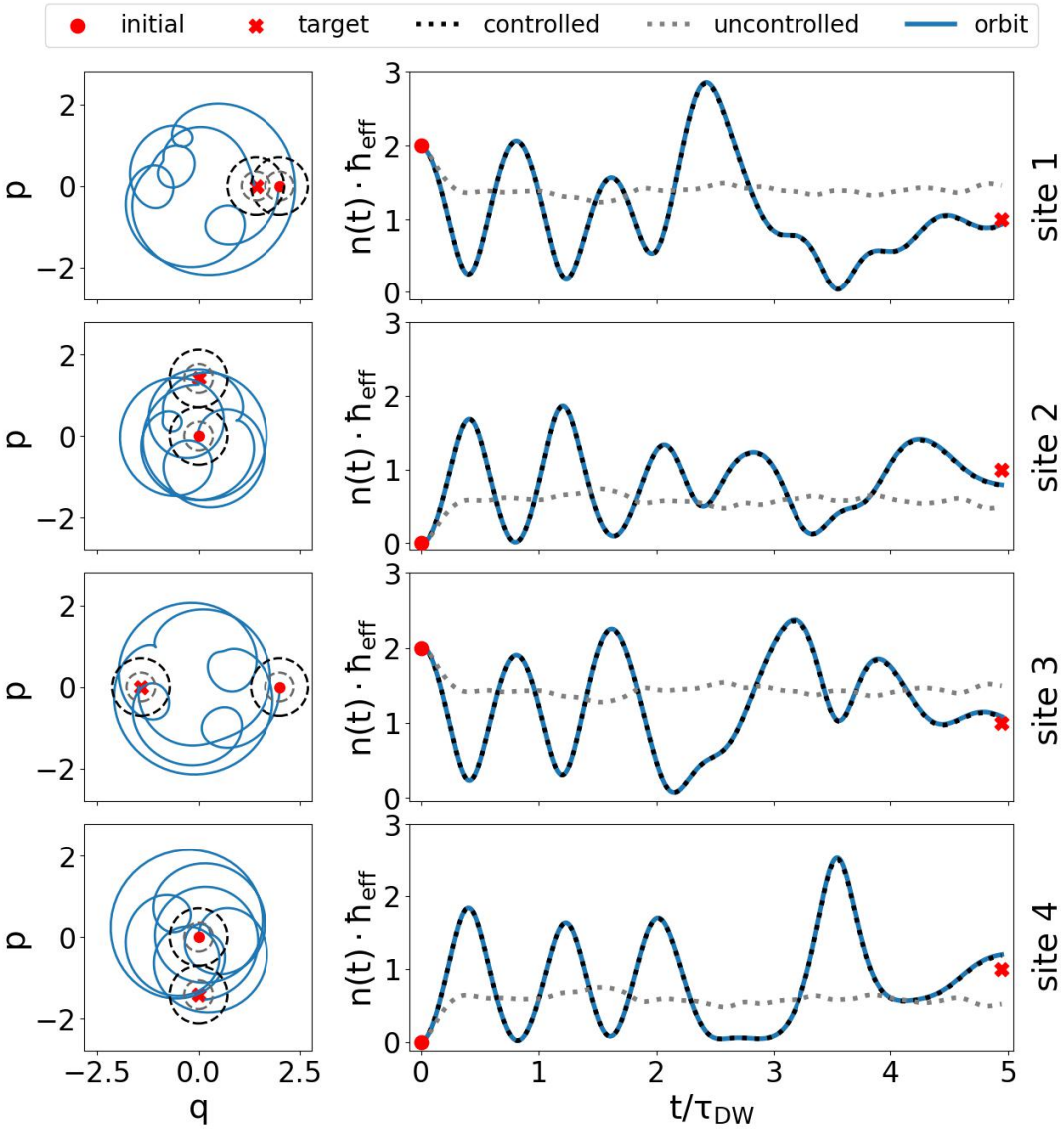

Figure 12.2: Control trajectory to target an excited momentum eigenstate. The trajectory connecting the centroids of the initial density wave $\vec{\phi}_\alpha = \vec{\phi}_{\mathrm{DW}} = \sqrt{2}/\sqrt{\hbar_{\mathrm{eff}}}(1,0,1,0)$ (red dot) with the final target state $\vec{\phi}_\beta = \vec{\phi}_{\mathrm{M},k=1} = 1/\sqrt{\hbar_{\mathrm{eff}}}(1,i,-1,-i)$ (red cross) is shown for the different sites in the left panel at the system parameter $\gamma = 1.965$. The respective σ-contours (Gaussian wave packet) for the initial and target coherent state's Wigner densities, Eq. (10.10), are depicted centered on their respective quadrature centroids with $\hbar_{\mathrm{eff}} = 1$ (black dashed circles) and $\hbar_{\mathrm{eff}} = 1/4$ (gray dashed circles). Generally, the area inside the circles shrinks proportionally to $\hbar_{\mathrm{eff}}$. The time-dependent control chemical potentials shown in the right panel are determined by the respective site occupations by Eq. (11.3) and the offsets of μ'_j given in the text in Sec. 12. Initially, the motion is similar to the integrable behavior of the density wave, but the chaotic nature of the control trajectory quickly dominates and it reaches the target at the time $t = 4.9\tau_{\mathrm{DW}}$. On the right column, the classical occupations are displayed in solid blue lines which are needed for the control Hamiltonian. The expectation values of the occupations are shown for the quantum propagation of the coherent state evolving under the original Bose-Hubbard Hamiltonian (uncontrolled, gray dotted). They deviate rapidly from the classical solution. Under the control Hamiltonian (controlled, black dotted) the expectation values shadow the control trajectory (solid blue) as predicted. Reprinted from Ref. [3].

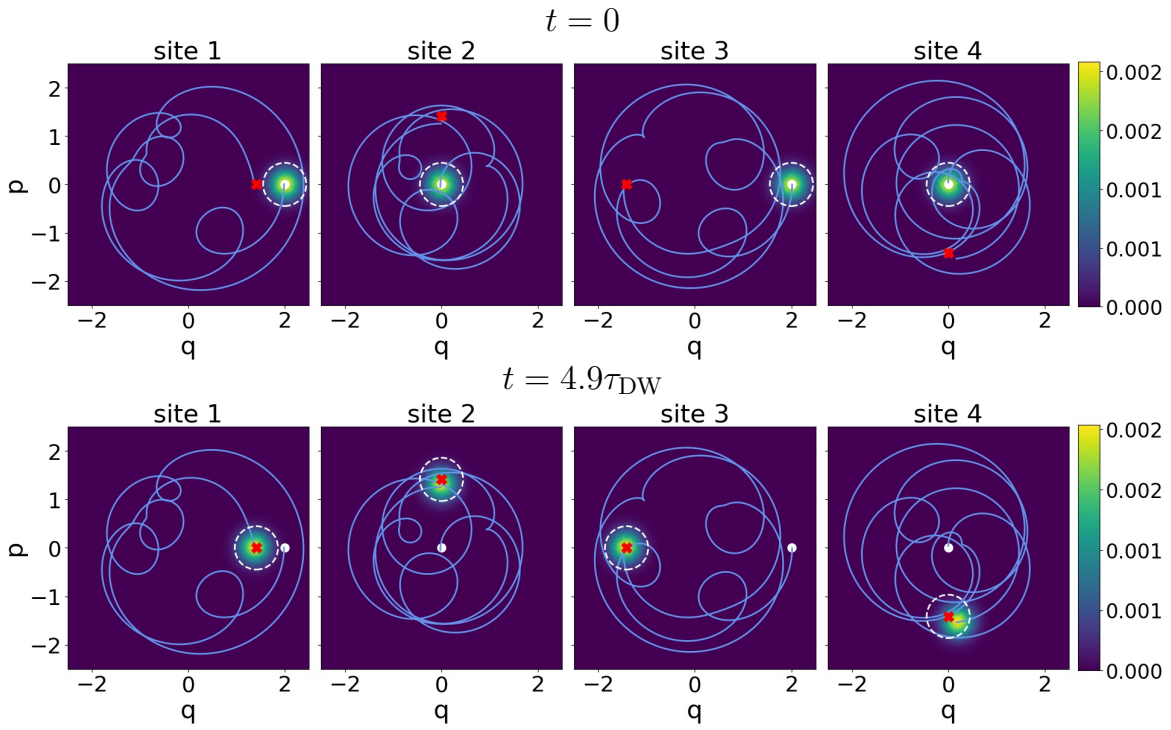

Figure 12.3: Coherent targeting along chaotic control trajectory. A coherent state is initialized centered on the density wave $\vec{\phi}_\alpha = \sqrt{2}/\sqrt{\hbar_{\mathrm{eff}}}(1,0,1,0)$ (white dot) in the upper panel. The width of the state is chosen via $\hbar_{\mathrm{eff}} = 1/10$ to enhance the visualization. The initial phase-space point connects to the target $\vec{\phi}_\beta = 1/\sqrt{\hbar_{\mathrm{eff}}}(1,i,-1,-i)$ (red cross) through a control trajectory found in the Bose-Hubbard mean-field limit (indicated as light blue line). The 2σ-curves of the initial and target state are represented via white dashed circles. A TWA simulation shows that driving the control system with the occupations of the control trajectory results in the coherent state evolving along the predesigned path, keeping its minimum uncertainty form. After the control time $t_c = 4.9\tau_{\mathrm{DW}}$ the propagated state lands well inside the volume of the target state in the lower panel. Reprinted from Ref. [3], where we recommend the animation visualizing the time evolution in its supplementary materials.

13. Protocol Robustness

Three mechanisms that might potentially degrade the quality of a particular application of coherent quantum targeting are: i) the proximity of initial and target state centroids from initial and final conditions of the control trajectory, respectively; ii) the precision with which the interactions can be made to vanish; and iii) the faithfulness with which the time-dependencies of the set of $\{\mu_j(t)\}$ match the occupancies of the control trajectory. These mechanisms are discussed below individually. Note that an analysis of the latter item is presumably model dependent, and among other issues, might depend on the type of noise inherent in creating the $\{\mu_j(t)\}$. Nevertheless, the effects of uncorrelated (white) noise in time are considered as a simple starting point.

13.1. Proximity – Off-Center Start

As mentioned in Sec. 11 and proved in App. E, the specific quadratic nature of $\hat{H}_c$ guarantees that a coherent state initially (exactly) centered on the control trajectory follows this trajectory perfectly without any spreading, and satisfies the associated time-dependent Schrödinger equation. Due to the quadratic nature of the control Hamiltonian, any coherent state centered anywhere remains a coherent state for all times. However, they do not follow the control trajectory. As we connect phase-space cells (Sec. 9), the initial and final coordinates of any control trajectory are slightly shifted from the initial and desired target states centroids, respectively. Letting t_c denote the time at which the control (heteroclinic) trajectory arrives closest to the target point, the shifts can be expressed as the norms

$$\delta x_{\text{initial}} = ||\vec{x}_\alpha - \vec{x}(0)||, \qquad \delta x_{\text{target}} = ||\vec{x}_\beta - \vec{x}(t_c)||, \tag{13.1}$$

resulting in a non-perfect overlap between the target state $|\vec{\phi}_\beta\rangle_{\text{coh}}$ and the actual time evolved final state

$$|\vec{\phi}_\alpha(t_c)\rangle_{\text{coh}} \;=\; \exp\!\left\{-\frac{i}{\hbar}\int_0^{t_c} dt\hat{H}_{\text{c}}\,(t)\right\}|\vec{\phi}_\alpha\rangle_{\text{coh}}. \tag{13.2}$$

The shifts are minimized in the search for a control trajectory while simultaneously keeping the protocol time t_c near its minimum. Since this distance only has a meaning relative to the volume of the coherent state, an $\hbar_{\text{eff}}$ dependence gets introduced into the fidelity $\mathcal{F}$ of the control process. States with larger filling factors and thus smaller volume are more affected by the shifts as shown in Fig. 13.1. Based on the knowledge of $\delta x_{\text{initial}}$ and δx_{target} bounds can be derived for the fidelity of the protocol:

$$\mathcal{F}_{\min} = \exp\!\left\{-\frac{\left(\delta x_{\text{initial}} + \delta x_{\text{target}}\right)^2}{2\hbar_{\text{eff}}}\right\}, \quad \mathcal{F}_{\max} = \exp\!\left\{-\frac{\left(\delta x_{\text{initial}} - \delta x_{\text{target}}\right)^2}{2\hbar_{\text{eff}}}\right\}. \tag{13.3}$$

Beyond these bounds, one can express the exact fidelity via

$$\mathcal{F} = \left| {}_{\text{coh}}\left\langle \vec{\phi}_\beta \right| e^{-\frac{i}{\hbar}\int_0^{t_c} dt \hat{H}_c(t)} \left| \vec{\phi}_\alpha \right\rangle_{\text{coh}} \right|^2 = \exp\left\{ -\frac{\delta\vec{x}^2}{2\hbar_{\text{eff}}} \right\}, \tag{13.4}$$

where $\delta\vec{x}$ is the distance between the centroids of the target and final state. It could be derived using an adapted version of Heller's linearized wave packet dynamics [197], which would be rather involved due to the dependencies on the stability matrix. Here, it is simpler to numerically extract

$$\delta\vec{x} = \vec{x}_\beta - \tilde{\vec{x}}(t_c; (\vec{q}(t), \vec{p}(t))_c)$$

by propagating the unshifted mean-field state $\tilde{\vec{x}}(0; (\vec{q}(t), \vec{p}(t))_c) = \vec{x}_\alpha$ via the control Hamiltonian function with the control trajectory $(\vec{q}(t), \vec{p}(t))_c$. Interest-

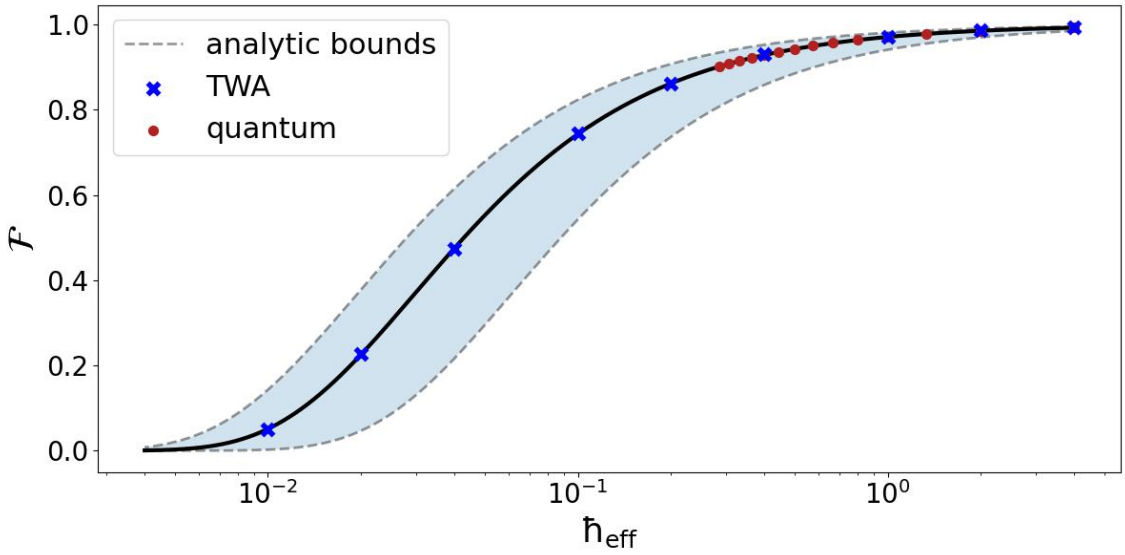

Figure 13.1: Fidelity of the targeting protocol. The protocol depends on the specific control trajectory used for targeting. The initial and final distance from the particular trajectory to the centroids of the respective states introduce an implicit $\hbar_{\text{eff}}$ dependence into the fidelity. Upper and lower bounds depending on those distances are depicted. The exact fidelity (black curve) depends on the distance of the final states centroid to the actual target state and can be obtained numerically. The results obtained from both TWA and quantum simulations match the fidelity curve. Note that the fidelity would remain unity for all $\hbar_{\text{eff}}$ if shift operators are used to translate the initial and final coherent states onto the control trajectory. Reprinted from Ref. [3].

ingly, even though the control method is semiclassical in nature, the harmonic nature of the Hamiltonian causes the protocol to have almost perfect fidelity in the dilute quantum limit and then fall off for states with larger filling factor, i.e., inverse $\hbar_{\text{eff}}$ as visible in Fig. 13.1.

13.2. Residual Interactions

We require zero interaction for the coherent targeting in the ideal case and demonstrate that any residual interaction potentially degrades the fidelity. Despite the fact that there can be great experimental control over interactions [101], we discuss nevertheless the situation in which the strength of the interaction cannot be turned off precisely, and there is a small perturbative residual interaction.

To treat this mechanism, we assume that the residual strength $\epsilon(t)$ can be measured and is characterized. This would add a perturbative term to the control Hamiltonian, Eq. (11.4), as follows

$$\hat{H}_{\mathrm{c}}^{\epsilon}(t) = -\sum_{j=1}^{L}\left(\hat{a}_j^{\dagger}\hat{a}_{j+1} + \hat{a}_{j+1}^{\dagger}\hat{a}_j - \mu_j(t)\hat{n}_j\right) + \frac{\epsilon(t)}{2}\sum_{j=1}^{L}\hat{n}_j\left(\hat{n}_j - 1\right). \tag{13.5}$$

Consequently, the perturbed control Hamiltonian $\hat{H}_{\mathrm{c}}^{\epsilon}$ slightly becomes anharmonic, assuming residual interaction $\epsilon(t) \ll 1$ is small compared to the hopping $J = 1$. The effect of such residual interactions is twofold. First, the interactions lead to a deformation of the initially minimum-uncertainty coherent states like in the uncontrolled case in Fig. 11.1. There in contrast to now, we observe equilibration due to the unchanged (strong) interactions. Second, constructing the control Hamiltonian with $(\vec{q}(t), \vec{p}(t))_c$ results in a new perturbed trajectory missing the desired target. Both effects are illustrated in Fig. 13.2 for a constant

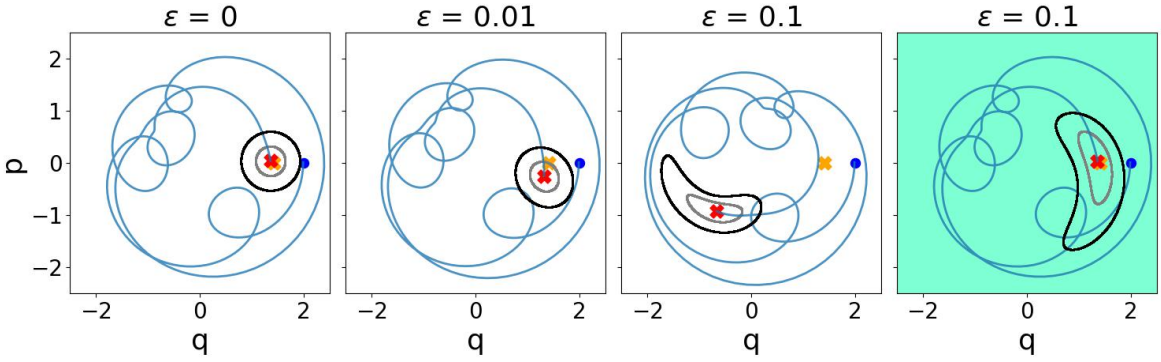

Figure 13.2: Effect of constant weak residual interactions. The trajectory no longer ends near the target and is no longer perfectly stable, which distorts the contours of the Wigner transform. Shown for only the first site, the final point of the control trajectory ends at the red cross, which is increasingly far from the target (orange cross) as ϵ increases. The spreading also increases with ϵ as illustrated for the σ-contour of the propagated Wigner density for $\hbar_{\mathrm{eff}} = 1$ (black) and $\hbar_{\mathrm{eff}} = 1/4$ (gray). For very small ϵ $(= 0.01)$, both effects remain negligible. However for $\epsilon = 0.1$, the control trajectory completely overshoots the target and there is a strong deformation of the coherent state. Accounting for ϵ in the $\mu_j(t)$, the overshoot is corrected, however the spreading remains, as shown in the most right panel. The different state contour areas are a result of the depicted σ-contour being only a cut through a higher-dimensional object. Reprinted from Ref. [3].

residual interaction $\epsilon(t) = \epsilon$, as well as the improvement using the appropriately modified $\{\mu_j(t)\}$ in the right panel with teal background. If the behavior of $\epsilon(t)$ is known, it is quite simple to take into account. Let us consider Hamilton's equations, just as before in Eq. (11.1). We use them to determine the $\{\mu_j(t)\}$, except with the inclusion of the ϵ term. Then, we resolve the equations as before, the result is the replacement

$$\mu_j(t) \Longrightarrow \mu_j(t) - \epsilon(t) \tag{13.6}$$

in Eq. (13.5). It suffices to subtract the residual interactions $\epsilon(t)$ from the chemical potential fields $\{\mu_j(t)\}$ to counteract the over or undershooting of the target. With this modification, even higher values of $\epsilon = 0.1$ give us an acceptable transport path. The end point of perturbed control trajectory (red cross) remains close to the target point (orange cross) in the right panel of Fig. 13.2 with teal background.

If the residual interaction ϵ is not compensated in the chemical potentials $\{\mu_j(t)\}$, the fidelity decay with ϵ is more significant as $\hbar_{\text{eff}} \to 0$ in Fig. 13.3. This indicates that the dominant error source is the perturbed control trajectory not arriving at the target. Similar to the off-centered start, a non-zero distance of the final state to the target state more significantly affects the overlap of states with smaller volume (larger mean particle number). If correcting the $\hat{H}_c$ by adjusting the driving by the replacement via Eq. (13.6), an overall improved robustness to the residual interactions is obtained. Moreover, notably, the $\hbar_{\text{eff}} = 1/4$ coherent state is less affected than the $\hbar_{\text{eff}} = 1$ one, i.e., smaller volume states are robuster through the correction. This is in line with the remaining error source due to the deformation in the shape of the state's Wigner function, which is less significant for smaller volumes scaling with the effective Planck constant.

For the quantum data in Fig. 13.3, we provide some details of the numerical simulations with residual interactions. As mentioned, TWA is not exact, when the control Hamiltonian is not quadratic due to the remaining interaction ϵ. Hence, we use full quantum simulations in Fig. 13.3 for coherent states. Since the total particle number is a conserved quantum number, we simulate larger and larger particle sector individually, until a cutoff in the norm of the coherent state is reached. We choose at least 10^{-4} for the cutoff, since no significant changes appear afterward. For example, we use a cutoff particle number $N_{\text{cut}} = 8$ (38) for $\hbar_{\text{eff}} = 1$ (1/4), which translates to a coherent state particle number $N_{\text{coh}} = 4$ (16) in Fig. 13.3, in order to reach the desired accuracy. Within each particle sector, we solve the time-dependent linear Schrödinger equation via numerical integration for each wave function coefficient. Due to the fact that the numerical effort and storage scales at least with the Hilbert space dimension, the maximal coherent state particle number N_{coh} is strongly limited and thus how low $\hbar_{\text{eff}}$ we can simulate.

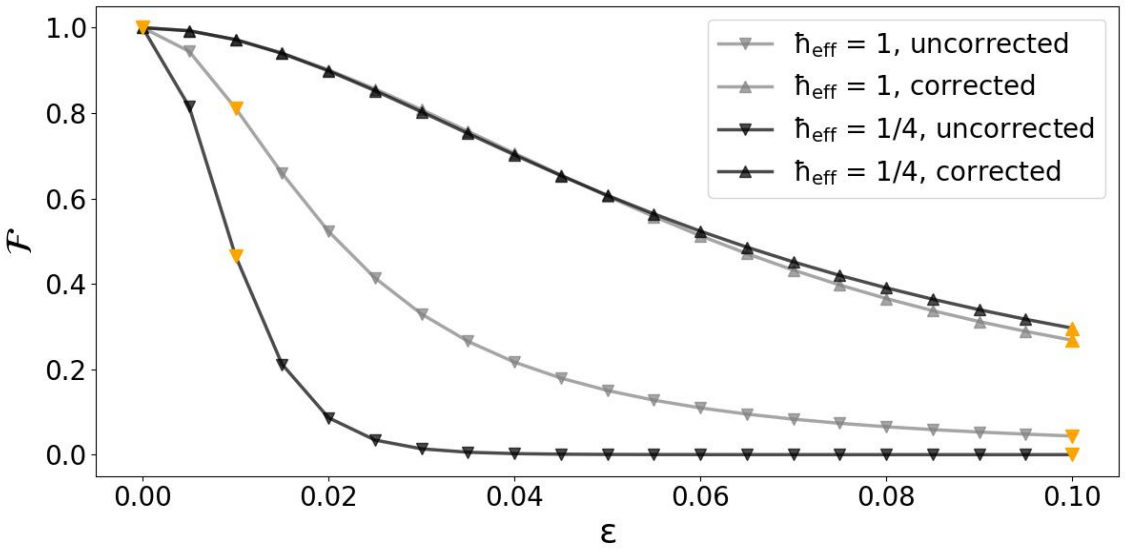

Figure 13.3: Constant residual interactions with and without compensation. For a constant residual interaction term $\epsilon(t) = \epsilon$, the fidelity of an uncompensated protocol quickly decays (down-facing triangles). The $\hbar_{\mathrm{eff}} = 1/4$ simulation (black) decays much faster than $\hbar_{\mathrm{eff}} = 1$ one (gray). The over- or undershooting of the target is the dominant difficulty. If the functional behavior of $\epsilon(t)$ is known, it can be accounted for following the replacement in Eq. (13.6) for the chemical potentials. This leads to a significant overall improvement of the fidelity (up-facing triangles), even favoring the smaller $\hbar_{\mathrm{eff}}$ case, due to the deformation being the remaining error. Since TWA is no longer exact with the interaction term present, the overlaps have been calculated in a full quantum simulation. The orange triangles mark the cases depicted in Fig. 13.2. Reprinted from Ref. [3].

13.3. White Noise in the Control Fields

Let us return to the setup of Sec. 11. We start on the trajectory and have no residual interactions. We discuss the final potential mechanism that might degrade the fidelity of the control protocol: how exact the time-dependence in $\mu_j(t)$ can be produced experimentally. As a simple modeling starting point, imagine that there is a small amount of white (uncorrelated) noise generated in the chemical potentials $\mu_j(t)$. We consider adding to each individual $\mu_j(t)$ white noise (uncorrelated over time and site index) of some given root-mean-square (RMS) magnitude. This changes the mean-field trajectory and its endpoint differs from the ideal control path. As a function of the white noise strength (i.e., the RMS of a white noise realization), the RMS distance δ_{RMS} between noisy and ideal trajectory endpoints are calculated for 50 realizations. The averaged results are shown in Fig. 13.4 and the run-to-run variance (blue bars at the data crosses) is even with 50 realizations already low. We view only the mean-field deviation between the end points. This is sufficient, since the control procedure stays quadratic in nature. The quantum simulation of the control Hamiltonian follows the shaken mean-field exactly despite being perturbed by white noise. Therefore, the error in a quantum simulation with a given $\hbar_{\mathrm{eff}}$ is

determined roughly by Eq. (13.4) using RMS distance δ_{RMS} for the deviation δx.

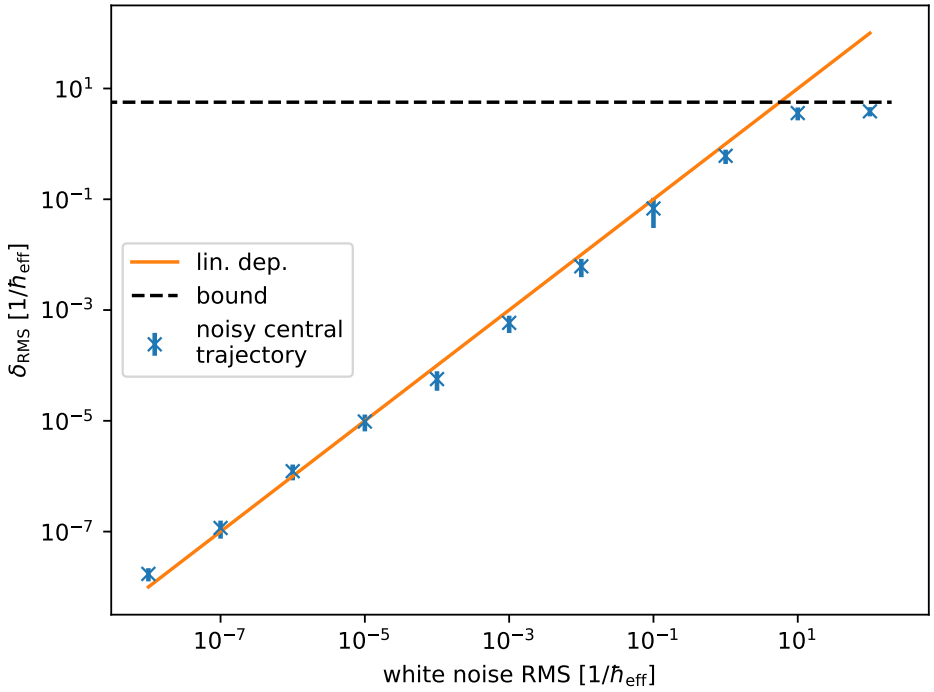

Figure 13.4: Final deviation of the target due to white noise. An RMS average is calculated over 50 noise realizations for the final distance to the unperturbed trajectory. There is a linear dependence for low amplitudes due to the stability of the target protocol and cancellation of random changes. For strong noise magnitude (dominant with respect to the control $\mu_j(t)$), the final point is random and the distance is bounded by the phase-space diameter. The errorbars display the run-to-run standard variance. Reprinted from Ref. [3].

Our simulations show that the RMS deviation depends linearly on the strength of the white noise up to a level beyond which it saturates. This is expected, since the control trajectory is a stable solution in the control Hamiltonian and the perturbations are uncorrelated and random with a vanishing mean. Hence, added white noise results in a perturbed trajectory that stays close to the ideal transport trajectory. Integrating the time evolution leads to significant cancellations of the uncorrelated deviations. The trajectory with noise only slowly diffuses away from the ideal, which leads to a linear deviation in Fig. 13.4 for small RMS strengths.

For perturbations comparable to the phase-space size (diameter of S^{2L-1}-sphere), i.e., occupations ($\sim 1/\hbar_{\mathrm{eff}}$), the actual control fields $\mu_j(t)$ are more or less negligible and the motion is random. Nevertheless, the deviation to the

target point is bounded by the phase-space size. Therefore, the curve saturates for strong enough white noise. Of course, such strong noise would be infeasible in an experimental setup in the first place, as it would make any attempt to control the setup futile.

In real experiments, a combination of the three possible deficiencies and also correlated noise must be considered. We choose to handle them in separated form based on two reasons: one, the exact form of imperfections will be highly setup specific. Second, we investigate them separately to find their effects. Unfortunately, this means there could be a negative cascade of all three deficiencies, an off-center start, a residual interaction and noise, which downgrade the results dramatically. However, such an analysis should be done with a specific experiment in mind.

14. Summary – Controlling Many-Body Chaos

In this theoretical discussion, we outline a new approach to utilize chaos as a resource in the many-body quantum context of coherent targeting. Usually, the presence of chaos poses fundamental challenges for controlling the evolution of a dynamical system being classical or quantum in nature due to the intrinsic instability of chaotic dynamics and the corresponding delocalization effect. Nevertheless for classical systems, it is long known that we can convert the inherent difficulties caused by instability and ergodicity into a resource [49]. Recently, it was demonstrated that with respect to quantum systems, an additional requirement is needed, i.e., the suppression of quantum state spreading [63] is necessary. Done originally in a Schrödinger or single-particle context, we extend the ideas into the many-body domain, here for ultracold atoms in an optical lattice. By identifying a time-dependent control Hamiltonian, we propose a quantum simulator controlling many-body quantum chaos.

Semiclassical methods allow for extending chaotic classical targeting to coherent quantum targeting. Mean-field trajectories and their stability analysis then provide us the time-dependent perturbations need for the quantum control. Conveniently, the quadrature phase-space formulation of a many-body system of ultracold bosons defines a mean-field limit, i.e. large filling factor, kin to ordinary Hamiltonian dynamics. In this way, we adapt the previous work [64] for Schrödinger dynamics in single-particle systems to the many-body bosonic world. We use the same class of fast heteroclinic trajectories that provide time-dependent chemical potentials determining the control Hamiltonian.

Analogous to the single-particle context [63, 64], the protocol is designed for guiding localized coherent quantum states. Our results for the Bose-Hubbard system are shown for minimum-uncertainty coherent states, but apply equally to the broader and important number-projected coherent states. Despite sounding like a small extension, this additional class of states includes many experimental relevant quantum states, e.g. macroscopic occupation of zero-momentum states. In order to control the spreading of these many-body state, a control system is in-

troduced that is essentially a time-dependent harmonic oscillator driven with the on-site occupations along the specific control trajectory. In practice, this means that interactions between the bosons are turned off in an experiment, which is something that in optical lattice systems can usually be achieved to high precision, e.g. using Feshbach resonances as a basis for one possible method [101, 176]. Together with the fact that the protocol simplifies to controlling the chemical potentials of the individual sites in a smooth, time-dependent fashion, we believe this protocol to be suitable for practical experimental implementation. Due to the harmonic nature of the system and the $U(1)$-symmetry of the dynamics any (number-projected) coherent state placed on the control trajectory satisfies the time evolution of the system exactly. This means that the protocol provides a tool to propagate a broad range of states from arbitrary initial and target points in phase space under the assumption that the underlying dynamics is sufficiently ergodic, opening up new possibilities in state preparation for optical lattices. An example is shown of a relatively short trajectory that can be used to target a homogeneous lattice state with well-defined, non-trivial phases between the condensates.

There are a few aspects of quantum targeting that may impact any assessment of how robust it can be against imperfections. First, the ideal would be to make the tiny shifts of the initial state centroids to the initial conditions of the optimal control (heteroclinic) trajectories. Likewise, the final state centroids on those trajectory endpoints would be slightly shifted to the target state's values. In fact, the initial shift is the single most important element in classical targeting, whereas suppressing the state spreading is the critical element in the quantum case. By virtue of the uncertainty principle, the optimal trajectory is already well represented inside the quantum state's Wigner transform. By not performing the shifts, a decrease of the fidelity is introduced into the protocol, which gets worse as the filling factor increases. This is observed numerically by calculating the overlap between the propagated and desired target state.

A second imperfection would be due to the practical impossibility to turn the interactions completely off, which left uncompensated, quickly break down the control protocol. It is anticipated that the on-site interaction strength can, in many circumstances [101–103], be controlled experimentally to high precision. However, if any non-vanishing residual interaction can be characterized, then a simple rectification expressed in Eq. (13.6) solves the over- or undershooting effect, which would be the main contributor to a fidelity decay. The local deformation of the initially circular Wigner density contours at the target state remains, but improves with increasing filling factor. A third issue arises due to imperfect control over the $\{\mu_j(t)\}$ and may require appropriate modeling of noise or other imperfections in a particular physical setup. This is left for future consideration. However, in the case of white noise, the strength of this type of noise has a linear dependence on the distance deviation in the targeting protocol and the control protocol is not particularly sensitive.

For the examples given, it is necessary to introduce chemical potential offsets in order to place an initial state and a target state on the same energy surface

such that chaotic trajectories can provide transport paths between them. If it is desired that the offsets vanish at the end, although not discussed here, it would be possible to consider adiabatically turning off the offsets and seeking some modified chaotic transport path between the initial and target states. For example, the momentum target state of Sec. 12 would become a fixed state of the system without interactions and chemical potential offsets. Additional time-dependence in the chemical potential offsets does not add much, if any, additional complications with respect to solving Hamilton's equations, but it adds an extra dimension to the complexity of the search for an optimal control trajectory. This issue of possible unwanted final chemical potential offsets does not arise if the initial and targets states are identical, as for the periodic trajectory cases, as they are automatically on the same energy surface without offsets. By targeting these periodic trajectories, the control protocol can be applied to the preparation of many-body time crystals [190, 198].

The presented one-dimensional examples are of greater utility and versatility than they might appear at first sight. By mapping the sites into higher-dimensional lattices [174] such that the nearest-neighbor associations are preserved, it is possible to control much larger and higher-dimensional lattices without suffering from the exponential growth of search volumes in phase space. For the details, we refer to our publication [3]. There we continue to study initial and target states that respect certain symmetric lattice configurations. We show that the complexity of optimal coherent quantum targeting in higher-dimensional lattices is not larger than finding control trajectories in the one-dimensional ring to which the mean-field dynamics can be mapped. On the other hand, for arbitrary lattice configurations in high dimensions, a systematic search for control trajectories becomes exponentially challenging with system size.

The problem of huge search spaces is an optimization challenge shouting for machine learning techniques which we discuss in the outlook, namely Chap. IV. The topic of machine learning however brings us to the next chapter, but in a different context: we parametrize many-body wave-functions via neural networks which enables us to represent low energy states of large system sizes in order to investigate chaotic signatures appearing by enlarging the system.

III. Towards Larger System Sizes: Neural Quantum States

A problem persisting throughout the present work is the exponential scaling of the Hilbert space dimension in system size. Generally speaking, we simulate larger and larger system sizes, especially when we want to approach a semiclassical[1] or thermodynamical regime. Unfortunately, exact numerical techniques, which are based on exact diagonalization of the many-body Hamiltonian, become unfeasible not only storage-wise, but also in terms of computational time. The dilemma is that we need larger system sizes to answer many current research questions, ranging from fundamental research - such as determining the existence of many-body localization [21, 133] - to explaining experimental data [199], predicting new (many-body) quantum effects, or discovering new materials with novel properties. Our focus is narrower: we investigate if chaos can be extend into lower and lower energy scales when a many-body system is enlarged. A first question we address is: can chaos emerge in a finite size system at ever lower energy scales as the size is increased?

The Hilbert space is growing exponentially and storage needed for states and operators, as well as algorithms scale linearly, quadratically or even at higher orders with the Hilbert space. There are ways to tackle the prefactors of these scalings or clever approximations which can be used for certain problems, but as always they have their limits or are not applicable for one's own system. In our case, methods of machine learning push the computational limits, meaning we gain a foothold into simulating large (many-body) quantum systems.

With the rapid progress of machine learning, using neural networks - universal function approximators [122] - as an ansatz for the (many-body) wave-function emerges as a promising approach. In the third chapter, we examine this relatively recent approach to addressing these computational challenges inherent in the simulation of quantum many-body systems. By utilizing neural networks as a variational ansatz in combination with Monte Carlo sampling, we adopt the framework of Variational Monte Carlo (VMC) methods. The far-reaching adaptation of artificial intelligence applications into everyday life renders neural networks ubiquitous. Within this context, Monte Carlo methods provide a means to circumvent severe computational bottlenecks in quantum physics.

[1] For the semiclassical limit, we are actually interested in expanding the local Hilbert space in order to have greater particle numbers and a lower effective Planck constant. This leads to polynomial growth in the Hilbert space dimension if the system size is fixed. However ahead, we are primarily interested in extending the system size at a constant filling factor (particle number scales with system size).

When integrated with neural network architectures, this approach belongs to the field of *Neural Quantum States* (NQS) - a term that has quickly gained recognition within the physics community. Introduced with the seminal work of Carleo and Troyer [113], the field has since experienced rapid development [119]. For an extensive introduction to NQS, particularly regarding time-dependent phenomena, we refer to Ref. [200].

Furthermore, this approach benefits from recent advances in computational infrastructure, particularly the availability of highly optimized accelerators such as GPUs and TPUs, which enable highly parallelized training and evaluation of neural network-based quantum states. For the programming environment, we employ the *jVMC* package [116], which is built upon the *JAX* ecosystem [201]. Three key advantages of using JAX and jVMC are: access to pre-implemented state-of-the-art algorithms, the open-source nature of the code allowing for algorithmic modifications, and hardware flexibility that facilitates efficient execution on heterogeneous computing nodes.

15. Introduction to Neural Quantum States

A (many-body) quantum state is specified by all its complex amplitudes

$$|\Psi\rangle = \sum_{\vec{s}} \Psi(\vec{s}) \, |\vec{s}\rangle \,, \tag{15.1}$$

where we sum over a representation $\{\vec{s}\}$ of the Hilbert space $\mathcal{H}$ basis. If we want to be exact, we need to store each amplitude $\Psi(\vec{s})$. Quickly, the amount of complex values becomes untractable, since the Hilbert space grows exponentially with system size. The fundamental and simple idea is to compress the representation via an NQS ansatz

$$\left|\Psi_{\vec{\Theta}}\right\rangle = \sum_{\vec{s}} \Psi_{\vec{\Theta}}(\vec{s}) \, |\vec{s}\rangle \,, \tag{15.2}$$

such that we only store the parameters $\vec{\Theta}$ of the ansatz $\left|\Psi_{\vec{\Theta}}\right\rangle$. We encode the amplitudes $\Psi_{\vec{\Theta}}(\vec{s})$ by the neural network and do on-demand evaluations later on. If the number of network parameters scales polynomially less than the Hilbert space dimension, $\#\vec{\Theta} \ll \dim \mathcal{H}$, and if we have an adequate description, the ansatz solves our storage problem. We want to mention some of the advantages neural networks bring with them:

- They are universal function approximators [122], which generally gives us the necessary accuracy by choosing the parameter number of the neural network large enough via extending the network in layer size and depth. Next to the sizes and number of each layer, the non-linear activation functions in-between the layers are essential for learning complex connections. A generic feed forward network is illustrated in Fig. 1.3 from the introduction showing the passing from input to output layer through the hidden layers.

- The numerical evaluations of the network $\Psi_{\vec{\Theta}}(\vec{s})$ and of its gradients $\nabla_{\vec{\Theta}}\psi_{\vec{\Theta}}(\vec{s})$ (mostly linear algebra) are accelerated on common hardware (GPUs and also TPUs) and can be done in a highly parallelized manner. Both are the backbone for the success of Monte Carlo estimations later on.

- We can utilize the vast variety of network architectures and optimization methods developed for neural networks, and we especially want to mention *optax* inside the JAX ecosystem providing sophisticated gradient descent methods [201] and of course the NQS implementation jVMC founded by [116].

Up to this point, the NQS ansatz theoretically solves the storage problem by compressing the quantum state into the network parameters, but we need to handle the evaluation and optimization problems. The optimization is handled later on in Sec. 17. Let us reformulate many-body quantum physics in terms of VMC and start with the expectation values of an operator $\hat{O}$ and rewrite it for Monte Carlo estimation

$$\langle \hat{O} \rangle = \frac{\left\langle \Psi_{\vec{\Theta}} \middle| \hat{O} \middle| \Psi_{\vec{\Theta}} \right\rangle}{\left\langle \Psi_{\vec{\Theta}} \middle| \Psi_{\vec{\Theta}} \right\rangle} = \sum_{\vec{s}} \frac{|\Psi_{\vec{\Theta}}(\vec{s})|^2}{\left\langle \Psi_{\vec{\Theta}} \middle| \Psi_{\vec{\Theta}} \right\rangle} O^{\mathrm{loc}}_{\vec{\Theta}}(\vec{s}), \tag{15.3}$$

where we define the local estimator of an operator via

$$O^{\mathrm{loc}}_{\vec{\Theta}}(\vec{s}) = \sum_{\vec{s}'} \langle \vec{s} | \hat{O} | \vec{s}' \rangle \frac{\Psi_{\vec{\Theta}}(\vec{s}')}{\Psi_{\vec{\Theta}}(\vec{s})}. \tag{15.4}$$

For efficient evaluation of Eq. (15.4), we are restricted to a sparse operator $\hat{O}$, since then the elements $\langle \vec{s} | \hat{O} | \vec{s}' \rangle$ are tractable for given $\vec{s}$ in order to perform the sum over the connected $\vec{s}'$.

In Eq. (15.3), the operator expectation value is transformed to an ordinary expectation value obtained from the probability distribution $|\Psi_{\vec{\Theta}}(\vec{s})|^2 / \left\langle \Psi_{\vec{\Theta}} \middle| \Psi_{\vec{\Theta}} \right\rangle$ of the wave-function. It provides a Monte Carlo estimate with a reasonable estimator via the NQS $\left| \Psi_{\vec{\Theta}} \right\rangle$ itself. Some machine learning fields require training data. NQS are optimized in the VMC framework, where the optimization is principle driven. Compared to the maximal entropy principle, we do not need empirical data to optimize. Instead we create our data, the samples $\vec{s}$, by our network itself. Our network encodes the amplitudes and their modulus squared values are representing a probability distribution. Therefore, we obtain samples from drawing from the wave-function probability distribution and evaluating Eq. (15.3) via a Monte Carlo sum

$$\langle \hat{O} \rangle \equiv \frac{1}{N_{\mathrm{s}}} \sum_{\vec{s} \sim |\Psi_{\vec{\Theta}}(\vec{s})|^2}^{\mathrm{MC}} O^{\mathrm{loc}}_{\vec{\Theta}}(\vec{s}), \tag{15.5}$$

where N_{s} is the number of samples and the equality holds for infinitely many samples $N_{\mathrm{s}} \to \infty$. However in the VMC setup, the estimation error of $\langle \hat{O} \rangle$

scales as $\sqrt{\operatorname{var} \hat{O}}/\sqrt{N_\mathrm{s}}$ independently of the dimensions [202] (assuming $\operatorname{var} \hat{O}$ is finite) and goes to zero with the inverse of the square root of the samples. The mindful reader might have a concern about the amplitude appearing in the denominator of Eq. (15.4). Fortunately, possibility of sampling a vanishing amplitude is excluded due to the probability $\vec{s} \sim |\Psi_{\vec{\Theta}}(\vec{s})|^2$.

One option for the Monte Carlo sampling, which is always possible, is to employ a Metropolis-Hastings algorithm to obtain random samples accordingly to the wave-function probabilities. It relays on setting up transition rules between samples which are accepted by ratios of the probabilities. By doing so and after enough transition steps, one obtains the independent and identically distributed samples by the probability distribution $\vec{s} \sim |\Psi_{\vec{\Theta}}(\vec{s})|^2$ independently of the initial chosen sample. The advantage is its general and straight-forward usage and the NQS does not have to emit normalized amplitudes because of the transmission amplitudes depending only on ratios of probabilities. However, there is an efficiency problem of correlated samples. It requires to carefully adjust the number of transition sweeps before taking individual sample sets. In some cases, the high number of necessary transition steps significantly worsen the performance [203], as the sampling time scales linearly with the sweeps. Due to this downside of correlations in the samples via Metropolis-Hastings Monte Carlo sampling, we choose to primarily employ a second option relying on normalized autoregressive networks which is discussed in next section.

16. Autoregressive Networks and Sampling

As the correlations between samples are an obstacle for efficient sampling, we decide to circumvent this problem. We obtain configurations $\vec{s}$ by uncorrelated sampling via an autoregressive network. There is a trade-off in expressibility, the architecture must allow the output not only to be the wave-function amplitude but also the factorization condition into conditional probabilities

$$\begin{aligned} P(\vec{s}) &= \prod_{i=1}^{L} P(s_i|\vec{s}_{<i}) \\ &= P(s_1|\vec{s}_{<1} = \emptyset)\, P(s_2|\vec{s}_{<2} = \{s_1\}) \dots P(s_L|\vec{s}_{<L} = \{s_1, \dots, s_{L-1}\}). \end{aligned} \tag{16.1}$$

Hence, $P(s_i|\vec{s}_{<i})$ allows us to sequentially sample the entries s_i until we have a full configuration $\vec{s}$. Conveniently, the jax ecosystem provides an optimized scan routine for neural networks. The resulting samples are uncorrelated by construction and can be used to evaluate Monte Carlo sums like in Eq. (15.5). A nice side effect is that the probabilities are also by construction normalized for autoregressive networks.

16.1. Neural Network Architectures

In the context of NQS, the term architecture refers to the specific design that determines how input configurations are processed to produce the complex-valued

wave-function amplitude. There are many classes of autoregressive neural networks we can choose from. We decide to focus on architectures whose original intent is as a language model. The physical correlation between particles resembles the correlation found between words in human speech motivating these types of networks for our application. For our purposes we use two classes of autoregressive neural networks from the large language models, namely the famous transformer (appearing in chatGPT) [204, 205] and the Receptance-Weighted-Key-Value network (RWKV) [206] which is a modified (and in the NQS community broadly used) recurrent neural network [119] with elements of the transformer.

Transformer

One of the most prominent architectures for autoregressive neural networks is the so-called transformer, since the famous paper [204] demonstrating its capability to serve as a large language model. We use only a part of the original architecture, the so-called decoder, and we modify its architecture illustrated in Fig. 16.1. The core feature of the network is the attention mechanism. The details are given in [204], but in a nutshell it contains trainable parameters encoding the correlations between different occupation numbers on different sites. The resulting representation is passed through a feed-forward network, which processes these correlations, and this procedure is iterated across the layers corresponding to the depth of the transformer. The transformer does the procedure separately in parallel by the number of heads. In the end, each head's output is summed up for the final output. It is crucial that the attention - allowing for all-to-all connectivity - is masked in order to obtain a causal order ensuring conditional probabilities of the form in Eq. (16.1).

Before the attention block in Fig. 16.1, the input occupation numbers are each assigned a higher-dimensional embedding and a site-based encoding is added. Especially for bosonic systems, this procedure gives each occupation number a site-specific channel emphasizing differences between the occupation numbers and sites. According to empirical observations [204], the transformer models are more suitable to training if channels can be hot (1) or cold (0) instead of having for each site only one channel with different "cold" and "hot" values, namely $(0, \ldots, \dim \mathcal{H}_{\text{loc}} - 1)$. Learning the difference during the training is challenging. The embedding simplifies this by mapping the "cold" and "hot" values into a number of feature dimensions. We choose the common scaling of the attention block with the embedding dimension as a feature dimension [204]. Before we obtain the conditional probabilities, the "Neck" in Fig. 16.1 transforms the output from the embedding size back to the local Hilbert space dimension required for obtaining the probabilities which are normalized by applying the *softmax* function at the end.

In order to sample one configuration $\vec{s}$, we run the model L times consecutively and obtain in each run the conditional probabilities $P(s_i|\vec{s}_{<i})$ and draw the next occupation s_i as depicted in Fig. 16.1. Altogether, we have then the whole

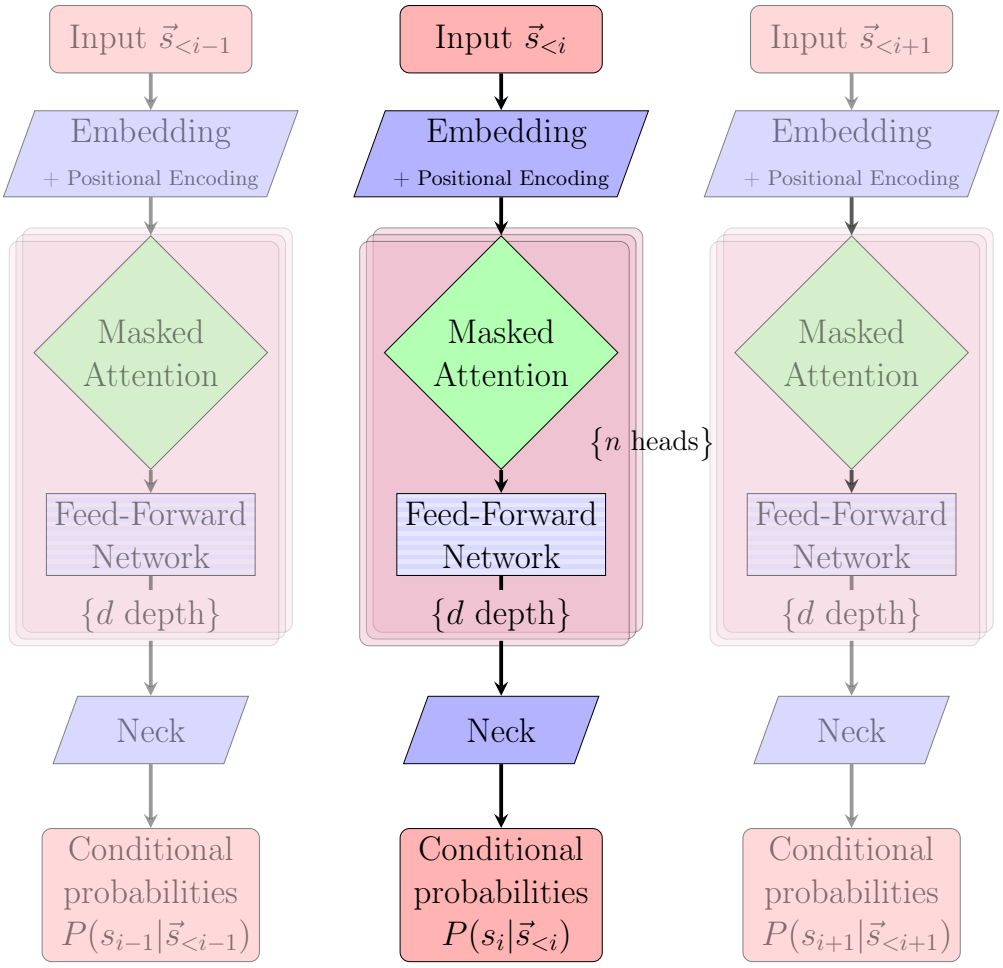

Figure 16.1: Sampling procedure and schematic architecture of the transformer model. During sampling at each step i, the incomplete configuration $\vec{s}_{<i}$ is processed, giving the conditional probability $P(s_i|\vec{s}_{<i})$ for the next occupation number s_i. Details about the building blocks are explained in the text, whereas the central part is the "Masked Attention" encoding correlations.

probability given by Eq. (16.1). If an amplitude $\Psi_{\vec{\Theta}}(\vec{s}) = \sqrt{P(\vec{s})}\exp(i\varphi(\vec{s}))$ is necessary, the network calculates the phase $\varphi(\vec{s})$ of the configuration $\vec{s}$ separately. A small, but important and convenient detail is that we work in the logarithmic space, meaning that the output is the logarithmic complex amplitude $\ln\Psi_{\vec{\Theta}}(\vec{s}) = \ln(P(\vec{s}))/2 + i\varphi(\vec{s})$.

The main advantage is that it can encode long-range correlations[2], the main reason, why we mostly use the transformer to encode phases. Phases are especially important, when we adiabatically transport eigenstates over a system parameter in Sec. 20 ahead.

One Monte Carlo sampling batch with N_s samples requires $N_\mathrm{s} \times L$ evaluations, but due to the high parallelization on GPUs this can be done relatively efficiently. Nevertheless at larger system sizes, this is a significant disadvantage: it requires evaluating L times the whole network and each evaluation also scales

[2]Important especially in human language, e.g. the German language has the annoying property of separating subject and verb throughout the whole sentence.

linearly with the system size $O(L)$. Hence, the sampling of a single configuration scales with $O(L^2)$, which slows down the sampling time when we approach larger systems. A second minor catch of the transformer is the memory usage, which also scales quadratically $O(L^2)$ with the system size (input token length [204]). These two considerations lead us to look for alternative architectures and we decide to employ the following architecture, which is an interpolation between the transformer and the recurrent neural network with sequential sampling. The hope is then that one has the advantages of both networks combined.

Receptance Weighted Key Value – RWKV

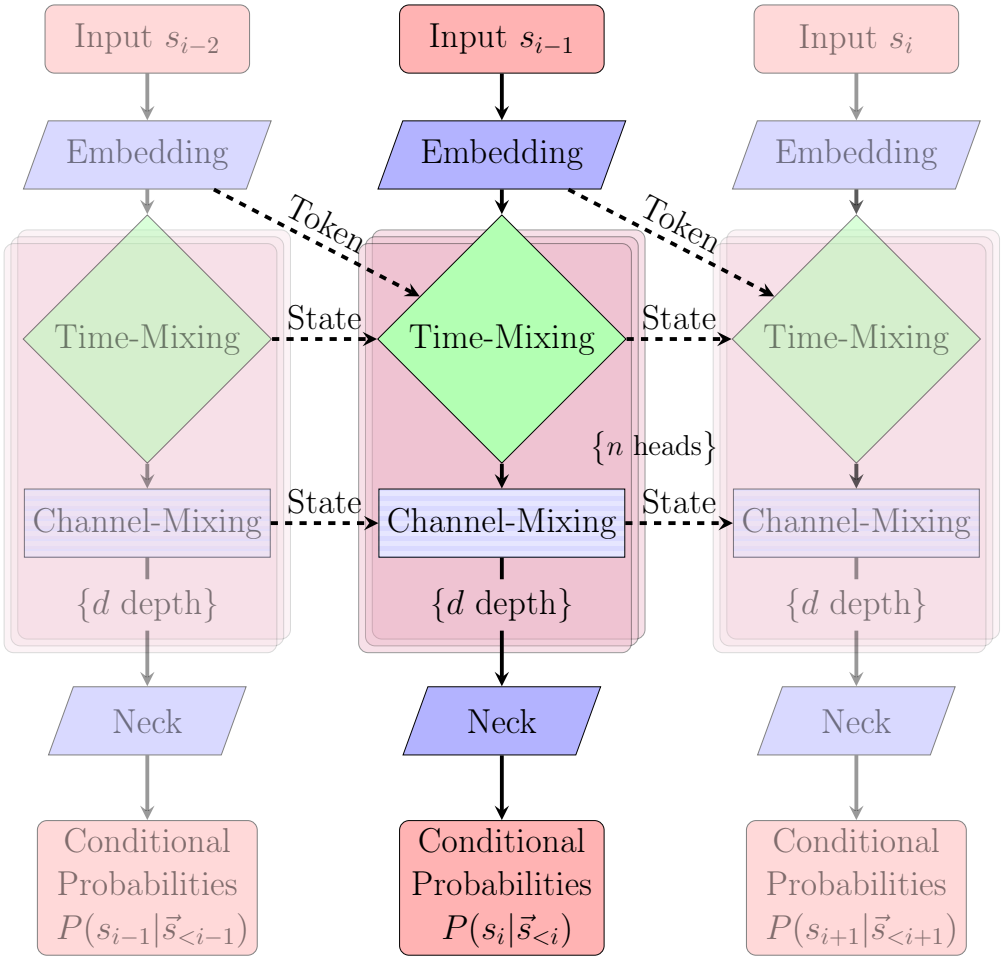

Figure 16.2: Schematic description of the RWKV architecture and sampling procedure. The RWKV model has the advantage of full and sequential evaluation, which makes it favorable for autoregressive sampling in larger systems. In the sequential mode, it only relies on s_{i-1} and the previous token and two states passed by the "Time- and Channel-Mixing" cells. Its output are the conditional probabilities $P(s_i|\vec{s}_{<i})$for the next occupation number s_i, which we use for the sampling. Next to the illustrated sequential sampling procedure, a full evaluation is possible to directly obtain the wave-function amplitude of a sample in one shot.

Compared to the transformer architecture for NQS, we use almost exclusively the Receptance Weighted Key Value (RWKV) network for the results in Secs. 19 and 20. The architecture is inspired by the transformer with features of the recurrent neural network and is introduced by [206]. The structure illustrated in Fig. 16.2 is similar to the transformer, the input goes through an embedding layer and the output goes through a "Neck" layer beforehand. In-between, we have "Time- and Channel-Mixing" blocks replacing the attention mechanism of the transformer for encoding correlations between occupation numbers in the configurations. We refer to [206] for further details about the architecture. In addition to a full evaluation at once, the structure is built in such a way that a sequential evaluation is possible for obtaining Monte Carlo samples. This is illustrated in Fig. 16.2 by the evaluation only depending on the previous s_{i-1}. Due to the sequential evaluation, it saves execution time and memory space. Both scale with $O(L)$, which is advantageous when going to larger system sizes ($L > 20$) compared to the transformer architecture, where the execution time is of order $O(L^2)$ and thereby a factor of the system size slower.

The biggest disadvantage compared to the transformer comes from the state and token passing, illustrated in Fig. 16.2, it encourages the vanishing of correlations over the inputs over system size during the training, which can lead to poor performance in lattice topologies with more than one-dimensional connections, i.e., when each site has more than two edges/neighbors. However, the vanishing of long-distance correlations should be less than in the recurrent neural network due to the construction of the "Time-Mixing" and "Channel-Mixing" cells [206].

16.2. Particle-Conserved Autoregressive Sampling

With the Bose-Hubbard system in mind, we are interested in a section of the Hilbert space with fixed particle number. We focus on the particle number in a bosonic many-body system, but the implementation is analogous for certain other abelian quantum number restrictions, e.g. magnetization in spin chains. The way we implement particle-aware sampling is to restrict the conditional probabilities such that configurations with too many and too few are masked and never sampled [207]. Keeping the autoregressive structure, one can alternatively disregard samples with the wrong total particle number, but this approach is hugely inefficient. In particular for large system sizes, obtaining by chance the right total particle number is exponentially unlikely leading to exponential many wasted configurations in the sampling. Hence the first strategy is the only viable option for us.

Masking requires the modification of the stepwise output of an autoregressive network, i.e., the cumulative particle number must be such that the final total particle number can be reached. Therefore, we exclude the other occupation values in each sequential sampling, such that we reach the total particle number. We show the schematics for a four-sited system with $N = 6$ particles in Tab. 16.1. Grayed-out cells are occupation configurations which lead to more or fewer particles. The masking of each row for the site i depends on the previ-

site i		1	2	3	4
input $\vec{s}_{<i}$		$\emptyset$	$s_1 = 1$	$s_1 = 1$ $s_2 = 2$	$s_1 = 1$ $s_2 = 2$ $s_3 = 2$
output $P(s_i\|\vec{s}_{<i})$	0	0.143	0.2	0.1	0.55
	1	0.143	0.25	0.1	0.05
	2	0.143	0.3	0.1	0.15
	3	0.143	0.1	0.6	0.025
	4	0.143	0.1	0.01	0.1
	5	0.143	0.025	0.08	0.025
	6	0.143	0.025	0.01	0.1
		$P(s_1)$	$P(s_2\|\vec{s}_{<2})$	$P(s_3\|\vec{s}_{<3})$	$P(s_4\|\vec{s}_{<4})$

Table 16.1: The conditional probabilities are masked in order to only allow for the correct particle number sector to be sampled. Grey cells are forbidden due to the particle number restriction, blue cells are the chosen occupations in this example. Note that the previous choices influence the next column such that at the last site only one entry is allowed. The masking requires renormalization of the amplitudes, since masking the forbidden occupations changes the normalization of an autoregressive network. The depicted sampling procedure is exemplary for $N = 6$ and $L = 4$, we have the renormalized probability $P(\vec{s} = (1, 2, 2, 1)) = \frac{0.143}{1} \times \frac{0.3}{0.975} \times \frac{0.6}{0.9} \times \frac{0.05}{0.05} = 0.0293$.

ous sampled configuration $\vec{s}_{<i}$ and it renormalizes the conditional probabilities. With the dynamical masking, we have an autoregressive network at hand which respects the constraint of total particle number conservation in a Hilbert space and is normalized.

16.3. Sampling Without Repetition – Gumbel Top-K Trick

There is an inefficiency we need to address later on if the wave-function is peaked around certain states. Off-peak contributions are rare in the sampling process, but needed for accuracy[3]. This brings us to sampling without repetition; it follows the algorithm developed in [203] and we implement it for the jVMC package. It relies on the *Gumbel Top-K Trick* [208], which adjusts the weights taking the non-repeating samples into account. We extend the algorithm to work for a general local Hilbert space dimension and with any autoregressive neural network which allows stepwise output. We verify the implementation in Fig. 16.3 in a bosonic system with particle conservation by testing that all occurrences of the samples in the sampling procedure coincide with the wave-function probabilities. We do this with and without repetitions in the samples, showing that the autoregressive sampling reproduces the probability distribution $|\Psi_{\vec{\Theta}}(\vec{s})|^2$.

The essential requirements for autoregressive neural networks are given for our

[3] If the off-peak contributions are irrelevant for the application, one can just approximate the ansatz with these peaked contributions.

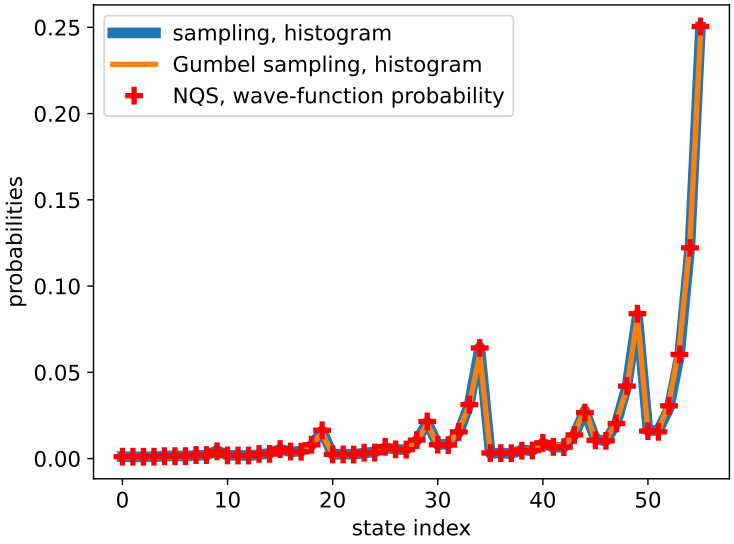

Figure 16.3: Verification of the sampling-without-repetition algorithm, also dubbed Gumbel sampling: the NQS wave-function probabilities (red pluses) agree with both histograms obtained from sampling with and without repetitions (blue and orange lines). The NQS parameters are randomly initialized and the number of samples used in the histogram is $2 \cdot 10^4$. Further system parameters are the system size $L = 6$, the total particle number $N = 3$ and the local Hilbert space dimension $\dim \mathcal{H}_{\text{loc}} = N + 1 = 4$. For illustration in the histogram, the states $\vec{s}$ are indexed by consecutive numbering which is not further specified. There are small, not visible deviations due to the finite amount of samples in the Monte Carlo estimation of the histograms.

purposes. We proceed to the training section, where we discuss how parameter gradients of the NQS enable us to achieve several (optimization) tasks.

17. Training – Neural Quantum States

In machine learning the term "training" usually signifies some sort of optimization technique reproducing training data. In our case, we discuss three objectives: first, maximizing the entropy (annealing) of the wave-function which is a preparation step and second, minimizing the energy of the wave-function in order to approximate the ground state of a Hamiltonian. Third is a system-parameter propagation via adiabatic transport which does not fall into an optimization technique, but still uses parameter gradients for the propagation.

For convenience, we use two general quantities appearing throughout the section: the gradient of the logarithmic amplitudes

$$\Gamma_k^{\vec{\Theta}}(\vec{s}) = \partial_k \ln \Psi_{\vec{\Theta}}(\vec{s})$$

and the local operator from Eq. (15.4)

$$O_{\vec{\Theta}}^{\text{loc}}(\vec{s}) = \sum_{\vec{s}'} \langle \vec{s} | \hat{O} | \vec{s}' \rangle \frac{\Psi_{\vec{\Theta}}(\vec{s}')}{\Psi_{\vec{\Theta}}(\vec{s})}$$

for a general operator $\hat{O}$. As mentioned, the latter can only be efficiently calculated if the operator $\hat{O}$ is sparse, which is always the case in our applications for the Bose-Hubbard Hamiltonian (in the site-representation) ahead. The sparsity of the operator leads to only a few non-zero $\langle \vec{s} | \hat{O} | \vec{s}' \rangle$ values and reduces the sum $\sum_{\vec{s}'}$ to these non-zero entries for each $\vec{s}$. Furthermore, $\Gamma_k^{\vec{\Theta}}$ can be efficiently evaluated using back and forward propagation in the neural network for the gradient [116].

17.1. Maximizing Entropy – Annealing and Delocalization

When we initialize a network, we can have configurations of network parameters which are ill-conditioned. They cause the training to fail or to be stuck at a local minimum. We circumvent the issue by training the network parameters to have a broad distribution for the probabilities in order to force Hilbert space exploration. The measure therefore naturally is the entropy of the Born-distribution. Assuming a normalized neural quantum state $\Psi_{\vec{\Theta}}(\vec{s}) = \left\langle \vec{s} \middle| \Psi_{\vec{\Theta}} \right\rangle$ (e.g. an autoregressive model), the entropy of the Born distribution is given by

$$S_{|\Psi_{\vec{\Theta}}\rangle} = -\sum_{\vec{s}} |\Psi_{\vec{\Theta}}(\vec{s})|^2 \ln\Big(|\Psi_{\vec{\Theta}}(\vec{s})|^2\Big) \tag{17.1}$$

which can be estimated directly via Monte Carlo sampling

$$S_{|\Psi_{\vec{\Theta}}\rangle} = -\frac{1}{N_\mathrm{s}} \sum_{\vec{s}\sim|\Psi_{\vec{\Theta}}(\vec{s})|^2}^{\mathrm{MC}} \ln\Big(|\Psi_{\vec{\Theta}}(\vec{s})|^2\Big). \tag{17.2}$$

In order to maximize $S_{|\Psi_{\vec{\Theta}}\rangle}$, we apply a gradient ascent to the entropy, i.e., we update the parameters of the NQS $\left|\Psi_{\vec{\Theta}}\right\rangle$ via the gradient descent method based on the negative of the Born-distribution entropy gradient

$$-\partial_{\Theta_k} S_{|\Psi_{\vec{\Theta}}\rangle} = \frac{2}{N_\mathrm{s}} \sum_{\vec{s}\sim|\Psi_{\vec{\Theta}}(\vec{s})|^2}^{\mathrm{MC}} \mathrm{Re}\Big\{\Gamma_k^{\vec{\Theta}}(\vec{s})\Big\}(\ln|\Psi_{\vec{\Theta}}(\vec{s})|^2 - 1), \tag{17.3}$$

where we explicitly assume a normalized (autoregressive) ansatz $\Psi_{\vec{\Theta}}(\vec{s})$.

Next to the preparation step for the ground-state training, we also evaluate the Born-distribution entropy to determine the localization in a given basis. The limiting cases are

$$\begin{aligned} S_{|\Psi\rangle} &= 0, && \text{if } |\Psi\rangle = |\vec{s}^*\rangle \\ S_{|\Psi\rangle} &= \ln(\dim \mathcal{H}), && \text{if } |\Psi\rangle = (\dim \mathcal{H})^{-1/2} \sum_{\vec{s}} |\vec{s}\rangle \end{aligned} \tag{17.4}$$

of localized and completely delocalized states.

Motivated by the logarithmic dependence on the Hilbert space dimension and thereby the linear dependence on system size, we classify a linear scaling of the entropy $S_{|\Psi_{\vec{\Theta}}\rangle}$ as a delocalizing state. If $S_{|\Psi_{\vec{\Theta}}\rangle}$ grows sub-linear, saturates or

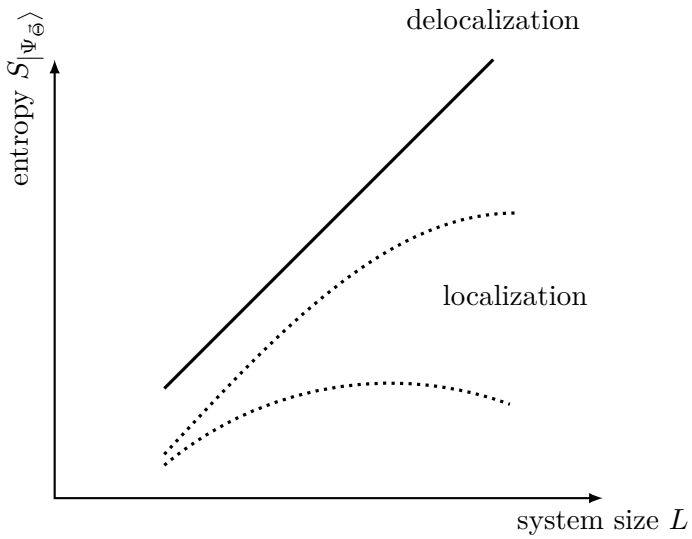

Figure 17.1: Schematic illustration of the Born-distribution entropy depending on localizing or delocalizing states. Linear dependence (solid line) classifies a state as delocalizing, whereas all sub-linear behavior (dashed lines) with system size is a state localizing in a given basis. Further explanation is in the main text.

decreases, we classify the state as localizing with increasing system size. Figure 17.1 gives a visual interpretation. A sub-linear behavior indicates that a state asymptotically occupies a vanishing fraction of the Hilbert space in the given basis. An asymptotic scaling beyond linear is impossible, since $S_{|\Psi_{\vec{\Theta}}\rangle}$ is bounded via the limits in Eq. (17.4).

17.2. Minimizing Energy – Ground-State Search

If we are interested in the ground state of large systems, we aim at the global minimum for the expectation value of the Hamilton operator. By using Eq. (15.3), we can express it as the following minimization problem

$$\begin{aligned} E_0 &= \min_{\vec{\Theta}} E_{\vec{\Theta}} \\ &= \min_{\vec{\Theta}} \left\{ \sum_{\vec{s}} \frac{|\Psi_{\vec{\Theta}}(\vec{s})|^2}{\left\langle \Psi_{\vec{\Theta}} \middle| \Psi_{\vec{\Theta}} \right\rangle} E^{\mathrm{loc}}_{\vec{\Theta}}(\vec{s}) \right\} \end{aligned} \tag{17.5}$$

over the variational parameters $\vec{\Theta}$ of the neural network. A direct way is to apply a gradient descent algorithm which relies purely on the gradient of the energy in Eq. (17.5) [116]

$$\begin{aligned} \partial_{\Theta_k} E_{\vec{\Theta}} = 2\,\mathrm{Re}&\left\{ \sum_{\vec{s}} \frac{|\Psi_{\vec{\Theta}}(\vec{s})|^2}{\left\langle \Psi_{\vec{\Theta}} \middle| \Psi_{\vec{\Theta}} \right\rangle} \Gamma^{\vec{\Theta}}_k(\vec{s})^* E^{\mathrm{loc}}_{\Theta}(\vec{s}) \right\} \\ - 2\,\mathrm{Re}&\left\{ \left(\sum_{\vec{s}} \frac{|\Psi_{\vec{\Theta}}(\vec{s})|^2}{\left\langle \Psi_{\vec{\Theta}} \middle| \Psi_{\vec{\Theta}} \right\rangle} \Gamma^{\vec{\Theta}}_k(\vec{s})^* \right) \left(\sum_{\vec{s}} \frac{|\Psi_{\vec{\Theta}}(\vec{s})|^2}{\left\langle \Psi_{\vec{\Theta}} \middle| \Psi_{\vec{\Theta}} \right\rangle} E^{\mathrm{loc}}_{\vec{\Theta}}(\vec{s}) \right) \right\}, \end{aligned}$$

which can be written as a Monte Carlo estimation

$$\begin{aligned}\partial_{\Theta_k} E_{\vec{\Theta}} &= 2\,\mathrm{Re}\left\{ \frac{1}{N_\mathrm{s}} \sum_{\vec{s}\sim|\Psi_{\vec{\Theta}}(\vec{s})|^2}^{\mathrm{MC}} \Gamma_k^{\vec{\Theta}}(\vec{s})^* E_{\vec{\Theta}}^{\mathrm{loc}}(\vec{s}) \right\} \\ &\quad - 2\,\mathrm{Re}\left\{ \left(\frac{1}{N_\mathrm{s}} \sum_{\vec{s}\sim|\Psi_{\vec{\Theta}}(\vec{s})|^2}^{\mathrm{MC}} \Gamma_k^{\vec{\Theta}}(\vec{s})^* \right) \left(\frac{1}{N_\mathrm{s}} \sum_{\vec{s}\sim|\Psi_{\vec{\Theta}}(\vec{s})|^2}^{\mathrm{MC}} E_{\vec{\Theta}}^{\mathrm{loc}}(\vec{s}) \right) \right\} \\ &= \mathrm{covar}(\Gamma_k^{\vec{\Theta}*}, E_{\vec{\Theta}}^{\mathrm{loc}}),\end{aligned} \tag{17.6}$$

which is conveniently a covariance of the logarithmic wave-function gradient and the local energy estimator. With the gradient given, the update of the parameters is

$$\Theta_k^{n+1} = \Theta_k^n - \tau \partial_{\Theta_k} E_{\vec{\Theta}}\Big|_{\vec{\Theta}^n}, \tag{17.7}$$

where τ is a small enough learning rate. Equation (17.7) gets slightly modified by the particular gradient-descent algorithm of choice. Ahead in our training procedures, we mostly utilize the ADAMw algorithm from the optax-package, part of the jax ecosystem [201].

The second way is an extension and physics-inspired, namely we propagate the NQS in imaginary time. We apply $\exp(-\tau H)\,|\psi_\Theta\rangle$ and project back to the variational manifold of the NQS. Hence, this method is referred to as the (imaginary) Time-Dependent Variational Principle (TDVP), and in the imaginary-time domain it is also known as Stochastical Reconfiguration (SR) [209]. Without giving the derivation, the advantage is that SR takes the variational manifold of the NQS into account, which is visible by the update-rule [116, 210]

$$\Theta_k^{n+1} = \Theta_k^n - \tau\,\mathrm{Re}\left\{S^{-1}\right\}_{k,k'} \partial_{\Theta_{k'}} E_{\vec{\Theta}}\Big|_{\vec{\Theta}^n} \tag{17.8}$$

where the matrix S encodes the local variational manifold of the NQS and is the so-called *quantum Fisher matrix*. Note that we employ the Einstein-sum convention, i.e., we sum over indices appearing twice (here k'). We can write S as an Monte Carlo estimate [116]

$$\begin{aligned}S_{k,k'} &= \frac{1}{N_\mathrm{s}} \sum_{\vec{s}\sim|\Psi_{\vec{\Theta}}(\vec{s})|^2}^{\mathrm{MC}} \Gamma_k^{\vec{\Theta}}(\vec{s})^* \Gamma_{k'}^{\vec{\Theta}}(\vec{s}) \\ &\quad - \left(\frac{1}{N_\mathrm{s}} \sum_{\vec{s}\sim|\Psi_{\vec{\Theta}}(\vec{s})|^2}^{\mathrm{MC}} \Gamma_k^{\vec{\Theta}}(\vec{s})^* \right) \left(\frac{1}{N_\mathrm{s}} \sum_{\vec{s}\sim|\Psi_{\vec{\Theta}}(\vec{s})|^2}^{\mathrm{MC}} \Gamma_{k'}^{\vec{\Theta}}(\vec{s}) \right) \\ &= \mathrm{covar}(\Gamma_k^{\vec{\Theta}*}, \Gamma_{k'}^{\vec{\Theta}}).\end{aligned} \tag{17.9}$$

For its derivation and further details, we refer again to [116].

In our case, we use an adjusted version, namely *MinSR* developed by [117], calculating the inverse of the quantum Fisher matrix more efficiently in the number of parameters. Its numerical effort scales linearly with the number of neural

network parameters. The trade-off is that MinSR scales worse (quadratically) with the number of samples used in the Monte Carlo estimation. However as shown by [117], a low number of samples is usually sufficient to progress in the energy minimization.

Later on for the ground-state search in Sec. 19, we usually use a combination of both, gradient descent algorithm and stochastical reconfiguration. Our empirical observation is that the progress in the training benefits from switching between different optimization methods. It helps overcome plateaus of slow training progress and improving the result in the end.

To evaluate the training progress and check that an NQS $\left|\Psi_{\vec{\Theta}}\right\rangle$ approaches an eigenstate, we estimate the energy variance

$$\operatorname{var} E_{\vec{\Theta}} = \left\langle \Psi_{\vec{\Theta}} \right| \hat{H}^2 \left| \Psi_{\vec{\Theta}} \right\rangle - \left\langle \Psi_{\vec{\Theta}} \right| \hat{H} \left| \Psi_{\vec{\Theta}} \right\rangle^2.$$

Assuming that the training is improving, we get closer towards fulfilling the eigenstate equation $\hat{H}\left|\Psi_{\vec{\Theta}}\right\rangle = E\left|\Psi_{\vec{\Theta}}\right\rangle$ which leads to energy variance to vanish, $\operatorname{var} E_{\vec{\Theta}} \to 0$. We use the relative energy variance $\operatorname{var} E_{\vec{\Theta}}/E_{\vec{\Theta}}^2$ (dimensionless) in order to compare simulations with different system parameters. The rescaling with the squared mean energy $E_{\vec{\Theta}}^2$ makes the relative energy variance scale invariant and allows to have meaningful comparisons between different orders of magnitudes in the energies. A vanishing (relative) energy variance does not imply that the ground state is found, but in gapped systems the imaginary TDVP usually ends up at the lowest eigenenergy [119]. Exceptions can in most cases be identified by comparing results from reruns with different random seeds[4], network parameters or architectures.

17.3. Following an Eigenstate – Adiabatic Transport

To go beyond ground states, assume we have the setup that our Hamiltonian is decomposed in

$$\hat{H} = \hat{H}_0 + \lambda \hat{V}, \tag{17.10}$$

where we have the n-th eigenstate approximated by an NQS $|\Psi_{\vec{\Theta},n}\rangle$ for the initial Hamiltonian $\hat{H}_0$. For simplicity, we assume further that the NQS is normalized and we aim to follow this eigenstate throughout turning the perturbation $\hat{V}$ on. Via discrete steps of size $\delta\lambda$ we want to adiabatically tune $|\Psi_{\vec{\Theta},n}\rangle$ via its parameters $\vec{\Theta} = \vec{\Theta}(\lambda)$ to stay an eigenstate[5], i.e.,

$$\hat{H}_j|\Psi_{\vec{\Theta}^j,n}\rangle = E_n^j|\Psi_{\vec{\Theta}^j,n}\rangle, \tag{17.11}$$

[4]Random seeds are used to initiate different states of the random number generator in JAX [201]. With these seeds specified, one can have random numbers which are reproducible.

[5]The notation is convoluted, I beg the reader for forgiveness. We drop here the explicit dependence of the parameter on the perturbation strength λ.

where $\hat{H}_j = \hat{H}_0 + j\delta\lambda\hat{V}$ is the instantaneous Hamiltonian and E_n^j denotes the n-th eigenenergy of $\hat{H}_j$. It resembles closely the adiabatic theorem [211], but there is no explicit time evolution. Instead, we directly evolve the parameters of the NQS based on first-order perturbation theory

$$(\hat{H}_j - E_n^j)|\Psi^{(1)}_{\vec{\Theta},n}\rangle = \left(\mathbb{1} - |\Psi^{(0)}_{\vec{\Theta},n}\rangle\langle\Psi^{(0)}_{\vec{\Theta},n}|\right)\hat{V}|\Psi^{(0)}_{\vec{\Theta},n}\rangle \tag{17.12}$$

where $|\Psi^{(0)}_{\vec{\Theta},n}\rangle$ is the unperturbed zero-order and $|\Psi^{(1)}_{\vec{\Theta},n}\rangle$ is its first-order correction. For better readability, we drop the eigenstate index n and the adiabatic step numbering j. On the parameter side, we express the expansion up to the first order

$$\begin{aligned}|\Psi_{\vec{\Theta}(\lambda+\delta\lambda)}\rangle &= |\Psi_{\vec{\Theta}(\lambda)}\rangle + \delta\lambda\left|\partial_{\Theta_l}\Psi_{\vec{\Theta}}\right\rangle\dot{\Theta}_l + O(\delta\lambda^2)\\ &= |\Psi^{(0)}_{\vec{\Theta},n}\rangle + \delta\lambda|\Psi^{(1)}_{\vec{\Theta},n}\rangle + O(\delta\lambda^2),\end{aligned}$$

and we directly identify the zero-order $|\Psi^{(0)}_{\vec{\Theta},n}\rangle = \left|\Psi_{\vec{\Theta}}\right\rangle$ and write $E_n^j = E$. From comparing the first orders, we express the gradient of the parameters $\dot{\Theta}_l$ via projecting on the variational manifold by applying $\langle\partial_k\Psi_{\vec{\Theta}}|$

$$\begin{aligned}\left\langle\partial_k\Psi_{\vec{\Theta}}\right|\hat{H}_j - E\left|\partial_l\Psi_{\vec{\Theta}}\right\rangle\dot{\Theta}_l =& \left\langle\partial_k\Psi_{\vec{\Theta}}\right|V\left|\Psi_{\vec{\Theta}}\right\rangle\\ &- \left\langle\Psi_{\vec{\Theta}}\right|V\left|\Psi_{\vec{\Theta}}\right\rangle\langle\partial_k\Psi_{\vec{\Theta}}\left|\Psi_{\vec{\Theta}}\right\rangle\\ (-S_1 + S_2)_{kl}\dot{\Theta}_l =& F_k,\end{aligned} \tag{17.13}$$

where two parameter-gradient matrices appear:

$$(S_1)_{kl} = E\left\langle\partial_k\Psi_{\vec{\Theta}}\middle|\partial_l\Psi_{\vec{\Theta}}\right\rangle$$

is the energy-scaled Fisher quantum matrix and we call

$$(S_2)_{kl} = \left\langle\partial_k\Psi_{\vec{\Theta}}\right|\hat{H}\left|\partial_l\Psi_{\vec{\Theta}}\right\rangle$$

the Fisher energy quantum matrix. We interpret

$$F_k = \left\langle\partial_k\Psi_{\vec{\Theta}}\right|V\left|\Psi_{\vec{\Theta}}\right\rangle - \langle V\rangle\langle\partial_k\Psi_{\vec{\Theta}}\left|\Psi_{\vec{\Theta}}\right\rangle$$

as a force term depending on the perturbation. The term with $\hat{H}_j - E$ projects onto the subspace orthogonal to the direction of the current zero-order eigenstate from the variational manifold of the NQS. Otherwise, Eq. (17.13) is analogous to the SR-algorithm in Eq. (17.8), but instead of $\hat{H}$ we have $\hat{V}$ in the force field.

We calculate each object via a Monte Carlo sum[6]

$$
\begin{aligned}
S_{1,kl} &= \frac{E}{N_\mathrm{s}} \sum_{\vec{s}\sim|\Psi_{\vec{\Theta}}(\vec{s})|^2}^{\mathrm{MC}} \Gamma_k^{\vec{\Theta}}(\vec{s})^* \Gamma_l^{\vec{\Theta}}(\vec{s}) \\
S_{2,kl} &= \frac{1}{N_\mathrm{s}} \sum_{\vec{s}\sim|\Psi_{\vec{\Theta}}(\vec{s})|^2}^{\mathrm{MC}} \Gamma_k^{\vec{\Theta}}(\vec{s})^* \sum_{\vec{s}'} \langle \vec{s} | \hat{H} | \vec{s}' \rangle \frac{\Psi_{\vec{\Theta}}(\vec{s}')}{\Psi_{\vec{\Theta}}(\vec{s})} \Gamma_l^{\vec{\Theta}}(\vec{s}') \\
F_l &= \frac{1}{N_\mathrm{s}} \sum_{\vec{s}\sim|\Psi_{\vec{\Theta}}(\vec{s})|^2}^{\mathrm{MC}} \Gamma_l^{\vec{\Theta}}(\vec{s})^* V_{\vec{\Theta}}^{\mathrm{loc}}(\vec{s}) \\
&\quad - \left(\frac{1}{N_\mathrm{s}} \sum_{\vec{s}\sim|\Psi_{\vec{\Theta}}(\vec{s})|^2}^{\mathrm{MC}} \Gamma_l^{\vec{\Theta}}(\vec{s})^* \right) \left(\frac{1}{N_\mathrm{s}} \sum_{\vec{s}\sim|\Psi_{\vec{\Theta}}(\vec{s})|^2}^{\mathrm{MC}} V_{\vec{\Theta}}^{\mathrm{loc}}(\vec{s}) \right) \\
&= \mathrm{covar}(\Gamma_k^{\vec{\Theta}*}, V_{\vec{\Theta}}^{\mathrm{loc}})
\end{aligned}
\tag{17.14}
$$

and invert $(-S_1 + S_2)$ via the same technique in SR-optimization appearing in Eq. (17.8). Due to this similarity, we adapt the TDVP-class in jVMC [116] for the adiabatic transport to invert and regularize the matrix, such that our update in the parameter $\lambda \to \lambda + \delta\lambda$ is given by

$$
\Theta_k\big|_{\lambda+\delta\lambda} = \Theta_k\big|_{\lambda} + \delta\lambda\, \dot{\Theta}_k\big|_{\lambda}, \tag{17.15}
$$

where we choose the step size $\delta\lambda$ via one of the integrators implemented in jVMC. When applying Eq. (17.15), we need to take special care for the estimation of S_2. From our experience, it is the primary source of errors if estimated poorly.

Like in the ground state optimization, we utilize the energy variance as a convergence check of the adiabatic transport, as a sudden increase in the variance of the energy indicates a breakdown of the algorithm. A breakdown of the adiabatic transport does not have to be because of numerical error accumulation. Our goal is to see chaotic signatures and we aim specifically at avoided crossings in the energy spectrum [5]. These avoided crossings usually make the inverse $(-S_1 + S_2)$ numerically ill-conditioned due to the $\hat{H} - E$ term. We show in Fig. 17.2 how an avoided crossing (left panel) could affect the adiabatic transport. We want to motivate that even a breakdown of the method can reveal an avoided crossing. Two eigenstates get close enough such that inverting the matrix $(-S_1 + S_2)$ in Eq. (17.13) becomes unstable. A clear signature is the increase of the variance for the avoided-crossing pair of eigenstates, which is depicted in the right panel of Fig. 17.2. It is therefore essential to check for numerical accuracy; we need to exclude integration errors or representation deficits of the network. Both are numerically challenging and require a detailed and careful investigation of each adiabatic transport run for each eigenstate.

Of course, there is the possibility that the algorithm gives a valid approximation for the avoided crossing, in which case there is nothing to complain about. Nevertheless, a convergence check is equally necessary there. A direct crossing

[6]The energy E appearing in S_1 is evaluated via Monte Carlo estimation, too.

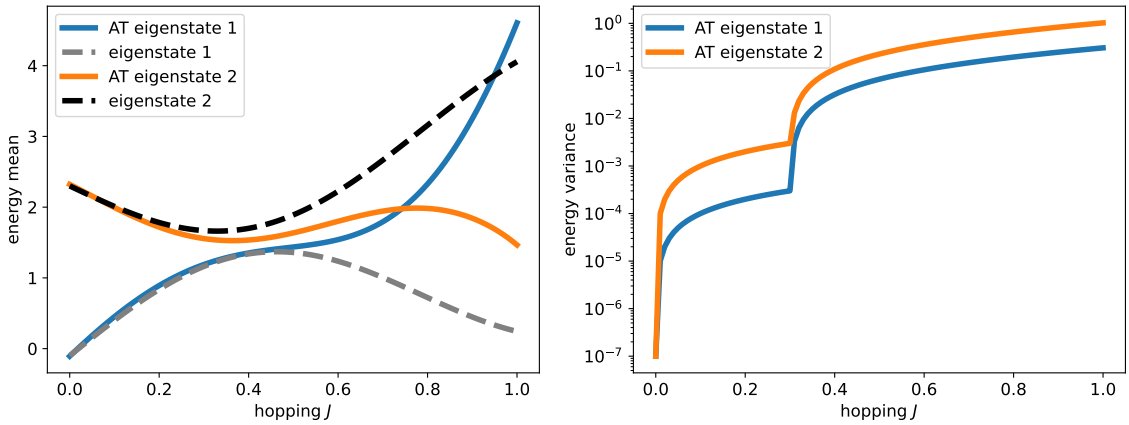

Figure 17.2: Schematic illustration of the expected behavior at an avoided crossing if the adiabatic transport (AT, orange and red solid lines) breaks down, as the energies diverge from the exact values (dashed lines). The adiabatic transport calculation must be checked for convergence, i.e., finer steps in the integration, etc. Later on in Sec. 20, the perturbation $\hat{V}$, is the hopping term in Eq. (18.2) ahead, such that we set λ as the hopping parameter J in the panels.

should be caught if the convergence test results in a closing gap with improving energy variance.

As a final note on the case of a normalized network like the transformer or RWKV in Eq. (17.13), we can express S_1 as the covariance of the gradient of the logarithmic amplitudes when adding the gradient of the normalization. It is not necessary for us, as these terms vanish, since the normalization is guaranteed by the construction of the network models. But if doing so, S_1 is the same Fisher quantum matrix as in Eq. (17.9) multiplied by the mean energy. For the second matrix S_2, adding the (vanishing) normalization gradient results in a more complicated expression, so we decided to omit this vanishing gradient in our derivation for both matrices.

With the details of the training introduced, we are finally ready for our results. But allow us to give a short excursion how the Bose-Hubbard model is an effective description of transmon chips at low energies, which is part of the motivation for our project with neural quantum states.

18. Excursion: Bose-Hubbard as an Effective Transmon Model

Our initial motivation for exploring NQS is to investigate signatures of quantum chaos within transmon-based quantum computing architectures [106, 107]. The system of interest are interacting transmon qubits described by the following

(minimal) Hamiltonian [128, 189]

$$\hat{H}_{\mathrm{T}} = T \sum_{\langle i,j \rangle} \hat{m}_i \hat{m}_j + 4E_{\mathrm{C}} \sum_{j=1}^{L} \hat{m}_j^2 - \sum_{j=1}^{L} E_{\mathrm{J},j} \cos \hat{\varphi}_j, \tag{18.1}$$

where we have for each transmon j the Cooper pair number operator $\hat{m}_j$ and the phase operator $\hat{\varphi}_j$. They are a conjugated pair of operators obeying the bosonic commutator relation $[\hat{m}_j, \hat{\varphi}_j] = 1$. The parameters of the Hamiltonian are the charging energy E_{C} (inversely proportional to the capacitance of the circuit), the Josephson energy, E_{J_i} (proportional to critical current of the circuit) and the coupling T (electric coupling via capacitance between transmons). All of the constants have units of energy, but using natural units ($\hbar = 1$), they are specified with frequencies and are in the range from MHz to GHz [212, 213]. For better distinguishably, we denote Cooper-pair operator with $\hat{m}$ in order to separate the notation from the occupation number operator $\hat{n}$ in the Bose-Hubbard model.

Because of the parameters' typical hierarchy [106, 127], e.g. $E_{\mathrm{J}_i} \gg E_{\mathrm{C}} > T$ [213], we are allowed to change the picture of Cooper-pair charges $|m_j\rangle$ to on-site excitations $|k_j\rangle$ in each single transmon. These excitation numbers build the computation basis and excitations beyond one ($k > 1$) are energetically punished by the chosen parameter hierarchy. We treat the coupling in a rotating-wave approximation, the resulting Hamiltonian is the Bose-Hubbard Hamiltonian, which is an effective model for low-energy states which includes the computational states of $|k_j = 0\rangle$ and $|k_j = 1\rangle$ at each site j. For the interested reader, a derivation we recommend is in [127] and following the steps, we obtain from Eq. (18.1) the slightly modified Bose-Hubbard Hamiltonian in the rotating-wave-approximation

$$\hat{H}_{\mathrm{BH}} = -\sum_{\langle i,j \rangle}^{L} J_{ij} \left(\hat{a}_j^\dagger \hat{a}_i + \hat{a}_i^\dagger \hat{a}_j \right) + \frac{U}{2} \sum_{j=1}^{L} \hat{a}_j^\dagger \hat{a}_j^\dagger \hat{a}_j \hat{a}_j + \sum_{j=1}^{L} \mu_j \hat{a}_j^\dagger \hat{a}_j. \tag{18.2}$$

The hopping term has a site-specific form compared to the previous chapters. To be precise, the parameter connections between the transmon Hamiltonian Eq. (18.1) and the Bose-Hubbard Hamiltonian Eq. (18.2) are the following [127]

$$\begin{aligned} U &= -E_{\mathrm{C}} \\ J_{ij} &= -\frac{T}{4\sqrt{2E_{\mathrm{C}}}} \sqrt[4]{E_{\mathrm{J}_i} E_{\mathrm{J}_j}} \\ \mu_j &= \sqrt{8E_{\mathrm{J},j} E_{\mathrm{C}}} - E_{\mathrm{C}}. \end{aligned} \tag{18.3}$$

Note that the interaction U is negative ($E_{\mathrm{C}} > 0$), therefore attractive, as well as the hopping J_{ij} being negative. The requirement for the validity of the effective Bose-Hubbard model assumes $E_{\mathrm{J}_i} \gg E_{\mathrm{C}} > T$. Typical system parameter values for transmon chips are $E_{\mathrm{C}} \sim 0.25\,\mathrm{GHz}$, $T \sim 5 - 50\,\mathrm{MHz}$ and $\bar{E}_{\mathrm{J}} \sim 12\,\mathrm{GHz}$ with disorder $\sigma_{E_{\mathrm{J}}} \sim 0.5\,\mathrm{GHz}$ [127, 132]. These values relate to the following parameter values in the Bose-Hubbard model $U \sim -0.25\,\mathrm{GHz}$, $\bar{J} \sim -6\,\mathrm{MHz}$ with $\sigma_J \sim$

0.01 MHz and $\bar{\mu} = 6\,\mathrm{GHz}$ with $\sigma_\mu \sim 0.12\,\mathrm{GHz}$. Due to small coupling $T \ll E_{\mathrm{J}_i}$, we are allowed to approximate the pair-dependent $J_{i,j}$ via an averaged hopping term

$$\bar{J} = J = -\frac{T}{4\sqrt{2E_{\mathrm{C}}}}\sqrt{\bar{E}_{\mathrm{J}}} \tag{18.4}$$

such that the variance of the Josephson energies only appears in the chemical potentials μ_j in the Bose-Hubbard model. We set the mean $\bar{\mu}$ of the chemical potentials to zero, since with particle conservation N (total number of excitations), the mean factors out via an energy-offset of $\bar{\mu}N$.

One last thing certainly leads to some confusion: in an excitation sector given by total $N \leq L$ excitations, the maximal energy state is usually close to a computational state due to the attractive interaction. Therefore, we are actually interested in the ground state of $-\hat{H}_{\mathrm{BH}}$ in Eq. (18.2) with the negative system parameter specified in text above (the standard deviations stay the same).

With the connection between the two systems established, we optimize NQS models for the ground states (highest eigenstates) for different transmon layouts via the effective Bose-Hubbard model looking for delocalization effects.

19. Ground-State Delocalization in Large Bose-Hubbard Lattices

In the following, we focus on three types of topologies: one-dimensional chains, two-dimensional square lattices with open boundaries and the brick-like architectures displayed in Fig. 19.1 which are used in IBM chips [106, 107]. At the time of writing we only managed the system sizes marked with colored rectangles with the system size labeled. For the disorder in the chemical potentials, we use fixed *jax random keys* which provide reproducible runs. In Fig. 19.1, a disorder realization is illustrated by the color coding of the lattice sites. For the network architectures, the output is not omitting a phase. All amplitudes can be chosen positive, since the Hamiltonian in Eq. (18.2) is stoquastic [214]. The network parameters which can be found in Tab. 19.1 are set fixed for all system-sizes in this section. For each of the three layouts, we choose the following optimization procedure: we start with ADAMw gradient descent optimization from the optax package part of the jax-ecosystem [201]. We continue with an imaginary-time MinSr-optimization [117] and finally we finish with a few hundred more steps of ADAMw gradient descent. This procedure turns out to be beneficial for our purposes in most trainings.

Slight adjustments are sometimes necessary, e.g. in some circumstances it helps to anneal the wave-function before the training starts, i.e., we maximize (via ADAM-optimizer and Eq. (17.3)) the entropy of the Born probabilities at the start of the training. The annealing steps help to overcome badly initialized networks and force Hilbert space exploration.

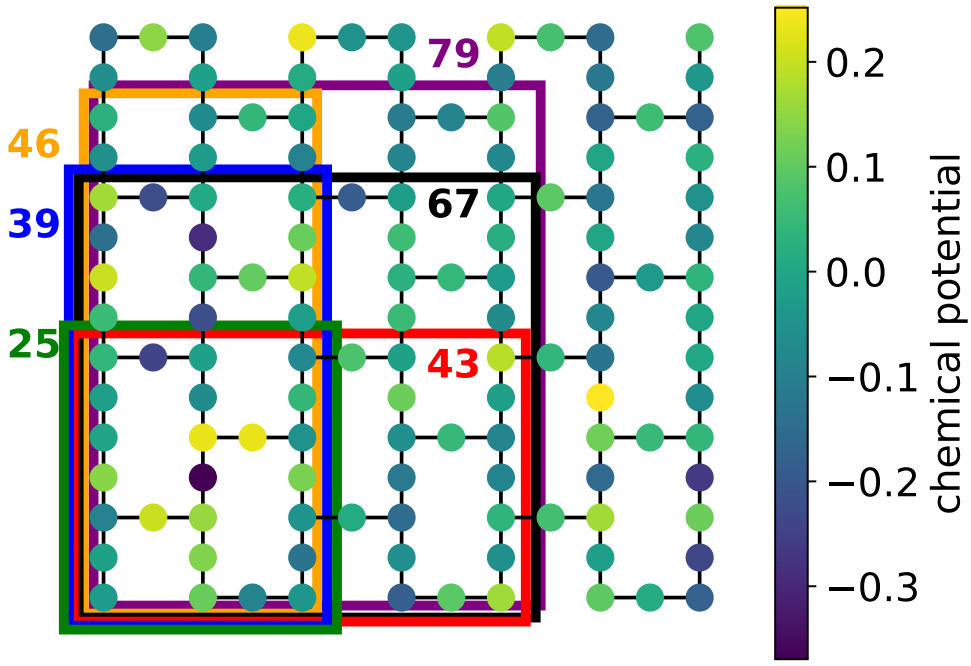

Figure 19.1: The transmon architecture of interest is a brick-like structure proposed by IBM for their quantum computer chips [106, 107]. The edges show couplings and the colors of the vertices show the strength for one site-specific disorder realization with $\sigma_\mu = 0.12$ (already in the Bose-Hubbard approximation).

Especially if the ground state has a peaked probability distribution, we see an improvement in the training progress using sampling without repetition. Therefore, we combine our optimization with Gumbel sampling discussed in Sec. 16.3, since sampling without repetition draws samples other than the dominantly peaked ones for more accurate expectation value estimation. It improves the Hilbert space exploration beyond the peak contributions and helps to correctly construct the gradient with fewer samples and therefore enhances the optimization procedure [203].

Before turning to larger system sizes, we compare the NQS results to the ground state obtained via exact diagonalization of the Hamiltonian for $L = 10$ sites, shown in Fig. 19.2. In the left panel, the relative deviation consistently drops below 10^{-3} which demonstrates excellent convergence. To illustrate the training performance from another perspective, the right panel illustrates the relative energy deviation against the relative energy variance. A clear linear correlation is observed, which has a scattered cluster at low relative energy and low relative energy variance. This behavior indicates that the training accuracy in the mean energy is limited by the statistical uncertainty associated with the finite number of Monte Carlo samples and the convergence criterion of vanishing energy variance is well satisfied. Here in this small system, we have $\dim \mathcal{H} = 2002$ at half filling ($N/L = 0.5$), but at unit filling ($N/L = 1$) we already approach unfeasible computational times due to $\dim \mathcal{H} = 92370$. Hence, exact methods have almost reached their limit and, in order to go significantly

RWKV - parameters	value
lDim (= dim $\mathcal{H}_{\text{loc}}$)	6
patch_size	2
hidden_size	16
num_heads	2
num_layers	6
embed_size	16
total	
number of parameters	12844

Table 19.1: Network parameters of the RWKV architecture used in the ground-state search. The total number of the network variational parameters are for $L > 10$ substantially lower than the Hilbert space dimension.

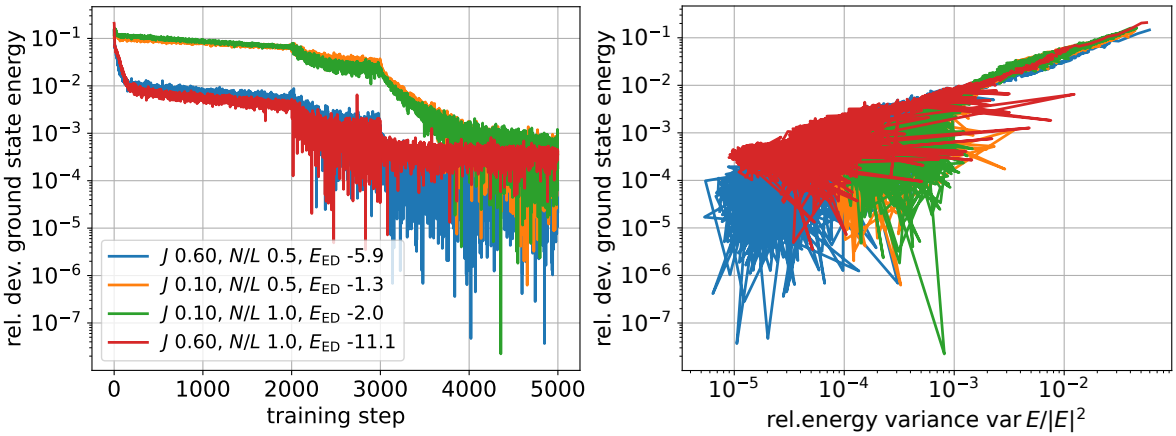

Figure 19.2: Comparing NQS approach with the RWKV architecture to the exact diagonalization reference for the ground state at $L = 10$, $N/L = 0.5$, 1 and hopping $J = 0.6$, 0.1 respectively. Interaction $U = 0.25$ and the chemical disorder strength $\sigma_\mu = 0.12$ are fixed in the displayed simulations. NQS energies reach an excellent agreement below 10^{-3} in the right panel for the relative deviation of the energy. The left panel visualizes the training progress via relative energy variance versus the relative energy deviation showing linear behavior and clustering at low values of deviation and variance indicating convergence. The RWKV-network parameters are specified in Tab. 19.1.

beyond $L > 10$, we now focus on the NQS approach.

As mentioned, with the network parameter in Tab. 19.1, we obtain the optimization results in Fig. 19.3 for large system sizes. For the time being, we only focus on the RWKV architecture and reach hopping strength only down to $J = 0.06$ for the brick layout in Fig. 19.1. Furthermore, we only present a single disorder realization in the chemical potentials $\vec{\mu}$ (jax random seed equal one). The right panels of Fig. 19.3 show the successful training for the filling factor $N/L = 1$ at hopping $J = 0.6$ via the relative energy variance-deviation illustration. We observe again linear correlations between the energy minimization and the energy variance indicating good convergence. For smaller system

sizes, we reach excellent relative energy variances ($\sim 10^{-3}$) indicating faithful ground state representation. Figures for all filling factors and hopping strengths are provided in Figs. F.1, F.2 and F.3 from App. F. There, the variance remains relatively high ($\sim 10^{-2}$) at lower hopping strengths. We suspect that increasing the number of parameters (and the number of samples in the Monte Carlo estimation) overcomes the training plateaus. Nevertheless, we are observing on the left panels of Fig. 19.3 that the entropy $S_{|\Psi_{\vec{\Theta}}\rangle}$ of the wave-function amplitudes in Eq. (17.5) always increases linearly with the system size L.

This behavior indicates delocalization of the ground state, our main result for this section, since we observe the predicted behavior discussed in Sec. 17.1 and illustrated in Fig. 17.1. Strictly speaking, the ground state is asymptotically filling a non-vanishing fraction of the exponential Hilbert space. Consequently, as depicted in Fig. 1.4 of the introduction, the particles are in a superposition of exponentially many Fock states. In the left panels of Fig. 19.3, we include further filling factors and hopping strengths and they all show the same behavior of delocalization. Even lowering the hopping strength to $J = 0.06$ in the lower right panel of Fig. 19.3, the linear increase of the entropy persists with a slightly lower magnitude. With these results for the presented disorder configurations, we suspect that non-zero hopping J (non-zero coupling T in the transmon model) always leads to a delocalization of the ground state (maximal energy state in the excitation section).

Our calculations show there is no transition towards any localization in the presented disorder realizations when we enlarge the system. We conjecture that there is no many-body localization of the Bose-Hubbard ground state at finite hopping, regardless which particle number sector we use. From the calculation in the Bose-Hubbard model, we infer that the delocalization is equally happening for the maximally excited state in each excitation sector of the transmon Hamiltonian modeling [106, 107]. However, we can not prove yet that there is never a phase transition for lower hopping, but we observe no indications towards one. We suspect lowering the coupling to $J \sim 0.006$ and below enables quantum computers to have enough localization of the eigenstates in the computational states to be feasible, but with system size the viability threshold gets successive smaller. Maybe leading to the requirement to decouple the transmons completely like in the approach Google peruses [139][7].

The ground state of the effective Bose-Hubbard model is only one eigenstate which is not always related to the computational states in the transmon Hamiltonian. As the entropy increases quite rapidly, only under small hopping J (small coupling T for the transmons) the connection is valid, since then we are close to a pure excitation state. Therefore, we explore the promising strategy of adiabatically transporting computational states, which we outline for the NQS in the next section.

[7] As mentioned in the introduction, Google's approach [139] uses overhead hardware which decouples the transmons during idle time (off-operations). This is not modeled by our transmon model and consequently our Bose-Hubbard calculations do not apply there.

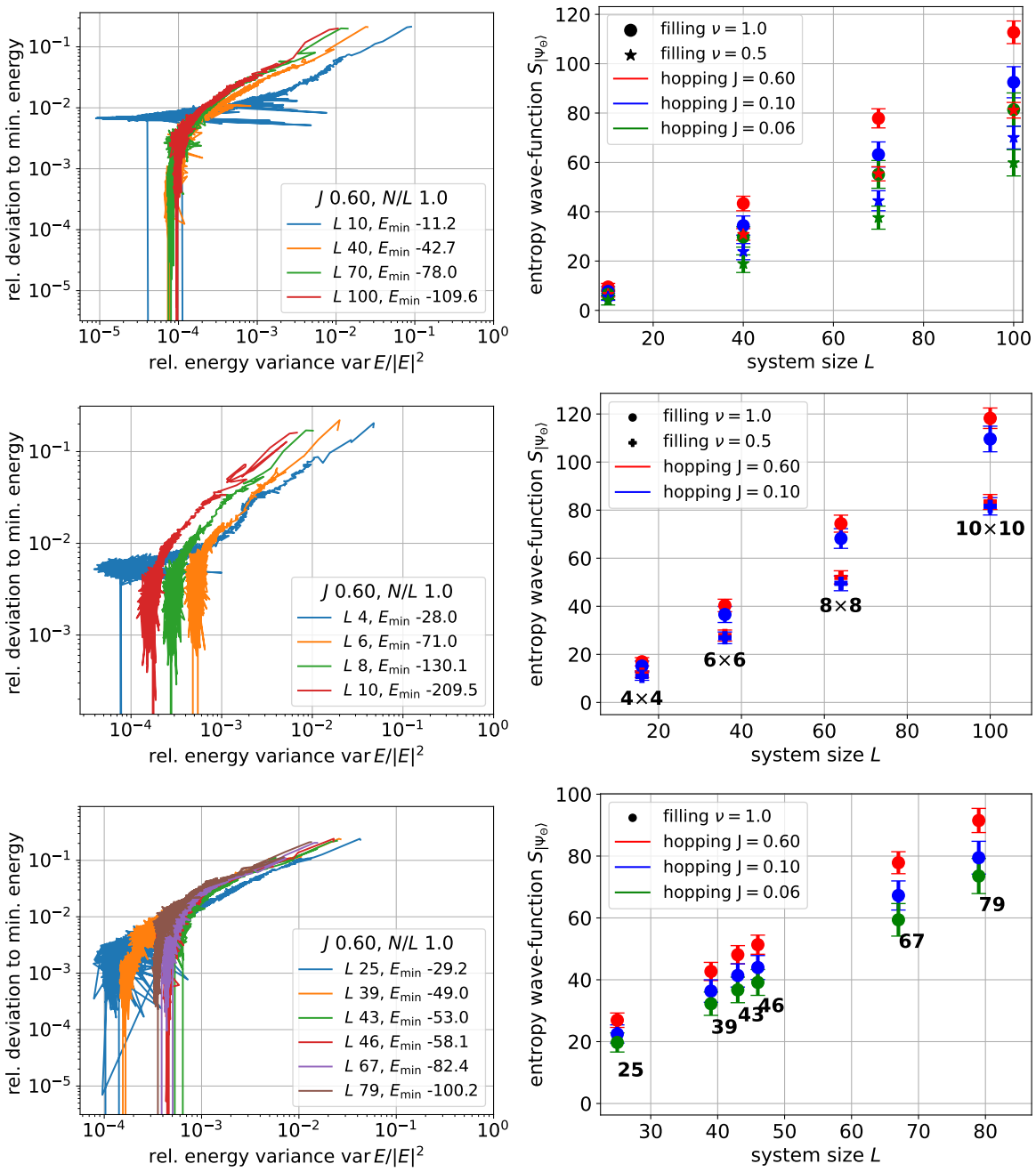

Figure 19.3: Results from the ground-state minimization: left panels show the correlation between the relative energy variance and difference between the minimal energy during the minimization for the one-dimensional chain (upper panel) with open boundaries, two-dimensional lattice (middle panel) with open boundaries and the brick structure (lower panel) at the hopping strength $J = 0.06$ and the filling factor $N/L = 1$. The right three panels show the Born-distribution entropy plotted over the system size for the same lattice topologies respectively. All configurations of system parameters show linear increase of the entropy, which is an indication of delocalization, and no transition towards localization is visible. The data for the brick-layout are labeled by system sizes displayed in Fig. 16.1. In all cases, we use the RWKV-network with the parameter specified in Tab. 19.1. The hopping and filling factor are specified in each panel individually, however the interaction $U = 0.25$ and the standard deviation of the chemical potentials $\sigma_\mu = 0.12$ are the same in each panel.

20. Proof of Concept: Adiabatic Transport of Exited States

With Fig. 17.2 in mind, we go to the proof-of-concept calculation, since at the time of writing we are currently developing the code for adiabatic transport. Its key challenge is to correctly find a suitable way to construct the parameter gradient in Eq. (17.13) of the NQS necessary to follow the adiabatic change of the system parameters. We present here the algorithm still relaying on an exact sampler of the Hilbert space, because we have issues estimating the matrix S_2 in Eq. (17.15). An exact sampler samples the whole distribution and uses the whole Hilbert space, accordingly only small system sizes are possible and we exclusively use $L = 6$ sites and $N = 3$ particles in the following. Like previously in the ground-state search, we set the interaction to $U = 0.25$, use one specific disorder realization for the chemical potentials with a linear width $\sigma_\mu = 0.12$ and scan the hopping parameter J in the range $[0.1, 0.3]$.

The subsequent challenge is to find a starting point for which we know the eigenstates of the system. Then we can use infidelity-optimization [215] to prepare an NQS for adiabatic transport via Eq. (17.13). At a first look, the case of zero hopping $J = 0$ is tempting. Every Fock state is an eigenstate, which is unfortunately maximally peaked. When taking such a Fock state and even with the help of Gumbel sampling (Sec. 16.3), our prepared NQS is specifically trained to the single peaked Fock state and its variational manifold from the network parameters is ill-conditioned for adiabatic transport. For the presented simulation ahead, we circumvent this issue and start at a finite hopping value $J = 0.1$, since we have access to all eigenstates due to the small system size. We try to overcome the initialization problem by exactly carrying out perturbation-theory steps from $J = 0$ in order to reach some small finite hopping value $J \sim 10^{-4} - 10^{-6}$ in the future[8].

With that said, we display the parameters of the RWKV-network in Tab. 20.1. The number of parameters (3826) is exceeding the Hilbert space dimension (56) by a factor of almost 69, i.e., we over-parameterize the wave-function of the eigenstates. In an actual application at large system size, this over-parametrization is not feasible, since the Hilbert space dimension is exceeding the computational resources. However, large language models require - in our experience - a minimum amount of parameters to perform as intended. Compared to the ground-state search, we need to add a phase to the output of the RWKV-network. It is calculated by a separated transformer block with its own number of layers. We need a phase, as excited states in contrast to ground states can not be chosen sign-free even for a stoquastic Hamiltonian.

The over-parametrization is indirectly visible in the infidelity-training results for the initial-state representation, since we easily achieve reaching infidelities below 10^{-8} in Fig. 20.1. The infidelity training applies an ADAMw gradient

[8] Alternatively, we can adjust the basis, i.e., we go over to the momentum basis of the Bose-Hubbard Hamiltonian. There $J = 0$ has unpeaked eigenstates. However, this basis has its downside not omitting a sparse Hamiltonian.

RWKV - parameters	value
lDim ($= \dim \mathcal{H}_{\text{loc}}$)	4
patch_size	3
embedding_dim	6
hidden_size	8
num_heads	1
num_layers	6
num_layers_phase	3
total	
number of parameters	3826

Table 20.1: Parameter of the RWKV-network used for the adiabatic transport calculations. The number of parameters exceeds the Hilbert space dimension ($\dim \mathcal{H} = 56$) by far. For an application with large system size ($L > 16$), the number of parameters has to be substantially lower than the Hilbert space dimension.

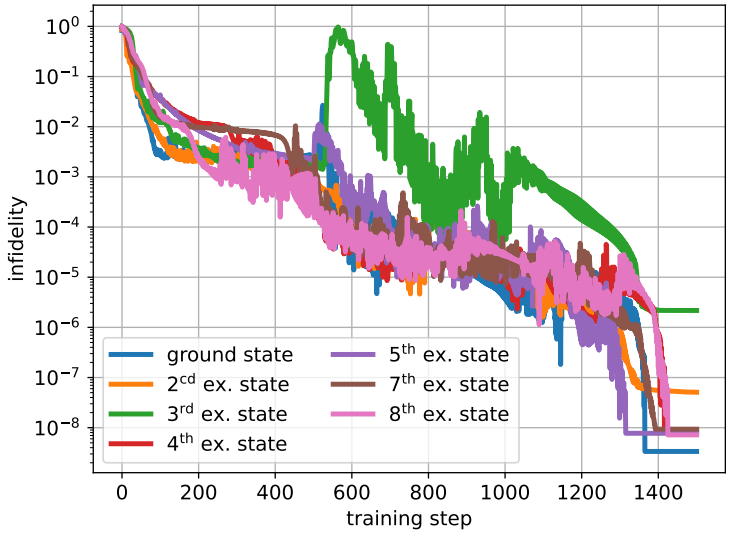

Figure 20.1: Infidelity optimization onto eigenstates at $J = 0.1$. Best convergence is for the ground state, a reason for this is that there is no phase to learn which simplifies the ansatz. For the excited states, we still see a good convergence down to infidelities of 10^{-6}. At training step 500, we switch to a SR-modified infidelity optimization improving the training (sometimes not immediately, see the green data for the 3rd excited state).

descent and a modified SR-inspired gradient descent optimization based on [215].

Figure 20.2 shows that the energies obtained from the adiabatic transport follow the eigenstate energies obtained by exact diagonalization closely in most times. A further indicator of successful adiabatic transport is the relative variance which increases slowly and stays below $10^{-3} - 10^{-4}$. Comparing the energy variance and energy curves in Fig. 20.2 between the 3rd and 4th eigenstate, the non-zero critical threshold of the relative variance looks to be around 10^{-3} before the energy deviates significantly.

There is an exception for the 4th excited state. We note in this case that a

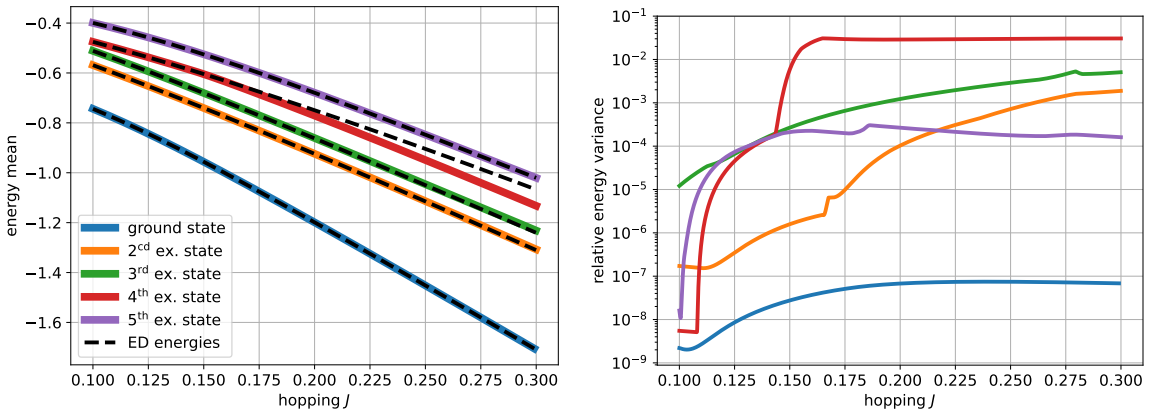

Figure 20.2: Proof of concept for the adiabatic transport in the Bose-Hubbard chain for $L = 6$ and $N = 3$. Only the fourth excited state (red solid line) shows a larger divergence from the exact diagonalization energies (dashed lines) in the left panel. Its point of failure is marked by the sudden increase in the energy variance (red line) in the right panel. All other energy variances are lower indicating a good eigenstate approximation throughout the adiabatic transport from $J = 0.1$ to 0.3.

small infidelity is not necessary for the method to succeed. Even though we reach an initial infidelity of 10^{-8} for the NQS, at $J \approx 0.14$ the adiabatic transport of the NQS significantly deviates from the eigenstate visible by the rapid increase in the energy variance of the NQS in the right panel of Fig. 20.2. This fourth excited state together with the first and sixth excited states (whose simulations have not finished) needs further investigation beyond convergence checks.

The case of an avoided crossing we have in Fig. 20.3, here the 7^{th} and 8^{th} excited eigenstates undergo this phenomena at roughly $J \approx 0.175$. For the adiabatic transport data, one sees the energy variance (right panel of Fig. 20.3) sharply increasing like in the schematics of Fig. 17.2. It demonstrates our idea of using adiabatic transport as a realizable indicator for the avoided-crossing phenomena. Surprisingly for the 7^{th} and especially the 8^{th} eigenstate, we observe dips and in the energy variances, when they come near the other eigenstate energy after the crossing. It resembles an diabatic switch of the NQS ansätze. Exactly this phenomenon and its possible connection to the Landau-Zener formula [216, 217] motivate us to proceed with the algorithm for future studies, where we want to reach larger system sizes and find avoided crossing at smaller hopping strength $J \sim 0.006$ being in the parameter regime modeling quantum computers transmon chips.

From the current negative results, e.g. the failure of the algorithm in the first, fourth and sixth excited state, we believe that the biggest challenge are the expressibility of the NQS and constructing the gradient in Eq. (17.15) faithfully. These open problems resemble the ones of the real-time evolution of the NQS [126, 200] and they inspire us for future research.

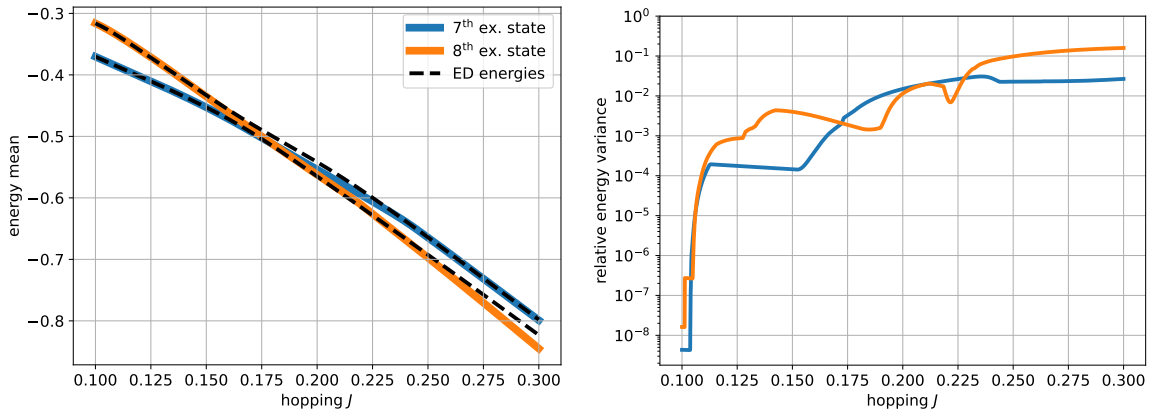

Figure 20.3: Avoided crossing between the 7^{th} and 8^{th} eigenstate in the proof of concept for the adiabatic transport in the Bose-Hubbard chain for $L = 6$ and $N = 3$. The adiabatic transport breaks down, i.e., the colorful lines diverge from the exact diagonalization results (dashed lines) in the left panel. This failure is mirrored in the sudden increase in the energy variances (right panel). However, we argue in the text that the avoided crossing can be still identified.

21. Summary – Neural Quantum States

Having access to the ground state of one hundred bosons on an up to one-hundred-sites lattice (Fig. 19.3), which has a Hilbert space dimension of up to $4.5 \cdot 10^{45}$, is (in our opinion) impressive. It shows that the physical information of a ground state can be compressed drastically to 12844 parameters which gives a compression factor of 10^{40}. Of course, the convergence measure, the relative variance of the energy, remains high at $\sim 10^{-2}$ for some simulations. Nonetheless, we are confident that with larger number of parameters, samples and tweaking the hyperparameters of the training the convergence can be improved below our quality threshold of 10^{-4} for a relative energy variance. Eventually, we want to improve the energy or entropy estimation via a zero-energy-variance extrapolation [218] over different network sizes.

More importantly and clearly missing, is a reference calculation of the ground state energy using tensor networks. They should give a good reference point for the one-dimensional ground states [219] and when using tensor-trees [220] also for two-dimensional ground states, maybe even including the brick structure from IBM [106, 107].

For the adiabatic transport, we demonstrated that the NQS can represent eigenstates and we can follow them in the system parameter space. The procedure is delicate and requires great care. Already in our proof-of-concept calculation, we stumble over a significant deviation for one eigenstate and the algorithm failed for the first excited state. Nevertheless, we observe an avoided crossing and we are certain that adiabatic transport will give us evidence of avoided crossings in larger systems of the Bose-Hubbard Hamiltonian. We are even confident that we can reach relevant parameters for quantum computers. Consequently, we are optimistic that adiabatic transport enables us to observe a clear signature of

chaos even at low energies in such systems. For that, we want to optimize the algorithm in general; in particular, we need to improve the Monte Carlo estimation of S_2 in Eq. (17.13). Then we will have access to larger system sizes. Like in the ground state estimation, we want to compare the results to implementations via tensor networks applied to excited states [221].

Overall with the advancement of the compute hardware, we are looking forward to what neural quantum states can achieve in the future. The performance of the hardware will certainly improve, but our larger concern is the expressibility of a given ansatz to approximate a quantum state in our opinion. Despite that the problem is not an issue for the ground-state optimization, since some steps in the training can be spurious without ruining the result afterward. In the case of adiabatic transport (and unitary time evolution), one spurious step makes the subsequent steps erroneous which cascades quickly and ruins the simulation. Therefore, we want to investigate especially the quality of adiabatic transport depending on the expressibility of the neural quantum state in the future. We see a starting point there is increasing the size of the network (via its depth/layers or width) or alternatively to change the architectures to more sophisticated network models.

IV. The Big Picture: Outlook

The journey presented in this thesis - from instabilities and chaos to structured insights into neural quantum states - has reached its end. We began by probing quantum chaos through Out-of-Time-Ordered Correlators (OTOCs), then explored the use of chaos as a resource for fast coherent targeting many-body occupied single-particle states, and finally uncovered chaotic hallmarks even in the ground states of large bosonic many-body systems.

Our primary workhorse, the Bose-Hubbard model, revealed a rich spectrum of phenomena and theoretical implications throughout this research thesis. Fascinatingly, while chaos emerges even in modest system sizes ($L > 2$), the integrable dimer ($L = 2$) shows a strikingly distinct OTOC dynamics compared to the generic chaotic case. Although seemingly a minor detail, the $2\lambda_s - \lambda_s$ transition illustrates that OTOCs can differentiate between integrability and chaos at early, pre-Ehrenfest timescales. Similar to other indicators mentioned in Fig. 1.1, we suspect that subtle differences in this regime - particularly in the semiclassical limit ($\hbar_{\text{eff}} \to 0$) - may decisively distinguish the two classes of systems or even spot their interim mixed regimes. Maybe even it can confirm our conjecture in such scenarios [1]. However, a central open question remains: how exactly does the transition from integrability to chaos unfold? We initiated this exploration through the kicked dimer in Sec. 6, providing a first attempt to quantify this crossover. Current collaborative work with Thomas Michel and Prof. Peter Schlagheck in Liège focuses on pushing OTOC numerics further, leveraging in-depth truncated Wigner approximation (TWA) studies to probe further into the semiclassical regime.

Another unresolved challenge concerns the semiclassical or thermodynamic limit in quantum systems, where thermal OTOCs and the bound on chaos [18] become relevant. For the double-well potential, our findings suggest that the regularization effect diminishes, and the unregularized OTOC appears to respect the chaos bound. However, whether this bound can be saturated in Bose-Hubbard models remains an open question. A promising hypothesis is that tuning the ground state near an unstable configuration - e.g. close to a bifurcation leading to a hyperbolic fixed point - could yield a finite quantum Lyapunov exponent at low temperatures. This tuning can be achieved not only via system parameters but also by enlarging the system size, which naturally connects to the framework of neural quantum states (NQS). Future advances in time-evolution techniques for NQS [200] may allow computation of low (zero-)temperature unregularized OTOCs for progressively larger systems. Two opposite scenarios are plausible for the thermodynamic limit of such large systems:

- Ground-state instabilities vanish as system size grows, erasing exponential OTOC growth.
- Instability emerges at scale when keeping the quantumness $\hbar_{\text{eff}}$ fixed, restoring exponential growth in the OTOC.

Which of these outcomes is true in the end remains to be seen. With rapid progress in AI and machine learning in the field of NQS [117, 119, 126], we are optimistic that such questions will become tractable in the near future, even so currently it is out of reach[1].

But our interests are broader, NQS-based approaches promise access not only to OTOCs but also to alternative, easier to accomplish, measures of chaos such as survival probabilities [222] etc. Especially compelling is the prospect of tracking adiabatic transport and identifying (avoided) level crossings, which may provide signatures of chaos in large systems, even in low-energy regimes beyond the ground state. Our current results on ground-state delocalization suggest this is plausible and we provided (small size) proof-of-concept simulations how to use adiabatic transport to observe avoided level crossings. We are keen on lifting the adiabatic transport method to the same and beyond the system sizes used for the ground-state simulations. Ultimately, we aim to extend these insights to excited-state regimes relevant for quantum computing architectures, such as those based on transmons [106, 107]. Demonstrating chaotic signatures in such systems could clarify whether quantum chaos poses a fundamental challenge for large-scale quantum computers in the future.

While not insurmountable, chaos likely represents a significant obstacle for ever larger quantum computers. But it is an obstacle that might even be exploited as a resource, as we demonstated for the Bose-Hubbard model and especially as controlling many-body quantum chaos remains an exciting frontier. Namely, there are several promising directions emerging for future investigations:

- Generalization to spin chains and fermionic systems, which introduces new challenges due to the absence of a faithful classical limit (absence of an $\hbar$-type of small parameter).
- Machine-learning-driven control, potentially replacing current heteroclinic trajectory identification methods. It is based on the idea that neural networks uncover hidden structures in the chaotic motion.
- Linking heteroclinic speed-ups to quantum speed limits [223], constrained by fundamental uncertainty principles. How do they interplay?
- Semiclassical interference-based control, guided by random matrix theory. A line of research we are currently pursuing with Prof. Steven Tomsovic and Lukas Beringer, in order to go beyond many-body occupied single-particle states.

[1] Although, as with commercially viable large scale quantum computers, "ten years away" may still apply.

Besides to theses theoretical extensions, we are interested in the actual deployment of the procedure in applications [89, 94, 173], in particular time crystals experiment [190, 198]. Here, the presented protocol needs to be adapted such that we find a suitable transport trajectory and also keep the experimental feasible control mechanisms in mind which can give restrictions not considered yet in our pure theoretical studies.

At the end we want also express some concerns: machine learning continues to reshape quantum research, offering new numerical tools yet raising the demand on energy consumption. While NQS approaches could eventually simulate OTOCs (Chap. I) and control Hamiltonians (Chap. II), their computational cost remains significant. Large ensemble calculations - such as those required to study many-body localization - amplify this burden, with millions of realizations often needed for statistical relevance. Such demands escalate the energy consumption and thereby raise environmental and financial concerns. Therefore, before embarking on large-scale numerical campaigns, a more deliberated analytical effort seems appropriated. Blindly running extensive simulations "into the blue" risks waste without clear theoretical motivation. We advocate for a strategy that balances analytical foresight with computational exploration to ensure meaningful progress without excessive costs. Nevertheless, we are excited what the future holds for simulating large quantum systems.

A. Classical Chaos and Instabilities

The purpose of this part is that we repeat some concepts of classical physics. In particular, the first section focuses on stability analysis of trajectories clarifying the difference between the (global) Lyapunov and (local) stability exponent. A second part derives the classical map for kicked Bose-Hubbard systems, where we concentrate on an explicit expression for the dimer.

To begin with, let us recall the established three criteria that a classical system has to fulfill to be chaotic [9, 10, 224]:

1. *Exponential sensitivity on the initial conditions*: small deviations grow exponentially with time to a certain extend[1]. The rate of exponential growth is the so-called classical *Lyapunov exponent* denoted throughout the thesis by λ_{L}.

2. *Mixing of the Hamiltonian flow*: any open region in phase space intersects another open region after a finite amount of time. It directly implies ergodicity of trajectories. Although, mixing is a stronger property than ergodicity, it is difficult to check. In practice therefore, ergodicity is used as a measure to numerically verify mixing for given trajectories.

3. *Dense set of periodic orbits*: near any point in the chaotic phase space, one can find periodic orbits infinitesimal close by. Unfortunately, their period can be arbitrary large. Therefore, this property is usually hard to verify and we do not use it in this thesis.

Chapter II utilizes the first and second properties of chaos as a theoretical framework to find efficient control trajectories connecting two phase-space cells. The usual initial exponential growth of the OTOC [18, 178] - discussed in Chap. I - is a direct hallmark of the first property of classical chaos. However, the OTOC is a quantum measure with no obvious connection to the exponential growth of initial deviations. In the App. B, we analyze the connection using the Wigner-Moyal expansion. In the first chapter of the thesis, we explain that the growth rate in the OTOC is not always the Lyapunov exponent associated to the classical exponential sensitivity in the above definition of chaos. In the following, we discuss the classical exponents further.

[1]The exponential growth can stop for a finite initial deviation, but in the limit of vanishing initial deviation the statement "deviations grow exponentially" is true.

A.1. Exponents

We elaborate on the differences between the local (short term) stability exponent and the global (long term) Lyapunov exponent.

A.1.1. (In)Stability Exponents

The aim is to investigate locally infinitesimal deviation $\Delta\vec{x}$ of a trajectory $\vec{x}$. Therefore, we linearize the equations of motion

$$\frac{\mathrm{d}}{\mathrm{d}t}\Delta\vec{x}(t) = \Sigma \left.\frac{\partial^2 H}{\partial\vec{x}\partial\vec{x}}\right|_{\vec{x}(t)} \Delta\vec{x}(t)\,, \tag{A.1}$$

where Σ is the symplectic matrix

$$\Sigma = \begin{pmatrix} 0 & \mathbb{1} \\ -\mathbb{1} & 0 \end{pmatrix}.$$

The above linearization assumes that the deviation $\Delta\vec{x}$ lies inside the quadratic approximation of the Hamiltonian H around a given trajectory $\vec{x}(t)$. We define the *stability exponent* λ_s by the maximal eigenvalue of the matrix $\Sigma \left.\frac{\partial^2 H}{\partial\vec{x}\partial\vec{x}}\right|_{\vec{x}(t)}$. It is a local property of a trajectory at $\vec{x}(t)$ at a given time t. If $\vec{x}(t) = \vec{x}_0$ is a fixed point, λ_s is equal to the long-time limit Lyapunov exponent λ_L, but only for the fixed point $\vec{x}_0$ itself. If the fixed point $\vec{x}_0$ is emerged in a chaotic region, there is a different Lyapunov exponent associated to the chaotic layer around the fixed point.

A.1.2. Lyapunov Exponents

Here, we repeat the concept of the (maximal) Lyapunov exponent

$$\lambda_\mathrm{L} = \lim_{\|\Delta\vec{x}_0\|\to 0} \lim_{t\to\infty} \frac{1}{t} \ln\!\left(\frac{\|\Delta\vec{x}(t)\|}{\|\Delta\vec{x}_0\|}\right).$$

Its calculation can be challenging, as in its formal definition two limits must be simultaneously carried out, i.e., the time limit to infinity and the initial deviation limit to zero [225, 226]. Both limits can lead to numerical issues [227].

A complete mathematical treatment of the generic time evolution of small deviations is obtained via the monodromy matrix $\overleftrightarrow{M}$ [9, 10, 180]

$$\Delta\vec{x}(t) = \overleftrightarrow{M}\,\Delta\vec{x}(0). \tag{A.2}$$

Note that this is the integrated version of Eq. (A.1) for general deviations $\Delta\vec{x}(t)$. Consequently, the differential equation for the monodromy matrix mirrors Eq. (A.1)

$$\frac{\mathrm{d}}{\mathrm{d}t}\overleftrightarrow{M}(t) = \Sigma\left.\frac{\partial^2 H}{\partial\vec{x}\partial\vec{x}}\right|_{\vec{x}(t)} \overleftrightarrow{M}(t) \tag{A.3}$$

yielding a connection to the (local) stability matrix $\Sigma\frac{\partial^2 H}{\partial\vec{x}\partial\vec{x}}$. The largest eigenvalue of $\overleftrightarrow{M}$ is the Lyapunov exponent via $\sim \exp(\lambda_{\mathrm{L}} t)$. As any generic deviation grows in leading order with the largest eigenvalue of the monodromy matrix, the two versions of the definition coincide. Generally, the logarithmic and time-rescaled eigenvalues of $\overleftrightarrow{M}$ form the so-called *Lyapunov spectrum* $\{\lambda_{\mathrm{L},i}\}$. A result of the symplectic structure of Hamiltonian systems is the pairing rule $\{\lambda_{\mathrm{L},i}, -\lambda_{\mathrm{L},i}\}$ [180]. It is a reflection of the Liouville theorem, which states that the phase-space volume is conserved under Hamiltonian flow. For more details about consequences originating from the symplectic structure, we refer to [147, 180].

Additionally, there is also the notion of the finite-time Lyapunov exponents [227]. Those usually become relevant in an intermediate time regime. In this work, we primarily focus on the short-time stability exponent and on the long-time Lyapunov exponent, while not studying dynamics at intermediate timescales (still beyond the Ehrenfest timescale).

A.2. Mean-Field System for the Kicked Dimer

We give a brief outline how to obtain the classical version of the discrete map for the kicked Bose-Hubbard dimer. We present two approaches, the first method is straightforward and generalizable to systems with more sites, while the second method uses the reduced coordinates (population imbalance and relative phase) and is applicable only to the dimer.

A.2.1. The First Approach – Direct Computation of the Map

Using the complex mean-field notation, the classical map can be obtained by two separate τ-time evolutions of the hopping and interaction part. Starting with a mean-field configuration $\vec{\phi}^n$, the two-step map $\vec{\phi}^n \to \vec{\psi}^{n+1} \to \vec{\phi}^{n+1}$ is given by

$$\begin{aligned} \psi_j^{n+1} &= e^{-iU\tau|\phi_j^n|^2}\phi_j^n \\ \vec{\phi}^{n+1} &= e^{iJ\tau\mathbf{T}}\vec{\psi}^{n+1} \end{aligned} \tag{A.1}$$

for a general number of sites L, where $\mathbf{T}$ is the next-neighbor hopping matrix given by $\mathbf{T}_{ij} = \delta_{i,j+1} + \delta_{i,j-1}$. Here, we implicitly assume periodic boundaries, i.e., the indices are taken modulo L. For the special case of the dimer $L = 2$, we can make Eq. (A.1) explicit. By diagonalizing

$$\mathbf{T} = \begin{pmatrix} 0 & 2 \\ 2 & 0 \end{pmatrix} = \frac{1}{\sqrt{2}}\begin{pmatrix} 1 & 1 \\ 1 & -1 \end{pmatrix}\begin{pmatrix} 2 & 0 \\ 0 & -2 \end{pmatrix}\frac{1}{\sqrt{2}}\begin{pmatrix} 1 & 1 \\ 1 & -1 \end{pmatrix}, \tag{A.2}$$

we obtain

$$\begin{aligned} e^{iJ\tau\mathbf{T}} &= \frac{1}{\sqrt{2}}\begin{pmatrix}1 & 1\\ 1 & -1\end{pmatrix}\begin{pmatrix}e^{i2J\tau} & 0\\ 0 & e^{-i2J\tau}\end{pmatrix}\frac{1}{\sqrt{2}}\begin{pmatrix}1 & 1\\ 1 & -1\end{pmatrix} \\ &= \begin{pmatrix}\cos(2\tau J) & -i\sin(2\tau J)\\ -i\sin(2\tau J) & \cos(2\tau J)\end{pmatrix}. \end{aligned} \tag{A.3}$$

Since $\mathbf{T}$ is hermitian, the exponential matrix $e^{iJ\tau\mathbf{T}}$ is unitary. With this, the mapping equation of the kicked mean-field dimer is

$$\begin{aligned} \begin{pmatrix}\phi_1^{n+1}\\ \phi_2^{n+1}\end{pmatrix} &= \begin{pmatrix}\cos(2\tau J) & -i\sin(2\tau J)\\ -i\sin(2\tau J) & \cos(2\tau J)\end{pmatrix}\begin{pmatrix}e^{-iU\tau|\phi_1^n|^2}\phi_1^n\\ e^{-iU\tau|\phi_2^n|^2}\phi_2^n\end{pmatrix} \\ &= \begin{pmatrix}\cos(2\tau J)e^{-iU\tau|\phi_1^n|^2}\phi_1^n - i\sin(2\tau J)e^{-iU\tau|\phi_2^n|^2}\phi_2^n\\ \cos(2\tau J)e^{-iU\tau|\phi_2^n|^2}\phi_2^n - i\sin(2\tau J)e^{-iU\tau|\phi_1^n|^2}\phi_1^n\end{pmatrix}, \end{aligned}$$

where we use the site mean-field representation. Utilizing the particle conservation, the dynamics should be reducible into an one-degree system. However, expressing the above expression into the reduced system is difficult such that we want to avoid this by the next approach. There, we work within the reduced system to derive an explicit expression for the mapping in the dimer.

A.2.2. Second Approach – Reduced Map for the Dimer

Our goal is to end up with an one-dimensional reduced description of the dimer like in Sec. 4.2.1. We write the classical mean-field equations directly using the reduced system notation which uses

$$\begin{aligned} N &= n_1 + n_2, \qquad \phi = \tfrac{1}{2}(\varphi_1 + \varphi_2), \\ n &= \tfrac{1}{2}(n_1 - n_2), \quad \varphi = \varphi_1 - \varphi_2 \end{aligned}$$

obtained from the classical mean-field limit in Sec. 4.2.1. The two mean-field entries $\psi_j = \sqrt{n_j}e^{i\varphi_j}$ are expressed in terms of phases φ_j and occupations n_j. The Hamiltonian takes the form

$$H(N,\phi,n,\varphi) = -2J\sqrt{N^2-4n^2}\cos\varphi + \frac{UN}{2}\Big(\frac{2n^2}{N} + \frac{N}{2}\Big).$$

We can reduce the dynamics to an one-dimensional system with a single conjugated pair ($z = 2n/N, \varphi = \varphi_1 - \varphi_2$) given by the population imbalance z and relative phase φ. With these coordinates, the equations of motion are the following two coupled real-valued ODEs

$$\begin{aligned} \dot{z} &= 4J\sqrt{1-z^2}\sin\varphi \\ \dot{\varphi} &= -4J\frac{z\cos\varphi}{\sqrt{1-z^2}} - U\,z. \end{aligned} \tag{A.4}$$

We utilize Eq. (A.4) in order to calculate the discrete time evolutions via two separate steps in Eq. (A.1).

Interaction Step

We start with the first time evolution step considering only interactions U and setting $J = 0$. Using Eq. (A.4), this gives

$$\begin{aligned}\tilde{z}_{n+1} &= z_n \\ \tilde{\varphi}_{n+1} &= \varphi_n - U\tau z_n,\end{aligned}$$

where we denote the intermediate step by $(\tilde{z}_{n+1}, \tilde{\varphi}_{n+1})$. The intermediate map is simple in this form, as the conjugated pair (z, φ) is partially decoupled.

Hopping step

We continue to propagate the intermediate pair $(\tilde{z}_{n+1}, \tilde{\varphi}_{n+1})$ a time step τ further in time, but this time only using hopping J and setting $U = 0$ in Eq. (A.4). Applying both steps results in the full propagation of the system by a period τ. Unfortunately, this case yields coupled equations of motion

$$\begin{aligned}\dot{z} &= +4J\sqrt{1-z^2}\sin\varphi \\ \dot{\varphi} &= -4J\frac{z\cos\varphi}{\sqrt{1-z^2}}\end{aligned}$$

needing some further manipulations. Therefore, we use that the energy is conserved[2]

$$\tilde{E} = -2J\sqrt{1-z^2}\cos\varphi = -2J\sqrt{1-\tilde{z}_{n+1}^2}\cos\tilde{\varphi}_{n+1}$$

and we rewrite the ODE for $\dot{z}$ and $\dot{\varphi}$ as

$$\begin{aligned}\dot{z} &= -2\tilde{E}\tan\varphi \\ \dot{\varphi} &= \frac{8J^2}{\tilde{E}} z\cos^2\varphi.\end{aligned}$$

Taking the second derivative of z and φ decouples the ODEs

$$\begin{aligned}\ddot{z} &= -2\tilde{E}\frac{1}{\cos^2\varphi}\dot{\varphi} = 16J^2 z \\ \ddot{\varphi} &= \frac{8J^2}{\tilde{E}}\Big(\cos^2\varphi\,\dot{z} - 2z\cos\varphi\,\sin\varphi\,\dot{\varphi}\Big) \\ &= 8J^2\Big(-2\cos\varphi\,\sin\varphi\;-\frac{16J^2}{\tilde{E}^2}z^2\cos^3\varphi\,\sin\varphi\Big) \\ &= 8J^2\Big(-2\cos\varphi\,\sin\varphi\;-\frac{16J^2}{\tilde{E}^2}\cos^3\varphi\,\sin\varphi \\ &\qquad + \frac{16J^2}{\tilde{E}^2}(1-z^2)\cos^3\varphi\,\sin\varphi\Big) \\ &= 8J^2\Big(2\cos\varphi\,\sin\varphi\;-\frac{16J^2}{\tilde{E}^2}\cos^3\varphi\,\sin\varphi\Big).\end{aligned}$$

[2]The energy is conserved in this timeframe of only hopping, it is not conserved in the whole time evolution.

The differential equation for z is solved by double integration in time and by inserting the initial condition (z_0, φ_0)

$$z(t) = z_0 \cos(4Jt) - \frac{2\tilde{E}\tan\varphi_0}{4J}\sin(4Jt),$$

i.e., we get

$$\begin{aligned}
z_{n+1} &= z(t)\Big|_{t=\tau, z_0=\tilde{z}_{n+1}, \varphi_0=\tilde{\varphi}_{n+1}} \\
&= z(t)\Big|_{t=\tau, z_0=z_n, \varphi_0=\varphi_n - U\tau z_n} \\
&= z_n\cos(4J\tau) + \sqrt{1-z_n^2}\sin(\varphi_n - U\tau z_n)\sin(4J\tau) \\
&= \sqrt{z_n^2 + (1-z_n^2)\sin^2(\varphi_n - U\tau z_n)} \\
&\quad \times \sin\Big(4J\tau + \operatorname{arctan2}(z_n, \sqrt{1-z_n^2}\sin(\varphi_n - U\tau z_n))\Big).
\end{aligned}$$

In contrast, the second-order differential equation for φ is inconvenient to solve directly. Luckily, we circumvent its calculation by using the energy conversation and the differential equation for $\dot{z}$ to find expressions for $\sin\varphi_{n+1}$ and $\cos\varphi_{n+1}$. Therefore, φ_{n+1} is accessible via the inverse function arctan2. First, the energy conservation gives us

$$\begin{aligned}
\cos\varphi_{n+1} &= \sqrt{\frac{1-\tilde{z}_{n+1}^2}{1-z_{n+1}^2}}\cos\tilde{\varphi}_{n+1} \\
&= \sqrt{\frac{1-z_n^2}{1-z_{n+1}^2}}\cos(\varphi_n - U\tau z_n).
\end{aligned}$$

Further, using the second equation of motion of $\dot{z}$ in Eq. (A.4) gives us

$$\begin{aligned}
\sin(\varphi_{n+1}) &= \frac{\dot{z}(\tau, z_0 = z_n, \varphi_0 = \varphi_n)}{4J\sqrt{1-z_{n+1}^2}} \\
&= \frac{-z_n\sin(4J\tau) + \sqrt{1-z_n^2}\sin(\varphi_n - U\tau z_n)\cos(4J\tau)}{\sqrt{1-z_{n+1}^2}}.
\end{aligned}$$

Hence, we express the relative phase via

$$\begin{aligned}
\varphi_{n+1} &= \operatorname{arctan2}(\cos\varphi_{n+1}, \sin\varphi_{n+1}) \\
&= \operatorname{arctan2}\left(\sqrt{\frac{1-z_n^2}{1-z_{n+1}^2}}\cos(\varphi_n - U\tau z_n),\right. \\
&\qquad \left.\frac{-z_n\sin(4J\tau) + \sqrt{1-z_n^2}\sin(\varphi_n - U\tau z_n)\cos(4J\tau)}{\sqrt{1-z_{n+1}^2}}\right) \\
&= \operatorname{arctan2}\left(\cos(\varphi_n - U\tau z_n), \frac{-z_n}{\sqrt{1-z_n^2}}\sin(4J\tau) + \sin(\varphi_n - U\tau z_n)\cos(4J\tau)\right),
\end{aligned}$$

where we use that arctan2 is scale invariant, meaning

$$\text{arctan2}(\alpha x, \alpha y) = \text{arctan2}(x, y)$$

for $\alpha > 0$.

Finally, we can express both (z_{n+1}, φ_{n+1}) via the previous time step such that we have the following mapping equations in the reduced system

$$\begin{aligned} z_{n+1} &= z_n \cos(4J\tau) + \sqrt{1 - z_n^2}\sin(\varphi_n - U\tau z_n)\sin(4J\tau), \\ \varphi_{n+1} &= \text{arctan2}\Big(\cos(\varphi_n - U\tau z_n), \frac{-z_n}{\sqrt{1 - z_n^2}}\sin(4J\tau) + \sin(\varphi_n - U\tau z_n)\cos(4J\tau)\Big). \end{aligned} \tag{A.5}$$

Their implementation is straightforward, since they are explicit and only involve standard functions.

An important remark is that we can achieve $z_{n+1} = z_n$ and $\varphi_{n+1} = \varphi_n - U\tau z_n$ if the condition $4J\tau = k\pi$ for $k \in \mathrm{Z}$ is met. We have integrable motion at these "resonances". As a consequence, we have windows of integrable dynamics along the discrete points $\tau_k = \frac{k\pi}{4J}$. In the case of Fig. 6.2, we see indications of bands in the heat-map. There, we investigate the dimer at the hopping $J = 0.218$ such that the first resonance is located at $\tau_{k=1} = \frac{\pi}{0.872} \approx 3.578$ which is clearly evident from the vanishing stability and Lyapunov exponents in Fig. 6.3 around $\tau_{k=1}$.

B. Wigner-Moyal expansion

In this part of the appendix, we shortly outline how to obtain Eq. (3.3) via a Wigner-Moyal expansion. We refer to [175, 228, 229] for an introduction of the phase-space formalism. We start with the exact phase-space expression for the expectation value of a general operator $\hat{O}$ given in the phase-space representation by

$$\langle \hat{O} \rangle = \mathrm{tr}\{\hat{\rho}\,\hat{O}\} = \iint_{\mathrm{PS}} \mathrm{d}^L q\, \mathrm{d}^L p\; W_\rho(\vec{q},\vec{p}) O_{\mathrm{W}}(\vec{q},\vec{p}),$$

where W_ρ is the Wigner function of a state described by its density operator $\hat{\rho}$, and O_{W} is the Wigner-Weyl symbol of the operator $\hat{O}$. Further, the integral $\iint_{\mathrm{PS}}$ goes over the accessible phase space (PS). Note here that O_{W} is a function, not an operator, i.e., $O_{\mathrm{W}}(\vec{q},\vec{p})$ is a complex number.

To proceed, we also need the Wigner-Weyl symbol of a product of operators $\hat{A}$ and $\hat{B}$, this product is given by the so-called star product of the corresponding Wigner-Weyl symbols as

$$\big[\hat{A}\hat{B}\big]_{\mathrm{W}}(\vec{q},\vec{p}) = A_{\mathrm{W}}(\vec{q},\vec{p}) \star B_{\mathrm{W}}(\vec{q},\vec{p}),$$

where the star product is an abbreviation for

$$\big[\hat{A}\hat{B}\big]_{\mathrm{W}}(\vec{q},\vec{p}) = A_{\mathrm{W}}(\vec{q},\vec{p}) \exp\Big\{\frac{i\hbar_{\mathrm{eff}}}{2}(\overleftarrow{\nabla}_{\vec{p}}\cdot\overrightarrow{\nabla}_{\vec{q}} - \overleftarrow{\nabla}_{\vec{q}}\cdot\overrightarrow{\nabla}_{\vec{p}})\Big\} B_{\mathrm{W}}(\vec{q},\vec{p}).$$

It can be expanded in powers of $\hbar_{\mathrm{eff}}$ as

$$\big[\hat{A}\hat{B}\big]_{\mathrm{W}}(\vec{q},\vec{p}) = A_{\mathrm{W}}(\vec{q},\vec{p}) B_{\mathrm{W}}(\vec{q},\vec{p}) + \frac{i\hbar_{\mathrm{eff}}}{2}\big\{A_{\mathrm{W}}(\vec{q},\vec{p}), B_{\mathrm{W}}(\vec{q},\vec{p})\big\} + O(\hbar_{\mathrm{eff}}^2). \tag{B.1}$$

B.1. Out-of-Time-Ordered Correlator

With Eq. (B.1) at hand, we apply the expression to Eq. (3.1) leading to the phase-space formulation of the OTOC

$$C(t) = \iint_{\mathrm{PS}} \mathrm{d}^L q\, \mathrm{d}^L p\; W_\rho(\vec{q},\vec{p}) \big[[\hat{A}(t),\hat{B}]\big]_{\mathrm{W}}(\vec{q},\vec{p}) \star \big[[\hat{A}(t),\hat{B}]\big]_{\mathrm{W}}(\vec{q},\vec{p}),$$

which up to this point is exact. We want to evaluate the OTOC up to the leading order in $\hbar_{\mathrm{eff}}$. We therefore expand the two star products inside the commutator $\big[[\hat{A}(t),\hat{B}]\big]_{\mathrm{W}}$ up to its first non-vanishing order in $\hbar_{\mathrm{eff}}$

$$\big[[\hat{A}(t),\hat{B}]\big]_{\mathrm{W}} = i\hbar_{\mathrm{eff}}\big\{[\hat{A}(t)]_{\mathrm{W}}(\vec{q},\vec{p}), B_{\mathrm{W}}(\vec{q},\vec{p})\big\} + O(\hbar_{\mathrm{eff}}^2).$$

Next we consider the $\hbar_{\text{eff}}$-expansion of the time-evolved operator $\left[\hat{A}(t)\right]_{\text{W}}$. It can be derived from expanding the Heisenberg equation of motion

$$\begin{aligned}\frac{\mathrm{d}}{\mathrm{d}t}\left[\hat{A}(t)\right]_{\text{W}}(\vec{q},\vec{p}) &= -\frac{i}{\hbar_{\text{eff}}}\left[\left[\hat{A}(t),\hat{H}\right]\right]_{\text{W}}(\vec{q},\vec{p}) + \left[\frac{\partial A}{\partial t}\right]_{\text{W}}(\vec{q},\vec{p}) \\ &= \left\{A_{\text{W}}(\vec{q},\vec{p}), H_{\text{W}}(\vec{q},\vec{p})\right\} + \frac{\partial A_{\text{W}}}{\partial t}(\vec{q},\vec{p}) + O(\hbar_{\text{eff}})\,, \end{aligned} \tag{B.1}$$

where the time evolution of the Wigner-Weyl symbol of the operator $\hat{A}$ (assuming no explicit time dependence) is given by integrating Eq. (B.1)

$$\begin{aligned}[\hat{A}(t)]_{\text{W}}(\vec{q},\vec{p}) =& A_{\text{W}}(\vec{q}(\vec{q},\vec{p},t),\vec{p}(\vec{q},\vec{p},t)) + O(\hbar_{\text{eff}}), \\ =& A_{\text{W}}(\vec{q},\vec{p},t) + O(\hbar_{\text{eff}}),\end{aligned}$$

where $\vec{q}(\vec{q},\vec{p},t)$ and $\vec{p}(\vec{q},\vec{p},t)$ are the classical evolved phase-space points. To shorten notation, we write $A_{\text{W}}(\vec{q},\vec{p},t) = A_{\text{W}}(\vec{q}(\vec{q},\vec{p},t),\vec{p}(\vec{q},\vec{p},t))$. The above calculation verifies that - in leading order of $\hbar_{\text{eff}}$ - the quantum and classical equations of motion agree, since the quantum commutator reduces to the classical Poisson bracket. Putting all together, we arrive to the leading-order expression of the OTOC

$$\begin{aligned}C(t) &= \hbar_{\text{eff}}^2 \iint_{\text{PS}} \mathrm{d}^L q_0\, \mathrm{d}^L p_0\, W_\rho(\vec{q}_0,\vec{p}_0)\left|\left\{A_{\text{W}}(\vec{q}_0,\vec{p}_0,t), B_{\text{W}}(\vec{q}_0,\vec{p}_0)\right\}\right|^2 + O(\hbar_{\text{eff}}^3) \\ &= \hbar_{\text{eff}}^2 \langle W_\rho(\vec{q}_0,\vec{p}_0)\left|\left\{A_{\text{W}}(\vec{q}_0,\vec{p}_0,t), B_{\text{W}}(\vec{q}_0,\vec{p}_0)\right\}\right|^2\rangle_{\text{PS}} + O(\hbar_{\text{eff}}^3),\end{aligned} \tag{B.2}$$

where we use the abbreviation $\langle . \rangle_{\text{PS}}$ for the phase-space integral. The Eq. (B.2) is the Truncated-Wigner Approximation (TWA) of the OTOC in its general form as stated in Eq. (3.3) of the main text.

B.2. Time Evolution via the Wigner Function

In Sec. 10.3, we present the Truncated Wigner Approximation (TWA) of the time evolution for the Wigner function in Eq. (10.13). This expression is simply derived by inserting the Wigner function into Eq. (B.1) and the fact that a state has no explicit time dependence. Henceforth with Eq. (10.13), we express the time evolution of an expectation value of a static operator $\hat{O}$

$$\langle \hat{O}(t)\rangle = \iint_{\text{PS}} \mathrm{d}^L q_0\, \mathrm{d}^L p_0\; W_\rho(\vec{q}_0,\vec{p}_0,t) O_{\text{W}}(\vec{q}_0,\vec{p}_0),$$

where $W_\rho(\vec{q},\vec{p},t)$ is the time-evolved Wigner function. Alternatively, the time evolution is put into the operator via the Heisenberg time evolution, i.e., $\hat{O}(t) = \hat{U}^\dagger(t)\hat{O}\hat{U}(t)$[1]. It is numerically more convenient and also more flexible to continue with the Heisenberg time evolution and expand it up to the leading order of $\hbar_{\text{eff}}$

$$\langle \hat{O}(t)\rangle = \iint_{\text{PS}} \mathrm{d}^L q_0\, \mathrm{d}^L p_0\; W_\rho(\vec{q}_0,\vec{p}_0) O_{\text{W}}(\vec{q}(\vec{q}_0,\vec{p}_0,t),\vec{p}(\vec{q}(\vec{q}_0,\vec{p}_0,t)) + O(\hbar_{\text{eff}}),$$

[1]This excludes the OTOC. Therefore, we have the previous section explicitly focusing on the OTOC.

which is the usual TWA expression for expectation values [104]. The general numerical procedure to calculate the TWA can be summarized in the following steps: first we obtain a set of initial configurations $\{(\vec{q}_0, \vec{p}_0)\}$ by Monte Carlo sampling of the initial Wigner function; second we propagate the configurations in time which gives us the set of pairs $\{(\vec{q}(\vec{q}_0, \vec{p}_0, t), \vec{p}(\vec{q}_0, \vec{p}_0, t))\}$. Finally we evaluate the classical expression of the operator $O_{\mathrm{W}}(\vec{q}(\vec{q}_0, \vec{p}_0, t), \vec{p}(\vec{q}(\vec{q}_0, \vec{p}_0, t))$ and average over the propagated configuration set.

If we are just interested in the time-evolved Wigner function, we create a histogram from the time-evolved configurations $\{(\vec{q}(\vec{q}_0, \vec{p}_0, t), \vec{p}(\vec{q}_0, \vec{p}_0, t))\}$ to get the propagated Wigner distribution. For example in Figs. 11.1 and 12.3 from Chap. II, we show the time snapshots of the Wigner function calculated by the TWA.

C. Localized Quantum States

Let us discuss quantum states which are localized around a single point in the classical phase space. Prime examples are coherent states and also (number-) projected coherent states. We only view bosonic many-body systems and do not discuss spin or fermion coherent states.

C.1. Coherent States

A coherent state is defined as the eigenstate of all annihilation operators $\hat{a}_j$ in a system. It can be explicitly expressed by

$$|\vec{\phi}\rangle_{\mathrm{coh}} = e^{-\|\vec{\phi}\|^2/2} e^{\vec{\phi}\cdot\hat{\vec{a}}^\dagger} |0\rangle \,, \tag{C.1}$$

where the eigenvalue equation is

$$\hat{a}_j |\vec{\phi}\rangle_{\mathrm{coh}} = \phi_j |\vec{\phi}\rangle_{\mathrm{coh}}. \tag{C.2}$$

Using Eq. (C.1), we verify that a coherent state is normalized

$$\begin{aligned} {}_{\mathrm{coh}}\langle\vec{\phi}|\vec{\phi}\rangle_{\mathrm{coh}} &= e^{-\|\vec{\phi}\|^2/2} \langle 0| e^{\vec{\phi}\cdot\hat{\vec{a}}} |\vec{\phi}\rangle_{\mathrm{coh}} \\ &= e^{\|\vec{\phi}\|^2/2} \langle 0|\vec{\phi}\rangle_{\mathrm{coh}} \\ &= e^{\|\vec{\phi}\|^2/2} \langle 0| e^{-\|\vec{\phi}\|^2/2} e^{\vec{\phi}\cdot\hat{\vec{a}}^\dagger} |0\rangle \\ &= 1. \end{aligned}$$

In the main text, we use the convention that the particle number of the coherent state coincides with the squared norm $N_{\mathrm{coh}} = \|\vec{\phi}\|^2$ of the complex mean field $\vec{\phi}$.

C.1.1. Quadrature Representation (Position and Momentum)

For bosonic many-body systems, we define the hermitian quadrature operators (which are the position and momentum operators in the case of the harmonic oscillator) as

$$\begin{aligned} \hat{q}_j &= \sqrt{\hbar_{\mathrm{eff}}}\, \frac{\hat{a}_j + \hat{a}_j^\dagger}{\sqrt{2}} \\ \hat{p}_j &= \sqrt{\hbar_{\mathrm{eff}}}\, \frac{\hat{a}_j - \hat{a}_j^\dagger}{i\sqrt{2}}. \end{aligned} \tag{C.3}$$

Therefore, the annihilation operator can be written by

$$\hat{a}_j = \frac{\hat{q}_j + i\hat{p}_j}{\sqrt{2\hbar_{\text{eff}}}}. \tag{C.4}$$

Further, the position representation of the coherent state is given by the following product over the system size

$$\langle \vec{q} | \vec{\phi} \rangle_{\text{coh}} = \prod_{j=1}^{L} \langle q_j | \phi_j \rangle_{\text{coh}}, \tag{C.5}$$

where the contribution of each site j is

$$\langle q_j | \phi_j \rangle_{\text{coh}} = e^{-|\phi_j|^2/2} \sum_{n=0}^{\infty} \frac{\phi_j^n}{\sqrt{n!}} \langle q_j | n \rangle \, .$$

The individual position representations of $\langle q_j | n \rangle$ are given by Hermite functions (eigenfunctions of the harmonic oscillator), which after carrying out the sum yields a Gaussian function [230]

$$\langle q_j | \phi_j \rangle_{\text{coh}} = \left(\frac{1}{\pi \hbar_{\text{eff}}} \right)^{1/4} e^{-|\phi_j|^2/2 + \phi_j^2/2 - (q_j/\sqrt{2\hbar_{\text{eff}}} - \phi_j)^2}.$$

We therefore express the multidimensional coherent state wave-function as

$$\langle \vec{q} | \vec{\phi} \rangle_{\text{coh}} = \left(\frac{1}{\pi \hbar_{\text{eff}}} \right)^{L/4} e^{-\frac{(\vec{q} - \vec{q}_\phi)^2}{2\hbar_{\text{eff}}} + i \frac{\vec{p}_\phi \cdot (\vec{q} - \vec{q}_\phi)}{\hbar_{\text{eff}}} + i \frac{\vec{p}_\phi \cdot \vec{q}_\phi}{2\hbar_{\text{eff}}}}, \tag{C.6}$$

where we write the complex mean-field as real and imaginary parts $\vec{\phi} = \frac{\vec{q}_\phi + i\vec{p}_\phi}{\sqrt{2\hbar_{\text{eff}}}}$.

Note that - in Chap. II - we have $\|\vec{\phi}\|^2 = N_{\text{coh}}$, but instead of $\|\vec{q}\|^2 + \|\vec{p}\|^2 = 2$ we use $\|\vec{q}\|^2 + \|\vec{p}\|^2 = 2L$. Thereby, we set the effective Planck constant to

$$\hbar_{\text{eff}} = \frac{L}{N_{\text{coh}}}.$$

C.1.2. Wigner Function of a Coherent State

Here, we calculate the Wigner function of a coherent state. First, we take the definition of the Wigner function in Eq. (3.5) and apply it to the case of a pure coherent state

$$W_{\vec{\phi}}(\vec{q}, \vec{p}) = \left(\frac{1}{\pi \hbar_{\text{eff}}} \right)^{L} \int_{-\infty}^{\infty} \mathrm{d}^L y \, \langle \vec{q} - \vec{y} | \vec{\phi} \rangle_{\text{coh coh}} \langle \vec{\phi} \mid \vec{q} + \vec{y} \rangle \, e^{2i\vec{p} \cdot \vec{y}/\hbar_{\text{eff}}}.$$

The next step is to insert the position representation, Eq. (C.6), for the coherent state

$$W_{\vec{\phi}}(\vec{q},\vec{p}) = \left(\frac{1}{\pi\hbar_{\text{eff}}}\right)^{3L/2} \int_{-\infty}^{\infty} \mathrm{d}^L y \; e^{-\frac{(\vec{q}-\vec{y}-\vec{q}_\phi)^2}{2\hbar_{\text{eff}}}+i\frac{\vec{p}_\phi\cdot(\vec{q}-\vec{y}-\vec{q}_\phi)}{\hbar_{\text{eff}}}+i\frac{\vec{p}_\phi\cdot\vec{q}_\phi}{2\hbar_{\text{eff}}}} \\ \times e^{-\frac{(\vec{q}+\vec{y}-\vec{q}_\phi)^2}{2\hbar_{\text{eff}}}-i\frac{\vec{p}_\phi\cdot(\vec{q}+\vec{y}-\vec{q}_\phi)}{\hbar_{\text{eff}}}-i\frac{\vec{p}_\phi\cdot\vec{q}_\phi}{2\hbar_{\text{eff}}}} e^{2i\vec{p}\cdot\vec{y}/\hbar_{\text{eff}}}.$$

In order to get to the textbook version [104], there are several manipulations needed. Starting with a simplification of the expression

$$W_{\vec{\phi}}(\vec{q},\vec{p}) = \left(\frac{1}{\pi\hbar_{\text{eff}}}\right)^{3L/2} \int_{-\infty}^{\infty} \mathrm{d}^L y e^{-\frac{(\vec{q}-\vec{y}-\vec{q}_\phi)^2}{2\hbar_{\text{eff}}}-i\frac{\vec{p}_\phi\cdot\vec{y}}{\hbar_{\text{eff}}}} e^{-\frac{(\vec{q}+\vec{y}-\vec{q}_\phi)^2}{2\hbar_{\text{eff}}}-i\frac{\vec{p}_\phi\cdot\vec{y}}{\hbar_{\text{eff}}}} e^{2i\vec{p}\cdot\vec{y}/\hbar_{\text{eff}}} \\ = \left(\frac{1}{\pi\hbar_{\text{eff}}}\right)^{3L/2} \int_{-\infty}^{\infty} \mathrm{d}^L y e^{-\frac{(\vec{q}-\vec{q}_\phi)^2}{\hbar_{\text{eff}}}} e^{-\frac{\vec{y}^2}{\hbar_{\text{eff}}}+2i\frac{(\vec{p}_\phi-\vec{p})\cdot\vec{y}}{\hbar_{\text{eff}}}},$$

we do a quadratic completion

$$-\frac{\vec{y}^2}{\hbar_{\text{eff}}}+2i\frac{(\vec{p}_\phi-\vec{p})\cdot\vec{y}}{\hbar_{\text{eff}}} = -\frac{\vec{y}^2}{\hbar_{\text{eff}}}+2i\frac{(\vec{p}_\phi-\vec{p})\cdot\vec{y}}{\hbar_{\text{eff}}}+\frac{(\vec{p}_\phi-\vec{p})^2}{\hbar_{\text{eff}}}-\frac{(\vec{p}_\phi-\vec{p})^2}{\hbar_{\text{eff}}}$$

to arrive at

$$W_{\vec{\phi}}(\vec{q},\vec{p}) = \left(\frac{1}{\pi\hbar_{\text{eff}}}\right)^{3L/2} e^{-\frac{(\vec{q}-\vec{q}_\phi)^2}{\hbar_{\text{eff}}}-\frac{(\vec{p}_\phi-\vec{p})^2}{\hbar_{\text{eff}}}} \times \int_{-\infty}^{\infty} \mathrm{d}^L y \; e^{-\frac{(\vec{y}+i(\vec{p}_\phi-\vec{p}))^2}{\hbar_{\text{eff}}}}.$$

The final integral is a standard Gaussian integral and gives a factor $(\pi\hbar_{\text{eff}})^{L/2}$. Finally, we arrive at

$$W_{\vec{\phi}}(\vec{q},\vec{p}) = \left(\frac{1}{\pi\hbar_{\text{eff}}}\right)^{L} e^{-\frac{(\vec{q}-\vec{q}_\phi)^2}{\hbar_{\text{eff}}}-\frac{(\vec{p}_\phi-\vec{p})^2}{\hbar_{\text{eff}}}}, \tag{C.7}$$

which is the Wigner function of a coherent state we use in Eq. (10.10). It is Gaussian in every phase-space dimension with a standard deviation $\sigma = \sqrt{\hbar_{\text{eff}}/2}$.

C.2. Number-Projected Coherent States

Our goal is to show the connection between the number-projected coherent and coherent state. We use projected states due to its restriction to one fixed total-particle-number sector in most of our calculations shown in Chaps. I and II. For a general complex mean-field (no normalization condition on $\vec{\phi}$ required), a projected coherent state is defined by

$$|\vec{\phi}\rangle^N_{\text{proj}} = \frac{1}{\sqrt{\|\vec{\phi}\|^{2N}N!}}\left(\vec{\phi}\cdot\hat{\vec{a}}^\dagger\right)^N|0\rangle\,. \tag{C.1}$$

We can rewrite the coherent state in terms of the projected coherent state

$$\begin{aligned}
|\vec{\phi}\rangle_{\text{coh}} &= e^{-\|\vec{\phi}\|^2/2} e^{\vec{\phi}\cdot\hat{\vec{a}}^\dagger} |0\rangle \\
&= e^{-\|\vec{\phi}\|^2/2} \sum_{N=0}^{\infty} \frac{\left(\vec{\phi}\cdot\hat{\vec{a}}^\dagger\right)^N}{N!} |0\rangle \\
&= e^{-\|\vec{\phi}\|^2/2} \sum_{N=0}^{\infty} \frac{\sqrt{\|\vec{\phi}\|^{2N}}}{\sqrt{N!}} \frac{\left(\vec{\phi}\cdot\hat{\vec{a}}^\dagger\right)^N}{\sqrt{\|\vec{\phi}\|^{2N} N!}} |0\rangle \\
&= e^{-\|\vec{\phi}\|^2/2} \sum_{N=0}^{\infty} \frac{\sqrt{\|\vec{\phi}\|^{2N}}}{\sqrt{N!}} |\vec{\phi}\rangle^N_{\text{proj}} \\
&= \sum_{N=0}^{\infty} W_{N,\vec{\phi}} |\vec{\phi}\rangle^N_{\text{proj}} ,
\end{aligned}$$

where we define the weights by

$$\begin{aligned}
W_{N,\vec{\phi}} &= e^{-\|\vec{\phi}\|^2/2} \frac{\sqrt{\|\vec{\phi}\|^{2N}}}{\sqrt{N!}} \\
&= e^{-N_{\text{coh}}/2} \sqrt{\frac{(N_{\text{coh}})^N}{N!}}.
\end{aligned}$$

At this point, we reinstall the convention $N_{\text{coh}} = \|\vec{\phi}\|^2$ fixing the normalization of the complex mean-field. This explains the name "projected", since projecting a coherent state to a fixed particle number gives the projected coherent state. Furthermore, we analyze the weights and find that the largest contributions to the coherent state come from the project coherent states with particle numbers close to N_{coh} [174]. From this subdivision, we can calculate the overlap between two coherent states as

$$\begin{aligned}
{}_{\text{coh}}\langle\vec{\psi}|\vec{\phi}\rangle_{\text{coh}} &= e^{-||\vec{\psi}||/2 + ||\vec{\phi}||^2/2 - \vec{\psi}\cdot\vec{\phi}} \\
&= \sum_{N=0}^{\infty} W_{N,\vec{\psi}} W_{N,\vec{\phi}} \, {}^N_{\text{proj}}\langle\vec{\psi}|\vec{\phi}\rangle^N_{\text{proj}} \\
&= \sum_{N=0}^{\infty} e^{-N_{\text{coh}}} \frac{N_{\text{coh}}^N}{N!} \, {}^N_{\text{proj}}\langle\vec{\psi}|\vec{\phi}\rangle^N_{\text{proj}} \\
&= \sum_{N=0}^{\infty} e^{-N_{\text{coh}}} \frac{(\vec{\psi}\cdot\vec{\phi})^N}{N!},
\end{aligned}$$

which reduces to the weighted sum of overlaps of the individual projected states given by [174]

$${}^N_{\text{proj}}\langle\vec{\psi}|\vec{\phi}\rangle^N_{\text{proj}} = \frac{(\vec{\psi}\cdot\vec{\phi})^N}{N_{\text{coh}}^N}$$

assuming that both projected states have $N_{\text{coh}} = \|\vec{\phi}\|^2 = \|\vec{\psi}\|^2$.

Wigner Function of a Projected Coherent State

The Wigner function of a projected coherent state (if $\vec{\phi} \in \mathbb{R}^L$) is given by

$$W_{\vec{\phi}}^{\text{proj}}(\vec{q},\vec{p}) = \frac{1}{(\pi\hbar_{\text{eff}})^{L-1}} e^{-(\vec{q}_\perp^2+\vec{p}_\perp^2)/\hbar_{\text{eff}}} W_N(q_{\vec{\phi}}, p_{\vec{\phi}}), \tag{C.2}$$

where the derivation can be found in [174]. Thereby, $q_{\vec{\phi}}$, $p_{\vec{\phi}}$, $\vec{q}_\perp$ and $\vec{p}_\perp$ are the coordinates of the direction given by the vector $\vec{\phi}$ and of the perpendicular directions[1]. In these coordinates, the Wigner function separates into a Gaussian at the origin along the perpendicular directions and the Wigner function of a Fock state which given by

$$W_N(q,p) = \frac{(-1)^N}{\pi\hbar_{\text{eff}}} e^{-(q^2+p^2)/\hbar_{\text{eff}}} L_N(2(q^2+p^2)/\hbar_{\text{eff}})$$

with $L_N(x)$ being the N-th Laguerre polynomial. It should be possible to extend the expression Eq. (C.2) to complex $\vec{\phi}$, since we can always make a suitable coordinate transformation to end up $\vec{\phi}$ being real. For our applications, this is not of relevance, but should be checked if one uses it.

[1]The direction $(q_{\vec{\phi}}, p_{\vec{\phi}})$ are defined by the complex directions $\text{Re}\{\vec{\phi}\}/||\,\text{Re}\{\vec{\phi}\}||$ and $\text{Im}\{\vec{\phi}\}/||\,\text{Im}\{\vec{\phi}\}||$

D. Regularization in Harmonic Oscillator

We are present the details how to compute the OTOC with and without regularization for the harmonic oscillator. Let us repeat the standard harmonic oscillator Hamiltonian

$$\hat{H} \;=\; \frac{1}{2m}\hat{p}^2 + \frac{m\omega^2}{2}\hat{x}^2 \;=\; \hbar\omega\Big(\hat{a}^\dagger\hat{a} + \frac{1}{2}\Big),$$

where on the right hand side we already write the Hamiltonian in terms of the creation and annihilation operators

$$\hat{a} = \sqrt{\frac{m\omega}{2\hbar}}\Big(\hat{x} + \frac{i}{m\omega}\hat{p}\Big), \quad \hat{a}^\dagger = \sqrt{\frac{m\omega}{2\hbar}}\Big(\hat{x} - \frac{i}{m\omega}\hat{p}\Big)$$

or we express the position and momentum as

$$\hat{x} = \sqrt{\frac{\hbar}{2m\omega}}\big(\hat{a}^\dagger + \hat{a}\big), \quad \hat{p} = \sqrt{\frac{\hbar m\omega}{2}}\big(\hat{a}^\dagger - \hat{a}\big).$$

The time evolution in the Heisenberg picture can be calculated straightforwardly

$$\begin{aligned}\hat{a}(t) &= e^{-i\omega t}\hat{a}\\ \hat{a}^\dagger(t) &= e^{i\omega t}\hat{a}^\dagger\end{aligned}$$

such that the evolution of the position and momentum operators are

$$\begin{aligned}\hat{x}(t) &= \cos(\omega t)\hat{x} + \frac{\sin(\omega t)}{\omega m}\hat{p}\\ \hat{p}(t) &= \cos(\omega t)\hat{p} - m\omega\sin(\omega t)\hat{x},\end{aligned}$$

where we write $\hat{O} = \hat{O}(0) = \hat{O}_{\rm S}$ for the time-independent (Schrödinger) operators. Furthermore, the general thermal partition function is calculated by a summation over all eigenstates

$$\begin{aligned}Z(\beta) &= \mathrm{tr}\left\{e^{-\beta\hat{H}}\right\}\\ &= \sum_{n=0}^{\infty} e^{-\beta\hbar\omega(n+\frac{1}{2})}\\ &= \frac{e^{-\frac{\beta\hbar\omega}{2}}}{1-e^{-\beta\omega\hbar}}\\ &= \frac{1}{2}\sinh^{-1}\left(\frac{\beta\omega\hbar}{2}\right)\end{aligned}$$

such that we are ready to express the thermal OTOC.

We start with the unregularized correlators separating the whole calculation into the following steps:

- First, we observe

$$\mathrm{tr}\{\hat{a}^\dagger(t_1)^{k_1}\dots\hat{a}^\dagger(t_m)^{k_m}\hat{a}(s_1)^{l_1}\dots\hat{a}(s_n)^{l_n}\}\sim\delta_{\sum_{i=1}^m k_i,\sum_{j=1}^n l_j}$$

  for generic normal-ordered combinations of annihilation and creation operators at different times s_i, t_i. This is due to the fact that we need an equal amount of annihilation and creation operators in our trace for a non-vanishing result.

- In the occupation basis, the matrix representation of the annihilation and creation operators can be summarized by

$$\begin{aligned}
\left(\hat{a}(t)^k\right)_{n,m} &= \langle n|\,\hat{a}(t)^k\,|m\rangle \\
&= e^{-i\omega tk}\delta_{n,m-k}\sqrt{m\cdots(m-k+1)} \\
\left(\hat{a}^\dagger(t)^k\right)_{n,m} &= \langle n|\,\hat{a}^\dagger(t)^k\,|m\rangle \\
&= e^{+i\omega tk}\delta_{n,m+k}\sqrt{(m+1)\cdots(m+k+1)} \\
\left(\hat{a}(t_1)^k\hat{a}^\dagger(t_2)^l\right)_{n,m} &= \langle n|\,\hat{a}(t_1)^k\hat{a}^\dagger(t_2)^l\,|m\rangle \\
&= e^{-i\omega(t_2k-t_1l)}\delta_{n,m-k+l}\sqrt{(m+1)\cdots(m+l+1)} \\
&\quad\times\sqrt{(m+1+l-k)\cdots(m+l+1)}.
\end{aligned}$$

- Next, we express the usual expectation values of position and momentum for the canonical thermal ensemble $\hat{\rho}=\frac{1}{Z}e^{-\beta\hat{H}}$

$$\begin{aligned}
\langle\hat{x}(t)\rangle &= \sqrt{\frac{\hbar}{2m\omega}}\langle(\hat{a}^\dagger(t)+\hat{a}(t)\rangle \;=\; 0 \\
&= \langle\hat{x}(t)^{2k+1}\rangle \quad \text{for } k\in\mathbb{N}_0 \\
\langle\hat{p}(t)\rangle &= \sqrt{\frac{\hbar}{2m\omega}}\langle(\hat{a}^\dagger(t)+\hat{a}(t)\rangle \;=\; 0 \\
&= \langle\hat{p}(t)^{2k+1}\rangle \quad \text{for } k\in\mathbb{N}_0
\end{aligned}$$

  and we continue with the commutators

$$\begin{aligned}
\langle\big[\hat{x}(t),\hat{x}\big]\rangle_\beta &= \frac{\hbar i}{m\omega}\sin(\omega t) \\
\langle\Big|\big[\hat{x}(t),\hat{x}\big]\Big|^2\rangle_\beta &= \left(\frac{\hbar}{m\omega}\right)^2\sin^2(\omega t),
\end{aligned}$$

  which are temperature independent. We state the unregularized OTOC in Eq. (7.6) in the main text which purely oscillates without any temperature dependence.

We redo the above calculation steps using the regularized operators as defined in the main text in Eq. (7.1):

- The matrix representation of the annihilation and creation operators are summarized by

$$\begin{aligned}
\left(\hat{a}^{\eta,\mathrm{reg}}(t)\right)_{n,m} &= \langle n|\, \hat{a}^{\eta,\mathrm{reg}}(t)\, |m\rangle \\
&= e^{-i\omega t} e^{-\frac{\beta}{2\eta}\hbar\omega(n+m+1)} \delta_{n,m-1}\sqrt{m} \\
\left((\hat{a}^{\eta,\mathrm{reg}})^\dagger(t)\right)_{n,m} &= \langle n|\, (\hat{a}^{\eta,\mathrm{reg}})^\dagger(t)\, |m\rangle \\
&= e^{i\omega t} e^{-\frac{\beta}{2\eta}\hbar\omega(n+m+1)} \delta_{n,m+1}\sqrt{m+1} \\
\left((\hat{a}^{\eta,\mathrm{reg}})^\dagger(t_1)\hat{a}^{\eta,\mathrm{reg}}(t_2)\right)_{n,m} &= \langle n|\, (\hat{a}^{\eta,\mathrm{reg}})^\dagger(t_1)\hat{a}^{\eta,\mathrm{reg}}(t_2)\, |m\rangle \\
&= e^{i\omega(t_1-t_2)} e^{-\frac{2\beta}{\eta}\hbar\omega n} \delta_{n,m} n \\
\left(\hat{a}^{\eta,\mathrm{reg}}(t_2)(\hat{a}^{\eta,\mathrm{reg}})^\dagger(t_1)\right)_{n,m} &= \langle n|\, \hat{a}^{\eta,\mathrm{reg}}(t_2)(\hat{a}^{\eta,\mathrm{reg}}(t_1))^\dagger\, |m\rangle \\
&= e^{i\omega(t_1-t_2)} e^{-\frac{2\beta}{\eta}\hbar\omega(n+1)} \delta_{n,m}(n+1) \\
\left([(\hat{a}^{\eta,\mathrm{reg}})^\dagger(t_1), \hat{a}^{\eta,\mathrm{reg}}(t_2)]\right)_{n,m} &= e^{i\omega(t_1-t_2)} e^{-\frac{2\beta}{\eta}\hbar\omega n} \\
&\quad \times \Big(n - e^{-\frac{2\beta}{\eta}\hbar\omega}(n+1)\Big)\delta_{n,m} \\
\left([(\hat{x}^{\eta,\mathrm{reg}})^\dagger(t_1), \hat{x}^{\eta,\mathrm{reg}}(t_2)]\right)_{n,m} &= \frac{\hbar}{2m\omega}\Big\{\left([\hat{a}^{\eta,\mathrm{reg}}(t_1), (\hat{a}^{\eta,\mathrm{reg}}(t_2))^\dagger]\right)_{n,m} \\
&\quad + [(\hat{a}^{\eta,\mathrm{reg}})^\dagger(t_1), \hat{a}^{\eta,\mathrm{reg}}(t_2)]\Big\} \\
&= \frac{\hbar i}{m\omega}\sin(\omega(t_1-t_2)) e^{-\frac{2\beta}{\eta}\hbar\omega n} \\
&\quad \times \Big(n - e^{-\frac{2\beta}{\eta}\hbar\omega}(n+1)\Big)\delta_{n,m} \\
\left(\left|[(\hat{x}^{\eta,\mathrm{reg}})^\dagger(t_1), \hat{x}^{\eta,\mathrm{reg}}(t_2)]\right|^2\right)_{n,m} &= \left(\frac{\hbar}{2m\omega}\right)^2 \Big|\left([\hat{a}^{\eta,\mathrm{reg}}(t_1), (\hat{a}^{\eta,\mathrm{reg}}(t_2))^\dagger]\right)_{n,m} \\
&\quad + [(\hat{a}^{\eta,\mathrm{reg}})^\dagger(t_1), \hat{a}^{\eta,\mathrm{reg}}(t_2)]\Big|^2 \\
&= \left(\frac{\hbar}{m\omega}\right)^2 \sin^2(\omega(t_1-t_2)) e^{-\frac{4\beta}{\eta}\hbar\omega n} \\
&\quad \times \Big(n - e^{-\frac{2\beta}{\eta}\hbar\omega}(n+1)\Big)^2 \delta_{n,m},
\end{aligned}$$

  where we have to explicitly consider the mixed correlations.

- Using the collection from above, we can calculate the following first regularized expectation value

$$\begin{aligned}
\langle\big[\hat{x}^{2,\mathrm{reg}}(t), \hat{x}^{2,\mathrm{reg}}\big]\rangle_\beta &= \frac{1}{Z(\beta)}\frac{\hbar i}{m\omega}\sin(\omega t)\Big\{\sum_{n=0}^{\infty} n e^{-\beta\hbar\omega n} - \sum_{n=0}^{\infty}(n+1)e^{-\beta\hbar\omega(n+1)}\Big\} \\
&= 0
\end{aligned}$$

yielding quite a surprising result. The regularized (non-squared) commutator is zero whereas the unregularized correlator is oscillating. Going on to the regularized OTOC (squared commutator), we obtain

$$\begin{aligned}\langle\left|\left[\hat{x}^{4,\mathrm{reg}}(t),\hat{x}^{4,\mathrm{reg}}\right]\right|^2\rangle_\beta &= \frac{1}{Z(\beta)}\Big(\frac{\hbar}{m\omega}\Big)^2\sin^2(\omega t)\left\{\sum_{n=0}^{\infty}n^2e^{-\beta\hbar\omega n}\right.\\ &\left.+\sum_{n=0}^{\infty}(n+1)^2e^{-\beta\hbar\omega(n+1)}-\sum_{n=0}^{\infty}2n(n+1)e^{-\frac{\beta}{2}\hbar\omega(2n+1)}\right\}\\ &= \frac{1}{Z(\beta)}\sinh^2\left(\frac{\beta\omega\hbar}{4}\right)\sinh^{-2}\left(\frac{\beta\omega\hbar}{2}\right)\left(\frac{\hbar}{m\omega}\right)^2\sin^2(\omega t)\\ &= \Big(\frac{\hbar}{m\omega}\Big)^2\frac{\sin^2(\omega t)}{\cosh\left(\frac{\beta\omega\hbar}{2}\right)+1}\end{aligned}$$

which is the regularized result we state in Eq. (7.7) of the main text. The regularized OTOC is oscillating with the same frequency as the unregularized OTOC, but the amplitude depends on the temperature as depicted in Fig. 7.1.

E. Coherent Time Evolution in Control Systems

Following the supplementary of Ref. [3], we prove that a coherent state $|\vec{\phi}(t)\rangle_{\mathrm{coh}}$ centered on any mean-field solution $\vec{\phi}(t)$ of the control Hamiltonian Eq. (11.4) solves the controlled quantum time evolution

$$|\vec{\phi}(t)\rangle_{\mathrm{coh}} = \hat{U}_{\mathrm{c}}(t)|\vec{\phi}_0\rangle_{\mathrm{coh}} = \hat{\mathcal{T}}\exp\Big\{-i\int_0^t \hat{H}_{\mathrm{c}}(s)\,\mathrm{d}s\Big\}|\vec{\phi}_0\rangle_{\mathrm{coh}},$$

where $\vec{\phi}_0 = \vec{\phi}(0)$. More explicitly, we prove that the coherent state is the solution of the corresponding Schrödinger equation, i.e.,

$$i\frac{\mathrm{d}}{\mathrm{d}t}|\vec{\phi}(t)\rangle_{\mathrm{coh}} = \hat{H}_{\mathrm{c}}(t)|\vec{\phi}(t)\rangle_{\mathrm{coh}} \quad \text{for } \vec{\phi}(0) = \vec{\phi}_0, \tag{E.1}$$

which is an equivalent statement as the previous equation. For a simpler notation, we recall that the classical control Hamiltonian as given by Eq. (11.2) can also be written in terms of complex mean-fields

$$\mathcal{H}_{\mathrm{c}}(\vec{\phi},\vec{\phi}^*,t) = -\sum_{j=1}^{L}\left\{\phi_{j+1}^* + \phi_{j-1}^* - \mu_j(t)\phi_j^*\right\}\phi_j,$$

that evolve according to the equations of motion

$$\begin{aligned} i\dot{\phi}_j &= \frac{\partial\mathcal{H}_{\mathrm{c}}}{\partial\phi_j^*} = -\left\{\phi_{j+1} + \phi_{j-1} - \mu_j(t)\phi_j\right\} \\ i\dot{\phi}_j^* &= -\frac{\partial\mathcal{H}_{\mathrm{c}}}{\partial\phi_j} = \left\{\phi_{j+1}^* + \phi_{j-1}^* - \mu_j(t)\phi_j^*\right\}. \end{aligned}$$

Let us look at both sides of Eq. (E.1) individually. Starting with the left hand side, we take the time derivative of the coherent state acting on the mean-field solution

$$i\frac{\mathrm{d}}{\mathrm{d}t}|\vec{\phi}(t)\rangle_{\mathrm{coh}} = ie^{-\|\vec{\phi}\|^2/2}e^{\vec{\phi}(t)\cdot\hat{\vec{a}}^\dagger}\left(\sum_{j=1}^{L}\dot{\phi}_j(t)\hat{a}_j^\dagger\right)|0\rangle\,,$$

where we use that $\|\vec{\phi}\|^2 = N$ is conserved. Next we use the classical mean-field equations of motion from above to obtain

$$\begin{aligned} i\frac{\mathrm{d}}{\mathrm{d}t}|\vec{\phi}(t)\rangle_{\mathrm{coh}} &= -ie^{-\|\vec{\phi}\|^2/2}e^{\vec{\phi}(t)\cdot\hat{\vec{a}}^\dagger}\sum_{j=1}^{L}\left(\left\{\phi_{j+1}(t) + \phi_{j-1}(t) - \mu_j(t)\phi_j(t)\right\}\hat{a}_j^\dagger\right)|0\rangle \\ &= -\sum_{j=1}^{L}\left(\left\{\phi_{j+1}(t) + \phi_{j-1}(t) - \mu_j(t)\phi_j(t)\right\}\hat{a}_j^\dagger\right)|\vec{\phi}(t)\rangle_{\mathrm{coh}}. \end{aligned}$$

Now going to the right hand side of Eq. (E.1), we use the central property of a coherent state - given in Eq. (10.8) - that it is an eigenstate of the annihilation operators in order to obtain

$$\begin{aligned}\hat{H}_{\mathrm{c}}(t)|\vec{\phi}(t)\rangle_{\mathrm{coh}} &= -\sum_{j=1}^{L}\left(\left\{\hat{a}_{j+1}^{\dagger}+\hat{a}_{j-1}^{\dagger}+\mu_j(t)\hat{a}_j^{\dagger}\right\}\hat{a}_j\right)|\vec{\phi}(t)\rangle_{\mathrm{coh}} \\ &= -\sum_{j=1}^{L}\left(\left\{\phi_{j+1}(t)+\phi_{j-1}(t)+\mu_j(t)\phi_j(t)\right\}\hat{a}_j^{\dagger}\right)|\vec{\phi}(t)\rangle_{\mathrm{coh}}.\end{aligned}$$

This matches exactly the left hand side. Therefore, the proof of our statement is complete.

Some remarks we want to stress to the reader:

1. The proof for number-projected states is analogous using the property

   $$\hat{a}_j|\vec{\phi}(t)\rangle_{\mathrm{proj}}^{N} = \phi_j|\vec{\phi}(t)\rangle_{\mathrm{proj}}^{N-1}$$

   derived in [174].

2. The control trajectory used to drive the chemical potentials $\{\mu_j(t)\}$ is a specific case in Sec. 12, since it is a solution simultaneously to both the classical equations of motion in the control system, as well as the Bose-Hubbard mean-field limit. With that information, the above proof implies that a coherent state initially centered on the control trajectory arrives at the end of the trajectory with perfect fidelity.

3. For any specified control Hamiltonian of the form of Eq. (11.4) and recalling the equation for calculating the stability matrix, every initial mean-field condition or trajectory leads to the exact same time-dependent stability matrix. Thus, all trajectories have to rotate around the control trajectory and the stability matrix solution is a time-dependent orthogonal matrix. This implies that for a coherent state initially centered off the control trajectory by $||\delta\vec{x}_{\mathrm{init}}||$, this distance remains constant. By using the properties of the stability matrix, and Heller's linearized wave-packet dynamics [197], it would be possible to provide an analytical formula for the fidelity. This is shown for example in Fig. 13.1 based solely on the knowledge of the initial state and the control trajectory.

F. Plots of Ground-State Training Runs

Here, we present all training plots (energy-difference versus relative energy-variance in the left panels of Fig. 19.3) for the ground-state search results from Sec. 19. The order of displaying the lattice topologies is revised to minimize blank space. A linear correlation between energy difference and relative variance indicates a successful training run, where the final training state is limited by the statistical uncertainty from the finite number of Monte Carlo samples. If the curve bends downward, the training has reached a plateau: the variance no longer decreases, but the minimal energy has been reliably achieved.

Brick-Structure

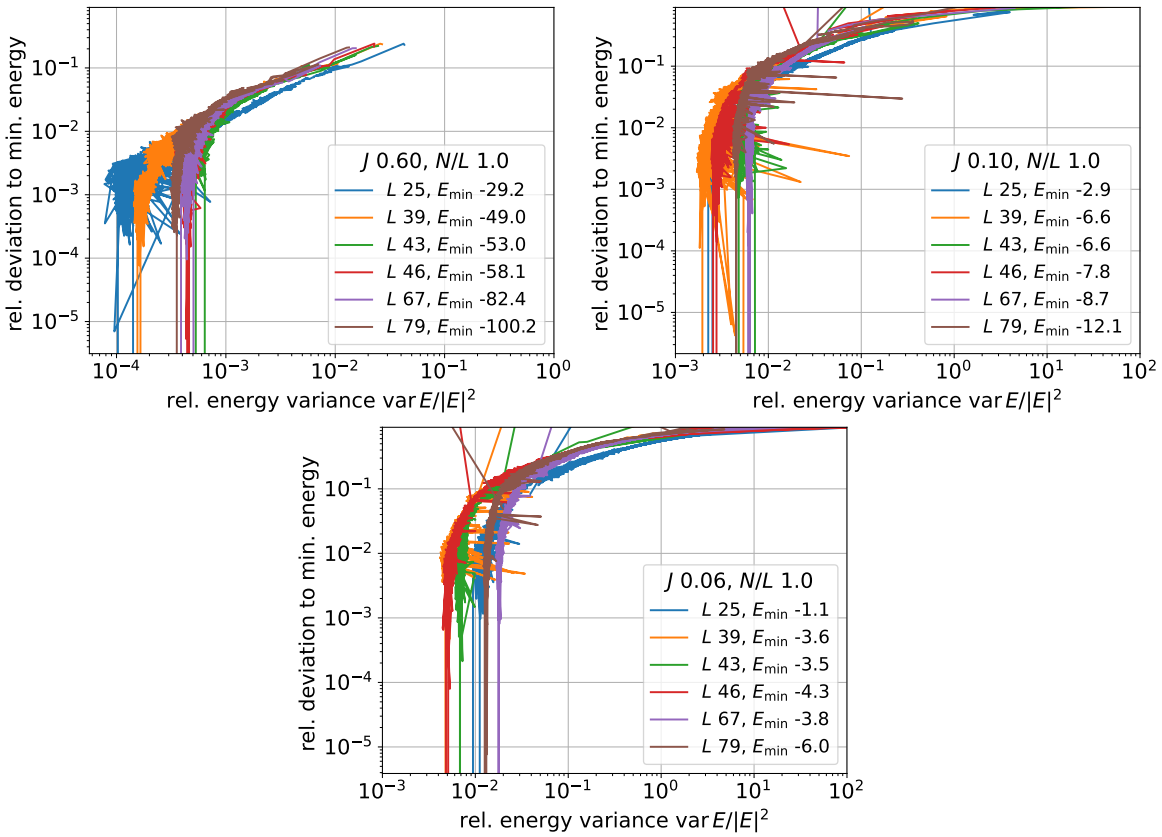

Figure F.1: Visualization of the ground-state minimization for the brick structure in Fig. 19.1: panels show the correlation between the energy variance and difference between the minimal energy during the minimization at the hopping strengths $J = 0.6, 0.1, 0.06$ and the filling factor $N/L = 1$ respectively. In all cases, we use the RWKV-network with the parameter specified in Tab. 19.1. The interaction $U = 0.25$ and the variance of the chemical potentials $\sigma_\mu = 0.12$ are the same in each panel.

One-Dimensional Chain

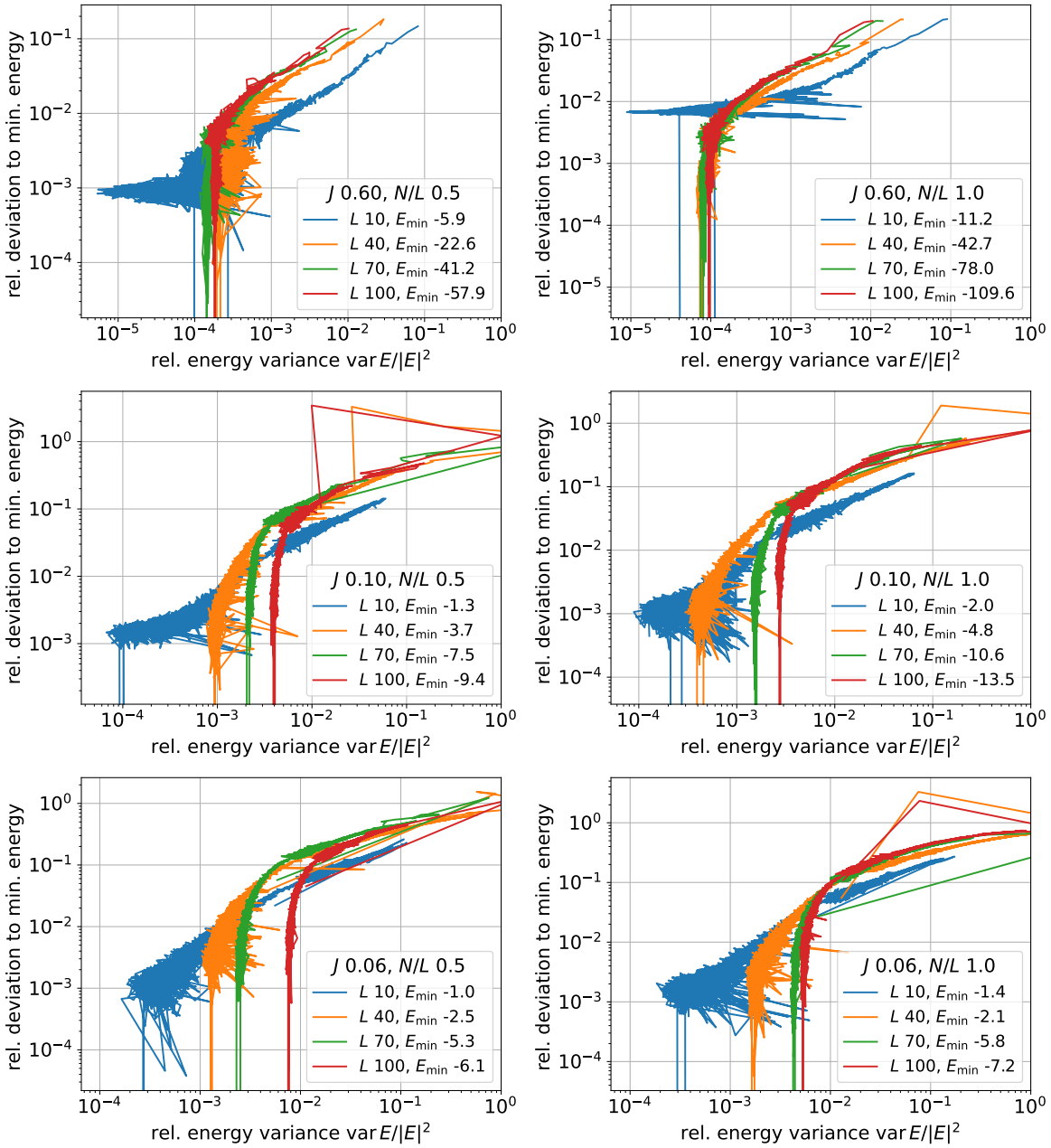

Figure F.2: Visualization of the ground-state minimization for the one-dimensional chain with open boundaries: panels show the correlation between the energy variance and difference between the minimal energy during the minimization at the hopping strengths $J = 0.6,\ 0.1,\ 0.06$ and the filling factors $N/L = 0.5,\ 1$ respectively. In all cases, we use the RWKV-network with the parameter specified in Tab. 19.1. The interaction $U = 0.25$ and the variance of the chemical potentials $\sigma_\mu = 0.12$ are the same in each panel.

Two-Dimensional Lattice

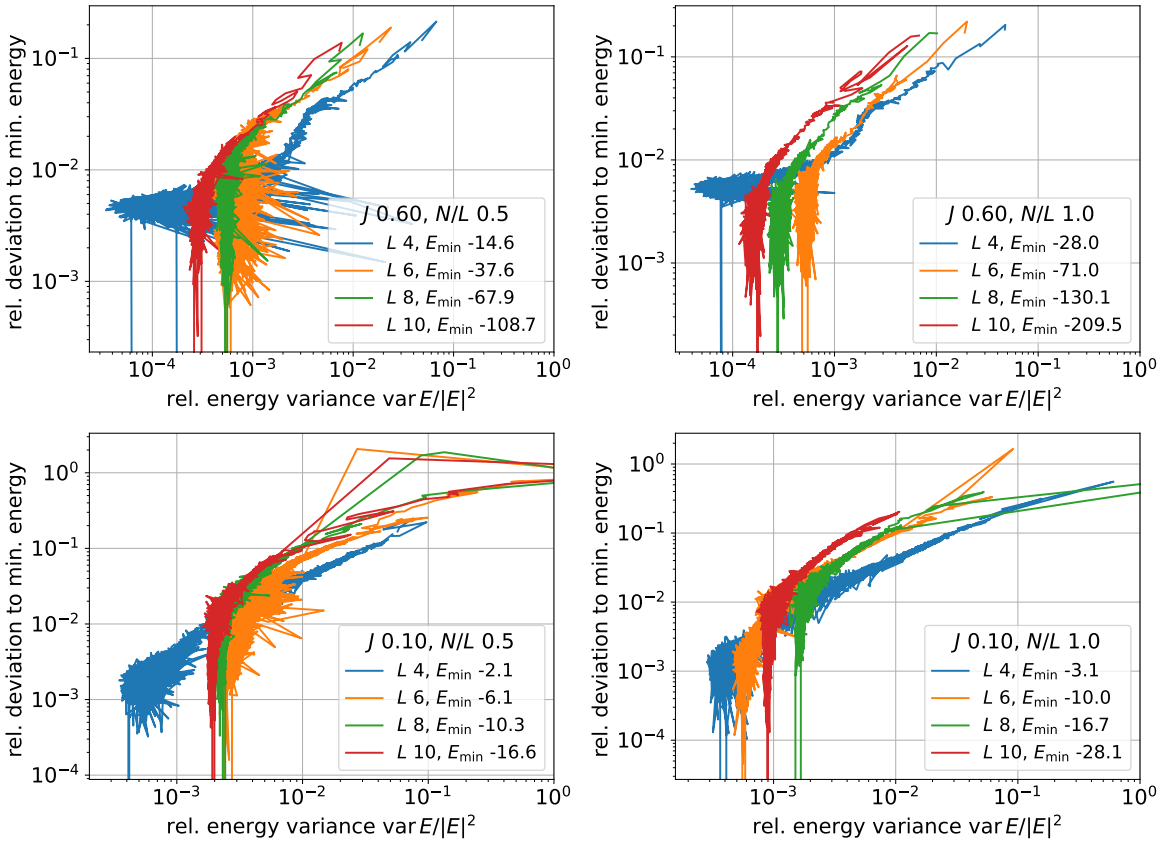

Figure F.3: Visualization of the ground-state minimization for the two-dimensional lattice with open boundaries: panels show the correlation between the energy variance and difference between the minimal energy during the minimization at the hopping strengths $J = 0.6, 0.1$ and the filling factors $N/L = 0.5, 1$ respectively. In all cases, we use the RWKV-network with the parameter specified in Tab. 19.1. The interaction $U = 0.25$ and the variance of the chemical potentials $\sigma_\mu = 0.12$ are the same in each panel.

Acknowledgments

Funding

I acknowledge funding from the **Studienstiftung des Deutschen Volkes** (German National Academic Foundation), the **Deutsche Forschungsgemeinschaft** (DFG, German Research Foundation) by the **Reinhart Koselleck** program (project number Ri681/15-1), and from the **Office of Naval Research Global** (award number N629092412053).

Special Thanks

For me, this thesis is and will be a lot more than these written words above. It reflects a journey during which I had the privilege to explore many subjects in depth, and, most importantly, the joy of working alongside people I deeply value and respect. I try to do justice for all the immense support, encouragement and joy I received from so many people while working on my PhD project.

- The first person I want to thank is my supervisor **Prof. Dr. Klaus Richter**. He suggested applying for the PhD scholarship of the German National Academic Foundation. Through the fellowship, I participated in many fascinating out-of-curriculum events. Meanwhile, my research interest went into different types of topics, taking their time, and he continued my funding after the scholarship. About almost everything related to physics, he has an all-embracing overview and the detailed knowledge in order to guide a PhD student in the direction of progress. I feel lucky to have had his guidance and his support to participate in many conferences. He put trust in me and gave me the freedom to pursue my research interests. A big thanks for supervising my PhD studies!

- Also, huge thanks go to **Prof. Dr. Juan Diego Urbina**; he is certainly the criminal who brought me into the field of semiclassical physics. Starting with the bachelor thesis, he held me captive in the field. The joint trips to conferences in Mumbai, Freiburg, Dresden, and Bremen have been a pleasure, and I will miss going to conferences with him for sure. I owe him a lot: answers for countless physical problems, supporting my ideas, rehearsing talks, and the trust in me to let to do my own thing when I want. His support was not limited in any way, he always had an open ear for all concerns and offered advice for everyday life. Thanks a lot!

- Next two persons, I want to thank **Dr. Jonas Rigo** and **Dr. Markus Schmitt**. Their commitment to teaching me variational Monte Carlo was a blast for me. I like to tinker with computational hardware, and they gave me access to their high-end computational resources. It made the third chapter about the neural quantum states possible. But more importantly, they invested a lot of time into teaching how to actually use GPUs in a fruitful way. Here I am especially thankful to Jonas for accompanying me throughout all the difficulties of developing and debugging code and fine-tuning hyperparameters. I am still amazed how our collaboration went from meeting him in Italy at my first conference about NQS.

- My gratitude extends to **Prof. Dr. Peter Schlagheck** for the long and continued collaborations in joint projects regarding OTOCs. I definitely enjoyed the regular Friday meetings. Next to fascinating physics, we almost always managed to drift off topic and discussed random things, definitely a joy before going into the weekend. In addition, I want to thank him for two visits in Liége.

- There is also **Prof. Dr. Steven Tomsovic** to whom I have to say that he is the only person making nice four-dimensional visualizations on a sheet of paper. Anyhow, I am thankful to him and **Lukas Beringer** for doing the Controlling Chaos project together. I certainly enjoyed having an application benefiting dramatically from chaos. Also, thanks for making the promotion video for our paper kind of weird by scaring off people hearing me saying "Bose-Hubbard systems".

- Furthermore, I want to mention all my collaborators: **Dr. Felix Meier**, **Dr. Daniel Waltner**, **Prof. Dr. Thomas Guhr** and **Thomas Michel**. Thank you all for doing challenging physics with me in our collaborations.

- My continued gratitude goes to **Prof. Dr. Annabelle Bohrdt**, not only for being the second referee, but most for the fun in the lectures about machine learning techniques applied in physics. I attended the lectures and the machine learning seminars with a huge amount of joy, and I learned a lot.

Now coming to the group from the chair: Upfront, I kind of have to express my apologies to the group during covid when I was testing an old and (very) loud GPU server (Doris dubbed it as the "Monstermaschine") in the guest office... it was fun! There are countless stories, all of them are memories I keep in my heart for sure! I want to share some of the stories and pay tribute to the office crowd making my time during the PhD amazing:

- Special thanks to my office mates **Fabian** and **Georg** for the great time chatting, laughing and supporting each other. I admire them surviving in the jungle I kinda created; it is an unforeseen consequence after the wish to have my own homegrown avocados at an infamous lunch break.

- **Wolfgang** accompanied me throughout my physics studies and is a person who can always enjoy a coffee. A major reason why I progressed in difficult tasks is due to these coffee breaks. We discussed and basically solved many of my problems there (I hope I helped him also a bit).

- Speaking about coffee, **Doris** comes to my mind. She helped not only in countless administrative matters, but also is a good soul and great conversational partner during the morning coffee, especially at the time of covid restrictions.

- **Florian** and **Lukas**: It was a pleasure meeting you as master students. Now, the dream team is combined in an office doing their PhDs. @**Florian**: remember that I won one chess game against you, definitely one of my biggest achievements. @**Lukas**: never change; it is a pleasure to work together and stay strong trying to grasp the semiclassical ideas of Steve.

- Thanks to the team of the sysadmins: **Wolfgang**, **Michael**, **Georg**, **Jacob**, **Vanessa**, **Fabian** and **Alexander** supporting and feeding my hunger for computational resources and tolerating the old GPU-machines I set up.

- My gratitude continues to my fellow PhD students **Alexander**, **Michael**, **Maximilian**, **Jacob**, **Ching-Hung**, **Torsten**, **Camilo**, **Vanessa**, **Sebastian** and **Andreas**, as well as to the Postdocs **Dr. Angelika Knothe-Schulz** and **Dr. Cosimo Gorini** for sharing time, coffee, food, drinks and many stories.

- For all administrative matters and beyond, I could count on the support from **Romy**, **Toni**, **Doris** and **Elke**. Most important, I could always count on the chair's coffee. Thanks for all the support!

For reading parts of the manuscript, I express my gratitude to **Jiangyue**, **Fabian**, **Alexander**, **Georg**, **Florian**, **Wolfgang**, **Lukas**, **Jonas**, **Klaus** and **Juan Diego**.

Last but certainly not least, I want to thank my friends and family. Of course, without them my life would be miserable and only consist of work.

- My highest respect goes to my partner (in crime) **Jiangyue (江月)** for the continuous support and the ability to withstand the stressed 马大头.

- I certainly depend on my family: my mom **Heidi** and my brothers **Konrad** and **Patrick**. Thanks for all the past, continuous and future support throughout my life.

As for my dad, **Sepp**, I kind of wished I would have finished the thesis a bit earlier such that my dad could have seen me finishing my PhD. He would have certainly liked seeing the defense. I devote the thesis to him, since he and my mom supported me throughout my life. A final thank you for the support.

Bibliography

[1] F. Meier, M. Steinhuber, J. D. Urbina, D. Waltner, and T. Guhr, "Signatures of the interplay between chaos and local criticality on the dynamics of scrambling in many-body systems", Phys. Rev. E **107**, 054202 (2023) (cit. on pp. v, 3, 12, 33–36, 38–41, 67, 123).

[2] M. Steinhuber, P. Schlagheck, J. D. Urbina, and K. Richter, "Dynamical transition from localized to uniform scrambling in locally hyperbolic systems", Phys. Rev. E **108**, 024216 (2023) (cit. on pp. v, 3, 12, 19, 21, 24, 25, 30–33, 67).

[3] L. Beringer, M. Steinhuber, J. Diego Urbina, K. Richter, and S. Tomsovic, "Controlling many-body quantum chaos: Bose-Hubbard systems", New Journal of Physics **26**, 073002 (2024) (cit. on pp. v, 6, 12, 67, 69, 70, 72, 77–85, 87, 88, 90, 91, 94, 149).

[4] M. V. Berry and K. E. Mount, "Semiclassical approximations in wave mechanics", Reports on Progress in Physics **35**, 315 (1972) (cit. on p. 1).

[5] F. Haake, S. Gnutzmann, and M. Kus, *Quantum signatures of chaos, fourth edition* (Springer, Heidelberg, 2018) (cit. on pp. 1, 2, 18, 19, 110).

[6] T. Engl, J. Dujardin, A. Argüelles, P. Schlagheck, K. Richter, and J. D. Urbina, "Coherent backscattering in Fock space: a signature of quantum many-body interference in interacting bosonic systems", Phys. Rev. Lett. **112**, 140403 (2014) (cit. on pp. 1, 18).

[7] K. Richter, J. D. Urbina, and S. Tomsovic, "Semiclassical roots of universality in many-body quantum chaos", Journal of Physics A: Mathematical and Theoretical **55**, 453001 (2022) (cit. on pp. 1, 2, 15, 16, 18, 68).

[8] T. Kottos and U. Smilansky, "Periodic orbit theory and spectral statistics for quantum graphs", Annals of Physics **274**, 76 (1999) (cit. on p. 1).

[9] M. Tabor, *Chaos and integrability in nonlinear dynamics: an introduction* (Wiley, New York, 1989) (cit. on pp. 1, 4, 45, 127, 128).

[10] H. Goldstein, *Classical mechanics* (Addison-Wesley, Reading, 1980) (cit. on pp. 1, 4, 45, 127, 128).

[11] O. Bohigas, M. J. Giannoni, and C. Schmit, "Characterization of chaotic quantum spectra and universality of level fluctuation laws", Phys. Rev. Lett. **52**, 1 (1984) (cit. on p. 1).

[12] J. Rammensee, J. D. Urbina, and K. Richter, "Many-body quantum interference and the saturation of out-of-time-order correlators", Phys. Rev. Lett. **121**, 124101 (2018) (cit. on pp. 1, 3, 18, 21).

[13] E. J. Heller and B. R. Landry, "Statistical properties of many particle eigenfunctions.", Journal of Physics A: Mathematical & Theoretical **40**, 9259 (2007) (cit. on p. 1).

[14] Q. Hummel, B. Geiger, J. D. Urbina, and K. Richter, "Reversible quantum information spreading in many-body systems near criticality", Phys. Rev. Lett. **123**, 160401 (2019) (cit. on pp. 1, 3, 15, 18, 19, 21, 22, 62).

[15] T. Xu, T. Scaffidi, and X. Cao, "Does scrambling equal chaos?", Phys. Rev. Lett. **124**, 140602 (2020) (cit. on pp. 1, 3, 15, 19–22, 62).

[16] S. Pappalardi, A. Russomanno, B. Žunkovi č, F. Iemini, A. Silva, and R. Fazio, "Scrambling and entanglement spreading in long-range spin chains", Phys. Rev. B **98**, 134303 (2018) (cit. on pp. 1, 3, 15, 18, 22).

[17] W. Kirkby, D. H. J. O'Dell, and J. Mumford, "False signals of chaos from quantum probes", Phys. Rev. A **104**, 043308 (2021) (cit. on p. 1).

[18] J. Maldacena, S. H. Shenker, and D. Stanford, "A bound on chaos", J. High Energy Phys. **2016**, 106 (2016) (cit. on pp. 2, 4, 16, 53, 59, 61, 64, 123, 127).

[19] E. Altman, "Many-body localization and quantum thermalization", Nature Physics **14**, 979 (2018) (cit. on p. 2).

[20] J. Eisert, M. Friesdorf, and C. Gogolin, "Quantum many-body systems out of equilibrium", Nature Physics **11**, 124 (2015) (cit. on p. 2).

[21] R. Nandkishore and D. A. Huse, "Many-body localization and thermalization in quantum statistical mechanics", Annual Review of Condensed Matter Physics **6**, 15 (2015) (cit. on pp. 2, 10, 95).

[22] S. Pilatowsky-Cameo, J. Chávez-Carlos, M. A. Bastarrachea-Magnani, P. Stránský, S. Lerma-Hernández, L. F. Santos, and J. G. Hirsch, "Positive quantum Lyapunov exponents in experimental systems with a regular classical limit", Phys. Rev. E **101**, 010202 (2020) (cit. on p. 2).

[23] M. Ueda, "Quantum equilibration, thermalization and prethermalization in ultracold atoms", Nature Reviews Physics **2**, 669 (2020) (cit. on p. 2).

[24] S. H. Shenker and D. Stanford, "Black holes and the butterfly effect", J. High Energy Phys. **3**, 67 (2014) (cit. on p. 2).

[25] A. I. Larkin and Y. N. Ovchinnikov, "Quasiclassical method in the theory of superconductivity", Soviet Physics JETP **28**, 1200 (1969) (cit. on pp. 2, 3, 16).

[26] S. Xu and B. Swingle, "Scrambling dynamics and out-of-time ordered correlators in quantum many-body systems: a tutorial", (2022), eprint: 2202.07060 (quant-ph) (cit. on pp. 2, 64).

[27] P. Hayden and J. Preskill, "Black holes as mirrors: quantum information in random subsystems", J. High Energy Phys. **2007**, 120 (2007) (cit. on p. 2).

[28] Y. Sekino and L. Susskind, "Fast scramblers", J. High Energy Phys. **10**, 065 (2008) (cit. on pp. 2, 64).

[29] Y. Gu and A. Kitaev, "On the relation between the magnitude and exponent of OTOCs", J. High Energy Phys. **2019**, 10.1007/jhep02(2019)075 (2019) (cit. on p. 2).

[30] V. Jahnke, K.-Y. Kim, and J. Yoon, "On the chaos bound in rotating black holes", J. High Energy Phys. **2019**, 10.1007/jhep05(2019)037 (2019) (cit. on p. 2).

[31] B. Kobrin, Z. Yang, G. D. Kahanamoku-Meyer, C. T. Olund, J. E. Moore, D. Stanford, and N. Y. Yao, "Many-body chaos in the Sachdev-Ye-Kitaev model", Phys. Rev. Lett. **126**, 030602 (2021) (cit. on pp. 2, 4, 18).

[32] Y. Gu, A. Kitaev, and P. Zhang, "A two-way approach to out-of-time-order correlators", J. High Energy Phys. **2022**, 10.1007/jhep03(2022)133 (2022) (cit. on p. 2).

[33] N. Tsuji and P. Werner, "Out-of-time-ordered correlators of the Hubbard model: Sachdev-Ye-Kitaev strange metal in the spin-freezing crossover region", Phys. Rev. B **99**, 115132 (2019) (cit. on p. 2).

[34] B. Swingle, G. Bentsen, M. Schleier-Smith, and P. Hayden, "Measuring the scrambling of quantum information", Phys. Rev. A **94**, 040302 (2016) (cit. on p. 2).

[35] M. Gärttner, J. G. Bohnet, A. Safavi-Naini, M. L. Wall, J. J. Bollinger, and A. M. Rey, "Measuring out-of-time-order correlations and multiple quantum spectra in a trapped-ion quantum magnet", Nature Physics **13**, 781 (2017) (cit. on p. 2).

[36] J. Li, R. Fan, H. Wang, B. Ye, B. Zeng, H. Zhai, X. Peng, and J. Du, "Measuring out-of-time-order correlators on a nuclear magnetic resonance quantum simulator", Phys. Rev. X **7**, 031011 (2017) (cit. on p. 2).

[37] A. M. Green, A. Elben, C. H. Alderete, L. K. Joshi, N. H. Nguyen, T. V. Zache, Y. Zhu, B. Sundar, and N. M. Linke, "Experimental measurement of out-of-time-ordered correlators at finite temperature", Phys. Rev. Lett. **128**, 140601 (2022) (cit. on p. 2).

[38] F. S. Lozano-Negro, C. M. Sánchez, A. K. Chattah, G. A. Álvarez, and H. M. Pastawski, "Global out-of-time-order correlators as a signature of scrambling dynamics of local observables", Phys. Rev. A **110**, 042410 (2024) (cit. on p. 2).

[39] E. B. Rozenbaum, S. Ganeshan, and V. Galitski, "Lyapunov exponent and out-of-time-ordered correlator's growth rate in a chaotic system", Phys. Rev. Lett. **118**, 10.1103/physrevlett.118.086801 (2017) (cit. on pp. 3, 18, 33).

[40] D. Villaseñor, S. Pilatowsky-Cameo, M. A. Bastarrachea-Magnani, S. Lerma-Hernández, L. F. Santos, and J. G. Hirsch, "Chaos and thermalization in the spin-boson Dicke model", Entropy **25**, 10.3390/e25010008 (2023) (cit. on p. 3).

[41] D. Waltner, "Semiclassical approach to mesoscopic systems", Springer Tracts in Modern Physics **245** (2012) (cit. on pp. 4, 6, 16, 18).

[42] P. Ehrenfest, "Bemerkung über die angenäherte Gültigkeit der klassischen Mechanik innerhalb der Quantenmechanik", Z. Phys. **45**, 455 (1927) (cit. on pp. 4, 6, 18, 68).

[43] J. Lee, D. Kim, and D.-H. Kim, "Typical growth behavior of the out-of-time-ordered commutator in many-body localized systems", Phys. Rev. B **99**, 184202 (2019) (cit. on p. 4).

[44] I. Kukuljan, S. š. Grozdanov, and T. Prosen, "Weak quantum chaos", Phys. Rev. B **96**, 060301 (2017) (cit. on p. 4).

[45] E. M. Fortes, I. Garcí a-Mata, R. A. Jalabert, and D. A. Wisniacki, "Signatures of quantum chaos transition in short spin chains", EPL **130**, 60001 (2020) (cit. on p. 4).

[46] S. M. Ulam, *On the possibility of extracting energy from gravitational systems by navigating space vehicles*, tech. rep. LAMS-2219 (Los Alamos National Laboratory, 1958) (cit. on pp. 5, 67).

[47] R. Farquhar, D. Muhonen, and S. A. Davis, "Trajectories and orbit maneuvers for the ISEE-3/ICE comet mission (1985)", J. Astronaut. Sci. **33**, 235 (1985) (cit. on pp. 5, 67).

[48] R. W. Farquhar, "The flight of ISEE-3/ICE: origins, mission history, and a legacy", J. Astronaut. Sci. **49**, 23 (2001) (cit. on pp. 5, 67).

[49] E. Ott, C. Grebogi, and J. A. Yorke, "Controlling chaos", Phys. Rev. Lett. **64**, 1196 (1990) (cit. on pp. 5, 67, 92).

[50] T. Shinbrot, E. Ott, C. Grebogi, and J. A. Yorke, "Using chaos to direct trajectories to targets", Phys. Rev. Lett. **65**, 3215 (1990) (cit. on pp. 5, 67).

[51] E. J. Kostelich, C. Grebogi, E. Ott, and J. A. Yorke, "Higher-dimensional targeting", Phys. Rev. E **47**, 305 (1993) (cit. on pp. 5, 67).

[52] E. M. Bollt, "Controlling chaos, targeting, and transport", PhD thesis (University of Colorado, 1995) (cit. on p. 5).

[53] C. G. Schroer and E. Ott, "Targeting in Hamiltonian systems that have mixed regular/chaotic phase spaces", Chaos **7**, 512 (1997) (cit. on p. 5).

[54] E. Ott, "Controlling chaos", Scholarpedia **1**, revision #91167, 1699 (2006) (cit. on p. 5).

[55] H. Poincaré, *Les méthodes nouvelles de la mécanique céleste*, Vol. 3 (Gauthier-Villars et fils, Paris, 1899) (cit. on p. 5).

[56] A. M. Lyapunov, "The general problem of the stability of motion", in Russian, PhD thesis (University of Kharkov, 1892) (cit. on p. 5).

[57] E. P. Wigner, "On the quantum correction for thermodynamic equilibrium", Phys. Rev. **40**, 749 (1932) (cit. on pp. 5, 74, 75).

[58] A. N. Kolmogorov, "New metric invariant of transitive dynamical systems and endomorphisms of Lebesgue spaces", Doklady of Russian Academy of Sciences **119**, 861 (1958) (cit. on p. 5).

[59] Y. G. Sinai, "On the notion of entropy of a dynamical system", Doklady of Russian Academy of Sciences **124**, 768 (1959) (cit. on pp. 5, 68).

[60] J. C. Leitão, J. M. V. P. Lopes, and E. G. Altmann, "Importance sampling of rare events in chaotic systems", Eur. Phys. J. B **90**, 181 (2017) (cit. on p. 5).

[61] B. V. Chirikov, "A universal instability of many-dimensional oscillator systems", Phys. Rep. **52**, 263 (1979) (cit. on p. 5).

[62] F. M. Izrailev, "Simple models of quantum chaos: spectrum and eigenfunctions", Phys. Rep. **196**, 299 (1990) (cit. on p. 5).

[63] S. Tomsovic, J. D. Urbina, and K. Richter, "Controlling quantum chaos: optimal coherent targeting", Phys. Rev. Lett. **130**, 020201 (2023) (cit. on pp. 5, 6, 67, 74, 79, 92).

[64] S. Tomsovic, J. D. Urbina, and K. Richter, "Controlling quantum chaos: time-dependent kicked rotor", Phys. Rev. E **108**, 044202 (2023) (cit. on pp. 5, 6, 67, 74, 79, 92).

[65] W. Heisenberg, "Über den anschaulichen Inhalt der quantentheoretischen Kinematik und Mechanik", Zeit. der Phys. **43**, 172 (1927) (cit. on p. 5).

[66] T. H. Johnson, S. R. Clark, and D. Jaksch, "What is a quantum simulator", EPJ Quant. Tech. **1**, 10 (2014) (cit. on p. 6).

[67] H. A. Gersch and G. C. Knollman, "Quantum cell model for bosons", Phys. Rev. **129**, 959 (1963) (cit. on p. 6).

[68] D. Jaksch, C. Bruder, J. I. Cirac, C. W. Gardiner, and P. Zoller, "Cold bosonic atoms in optical lattices", Phys. Rev. Lett. **81**, 3108 (1998) (cit. on pp. 6, 7, 71, 80).

[69] D. J. Tannor and S. A. Rice, "Control of selectivity of chemical reaction via control of wave packet evolution", J. Chem. Phys. **83**, 5013 (1985) (cit. on p. 6).

[70] P. Brumer and M. Shapiro, "Control of unimolecular reactions using coherent light", Chem. Phys. Lett. **126**, 541 (1986) (cit. on p. 6).

[71] R. S. Judson and H. Rabitz, "Teaching lasers to control molecules", Phys. Rev. Lett. **68**, 1500 (1992) (cit. on p. 6).

[72] W. S. Warren, H. Rabitz, and M. Dahleh, "Coherent control of quantum dynamics: the dream is alive", Science **259**, 1581 (1993) (cit. on p. 6).

[73] A. P. Peirce, M. A. Dahleh, and H. Rabitz, "Optimal control of quantum-mechanical systems: existence, numerical approximation, and applications", Phys. Rev. A **37**, 4950 (1988) (cit. on p. 6).

[74] R. Kosloff, S. A. Rice, P. Gaspard, S. Tersigni, and D. J. Tannor, "Wavepacket dancing: achieving chemical selectivity by shaping light pulses", Chem. Phys. **139**, 201 (1989) (cit. on p. 6).

[75] P. Doria, T. Calarco, and S. Montangero, "Optimal control technique for many-body quantum dynamics", Phys. Rev. Lett. **106**, 190501 (2011) (cit. on p. 6).

[76] S. v. Frank, M. Bonneau, J. Schmiedmayer, S. Hild, C. Gross, M. Cheneau, I. Bloch, T. Pichler, A. Negretti, T. Calarco, and S. Montangero, "Optimal control of complex atomic quantum systems", Sci. Rep. **6**, 34187 (2016) (cit. on p. 6).

[77] P. M. Poggi and D. A. Wisniacki, "Optimal control of many-body quantum dynamics: chaos and complexity", Phys. Rev. A **94**, 033406 (2016) (cit. on p. 6).

[78] D. Dong and I. R. Petersen, "Quantum control theory and applications: a survey", IET Control Theory Appl. **4**, 2651 (2010) (cit. on p. 6).

[79] M. R. James, "Optimal quantum control theory", Annu. rev. control robot. auton. syst. **4**, 343 (2021) (cit. on p. 6).

[80] S. Tomsovic and J. H. Lefebvre, "Can wave packet revivals occur in chaotic quantum systems?", Phys. Rev. Lett. **79**, 3629 (1997) (cit. on p. 6).

[81] J. Gong and P. Brumer, "Quantum chaos meets coherent control", Annu. Rev. Phys. Chem. **56**, 1 (2005) (cit. on p. 6).

[82] M. Gruebele and P. G. Wolynes, "Quantizing Ulam's Control Conjecture", Phys. Rev. Lett. **99**, 060201 (2007) (cit. on p. 6).

[83] M. Bitter and V. Milner, "Experimental demonstration of coherent control in quantum chaotic systems", Phys. Rev. Lett. **118**, 034101 (2017) (cit. on p. 6).

[84] G. Vanhaele and P. Schlagheck, "NOON states with ultracold bosonic atoms via resonance- and chaos-assisted tunneling", Phys. Rev. A **103**, 013315 (2021) (cit. on p. 6).

[85] G. Vanhaele, A. Bäcker, R. Ketzmerick, and P. Schlagheck, "Creating triple-NOON states with ultracold atoms via chaos-assisted tunneling", Phys. Rev. A **106**, L011301 (2022) (cit. on p. 6).

[86] J. Madronero, A. Ponomarev, A. R. R. Carvalho, S. Wimberger, C. Viviescas, A. Kolovsky, K. Hornberger, P. Schlagheck, A. Krug, and A. Buchleitner, "Quantum chaos, transport, and control - in quantum optics", Adv. in Atom. Mol. Opt. Phys. **53**, 33 (2006) (cit. on p. 6).

[87] I. Bloch, J. Dalibard, and W. Zwerger, "Many-body physics with ultracold gases", Rev. Mod. Phys. **80**, 885 (2008) (cit. on pp. 7, 80).

[88] J. Dalibard, F. Gerbier, G. Juzeliūnas, and P. Öhberg, "Artificial gauge potentials for neutral atoms", Rev. Mod. Phys. **83**, 1523 (2011) (cit. on p. 7).

[89] I. Bloch, J. Dalibard, and S. Nascimbène, "Quantum simulations with ultracold gases", Nature Physics **8**, 267 (2012) (cit. on pp. 7, 125).

[90] C.-C. Chien, S. Peotta, and M. Di Ventra, "Quantum transport in ultracold atoms", Nature Physics **11**, 998 (2015) (cit. on p. 7).

[91] T. Langen, R. Geiger, and J. Schmiedmayer, "Ultracold atoms out of equilibrium", Annu. Rev. Condens. Matter Phys. **6**, 201 (2015) (cit. on p. 7).

[92] F. Schäfer, T. Fukuhara, S. Sugawa, Y. Takasu, and Y. Takahashi, "Tools for quantum simulation with ultracold atoms in optical lattices", Nat. Rev. Phys. **2**, 411 (2020) (cit. on p. 7).

[93] B. Yang, H. Sun, R. Ott, H.-Y. Wang, T. V. Zache, J. C. Halimeh, Z.-S. Yuan, P. Hauke, and J.-W. Pan, "Observation of gauge invariance in a 71-site Bose-Hubbard quantum simulator", Nature **587**, 392 (2020) (cit. on p. 7).

[94] E. Altman, K. R. Brown, G. Carleo, L. D. Carr, E. Demler, C. Chin, B. DeMarco, S. E. Economou, M. A. Eriksson, K.-M. C. Fu, M. Greiner, K. R. Hazzard, R. G. Hulet, A. J. Kollár, B. L. Lev, M. D. Lukin, R. Ma, X. Mi, S. Misra, C. Monroe, K. Murch, Z. Nazario, K.-K. Ni, A. C. Potter, P. Roushan, M. Saffman, M. Schleier-Smith, I. Siddiqi, R. Simmonds, M. Singh, I. Spielman, K. Temme, D. S. Weiss, J. Vučković, V. Vuletić, J. Ye, and M. Zwierlein, "Quantum simulators: architectures and opportunities", PRX Quantum **2**, 017003 (2021) (cit. on pp. 7, 125).

[95] C. Braun, R. Saint-Jalm, A. Hesse, J. Arceri, I. Bloch, and M. Aidelsburger, "Real-space detection and manipulation of topological edge modes with ultracold atoms", Nature Physics **20**, 1306 (2024) (cit. on p. 7).

[96] D. Bluvstein, S. J. Evered, A. A. Geim, S. H. Li, H. Zhou, T. Manovitz, S. Ebadi, M. Cain, M. Kalinowski, D. Hangleiter, J. P. B. Ataides, N. Maskara, I. Cong, X. Gao, P. S. Rodriguez, T. Karolyshyn, G. Semeghini, M. J. Gullans, M. Greiner, V. Vuletić, and M. D. Lukin, "Logical quantum processor based on reconfigurable atom arrays", Nature (2023) (cit. on p. 7).

[97] J. Eilbeck, P. Lomdahl, and A. Scott, "The discrete self-trapping equation", Physica D: Nonlinear Phenomena **16**, 318 (1985) (cit. on pp. 7, 35).

[98] L. P. Pitaevskii and S. Stringari, *Bose-Einstein condensation* (Oxford University Press, Oxford, 2003) (cit. on p. 7).

[99] A. R. Kolovsky and A. Buchleitner, "Quantum chaos in the Bose-Hubbard model", EPL **68**, 632 (2004) (cit. on pp. 7, 72, 73).

[100] L. Pausch, E. G. Carnio, A. Rodríguez, and A. Buchleitner, "Chaos and ergodicity across the energy spectrum of interacting bosons", Phys. Rev. Lett. **126**, 150601 (2021) (cit. on pp. 7, 72).

[101] C. Chin, R. Grimm, P. Julienne, and E. Tiesinga, "Feshbach resonances in ultracold gases", Rev. Mod. Phys. **82**, 1225 (2010) (cit. on pp. 7, 80, 88, 93).

[102] G.-X. Su, H. Sun, A. Hudomal, J.-Y. Desaules, Z.-Y. Zhou, B. Yang, J. C. Halimeh, Z.-S. Yuan, Z. Papić, and J.-W. Pan, "Observation of many-body scarring in a Bose-Hubbard quantum simulator", Phys. Rev. Research **5**, 023010 (2023) (cit. on pp. 7, 80, 93).

[103] A. Impertro, S. Karch, J. F. Wienand, S. Huh, C. Schweizer, I. Bloch, and M. Aidelsburger, "Local readout and control of current and kinetic energy operators in optical lattices", arXiv:2312.13268 [cond-mat.quant-gas] (2023) (cit. on pp. 7, 80, 81, 93).

[104] W. Schleich, *Quantum optics in phase space* (Wiley, 2011) (cit. on pp. 7, 17, 19, 37, 137, 141).

[105] N. Baldelli, C. R. Cabrera, S. Julià-Farré, M. Aidelsburger, and L. Barbiero, "Frustrated extended Bose-Hubbard model and deconfined quantum critical points with optical lattices at the antimagic wavelength", Phys. Rev. Lett. **132**, 153401 (2024) (cit. on p. 8).

[106] J. Gambetta, *Expanding the IBM quantum roadmap to anticipate the future of quantum-centric supercomputing*, (2022) (cit. on pp. 8, 10, 111–114, 116, 121, 124).

[107] IBM, *Technology for the quantum future*, (2025) `https://www.ibm.com/quantum/technology` (cit. on pp. 8, 10, 111, 113, 114, 116, 121, 124).

[108] M. Krenn, J. Landgraf, T. Foesel, and F. Marquardt, "Artificial intelligence and machine learning for quantum technologies", Phys. Rev. A **107**, 010101 (2023) (cit. on pp. 8, 9).

[109] A. Bohrdt, C. S. Chiu, G. Ji, M. Xu, D. Greif, M. Greiner, E. Demler, F. Grusdt, and M. Knap, "Classifying snapshots of the doped Hubbard model with machine learning", Nature Physics **15**, 921 (2019) (cit. on p. 8).

[110] H. Nam Nguyen, F. Motzoi, M. Metcalf, K. Birgitta Whaley, M. Bukov, and M. Schmitt, "Reinforcement learning pulses for transmon qubit entangling gates", Machine Learning: Science and Technology **5**, 025066 (2024) (cit. on p. 8).

[111] D. Köglmayr and C. Räth, "Extrapolating tipping points and simulating non-stationary dynamics of complex systems using efficient machine learning", Scientific Reports **14**, 507 (2024) (cit. on p. 8).

[112] F. A. Rodrigues, "Machine learning in physics: a short guide", EPL **144**, 22001 (2023) (cit. on p. 8).

[113] G. Carleo and M. Troyer, "Solving the quantum many-body problem with artificial neural networks", Science **355**, 602 (2017) (cit. on pp. 8, 9, 96).

[114] F. Vicentini, A. Biella, N. Regnault, and C. Ciuti, "Variational neural-network ansatz for steady states in open quantum systems", Phys. Rev. Lett. **122**, 250503 (2019) (cit. on p. 9).

[115] G. Carleo, K. Choo, D. Hofmann, J. E. Smith, T. Westerhout, F. Alet, E. J. Davis, S. Efthymiou, I. Glasser, S.-H. Lin, M. Mauri, G. Mazzola, C. B. Mendl, E. van Nieuwenburg, O. O' Reilly, H. Théveniaut, G. Torlai, F. Vicentini, and A. Wietek, "Netket: a machine learning toolkit for many-body quantum systems", SoftwareX **10**, 100311 (2019) (cit. on p. 9).

[116] M. Schmitt and M. Reh, "jVMC: Versatile and performant variational Monte Carlo leveraging automated differentiation and GPU acceleration", SciPost Phys. Codebases, 2 (2022) (cit. on pp. 9, 96, 97, 105–107, 110).

[117] A. Chen and M. Heyl, "Empowering deep neural quantum states through efficient optimization", Nature Physics **20**, 1476 (2024) (cit. on pp. 9, 107, 108, 113, 124).

[118] M. Medvidović and J. R. Moreno, "Neural-network quantum states for many-body physics", The European Physical Journal Plus **139**, 10.1140/epjp/s13360-024-05311-y (2024) (cit. on p. 9).

[119] H. Lange, A. Van de Walle, A. Abedinnia, and A. Bohrdt, "From architectures to applications: a review of neural quantum states", Quantum Science and Technology **9**, 040501 (2024) (cit. on pp. 9, 96, 99, 108, 124).

[120] A. Bohrdt, S. Kim, A. Lukin, M. Rispoli, R. Schittko, M. Knap, M. Greiner, and J. Léonard, "Analyzing nonequilibrium quantum states through snapshots with artificial neural networks", Phys. Rev. Lett. **127**, 150504 (2021) (cit. on p. 9).

[121] J. B. Rigo and A. K. Mitchell, "Machine learning effective models for quantum systems", Phys. Rev. B **101**, 241105 (2020) (cit. on p. 9).

[122] K. Hornik, M. Stinchcombe, and H. White, "Multilayer feedforward networks are universal approximators", Neural Networks **2**, 359 (1989) (cit. on pp. 9, 95, 96).

[123] R. Orús, "A practical introduction to tensor networks: matrix product states and projected entangled pair states", Annals of Physics **349**, 117 (2014) (cit. on p. 9).

[124] S. Paeckel, T. Köhler, A. Swoboda, S. R. Manmana, U. Schollwöck, and C. Hubig, "Time-evolution methods for matrix-product states", Annals of Physics **411**, 167998 (2019) (cit. on p. 9).

[125] J. I. Cirac, D. Pérez-García, N. Schuch, and F. Verstraete, "Matrix product states and projected entangled pair states: concepts, symmetries, theorems", Rev. Mod. Phys. **93**, 045003 (2021) (cit. on p. 9).

[126] M. Schmitt and M. Heyl, "Quantum many-body dynamics in two dimensions with artificial neural networks", Phys. Rev. Lett. **125**, 100503 (2020) (cit. on pp. 9, 120, 124).

[127] S.-D. Börner, C. Berke, D. P. DiVincenzo, S. Trebst, and A. Altland, "Classical chaos in quantum computers", Phys. Rev. Res. **6**, 033128 (2024) (cit. on pp. 10, 11, 112).

[128] J. Koch, T. M. Yu, J. Gambetta, A. A. Houck, D. I. Schuster, J. Majer, A. Blais, M. H. Devoret, S. M. Girvin, and R. J. Schoelkopf, "Charge-insensitive qubit design derived from the Cooper pair box", Phys. Rev. A **76**, 042319 (2007) (cit. on pp. 10, 112).

[129] R. Versluis, S. Poletto, N. Khammassi, B. Tarasinski, N. Haider, D. J. Michalak, A. Bruno, K. Bertels, and L. DiCarlo, "Scalable quantum circuit and control for a superconducting surface code", Phys. Rev. Appl. **8**, 034021 (2017) (cit. on p. 10).

[130] J. B. Hertzberg, E. J. Zhang, S. Rosenblatt, E. Magesan, J. A. Smolin, J.-B. Yau, V. P. Adiga, M. Sandberg, M. Brink, J. M. Chow, and J. S. Orcutt, "Laser-annealing josephson junctions for yielding scaled-up superconducting quantum processors", npj Quantum Information **7**, 10.1038/s41534-021-00464-5 (2021) (cit. on p. 10).

[131] S. Krinner, N. Lacroix, A. Remm, A. Di Paolo, E. Genois, C. Leroux, C. Hellings, S. Lazar, F. Swiadek, J. Herrmann, G. J. Norris, C. K. Andersen, M. Müller, A. Blais, C. Eichler, and A. Wallraff, "Realizing repeated quantum error correction in a distance-three surface code", Nature **605**, 669 (2022) (cit. on p. 10).

[132] C. Berke, E. Varvelis, S. Trebst, A. Altland, and D. P. DiVincenzo, "Transmon platform for quantum computing challenged by chaotic fluctuations", Nature Communications **13**, 10.1038/s41467-022-29940-y (2022) (cit. on pp. 10, 11, 112).

[133] K. Tikhonov and A. Mirlin, "From Anderson localization on random regular graphs to many-body localization", Annals of Physics **435**, Special Issue on Localisation 2020, 168525 (2021) (cit. on pp. 10, 95).

[134] E. Ledinauskas and E. Anisimovas, "Universal performance gap of neural quantum states applied to the Hofstadter-Bose-Hubbard model", SciPost Phys. **18**, 011 (2025) (cit. on p. 10).

[135] K. Çeven, M. Ö. Oktel, and A. Kele ş, "Neural-network quantum states for a two-leg Bose-Hubbard ladder under magnetic flux", Phys. Rev. A **106**, 063320 (2022) (cit. on p. 10).

[136] F. Döschl, F. A. Palm, H. Lange, F. Grusdt, and A. Bohrdt, "Neural network quantum states for the interacting hofstadter model with higher local occupations and long-range interactions", Phys. Rev. B **111**, 045408 (2025) (cit. on p. 10).

[137] M. Y Pei and S. R Clark, "Specialising neural-network quantum states for the Bose Hubbard model", Journal of Physics B: Atomic, Molecular and Optical Physics **57**, 215301 (2024) (cit. on p. 10).

[138] H. Saito and M. Kato, "Machine learning technique to find quantum many-body ground states of bosons on a lattice", Journal of the Physical Society of Japan **87**, 014001 (2018) (cit. on p. 10).

[139] F. Arute, K. Arya, R. Babbush, D. Bacon, J. Bardin, R. Barends, R. Biswas, S. Boixo, F. Brandao, D. Buell, B. Burkett, Y. Chen, J. Chen, B. Chiaro, R. Collins, W. Courtney, A. Dunsworth, E. Farhi, B. Foxen, A. Fowler, C. M. Gidney, M. Giustina, R. Graff, K. Guerin, S. Habegger, M. Harrigan, M. Hartmann, A. Ho, M. R. Hoffmann, T. Huang, T. Humble, S. Isakov, E. Jeffrey, Z. Jiang, D. Kafri, K. Kechedzhi, J. Kelly, P. Klimov, S. Knysh, A. Korotkov, F. Kostritsa, D. Landhuis, M. Lindmark, E. Lucero, D. Lyakh, S. Mandrà, J. R. McClean, M. McEwen, A. Megrant, X. Mi, K. Michielsen, M. Mohseni, J. Mutus, O. Naaman, M. Neeley, C. Neill, M. Y. Niu, E. Ostby, A. Petukhov, J. Platt, C. Quintana, E. G. Rieffel, P. Roushan, N. Rubin, D. Sank, K. J. Satzinger, V. Smelyanskiy, K. J. Sung, M. Trevithick, A. Vainsencher, B. Villalonga, T. White, Z. J. Yao, P. Yeh, A. Zalcman, H. Neven, and J. Martinis, "Quantum supremacy using a programmable superconducting processor", Nature **574**, 505 (2019) (cit. on pp. 10, 116).

[140] F. Yan, P. Krantz, Y. Sung, M. Kjaergaard, D. L. Campbell, T. P. Orlando, S. Gustavsson, and W. D. Oliver, "Tunable coupling scheme for implementing high-fidelity two-qubit gates", Phys. Rev. Appl. **10**, 054062 (2018) (cit. on p. 10).

[141] Y. Xu, J. Chu, J. Yuan, J. Qiu, Y. Zhou, L. Zhang, X. Tan, Y. Yu, S. Liu, J. Li, F. Yan, and D. Yu, "High-fidelity, high-scalability two-qubit gate scheme for superconducting qubits", Phys. Rev. Lett. **125**, 240503 (2020) (cit. on p. 10).

[142] Y. Chen, C. Neill, P. Roushan, N. Leung, M. Fang, R. Barends, J. Kelly, B. Campbell, Z. Chen, B. Chiaro, A. Dunsworth, E. Jeffrey, A. Megrant, J. Y. Mutus, P. J. J. O'Malley, C. M. Quintana, D. Sank, A. Vainsencher, J. Wenner, T. C. White, M. R. Geller, A. N. Cleland, and J. M. Martinis, "Qubit architecture with high coherence and fast tunable coupling", Phys. Rev. Lett. **113**, 220502 (2014) (cit. on p. 10).

[143] J. E. Avron, A. Raveh, and B. Zur, "Adiabatic quantum transport in multiply connected systems", Rev. Mod. Phys. **60**, 873 (1988) (cit. on p. 10).

[144] B. Žunkovi č, P. Torta, G. Pecci, G. Lami, and M. Collura, "Variational ground-state quantum adiabatic theorem", Phys. Rev. Lett. **134**, 130601 (2025) (cit. on p. 10).

[145] D. Pfau, S. Axelrod, H. Sutterud, I. von Glehn, and J. S. Spencer, "Accurate computation of quantum excited states with neural networks", Science **385**, eadn0137 (2024), eprint: `https://www.science.org/doi/pdf/10.1126/science.adn0137` (cit. on p. 10).

[146] K. Choo, G. Carleo, N. Regnault, and T. Neupert, "Symmetries and many-body excitations with neural-network quantum states", Phys. Rev. Lett. **121**, 167204 (2018) (cit. on p. 11).

[147] J. Rammensee, "Semiclassical treatment of interference phenomena in bosonic quantum many-body systems", PhD thesis (Universität Regensburg, 2019) (cit. on pp. 16, 18, 129).

[148] R. A. Jalabert, I. García-Mata, and D. A. Wisniacki, "Semiclassical theory of out-of-time-order correlators for low-dimensional classically chaotic systems", Phys. Rev. E **98**, 062218 (2018) (cit. on pp. 16, 21).

[149] J. Kurchan, "Quantum bound to chaos and the semiclassical limit", J. Stat. Phys. **171**, 965 (2018) (cit. on p. 16).

[150] T. R. Michel, J. Diego Urbina, and P. Schlagheck, "Quasiclassical theory of out-of-time-ordered correlators", Journal of Physics A: Mathematical and Theoretical **58**, 275303 (2025) (cit. on p. 16).

[151] I. García-Mata, M. Saraceno, R. A. Jalabert, A. J. Roncaglia, and D. A. Wisniacki, "Chaos signatures in the short and long time behavior of the out-of-time ordered correlator", Phys. Rev. Lett. **121**, 210601 (2018) (cit. on pp. 18, 33, 49).

[152] M. Gutzwiller, *Chaos in classical and quantum mechanics*, Interdisciplinary Applied Mathematics (Springer New York, 1991) (cit. on p. 18).

[153] M. Brack and R. Bhaduri, *Semiclassical physics*, Frontiers in physics (Avalon Publishing, 1997) (cit. on p. 18).

[154] M. Akila, D. Waltner, B. Gutkin, P. Braun, and T. Guhr, "Semiclassical identification of periodic orbits in a quantum many-body system", Phys. Rev. Lett. **118**, 164101 (2017) (cit. on p. 18).

[155] P. Braun, D. Waltner, M. Akila, B. Gutkin, and T. Guhr, "Transition from quantum chaos to localization in spin chains", Phys. Rev. E **101**, 052201 (2020) (cit. on p. 18).

[156] B. Craps, M. De Clerck, D. Janssens, V. Luyten, and C. Rabideau, "Lyapunov growth in quantum spin chains", Phys. Rev. B **101**, 174313 (2020) (cit. on p. 18).

[157] T. Engl, J. D. Urbina, and K. Richter, "Periodic mean-field solutions and the spectra of discrete bosonic fields: trace formula for Bose-Hubbard models", Phys. Rev. E **92**, 062907 (2015) (cit. on p. 18).

[158] E. Fortes, I. Garcia-Mata, R. Jalabert, and D. Wisniacki, "Gauging classical and quantum integrability through out-of-time-ordered correlators", Phys. Rev. E **100**, 10.1103/PhysRevE.100.042201 (2019) (cit. on pp. 18, 21).

[159] A. Polkovnikov, K. Sengupta, A. Silva, and M. Vengalattore, "Colloquium: nonequilibrium dynamics of closed interacting quantum systems", Rev. Mod. Phys. **83**, 863 (2011) (cit. on p. 18).

[160] Y. S. Kim and M. E. Noz, *Phase space picture of quantum mechanics* (World Scientific, 1991) (cit. on p. 19).

[161] R. F. O'Connell, "Book review: "Quantum mechanics in phase space: an overview with selected papers", edited by C. K. Zachos, D. B. Fairlie, T. L. Curtright", International Journal of Quantum Information **06**, 415 (2008) (cit. on p. 19).

[162] J. Estève, C. Gross, A. Weller, S. Giovanazzi, and M. K. Oberthaler, "Squeezing and entanglement in a Bose-Einstein condensate", Nature **455**, 1216 (2008) (cit. on pp. 20, 32).

[163] B. Geiger, *From few to many particles: semiclassical approaches to interacting quantum systems*, Vol. 55 (University of Regensburg, Aug. 2020) (cit. on p. 22).

[164] E. Il'ichev, M. Grajcar, R. Hlubina, R. P. J. IJsselsteijn, H. E. Hoenig, H.-G. Meyer, A. Golubov, M. H. S. Amin, A. M. Zagoskin, A. N. Omelyanchouk, and M. Y. Kupriyanov, "Degenerate ground state in a mesoscopic $YBa_2Cu_3O_{7-x}$ grain boundary Josephson junction", Phys. Rev. Lett. **86**, 5369 (2001) (cit. on p. 22).

[165] M. Albiez, R. Gati, J. Fölling, S. Hunsmann, M. Cristiani, and M. K. Oberthaler, "Direct observation of tunneling and nonlinear self-trapping in a single bosonic Josephson junction", Phys. Rev. Lett. **95**, 010402 (2005) (cit. on p. 22).

[166] S. Fölling, S. Trotzky, P. Cheinet, M. Feld, R. Saers, A. Widera, T. Müller, and I. Bloch, "Direct observation of second-order atom tunnelling", Nature **448**, 1029 (2007) (cit. on p. 22).

[167] D. Witthaut, F. Trimborn, and S. Wimberger, "Dissipation induced coherence of a two-mode Bose-Einstein condensate", Phys. Rev. Lett. **101**, 200402 (2008) (cit. on p. 22).

[168] P. Cheinet, S. Trotzky, M. Feld, U. Schnorrberger, M. Moreno-Cardoner, S. Fölling, and I. Bloch, "Counting atoms using interaction blockade in an optical superlattice", Phys. Rev. Lett. **101**, 090404 (2008) (cit. on p. 22).

[169] E. Kierig, U. Schnorrberger, A. Schietinger, J. Tomkovic, and M. K. Oberthaler, "Single-particle tunneling in strongly driven double-well potentials", Phys. Rev. Lett. **100**, 190405 (2008) (cit. on pp. 22, 32).

[170] J. Tomkovič, W. Muessel, H. Strobel, S. Löck, P. Schlagheck, R. Ketzmerick, and M. K. Oberthaler, "Experimental observation of the Poincaré-Birkhoff scenario in a driven many-body quantum system", Phys. Rev. A **95**, 011602 (2017) (cit. on p. 22).

[171] H. Lipkin, N. Meshkov, and A. Glick, "Validity of many-body approximation methods for a solvable model: (i). exact solutions and perturbation theory", Nuclear Physics **62**, 188 (1965) (cit. on p. 22).

[172] J. Negele and H. Orland, *Quantum many particle systems* (Basic Books, 1995) (cit. on p. 23).

[173] D. K. Campbell, "The remarkable BEC dimer", in Strongly coupled field theories for condensed matter and quantum information theory, edited by A. Ferraz, K. S. Gupta, G. W. Semenoff, and P. Sodano (2020), pp. 247–258 (cit. on pp. 23, 125).

[174] M. Steinhuber, "Semiclassical approach to the high-dimensional self-trapping of interacting cold atoms in optical lattices", Master Thesis (Universität Regensburg, 2020) (cit. on pp. 23, 35, 57, 59, 65, 70, 76, 94, 142, 143, 150).

[175] C. Gardiner, P. Zoller, and P. Zoller, *Quantum noise: a handbook of Markovian and non-Markovian quantum stochastic methods with applications to quantum optics*, Springer Series in Synergetics (Springer, 2004) (cit. on pp. 29, 135).

[176] H. Lignier, C. Sias, D. Ciampini, Y. Singh, A. Zenesini, O. Morsch, and E. Arimondo, "Dynamical control of matter-wave tunneling in periodic potentials", Phys. Rev. Lett. **99**, 220403 (2007) (cit. on pp. 32, 93).

[177] A. Lakshminarayan, "Out-of-time-ordered correlator in the quantum Bakers map and truncated unitary matrices", Phys. Rev. E **99**, 012201 (2019) (cit. on p. 33).

[178] E. B. Rozenbaum, S. Ganeshan, and V. Galitski, "Lyapunov exponent and out-of-time-ordered correlator's growth rate in a chaotic system", Phys. Rev. Lett. **118**, 086801 (2017) (cit. on pp. 42, 127).

[179] S. Aaronson and A. Arkhipov, "The computational complexity of linear optics", in Proceedings of the forty-third annual ACM symposium on theory of computing (2011), pp. 333–342 (cit. on p. 43).

[180] M. Child, *Semiclassical mechanics with molecular applications* (Oxford University Press, 2014) (cit. on pp. 45, 128, 129).

[181] E. J. Heller, "Bound-state eigenfunctions of classically chaotic Hamiltonian systems: scars of periodic orbits", Phys. Rev. Lett. **53**, 1515 (1984) (cit. on p. 51).

[182] J. L. O' Brien, A. Furusawa, and J. Vučković, "Photonic quantum technologies", Nature Photonics **3**, 687 (2009) (cit. on p. 67).

[183] T. D. Ladd, F. Jelezko, R. Laflamme, Y. Nakamura, C. Monroe, and J. L. O'Brien, "Quantum computers", Nature **464**, 45 (2010) (cit. on p. 67).

[184] B. Lenze, *Mathematik und quantum computing* (Logos Verlag, 2018) (cit. on p. 67).

[185] A. N. Kolmogorov, "Entropy per unit time as a metric invariant of automorphism", Doklady of Russian Academy of Sciences **124**, 754 (1959) (cit. on p. 68).

[186] G. P. Berman and G. M. Zaslavsky, "Condition of stochasticity of quantum nonlinear systems", Physica A **91**, 450 (1978) (cit. on p. 68).

[187] G. M. Zaslavsky, "Stochasticity in quantum systems", Phys. Rep. **80**, 157 (1981) (cit. on p. 68).

[188] S. Tomsovic, "Complex saddle trajectories for multidimensional quantum wave packet and coherent state propagation: application to a many-body system", Phys. Rev. E **98**, 023301 (2018) (cit. on pp. 70, 71, 73, 74).

[189] Y. Yanay, J. Braumüller, S. Gustavsson, W. Oliver, and C. Tahan, "Two-dimensional hard-core Bose-Hubbard model with superconducting qubits", npj Quantum Information **6**, 58 (2020) (cit. on pp. 71, 112).

[190] K. Sacha and J. Zakrzewski, "Time crystals: a review", Reports on Progress in Physics **81**, 016401 (2017) (cit. on pp. 71, 94, 125).

[191] V. P. Maslov and M. V. Fedoriuk, *Semiclassical approximation in quantum mechanics* (Reidel Publishing Company, Dordrecht, 1981) (cit. on p. 73).

[192] M. Greiner, O. Mandel, T. W. Hänsch, and I. Bloch, "Collapse and revival of the matter wave field of a Bose-Einstein condensate", Nature **419**, 51 (2002) (cit. on p. 75).

[193] J. E. Moyal, "The Monte Carlo method", Proc. Camb. Philos. Soc. **45**, 99 (1949) (cit. on p. 75).

[194] H. Weyl, "Quantum mechanics and group theory", Z. Phys. **46**, 1 (1927) (cit. on p. 75).

[195] M. J. Steel, M. K. Olsen, L. I. Plimak, P. D. Drummond, S. M. Tan, M. J. Collett, D. F. Walls, and R. Graham, "Dynamical quantum noise in trapped Bose-Einstein condensates", Phys. Rev. A **58**, 4824 (1998) (cit. on p. 75).

[196] A. Sinatra, C. Lobo, and Y. Castin, "The truncated Wigner method for Bose-condensed gases: limits of validity and applications", J. Phys. B: Atom. Molec. Phys. **35**, 3599 (2002) (cit. on p. 75).

[197] E. J. Heller, "Time-dependent approach to semiclassical dynamics", J. Chem. Phys. **62**, 1544 (1975) (cit. on pp. 87, 150).

[198] P. Hannaford and K. Sacha, "Time crystals enter the real world of condensed matter", Physics World **33**, 42 (2020) (cit. on pp. 94, 125).

[199] D. Wellnitz, G. A. Domínguez-Castro, T. Bilitewski, M. Aidelsburger, A. M. Rey, and L. Santos, "Emergent interaction-induced topology in Bose-Hubbard ladders", Phys. Rev. Res. **7**, L012012 (2025) (cit. on p. 95).

[200] M. Schmitt and M. Heyl, *Simulating dynamics of correlated matter with neural quantum states*, 2025, eprint: 2506.03124 (quant-ph) (cit. on pp. 96, 120, 123).

[201] DeepMind, I. Babuschkin, K. Baumli, A. Bell, S. Bhupatiraju, J. Bruce, P. Buchlovsky, D. Budden, T. Cai, A. Clark, I. Danihelka, A. Dedieu, C. Fantacci, J. Godwin, C. Jones, R. Hemsley, T. Hennigan, M. Hessel, S. Hou, S. Kapturowski, T. Keck, I. Kemaev, M. King, M. Kunesch, L. Martens, H. Merzic, V. Mikulik, T. Norman, G. Papamakarios, J. Quan, R. Ring, F. Ruiz, A. Sanchez, L. Sartran, R. Schneider, E. Sezener, S. Spencer, S. Srinivasan, M. Stanojević, W. Stokowiec, L. Wang, G. Zhou, and F. Viola, *The DeepMind JAX Ecosystem*, 2020 (cit. on pp. 96, 97, 107, 108, 113).

[202] W. H. Press, S. A. Teukolsky, W. T. Vettering, and B. P. Flannery, *Numerical recipes in Fortran, the art of scientific computing* (Cambridge University Press, 1992) (cit. on p. 98).

[203] A. Malyshev, M. Schmitt, and A. I. Lvovsky, *Neural quantum states and peaked molecular wave functions: curse or blessing?*, Aug. 2024, eprint: 2408.07625 (quant-ph) (cit. on pp. 98, 103, 114).

[204] A. Vaswani, N. Shazeer, N. Parmar, J. Uszkoreit, L. Jones, A. N. Gomez, L. Kaiser, and I. Polosukhin, *Attention is all you need*, 2023, arXiv:1706.03762 [cs.CL] (cit. on pp. 99, 101).

[205] OpenAI, *ChatGPT*, https://chat.openai.com/, Large language model developed by OpenAI. Version: o4-mini (accessed 2025-08-01), 2025 (cit. on p. 99).

[206] B. Peng, E. Alcaide, Q. Anthony, A. Albalak, S. Arcadinho, S. Biderman, H. Cao, X. Cheng, M. Chung, M. Grella, K. K. GV, X. He, H. Hou, J. Lin, P. Kazienko, J. Kocon, J. Kong, B. Koptyra, H. Lau, K. S. I. Mantri, F. Mom, A. Saito, G. Song, X. Tang, B. Wang, J. S. Wind, S. Wozniak, R. Zhang, Z. Zhang, Q. Zhao, P. Zhou, Q. Zhou, J. Zhu, and R.-J. Zhu, *RWKV: reinventing RNNs for the transformer era*, 2023, eprint: 2305.13048 (cs.CL) (cit. on pp. 99, 102).

[207] A. Malyshev, J. M. Arrazola, and A. I. Lvovsky, "Autoregressive neural quantum states with quantum number symmetries", 10.48550/arxiv.2310.04166 (2023), eprint: 2310.04166 (quant-ph) (cit. on p. 102).

[208] E. J. Gumbel, *Statistics of extremes* (Dover Publications Inc., New York, 2004) (cit. on p. 103).

[209] S. Sorella and L. Capriotti, "Green function Monte Carlo with stochastic reconfiguration: an effective remedy for the sign problem", Phys. Rev. B **61**, 2599 (2000) (cit. on p. 107).

[210] S.-i. Amari, R. Karakida, and M. Oizumi, "Fisher information and natural gradient learning in random deep networks", in Proceedings of the twenty-second international conference on artificial intelligence and statistics, Vol. 89, edited by K. Chaudhuri and M. Sugiyama, Proceedings of Machine Learning Research (2019), pp. 694–702 (cit. on p. 107).

[211] M. Born and V. Fock, "Beweis des Adiabatensatzes", Z. Phys. **51**, 165 (1928) (cit. on p. 109).

[212] V. Bouchiat, D. Vion, P. Joyez, D. Esteve, and M. H. Devoret, "Quantum coherence with a single Cooper pair", Phys. Scr. **1998**, 165 (1998) (cit. on p. 112).

[213] A. Blais, A. L. Grimsmo, S. M. Girvin, and A. Wallraff, "Circuit quantum electrodynamics", Rev. Mod. Phys. **93**, 025005 (2021) (cit. on p. 112).

[214] S. Bravyi, D. DiVincenzo, R. Oliveira, and B. Terhal, "The complexity of stoquastic local Hamiltonian problems", Quantum Information and Computation **8**, 0361 (2006) (cit. on p. 113).

[215] A. Sinibaldi, C. Giuliani, G. Carleo, and F. Vicentini, "Unbiasing time-dependent Variational Monte Carlo by projected quantum evolution", Quantum **7**, 1131 (2023) (cit. on pp. 118, 119).

[216] L. Landau, "Zur Theorie der Energieübertragung. II", Physikalische Zeitschrift der Sowjetunion **2**, 46 (1932) (cit. on p. 120).

[217] C. Zener, "Non-adiabatic crossing of energy levels", Proceedings of the Royal Society of London. Series A, Containing Papers of a Mathematical and Physical Character **137**, 696 (1932) (cit. on p. 120).

[218] W. Fu, W. Ren, and J. Chen, "Variance extrapolation method for neural-network variational Monte Carlo", Machine Learning: Science and Technology **5**, 015016 (2024) (cit. on p. 121).

[219] Y. Watanabe, R. W. Chhajlany, M. Lewenstein, T. Graß, and U. Bhattacharya, *Contemporary tensor network approaches to gapless and topological phases in an extended Bose-Hubbard ladder*, 2025, eprint: 2505.00106 (cond-mat.quant-gas) (cit. on p. 121).

[220] W. Krinitsin, N. Tausendpfund, M. Rizzi, M. Heyl, and M. Schmitt, "Roughening dynamics of interfaces in the two-dimensional quantum Ising model", Phys. Rev. Lett. **134**, 240402 (2025) (cit. on p. 121).

[221] H. Kim, M. Fishman, and D. Sels, "Variational adiabatic transport of tensor networks", PRX Quantum **5**, 020361 (2024) (cit. on p. 122).

[222] S. Tomsovic, P. Schlagheck, D. Ullmo, J.-D. Urbina, and K. Richter, "Post-Ehrenfest many-body quantum interferences in ultracold atoms far out of equilibrium", Phys. Rev. A **97**, 061606 (2018) (cit. on p. 124).

[223] S. Deffner and S. Campbell, "Quantum speed limits: from Heisenber's uncertainty principle to optimal quantum control", Journal of Physics A: Mathematical and Theoretical **50**, 453001 (2017) (cit. on p. 124).

[224] V. I. Arnol'd, *Mathematical methods of classical mechanics* (Springer, Berlin, 1978) (cit. on p. 127).

[225] V. Oseledets, "Oseledets theorem", Scholarpedia **3**, revision #142085, 1846 (2008) (cit. on p. 128).

[226] A. Politi, "Lyapunov exponent", Scholarpedia **8**, revision #137286, 2722 (2013) (cit. on p. 128).

[227] A. Prasad and R. Ramaswamy, "Characteristic distributions of finite-time Lyapunov exponents", Phys. Rev. E **60**, 2761 (1999) (cit. on pp. 128, 129).

[228] W. B. Case, "Wigner functions and Weyl transforms for pedestrians", American Journal of Physics **76**, 937 (2008) (cit. on p. 135).

[229] T. L. Curtright and C. K. Zachos, "Quantum mechanics in phase space", Asia Pacific Physics Newsletter **01**, 37 (2012) (cit. on p. 135).

[230] W. Nolting, *Grundkurs Theoretische Physik 5/1: Quantenmechanik - Grundlagen*, Springer-Lehrbuch (Springer Berlin Heidelberg, 2013) (cit. on p. 140).